EXTERNAL STIMULI DRIVEN TRANSFORMATIONS OF BN-HETEROCYCLES

by

Dengtao Yang

A thesis submitted to the Department of Chemistry

In conformity with the requirements for

the degree of Doctor of Philosophy

Queen's University

Kingston, Ontario, Canada

(October, 2017)

Abstract

BN-heterocycles have important applications in synthetic methodologies, chemical reactivity and optoelectronics. This thesis focuses on the investigation of the thermal and photo-responsive properties of BN-heterocycles as well as applications in optoelectronic devices. In search of more efficient photoelimination of BN-heterocycles, we found that BN-heterocycles could have different and unique transformations upon external stimuli. The preparation of the BN-polycyclic aromatic hydrocarbons (PAHs) is also described.

Boranes with the general formula of HBR_2 have been found to undergo a facile 1,1-hydroboration reaction with pyrido[1,2-*a*]isoindole, resulting in insertion of a BR_2 unit into a C-N bond and the formation of a variety of BN-heterocycles. Investigation on the thermal reactivity of the BN-heterocycles revealed that these molecules have two distinct and competitive thermal elimination pathways: HBR_2 elimination (or retro-hydroboration) versus R-H elimination, depending on the R group on the B atom and the chelate backbone.

Given the 1,3-dipolar nature pyrido[1,2-*a*]isoindole, a "one-pot" cycloaddition procedure of pyrido[1,2-*a*]isoindole and its analogues with dimesitylboron functionalized alkynes has been successfully developed for the synthesis of a series of $BMes_2$-functionalized N-heterocycles.

To further expand the photoelimination reaction to multiple BN-doped PAHs, new BN-heterocyclic compounds have been found to undergo double photoelimination, forming rare yellow fluorescent $(BN)_2$-arenes that contain two B-N units. Most significant is the discovery that the double elimination can also be driven by excitons generated electrically within electroluminescent (EL) devices, enabling the *in situ* solid-state conversion of BN-heterocycles to BN-arenes and the use of BN-arenes as emitters for EL devices. The *in situ* exciton-driven elimination (EDE) phenomenon has also been observed for other BN-heterocycles.

Besides changing external stimuli to improve the efficiency of elimination of BN-heterocycles, the internal factor - the effect of substituents on boron atom was also investigated. We found that

both electronic and steric effects have a significant and distinct impact on the photoreaction pathways of BN-heterocycles. With bulky, electron-donating aryl rings on the B atom, the photoelimination efficiency is enhanced. In contrast, with sufficiently electron-withdrawing aryl groups on the B atom, bulky or not, photoisomerization occurs exclusively with a high stereoselectivity.

Co-Authorship

Chapter 2: The DFT and TD-DFT calculations were performed by Soren K. Mellerup.

Chapter 3: The DFT and TD-DFT calculations were performed by Soren K. Mellerup. And the synthesis of compound **3.2** was carried out by Julian Radtke. Kuan Yuan provided the compounds (2-ethynylphenyl)dimesitylborane and (4-ethynylphenyl)dimesitylborane.

Chapter 4: The synthesis of compound **4.5** was carried out by Yonggang Shi. The X-ray structure of compound **4.5** was obtained by Prof. Tai Peng at at the Beijing Institute of Technology of China. And the original synthesis of compound **4.6** and **4.7** were carried out by Dr. Jiasheng Lu and Hiroyuki Shimogawa, respectively. The X-ray structure of compound of **4.6** was obtained in Prof. Atsushi Wakamiya group at Kyoto University. Electroluminescent devices were fabricated and tested by Dr. Shaolong Gong at the University of Toronto in the laboratory of Prof. Zheng-Hong Lu. The step-wise elimination of **4.6** was performed by Soren K. Mellerup. The DFT calculations of Figure 4.8 was performed by Dr. Xiang Wang.

Chapter 5: The DFT and TD-DFT calculations were performed by Soren K. Mellerup and Prof. Quan-Song Li at the Beijing Institute of Technology of China. The first synthesis of compound **5.2** was carried out by Dr. Jin-Bao Peng.

Acknowledgements

The most important acknowledgement of gratitude I wish to express is my supervisor Prof. Suning Wang for her continuous support of my PhD study and research, for her patience, motivation, and immense knowledge. Her guidance helped me in all the time of research and writing of papers and this thesis. I could not have imagined where I would go if she did not recruit me as her PhD student at the first place. During the past four years, I learned most is her attitude to science and research, and I still remember she told me – "we should do something important and original that could be written into textbooks in decades", which have changed my way of thinking of scientific research and will guide me for my whole academic career in the future.

I would also like to thank my research committee members Prof. Anne Petitjean and Prof. P. Andrew Evans for their help, advice, and valuable time towards my research and thesis. And I am sincerely grateful to Prof. Anne Petitjean for her references when I was looking for postdoc position. I also want to thank Dr. Françoise Sauriol for NMR spectroscopy, Dr. Jia-Xi Wang for Mass spectrometry, respectively.

I am also grateful for the wonderful time with many knowledgeable postdoctoral fellows and young talented chemists in the Wang group. First, I would like to express my gratitude to Dr. Xiang Wang who provided me generous and patient guidance when I first came to this lab. Also, I sincerely appreciate the friendship, suggestions, and encouragement from all the past and present group members I spent the last four years working alongside.

Lastly, I would like to thank my parents and my little sister for their immense support all along. I would also like to thank my wife Jie Zheng who has been fully supportive and understanding throughout all the good and bad times, especially those "fight" time. Also, there are plenty of friends in China I would like to thank for their encouragement when I feel frustrated and helpless.

Statement of Originality

I hereby certify that all of the work described within this thesis is the original work of the author.
Published (or unpublished) ideas and/or techniques from the work of others are fully acknowledged
in accordance with the standard referencing practices.

(Dengtao Yang)

(10, 2017)

Table of Contents

List of Figures

xix

List of Tables

List of Abbreviations

º	degrees
ºC	degree Celsius
δ	chemical shift
Δ	heating
ε	Molar extinction coefficient
λ	wavelength
μs	microsecond
τ	decay lifetime
Φ	Quantum efficiency
Å	angstrom
A	absorbance
=	double bond; equal to
Alq_3	tris(8-hydroxyquinolate)aluminum (III)
Anal. Calcd	Elemental analysis calculated
Ar	aromatic
a.u.	atomic unit
br	broad
BuLi or ^{n}BuLi	Butyllithium
CBP	4,4'-*N,N*'-dicarbazolebiphenyl
cd	candelas
CE	current efficiency
COSY	correlation spectroscopy
COT	cyclooctatriene
Cp	cyclopentadienyl

CT	cyclic voltammetry
d	doublet
DCM	dichloromethane
DFT	density functional theory
DMF	dimethylformamide
DMSO	dimethylsulfoxide
$E_{1/2}^{ox}$	half-cell oxidation potential
$E_{1/2}^{red}$	half-cell reduction potential
EL	electroluminescence
EML	emissive layer
EQE	external quantum efficiency
eq.	equivalents
Et	ethyl
ETL	electron transport layer
eV	electron Volts
FLP	frustrated Lewis pair
HMBC	heteronuclear multiple-bond correlation spectroscopy
HMQC	heteronuclear multi-quantum correlation spectroscopy
HSQC	heteronuclear single-quantum correlation spectroscopy
I	intensity
IC	internal conversion
ISC	intersystem crossing
h; hrs	hours
hυ	light
HOMO	highest occupied molecular orbital

HRMS	high-resolution mass spectrometry
HTL	hole transport layer
Hz	hertz
ITO	indium tin oxide
J	coupling constant
K	Kelvin
kJ	kilojoules
LDA	Lithium diisopropylamide
LUMO	lowest unoccupied molecular orbital
Me	methyl
MeCN	acetonitrile
Mes	mesityl
MHz	megahertz
mL	millilitre
mol	mole
NHC	*N*-heterocyclic carbene
NICS	nucleus independent chemical shift
NMR	nuclear magnetic resonance
NOESY	nuclear Overhauser effect spectroscopy
NPB	*N,N'*-di[(1-naphthyl)-*N,N'*-diphenyl]-(1,1'-biphenyl)-4,4'-diamine
OFET	organic field-effect transistor
OLED	organic light-emitting diode
OPV	organic photovoltaics
PAH	polycyclic aromatic hydrocarbon
Ph	phenyl

PHOLED	phosphorescent organic light-emitting diode
PMMA	poly(methyl methacrylate)
ppm	parts per million
ppy	phenylpyridine
rt; r.t.	room temperature
s	second
S_0	singlet ground state
$S_n (n>0)$	n^{th} singlet excited state
t	triplet; time
TADF	thermally activated delayed fluorescence
TD-DFT	time-dependent density functional theory
TMEDA	tetramethylethylenediamine
THF	tetrahydrofuran
UV	ultraviolet
V	volt; volume
Vis	visible

Chapter 1

Introduction

Due to the empty p-orbital of the boron atom (Figure 1.1), Organoboron compounds are an important class of molecules, which can be found in 1)organic synthesis and catalysis due to its Lewis acidity, and 2) optoelectronic materials and medicine involving boron-doped heterocycles.[1]
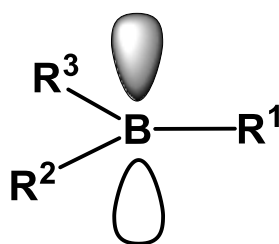
R^1 = alkyl, alkenyl, alkynyl, aryl; R^2, R^3 = H, alkyl, alkenyl, alkynyl, aryl

Figure 1.1 Organoboranes

In this thesis, we aim to design and synthesize novel BN-polycyclic aromatic hydrocarbons (PAHs) by improving the quantum efficiency of photoelimination of BN-heterocycles. In this chapter, applications of organoboranes in chemical reactivity and optoelectronics will be presented, followed by a review of synthesis and optoelectronic properties of boron-doped aromatic compounds. The photochemistry of organoboranes and recent research progress will be mentioned at the end. Due to the breadth of this work, subsequent chapters will also provide an introductory discussion more specific to each topic.

1.1 Reactivity of Organoboranes

Due to the vacant p-orbital of the boron atom, organoboranes are readily attacked on the boron atom by bases and nucleophiles. This property provides organoboranes a basis for a number of

1

synthetic and catalytic applications.[2-4] The impact of this element on modern organic chemistry over the last several decades is nothing short of remarkable.

1.1.1 Hydroboration

One of the most famous applications of organoboranes is 1,2-hydroboration, which was originally discovered by Herbert C. Brown[2] and recognized by the Nobel Prize in Chemistry. Hydroboration refers to the addition of a hydrogen-boron bond to C-C, C-N, and C-O double bonds, as well as C-C triple bonds (Figure 1.2). The *syn*-addition of organoboranes to multiple bond systems occurs with predictable selectivity, wherein the boron adds preferentially to the least hindered carbon atom (anti-Markovnikov). The products can undergo further reactions to produce alcohols via oxidation by hydrogen peroxide, and may also be used as starting materials for other reactions, such as Suzuki couplings.[4]
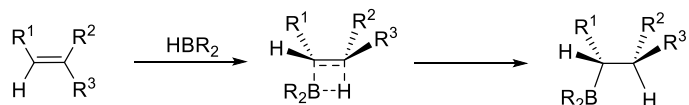
Figure 1.2 1,2-hydroboration[2]

Despite the large number of examples/uses of 1,2-hydroboration, the related 1,1-hydroboration reactions have, for the most part, eluded researchers. There are a few examples of formal alkyne 1,1-hydroboration involving the use of activating reagents.

In 2013, Curran and co-workers reported Lewis acid activated borenium-catalyzed hydroboration reactions of N-heterocyclic carbene−borane **1.1** with allyl-, alkenyl-, and alkynylsilane substrates (Figure 1.3).[5] In this system, for some substrates (*e.g.* bis-silylalkynes), formal 1,1-hydroboration reaction occurs by 1,2-silyl shifts.

2
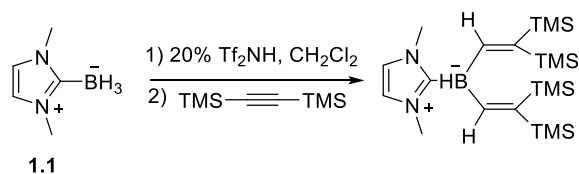
Figure 1.3 Borenium-catalyzed formal 1,1-hydroboration.[5]

Rivard group[6a] and Stephan group[6b] discovered an insertion reaction of C-N bonds of an N-heterocyclic carbene into a borane (Figure 1.4). In the ring expansion process reported by Stephan, a formal 1,1-hydroboration product was proposed to be one of the intermediates **1.2** through migration of the H atom from boron to the electron-deficient carbene carbon atom.
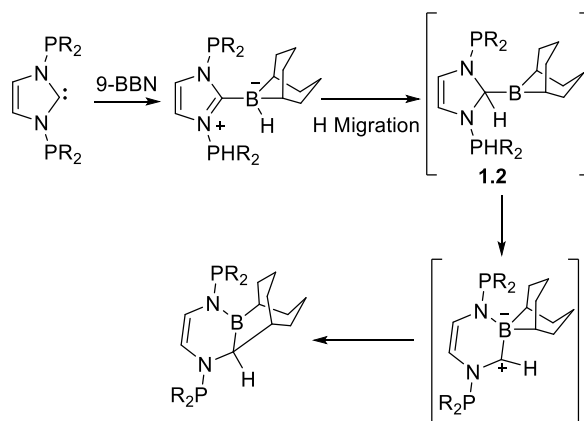
Figure 1.4 Carbene-9-BBN ring expansion.[6b]

1.1.2 Carboboration

In addition to hydroboration, carboboration is also known, which is studied much less than the former, because the formation boron−carbon bonds between boranes and multiple C-C bonds is considerably more difficult. Like hydroboration, carboboration also can be categorized into 1,2-carboboration and 1,1-carboboration.

1.1.2.1 1,2-Carboboration

1,2-Carboboration, similar to 1,2-hydroboration, refers to the addition of a carbon-boron bond to C-C multiple bonds, and recently has become popular, due to its synthetic usefulness. Considering the high energy of B-C bonds, this process usually needs catalysts. Very recently, several novel catalyst-free 1,2-carboboration with reactive boron species have been reported.

9-Chloro-9-borafluorene involving a 1,2-carboboration and a subsequent oxidative deborylation /C(sp^2)–C(sp^2) coupling has been reported by Fukushima *et al*, which enables the conversion of alkynes into the corresponding benzannulated and cyclodehydrogenated products with extended π-conjugated frameworks involving the formation of borepin (Figure 1.5).[7] This protocol could substantially expand the understanding of main group chemistry and provide a powerful synthetic tool for the construction of a wide variety of extended π-conjugated systems.
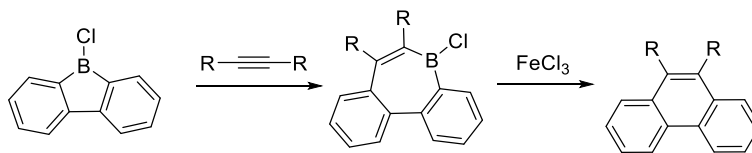
Figure 1.5 Boron-mediated Csp^2–Csp^2 coupling reactions.[7]
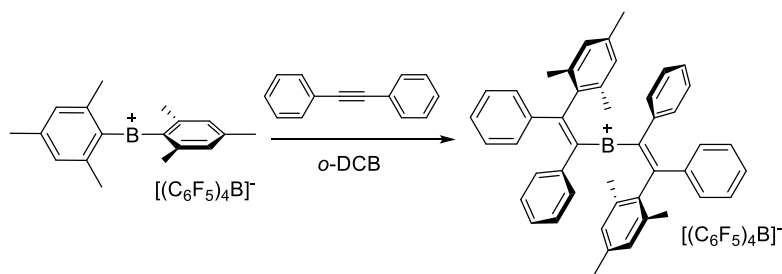
Figure 1.6 Twofold 1,2-carboboration reactions with dimesitylborinium ion (Mes$_2$B$^+$).[8]

Using the most electron-deficient isolable boron species - diarylborinium ion, Shoji and Fukushima found that the dimesitylborinium ion (Mes$_2$B$^+$) could undergo twofold 1,2-carboboration reactions with two equivalents of diphenylacetylene to yield an unprecedented

borinium ion with two substituted vinyl groups on the boron center (Figure 1.6), which is exceptionally rare due to the lack of steric protection on boron center.[8]

These two examples of 1,2-carboboration mentioned above mainly depends on the specific and reactive boron species. Very recently, Woerpel group discovered a *syn*-1,2-carboboration involving different commercially available boranes with seven membered-ring *trans*-alkenes **1.3** (Figure 1.7).[9] This reaction sequence permits the construction of compounds with up to five consecutive stereocenters. In contrast with other trialkylboranes, which can ignite in the presence of oxygen, these trialkylborane products are stable in air, as a result of steric protection and hyperconjugation of adjacent bonds. The carbon−boron and carbon−silicon bonds of the products can be oxidized to form synthetically useful triols.
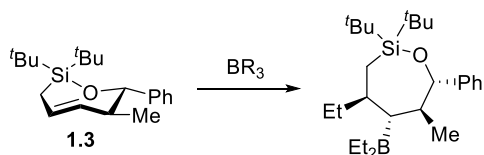
Figure 1.7 Uncatalyzed carboboration of seven-membered-ring *trans*-alkenes.[9]

1.1.2.2 1,1-Carboboration

Although 1,1-carboboration mechanistically proceeds through a very complicated process to reach the 1,1-carboboration products, it formally resembles an insertion of a vinylidene isomer of an alkyne into a B–C bond of a borane. Examples of the 1,1-carboboration reactions have long been known. [10,11] However, this reaction seems so far not to have been used on a large scale for general synthesis of alkenylboranes, because, generally, 1,1-carboboration cannot proceed without metal functionalized alkynes (M-C≡CR), due to the polarization of the M-C bonds. Most metal-assisted 1,1-carboborations in the literature involve a two-step activation of M-C≡CR bonds by the electron-deficient boron atom, either intermolecularly or intramolecularly. As shown in Figure 1.8, the

intermolecular 1,1-carboration goes through the activation of the M-C≡CR bond which results in the cleavage of this bond and the formation of a zwitterionic intermediate, followed by the migration of one R group. Normally, if the metal fragment contains another alkynyl group, the intramolecular activation of M-C≡CR bond would happen next, which can result in the formation of metalloles.[11]
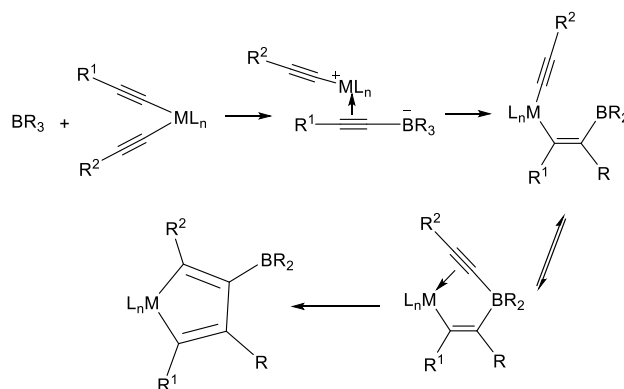
Figure 1.8 The formation of metalloles by 1,1-carboration.[11]

(i) toluene, 110 °C, 3d. (ii) Pd(PPh$_3$)$_4$ (10%), NaOH, THF/H$_2$O,
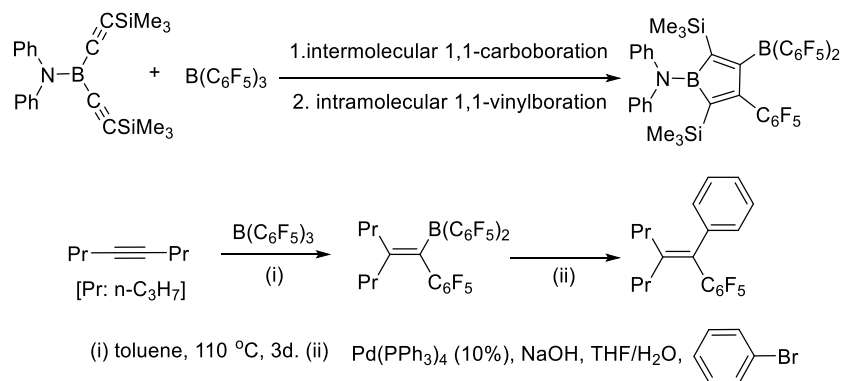
Figure 1.9 The formation of boroles and 1,1-carboration of internal alkynes.[12, 13]

Although 1,1-carborations have mainly been applied to the synthesis of metalloles, they have also been investigated for the synthesis of non-metal heterocycles. Erker and co-workers have pioneered this renaissance of 1,1-carboration. Recently, they reported the synthesis of the anti-

aromatic boroles by 1,1-carboboration/1,1-vinylboration reaction (Figure 1.9).[12] The 1,1-carboboration used to synthesize boroles was reported by the same research group earlier, which involves the simple activation of C≡C bonds through the treatment of internal alkynes with several highly electrophilic boranes (*e.g.* $B(C_6F_5)_3$) at elevated temperature (Figure 1.9).[13] In the reaction, one $C(sp)$-$C(sp^3)$ carbon-carbon single bond is broken in the course of the reaction and the corresponding *n*-propyl group migrates to the other alkyne terminus. Additionally, a C_6F_5 substituent migrates from boron to the adjacent carbon. The resulting trisubstituted alkenylboranes can be synthetically utilized for subsequent carbon-carbon bond formation in a Pd-catalyzed reaction that is related to Suzuki coupling.
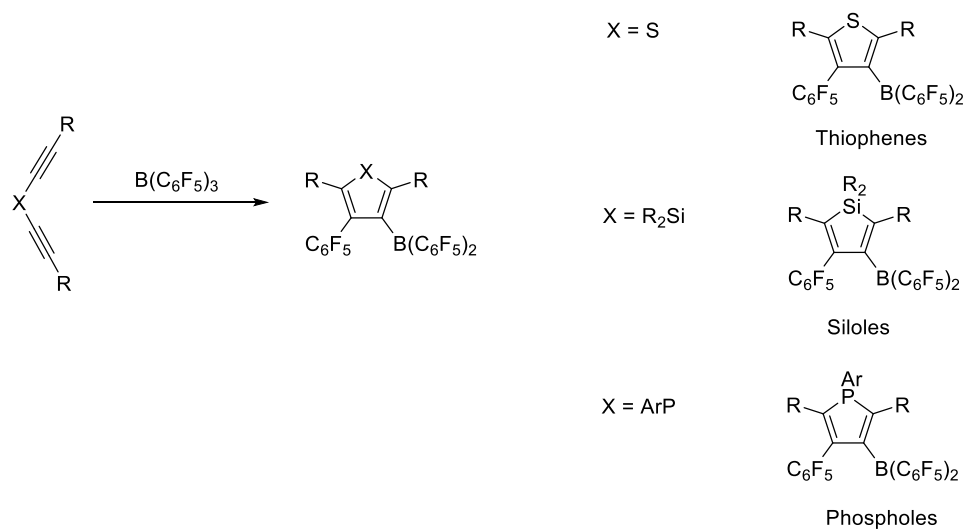
Figure 1.10 Synthesis of heterocycles via 1,1-carboboration.[14-16]

Erker and co-workers have extended the sequential 1,1-carboboration reaction to the synthesis of thiophene derivatives (Figure 1.10).[14] Substituted borylthiophenes were synthesized and these borylsubstituted heteroarenes were shown to be accessible to cross-coupling reactions. These 1,1-carboborations have also been applied to the synthesis of siloles[15] and phospholes[16] (Figure 1.10).

7

In summary, although the 1,1-carboboration reaction has been limited to electron-deficient substituted boranes (RBC_6F_5), it may provide novel entries to carbon–carbon σ-bond activation chemistry and synthesis of metal or main group atoms imbedded heterocycles, an area that will probably find increasing attention in the years to come.

1.1.3 Catalysis

The empty p-orbital renders three-coordinated boranes Lewis acidic, in which the low-lying LUMO can interact with the lone electron-pair in the high-lying HOMO of a Lewis base. Normally, combinations of Lewis acids and bases either form classical Lewis adducts, or bulky Lewis pairs which do not react with each other. The non-quenching Lewis pairs described as frustrated Lewis pairs (FLPs) was reported by Stephen et al, [17] which could be used to activate H_2 gas. On the other hand, boranes, acting as Lewis acids, have been applied to catalytic C-H borylation[18] and silylation[19] of alkenes, alkynes and arenes.

1.1.3.1 Small Molecule Activation

Both the unquenched Lewis acidity and basicity of "frustrated Lewis pairs (FLPs)" are available to be used in organic reactions and catalysis. Frustrated Lewis pairs are inter- or intramolecular combinations of bulky phosphines or amines with strongly electrophilic $RB(C_6F_5)_2$ components. Many examples of such frustrated Lewis pairs are able to cleave dihydrogen heterolytically, resulting in phosphonium cation/borate anion salts, which can either reversibly release H_2 gas, or serve as active metal-free catalysts for the hydrogenation of unsaturated species.

Since the seminal discovery by Stephan et al. of a metal-free system capable of reversibly activating H_2 in 2006, as shown in Figure 1.11, the field of FLPs chemistry has experienced an immense growth and expansion.[20] In Stephan's system, the zwitterionic species **1.4** is a rare example of a molecule that contains both protic and hydridic fragments, which was expected to

spontaneously release H_2. However, elimination of H_2 that generates the orange-red phosphino-borane **1.5** can only occur upon heating up to 150 °C. Addition of H_2 to the phosphino-borane at 25°C resulted in the rapid and facile regeneration of the zwitterionic salt.[17]
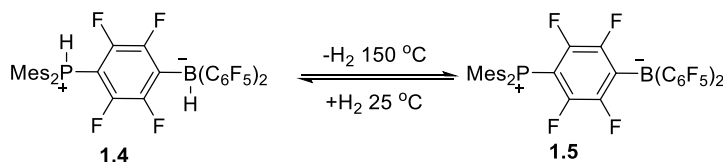
Figure 1.11 Reversible H_2 activation.[17]

Independently, Erker *et al.* investigated an interesting ethylene bridged phosphine-borane system for its reactivity with H_2 (Figure 1.12).[21] The zwitterionic salt **1.6**, formed through the heterolytic splitting of H_2 by the intramolecular frustrated Lewis pair **1.7**, shows a typical hydrido borate reactivity. It rapidly reduces benzaldehyde stoichiometrically to give the corresponding reduced alcohol derivative **1.8**.
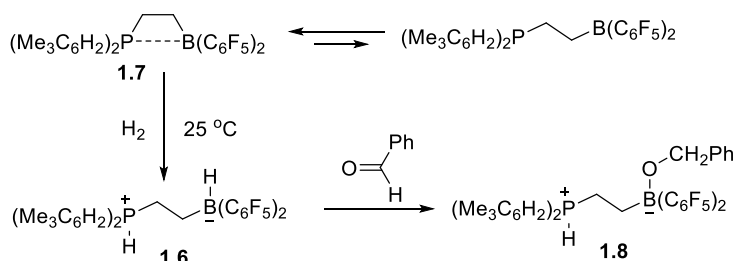
Figure 1.12 Ethylene bridged phosphineborane.[21]

All in all, the concept of "frustrated Lewis Pairs" (FLPs) advanced by Stephan, Erker and others shows the remarkable ability of these systems to reversibly activate hydrogen, which presents a bright future for hydrogenation catalysis and perhaps even for the field of hydrogen storage.

1.1.3.2 Catalysis in Organic Synthesis

Due to the seminal discovery of the tris(pentafluorophenyl)borane $B(C_6F_5)_3$-catalysed carbonyl hydrosilylation by Piers and co-workers,[22] the potent boron Lewis acid $(B(C_6F_5)_3)$ and related electron-deficient boron catalysts have been greatly involved in hydrogenation, borylation and silylation.

In 2013, Oestreich group discovered that $B(C_6F_5)_3$ could undergo hydride abstraction from cyclohexa-1,4-dienes **1.9** that bear a silicon group in the 3-position (Figure 1.13).[23] The $C(sp^3)$-H bond in dienes develops hydridic character through hyperconjugation with the C(sp3)-Si bond that later stabilizes the resulting intermediate **1.10**. With $[HB(C_6F_5)_3]^-$ as the counter anion, the intermediate **1.10** releases the free hydrosilane along with benzene at room temperature. They also found that $B(C_6F_5)_3$-catalyzed hydrogenation could release H_2 from cyclohexa-1,4-dienes without the assistance of silicon group.[24]
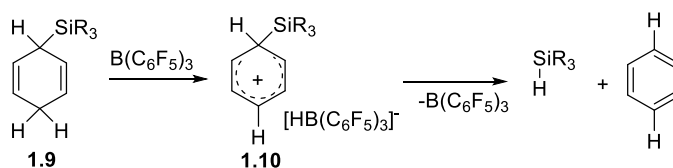
Figure 1.13 $B(C_6F_5)_3$-catalyzed hydrogen transfer from cyclohexa-1,4-dienes.[23]
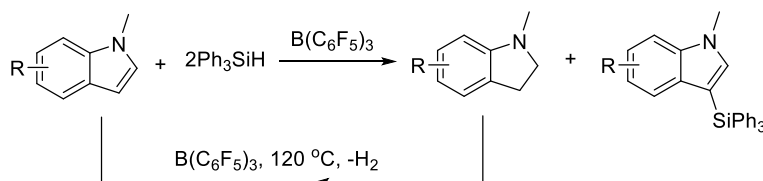
Figure 1.14 $B(C_6F_5)_3$-catalyzed convergent silylation of indoles.[25]

Due to the practical physicochemical properties of silylated arenes, it is very demanding to develop efficient transition-metal-free C−H silylation. There are many entries of borane catalyzed silylation of arenes, particularly heteroarenes like indole.[19b] Very recently, Zhang *et al* reported an

efficient, metal-free $B(C_6F_5)_3$-catalyzed method for rapid access to C3-silylated indoles, which could also transfer hydrogenated product indolines back to substrates in the disproportionation reaction, as shown in Figure 1.14.[25] In addition to metal-free catalyst and mild reaction conditions, there are several other advantages of this methodology: highly regioselectivity, no additive or H_2 acceptors and long-life catalytic performance.

Like the C−H silylation of arenes, research in C-H borylation has experienced substantial progress, from transition metal-catalyzed methods involving C-H bond activation[18a] to electrophilic aromatic substitution[18b] in which either positively charged boron reagents are involved or activators are used as catalysts. Lately, Klare and Oestreich disclosed a catalytic approach for the electrophilic C-H borylation of electron-rich (hetero)-arenes, thereby providing straightforward access to synthetically useful aryl boronates (Figure 1.15).[26] The catalyst $B(C_6F_5)_3$ was used as the initiator and the reaction proceeded without the addition of an external base or H_2 acceptor. Besides, the authors realized that this C-H borylation could be significantly accelerated by the addition of catalytic amounts of alkenes, which could accompany the first cycle of catalytic electrophilic C-H borylation reaction at room temperature.
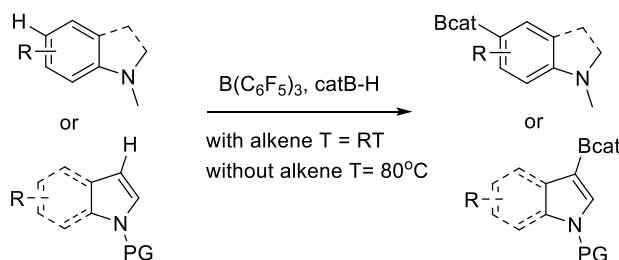
Figure 1.15 C−H borylation of electron-rich arenes.[26]

Recently, Fontaine and coworkers reported an intramolecular FLPs **1.11** used as catalysts for the C-H bond cleavage and dehydrogenative borylation of heteroarenes (Figure 1.16).[27] In this process, a Lewis basic amine is believed to abstract a proton, while the electron density of the

11

C(sp^2)-H bond is transferred to a Lewis acidic borane. They further developed a bench-stable organotrifluoroborate salts **1.12**,[28] which was hypothesized to substitute B–F bonds of **1.12** with B–H bonds with suitable hydride-based reductants, like pinacolborane (HBpin). Therefore, borane **1.11** used to catalyze borylation of heteroarenes can be generated by *in situ* deprotection of precatalyst **1.12**. The stability to air and moisture of **1.12** renders this procedure simpler, without recourse to use a glovebox and Schlenk techniques.
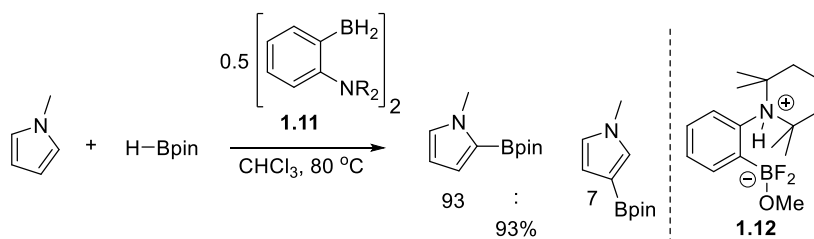
Figure 1.16. Metal-free catalytic C-H bond activation and borylation of heteroarenes.[27, 28]

1.2 Triarylboron-Functionalized Luminescent Molecules
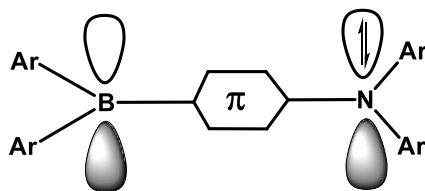
Figure 1.17 A typical donor-acceptor triarylboron compound.

The tri-substituted boron center is isoelectronic and isostructural to a carbocation, which makes it an excellent electron acceptor. To increase the stability of organoboranes towards nucleophilic attacks, bulky aryl groups are usually introduced to provide enough steric hindrance. The empty p-orbital also renders these compounds redox-active, allowing triarylboranes to undergo reversible reduction to form a stable radical anion. Due to the commercial availability of dimesitylboron fluoride, dimesitylboron functionalized compounds can be easily synthesized and are widely used as luminescent materials. When combined with an electron donating group (*e.g.* amine) (Figure

1.17), triarylboron compounds have been widely applied as charge transfer fluorescent molecules which can be used in optoelectronic devices,[29] and chemical sensors of small anions,[30] such as fluoride and cyanide.

1.2.1 Luminescence

Luminescence is the release of energy in the form of the emission of photons. Generally, the type of radiative process could be categorized into two different emission pathways: fluorescence ($10^{-12} \sim 10^{-7}$ s) and phosphorescence ($10^{-6} \sim 10^0$ s), which involve different spin states of electronic transitions, as shown in Figure 1.18. Usually, upon excitation the molecule absorbs light to reach excited states, where the higher excited states quickly undergo a vibrational relaxation to a lowest singlet excited state (S_1), which is defined as internal conversion if there is no change of spin multiplicity. The lowest singlet excited state (S_1) could go back to the ground state (S_0) either radiatively, which is called fluorescence, or non-radiatively, which releases energy as heat. If the spin multiplicity changes, it is defined as intersystem crossing (ISC), which could be either singlet (S_1) to triplet (T_1) or triplet (T_1) to singlet (S_1). Since the singlet-triplet transitions are forbidden according to the Pauli Exclusion Principle, T_1 converted from S_1 by ISC can relax to S_0 only when spin inversion occurs, which is named as phosphorescence. The consequence of spin inversion of $T_1 \rightarrow S_1$ is the longer decay time of phosphorescence, which could range from microseconds to seconds. Due to the lack of spin-orbit coupling, this spin-forbidden $S_1 \rightarrow T_1$ process of pure organic molecules is typically not favorable. The ISC efficiency could be enhanced by the presence of a heavy metal atom. Additionally, the excited molecule can transfer energy (ET) to its ground state molecule or other types of molecules like solvent with the formation of excimer or exciplex, respectively. Finally, the excited molecules have different structures from its ground state, in which the bonds are vulnerable to undergo chemical reaction, which is known as photochemistry.[31]
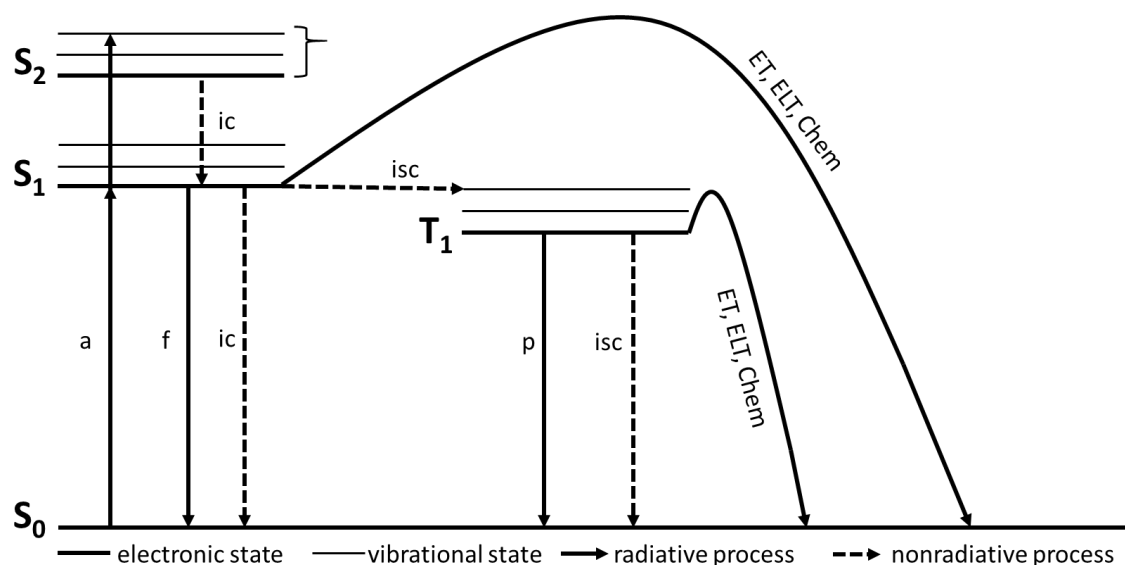
Figure 1.18 Jablonski diagram. (a: absorption; f: fluorescence; p: phosphorescence; ic: internal crossing; isc: intersystem crossing; ET: energy transfer; ELT: electron transfer; Chem: chemical reaction)

1.2.2 Triarylboranes in OLEDs

With respect to triarylboron compounds, most attention has been given to their optoelectronic properties, due to their ability to function both as efficient electron-transport layers and emissive materials in organic light-emitting diodes (OLEDs). The first triarylborane incorporated bi- or terthiophene as electron-transporting materials in OLEDs was reported by Shirota and co-workers.[32] Later, they reported two other compounds (Figure 1.19) which are functionalized with both triarylamine and dimesitylboron groups through the π-conjugated thiophene ring. The combination of the electron donating triarylamine group and the electron accepting BMes$_2$ group not only enables bright charge transfer luminescence but also facilitates the formation of amorphous films due to the steric bulkiness. Two electroluminescent devices using these two compounds as the emitting layer were fabricated, and bright blue-green (**1.13**) and green (**1.14**) electroluminescence were obtained.[33]

14
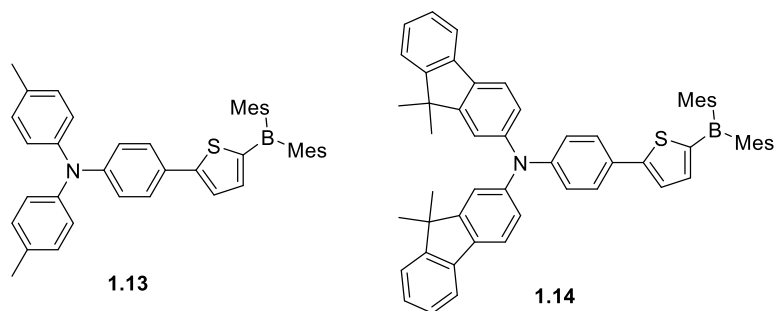
Figure 1.19 Triarylboranes as emitters.[33]

1.2.3 Triarylboranes as Fluoride Sensors

As mentioned before, although organoboranes can be stabilized from nucleophilic attack by introducing bulky aryl substituents, it still has very strong affinity toward small anions, such as fluoride and cyanide.[30] This property allows the use of boron systems for anions sensing, which can be used to ensure that the concentration of fluoride in drinking water does not exceed the recommended limit.[34]

In 2001, Yamaguchi and co-workers developed the first organoboron-based systems for fluoride sensors (Figure 1.20).[35] The highly bulky substituents of tris(9-anthryl)borane provide stability toward water and air. The addition of fluoride to the THF solution of borane results in a distinct color change from orange to colorless, which is an interesting and promising, although not suitable in an aqueous environment.
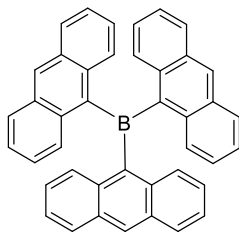
Figure 1.20 The first triaryborane for fluoride sensing.[35]

15

After extensive work, Gabbaï and co-workers developed a cationic phosphonium-borane system capable of detecting fluoride in pure water down to 4 ppm (Figure 1.21),[34] which is the maximum contaminant level set by the US Environmental Protection Agency. This system was reported to selectively detect fluoride even at the low pH value of 4.9, while competitive hydroxide binding to the boron center occurs at higher pH.
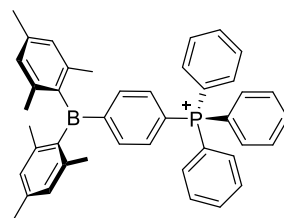
Figure 1.21 A cationic phosphonium-borane.[34]
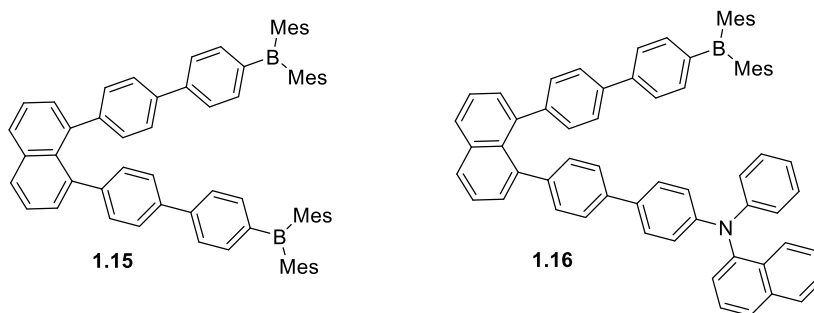
Figure 1.22 Triarylboron compounds as "turn off" (**1.15**) and "turn on" (**1.16**) fluoride sensors.[36]

In 2006, our group prepared two U-shaped branched organoboron compounds for fluorescent sensing of fluoride (Figure 1.22).[36] Both of them have distinct fluorescent responses to fluoride. The addition of F⁻ to a solution of diboron compound **1.15** quenched the emission due to the population of the empty *p* orbital of boron by F⁻, which makes this diboron compound **1.15** a "turn-off" sensor for F⁻. The response of boron-nitrogen compound **1.16** to F⁻ is in sharp contrast to that of the diboron compound **1.15**. The addition of F⁻ switched the green charge-transfer emission

between the N donor and the B acceptor to the blue π-π*emission localized on the N donor, which produces a sensitive and selective "turn-on" fluorescent sensor **1.16** for F[-].

1.3 Synthesis and Optoelectronic Properties of Boron-Doped Aromatic Compounds

Graphene, a two-dimensional (2D) honeycomb lattice of sp^2 carbon atoms, has attracted enormous attention due to its extraordinary physical properties, and is called "omnipotent material". Graphene research was recognized by Nobel Prize in Physics in 2010.[37] This "omnipotent material" actually is not omnipotent, due to its zero-bandgap property which impedes its semiconducting applications in electronic devices. To provide graphene with semiconducting properties, intensive studies have been recently carried out to increase and tune its bandgap. So far, one of the most effective methods is chemically doping heteroatoms into graphene, and nitrogen has become the most used and widely investigated dopant heteroatom.[38] Due to the isoelectronic relationship between boron and carbon cation as well as between boron-nitrogen (BN) unit and two carbon atoms (CC) motif, boron also becomes another important element that can induce novel and complementary properties.[39] Therefore, the bottom-up synthesis of such unexplored boron-doped heteroarenes (nanographenes) becomes popular as an alternative approach to obtain B-doped graphene with defined widths and edges. These structurally well-defined B-doped graphene fragments (nanographenes) could be synthesized as precursors for solution-phase polymerization or surface-assisted growth. On the other hand, these B-doped polycyclic aromatic hydrocarbons (PAHs) or B-doped nanographenes are accessible models for studying the fundamental structure-property relationship in B-doped (or BN-doped) graphenes. Hence, with respect to well-defined B-doped graphene, developing efficient approaches to synthesizing boron-incorporated PAHs is of high demand.

1.3.1 Boron-Doped Aromatic Compounds

Unlike the other types of organoboranes which usually need bulky substituents to gain stability, the boron-embedded planar π conjugated structures could gain remarkable chemical and thermal stability toward oxygen and water because of structural constraint. Along with the well-known electron-accepting nature and Lewis acidity, boron-doped aromatic compounds have been extensively studied as electron-transporting materials, and chemical sensors.

In 2012, Yamaguchi and co-workers synthesized two types of planar B-doped PAHs by dehydrogenative aromatic C−C coupling (Figure 1.23).[40] Both types of molecules have outstanding chemical and thermal stability. The p-orbitals of doped boron atoms have significant contributions to both the relevant unoccupied and occupied orbitals, leading to a narrow HOMO-LUMO bandgap as well as broad absorption and emission. They also found that reversible multi-redox properties could be achieved by introducing two B atoms into PAHs.
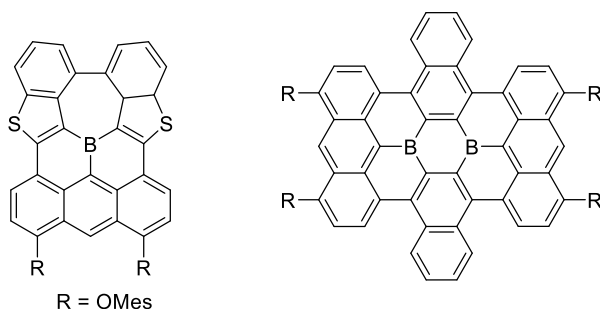
Figure 1.23 B-doped PAH prepared by Yamaguchi.[40]

Recently, new strategies involving Si-B exchange to access boron-containing PAHs have been developed by Wagner *et al*.[41] As the key step, Si-B exchange reaction was used to introduce boron atoms to the extraordinarily rigid molecular scaffolds, which could form boron-containing bisanthracene molecule **1.17** (Figure 1.24). Similar to Yamaguchi's diboron-doped PAHs, molecule **1.17** also proved to be an air- and moisture-stable, and redox-active blue luminophore.
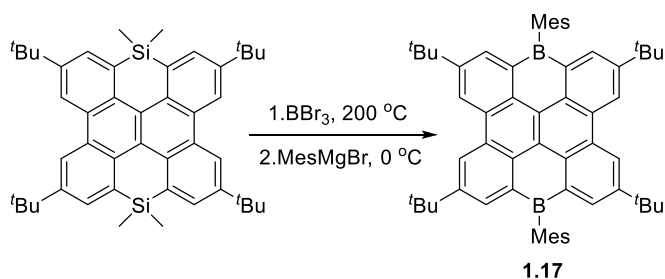
Figure 1.24 Synthesis of boron-containing bisanthracene by Wagner.[41]

Wagner and co-workers developed this Si-B exchange methodology further to achieve multiple examples of unsymmetrically benzannulated boron-doped PAHs (Figure 1.25).[42] The "one-pot" procedure involving the Si-B exchange reaction followed by a vicinal electrophilic diborylation is believed to be a general methodology, allowing to access a library of B-doped PAHs for optoelectronic devices as well as the structure-property relationship study.

Figure 1.25 Synthesis of doubly boron-doped PAHs using vicinal electrophilic diborylation.[42]

1.3.2 Boron and Nitrogen-Doped Aromatic Compounds

An alternative strategy to incorporate boron in organic π-conjugated systems is the replacement of a C=C bond with an isoelectronic BN unit. The fact that boron has three valence electrons and nitrogen has five valence electrons is responsible for the isoelectronic nature of BN units to C=C fragments. Consequently, although BN unit has the same number of valence electrons, that is, eight electrons, as a pair of carbon atoms, the dipolar nature of the B-N bond would dramatically transform the electronic properties and intermolecular interactions of BN-doped aromatic compounds.[43] Contrary to B-doped PAHs which have been developed only very recently, BN-

doped aromatic compounds have a long history of evolution since the first example of BN-arene was reported by Alfred Stock in 1926.[44] Much the same to many other topics of chemistry, not much attention was paid until the new millennium. Nowadays, the synthesis of BN-doped arenes has become one of the most popular topics in organic chemistry and material chemistry, and numerous new BN-doped aromatic compounds have been synthesized and demonstrated to have very distinct properties in optoelectronic materials.[43] The BN-arenes, more often described as azaborines, can be categorized into three isomers according to the particular substitution pattern, referred as 1,2-azaborine **1.18**, 1,3-azaborine **1.19**, and 1,4-azaborine **1.20** (Figure 1.26).[45] With respect to stability, these three azaborines and benzene follow the decreasing order of benzene, 1,2-azaborine, 1,4-azaborine and 1,3-azaborine. The stability of these isomers also results in different number of examples reported for each isomer. In other words, the study of the most stable isomer 1,2-azaborine and analogues within the 1,2-azaborine core is most reported and there are just a handful of examples of the least stable isomer 1,3-azaborine reported. Besides the numerous synthetic reports for azaborines or BN-arenes, a variety of examples indicate that these molecules possess remarkable performance in optoelectronic devices.[43]
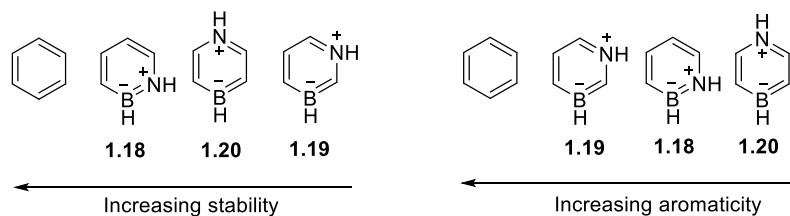
Figure 1.26 Computed stability and aromaticity trends of azaborine isomers.[45]

1.3.2.1 1,2-Azaborines

1,2-Azaborines refer to BN-arenes in which the boron and nitrogen connect to each other directly. Due to its highest stability among azaborine isomers, 1,2-azaborines have attracted great

attention with regards to their synthesis as well as application in optoelectronics, from 1,2-azaborine itself to larger polycyclic systems containing the 1,2-azaborine moiety.[43c] The synthesis of 1,2-azaborines was pioneered by Dewar and co-workers in the 1950s,[46] and then Liu and others started a renaissance of azaborine chemistry in new millennium.[43b]
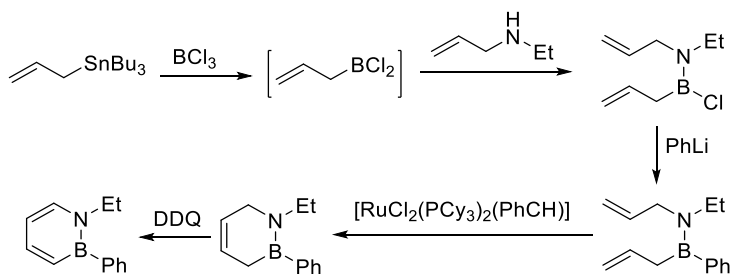
Figure 1.27 Mild synthesis of 1,2-azaborine by Ashe.[47]
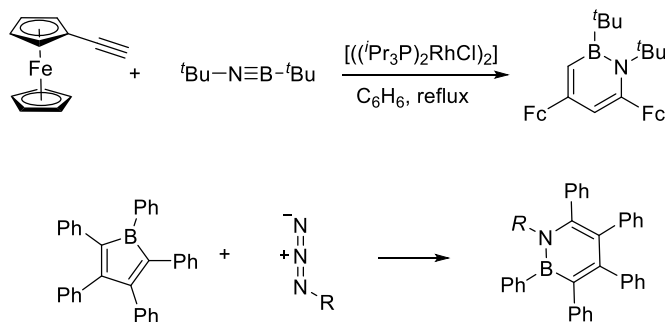
Figure 1.28 Two synthetic routes to approach 1,2-azaborines by Braunschweig.[50, 51]

In 2000, the Ashe group achieved a breakthrough in the synthesis of monocyclic 1,2-azaborines using mild conditions with typical organic synthesis.[47] In Ashe's synthesis, the ring closing metathesis (RCM) followed by oxidative dehydrogenation enable mild and efficient formation of 1,2-azaborines (Figure 1.27). Liu and co-workers extended Ashe's method to achieve 1,2-azaborines with different heteroatoms on boron.[48] Later, Liu also demonstrated the postfunctionalization of the boron atom on 1,2-azaborines, which paves the way to a diversity of

21

1,2-azaborines.[49] In addition, Braunschweig and co-workers developed two other synthetic routes for 1,2-azaborines: [2+2+2] cycloaddition[50] and ring expansion of borole and azide[51] (Figure 1.28).

Besides the synthesis of parent 1,2-azaborines, there are many advances of BN-arenes bearing the 1,2-azaborine fragment. Especially, the number and positions of BN units within BN-arenes have been found to significantly alter their photophysical and electronic porperties. In 2007, Piers *et al* developed a double Pt-catalyzed cyclization reaction of the ethynyl group to afford pyrene analogue **1.21** with fully internalized BN substitution (Figure 1.29).[53] They also extended this strategy to synthesize other types of BN substituted BN-arenes. During the investigation, they found that the different locations of BN could dramatically modulate the redox and photophysical properties of the organic π-systems. For instance, sharing the parent phenanthrene but different positions of the BN unit, their molecule **1.22** and Dewar's compound **1.23** have very different emission features.[53] Recently, our group also synthesized a previously unknown isomer of BN-phenanthrene photochemically, which displays unique photophysical properties and will be presented in Section 1.4.3.
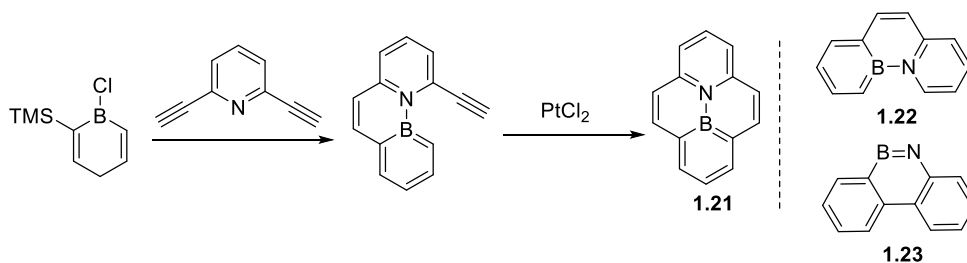
Figure 1.29 Synthesis of BN-pyrene through Pt-catalyzed cyclizations.[53]

The first example of 1,2-azaborine analogues showing excellent hole mobility was achieved by Hatakeyama, Nakamura, and co-workers in 2011 (Figure 1.30).[54] These BN-substituted PAHs were synthesized using a procedure of borylation assisted by BuLi followed by a tandem intramolecular electrophilic arene borylation. BN-PAHs **1.24** displayed high intrinsic hole mobility

(0.07 cm^2 V^{-1} s^{-1}), which is ten times higher than its all-carbon analogue, dibenzo-[g,p]chrysene, and even higher than the popular rubrene (0.05 cm^2 V^{-1} s^{-1}). Interestingly, *rac*-**1.26** displayed a hole mobility of 4.6×10^{-4} cm^2 V^{-1} s^{-1}, while the enantiomerically pure *P*-**1.26** showed a higher electron mobility of 4.5×10^{-3} cm^2 V^{-1} s^{-1} than the hole mobility (7.9×10^{-4} cm^2 V^{-1} s^{-1}).[55] It is believed that different packing structures of the hetero- and homochiral crystals of **1.26** are responsible to the difference of mobility. The first electronic device based on BN-PAHs was demonstrated by Pei and co-workers.[43c] They also found that flexible side chains which are usually used to improve the solubility of PAHs have a non-negligible impact on the OFETs mobility.[43c]
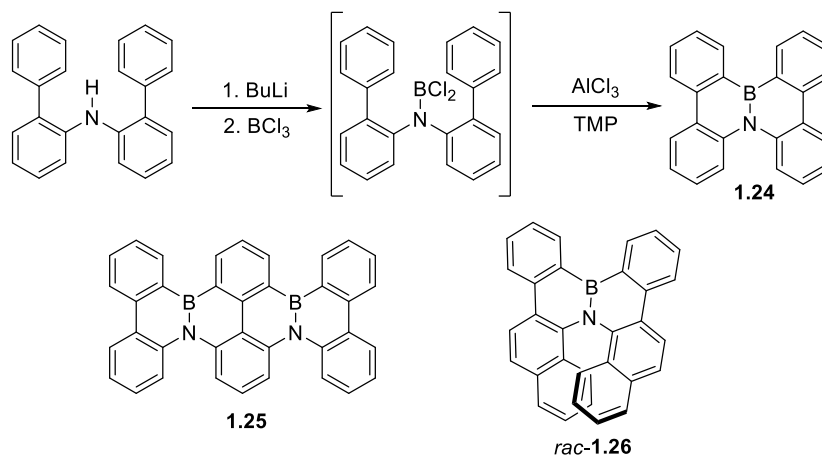
Figure 1.30 Synthesis of BN-substituted PAHs via tandem electrophilic borylation.[54, 55]

1.3.2.2 1,3-Azaborines

As the least stable azaborines, the synthesis of 1,3-azaborine derivatives remained elusive until Liu and co-workers disclosed the first synthetic example of 1,3-azaborines **1.27** in 2011 (Figure 1.31).[56] 1,3-aAzaborine **1.27** was demonstrated to be a stable structural motif with considerable aromatic character, and further functionalization on the boron atom was evidenced to be a general method.
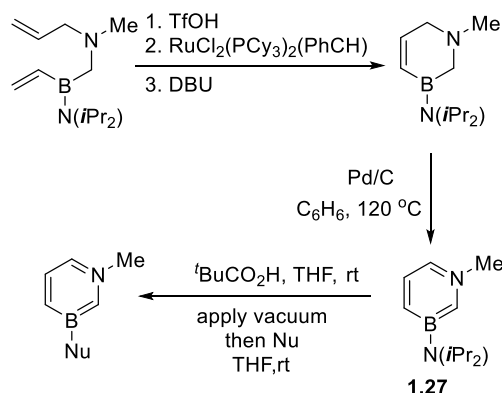
Figure 1.31 Synthesis and post-functionalizations of 1,3-azaborine by Liu.[56]

Currently, there are very few examples of polycyclic aromatic systems with an embedded 1,3-azaborinine motif, except for a class of NHC-based 1,3-azaborines reported by our group which were obtained via photoelimination, and will be presented in Section 1.4.3.

1.3.2.3 1,4-Azaborines
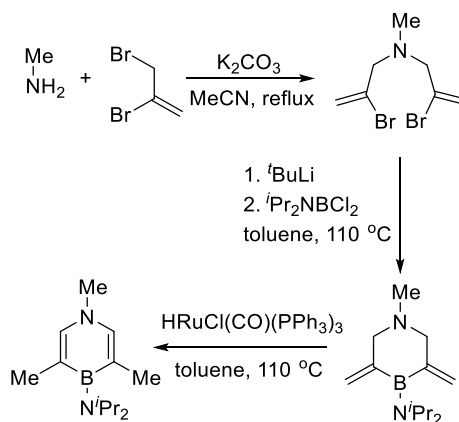
Figure 1.32 The synthetic sequence for monocyclic 1,4-azaborines by Liu.[58]

As an important member of azaborines, 1,4-azaborines have also received much attention in last decade. With respect to potential optoelectronic properties, generally, polycyclic dibenzofused 1,4-azaborines have been more popular than their monocyclic counterparts. After the first example of monocyclic 1,4-azaborine reported by Braunschweig and co-workers using a Rh-mediated

24

cyclization,[57] Liu *et al* recently disclosed a more versatile three-step synthesis producing a wide range of monocyclic 1,4-azaborines. Liu group also found that orientation and the placement of donor and acceptor substituents on boron and nitrogen atoms have significant impact on the optical properties of corresponding 1,4-azaborines (Figure 1.32).[58]
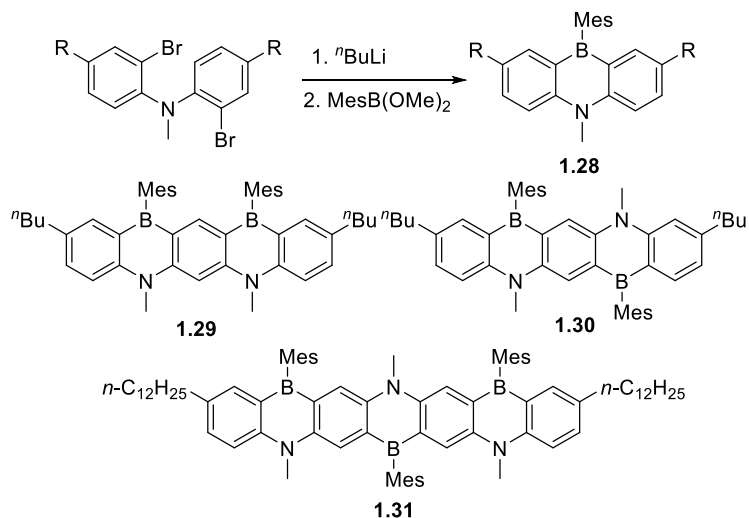
Figure 1.33 Synthesis of 1,4-azaborine-fused linear arenes by Kawashima.[59]

In terms of incorporating 1,4-azaborines in OLED devices, polycyclic dibenzofused 1,4-azaborines have many advantages, such as stability and similarity to all carbon PAHs. Since 2006, several years prior to the synthesis of the first monocyclic 1,4-azaborines, Kawashima and co-workers developed a general lithiation/borylation procedure for the incorporation of the 1,4-azaborine motif into PAHs (Figure 1.33).[59] This family of 1,4-azaborine-fused linear BN-PAHs (**1.28** - **1.31**) and their derivatives were not only explored as efficient fluorescent sensors for fluoride and cyanide anions, but also are expected to have promising potential applications in material science.

1.3.2.4 Other BN-doped PAHs

25

With the development of azaborine chemistry, BN-doped antiaromatic systems involving five-membered heterocycles and NBN-doped PAHs have also recently attracted great attention. In addition to the BN-indole synthesized by Liu group,[60] The Cui[61] and Müllen[62] groups reported the synthesis of (BN)$_2$-benzopentalene **1.32** and (BN)$_2$-dibenzo[*a,e*]pentalenes **1.33** and **1.34** almost at the same time, respectively (Figure 1.34). The different orientations of the BN units in **1.33** and **1.34** were reported to have significant influence on the antiaromaticity as well as the optical and electronic properties.
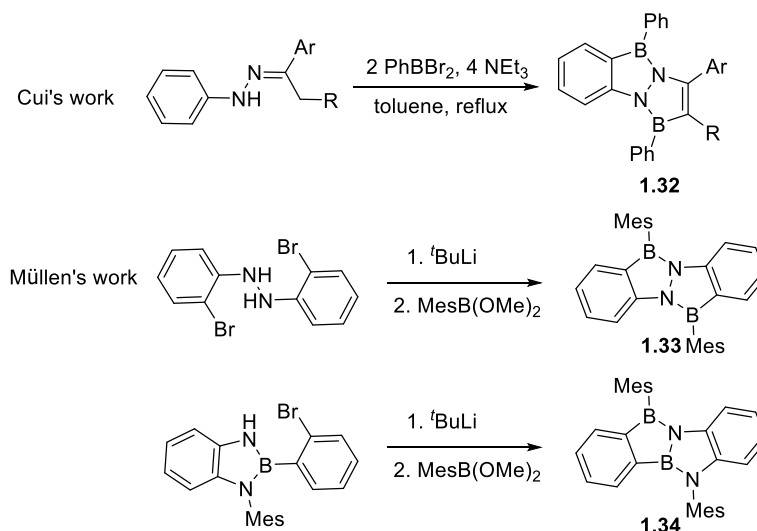
Figure 1.34 Synthesis of five-membered BN-heterocycles by Cui and Müllen.[61, 62]

The synthesis of NBN-doped PAHs is very popular because the incorporation of two nitrogen and one boron atoms imparts high chemical stability to zigzag-edged PAHs. Recently, Feng group[63] and Hatakeyama group[64] have independently developed two different approaches to NBN-zigzag-edged PAHs (Figure 1.35). Feng and co-workers developed a double borylation method involving the directing group of TMS and further demonstrated the possibilities for lateral extension through the synthesis of the higher homologue **1.35**. It was suggested that NBN-doped zigzag-edged graphene nanoribbons could be also synthesized via this route. On the other hand, Hatakeyama's

direct double borylation includes a demethylation process, which was found to be applicable for the synthesis of OBO- and SBS-PAHs (**1.36** and **1.37**) as well.[64]
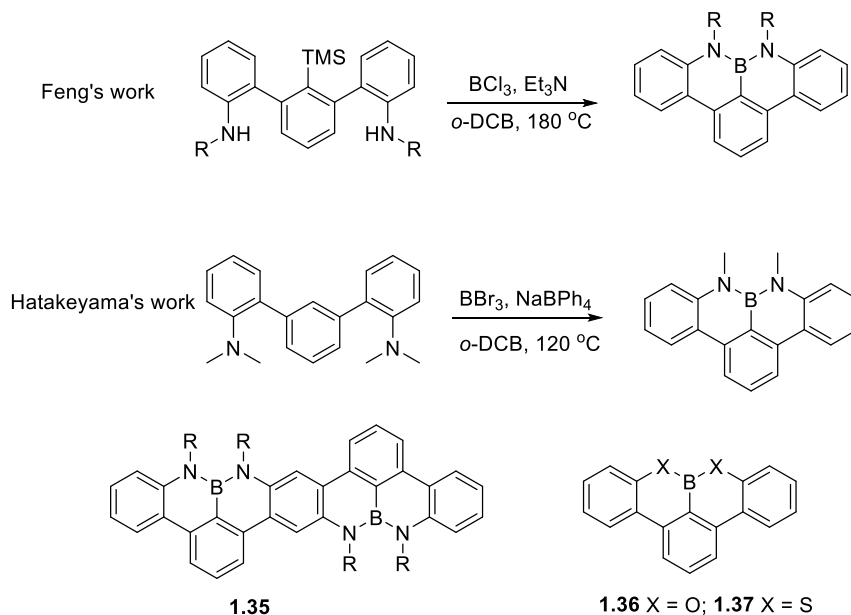
Figure 1.35 Synthesis of NBN-PAHs by Feng and Hatakeyama.[63, 64]
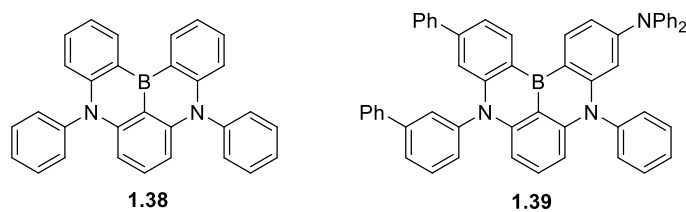
Figure 1.36 Thermally activated delayed fluorescence (TADF) NBN-PAHs.[65]

Remarkably, NBN-PAHs (**1.38** and **1.39**) have been shown to be ultrapure blue thermally activated delayed fluorescence (TADF) molecules by Hatakeyama and co-workers via efficient HOMO–LUMO separation by the multiple resonance effect (Figure 1.36).[65] The introduction of substituents is capable of increasing the oscillator strength of the S_0–S_1 transition (**1.38**: f = 0.205; **1.39**: f = 0.415) without affecting the localization of molecular orbitals (MOs), resulting in higher external quantum efficiency (EQE) up to 20.2% for the OLEDs. Besides, this novel molecular

27

design for separating the HOMO and LUMO and minimizing ΔE_{ST} (energy gap between S_1 and T_1) is believed to not only be useful for preparing excellent TADF emitters, but also as host materials for phosphorescent emitters.

1.3.3 Boron and Other Main Group Elements-Doped Aromatic Compounds

Unlike boron that is isoelectronic to a carbocation and the BN unit that is isoelectronic to a CC unit, boron and other elements (O, S, P) unit do not have isoelectronic relationships to CC analogues. Still, they have recently become another thriving area of research for the design and development of novel materials, parallel to B- and BN-doped PAHs.

1.3.3.1 Boron and Oxygen-Doped Aromatic Compounds

The study BO-doped aromatics has a long history since Letzinger and Nazy speculated boron–oxygen containing phenanthrene analogue in 1959.[66] BO-PAHs are much more developed than monocyclic 1,2-oxaborine. Several decades after the first example of 1,2-oxaborine synthesized through the condensation of an alkyl phenyl ketone and a borane, Ashe and co-workers reported another 1,2-oxaborine with different substituents via a ring expansion in 2007.[67] Very recently, Martin and co-workers disclosed a new synthesis of 1,2-oxoborine **1.40** using oxygen insertion into boroles (Figure 1.37).[68] Piers *et al* used a different insertion method involving CO_2 to synthesize the 1,2-oxobrine dimer.[69]
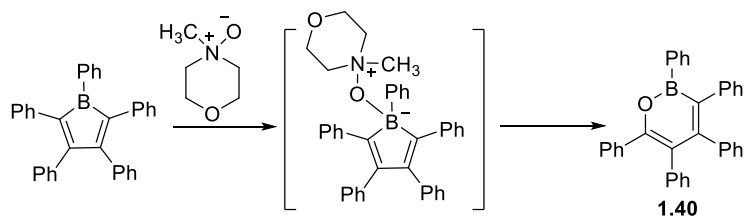
Figure 1.37 Synthesis of 1,2-oxoborine via oxygen insertion into borole by Martin.[68]

28

OBO-nanographenes have been independently reported by Hatakeyama (**1.41**)[70] and Müllen (**1.42** and **1.43**)[71] almost at the same time (Figure 1.38). With different aims, the R groups were introduced at different positions. Hatakeyama *et al* showed the parent helicene **1.41** (R = H) displayed excellent ambipolar conductivity, which could be attributed to the unique 3D π-stacking with a brickwork arrangement. Additionally, the introduction of four *t*butyl groups suppresses racemization, enabling enantiomerically pure helicene with deep blue fluorescence. The Müllen group revealed that OBO-nanographenes **1.42** have excellent stability and strong fluorescence, in contrast to the unstable all-carbon analogues. Dehydrogenation has been applied to generate the first example of heteroatom-doped peritetracenes **1.43**. Both of these simple and scalable protocols developed independently by Hatakeyama and Müllen are promising for further extension of the π-system, resulting in twisted double helicenes and stable planar zigzag-edged nanographenes.

1.41

Hatakeyama' molecule

1.42

1.43

Müllen's molecules
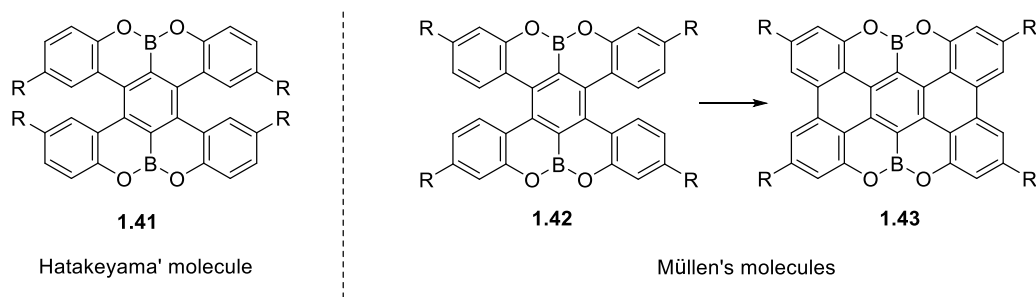
Figure 1.38 OBO-PAHs by Hatakeyama and Müllen.[70, 71]

1.3.3.2 Boron and Sulfur-Doped Aromatic Compounds
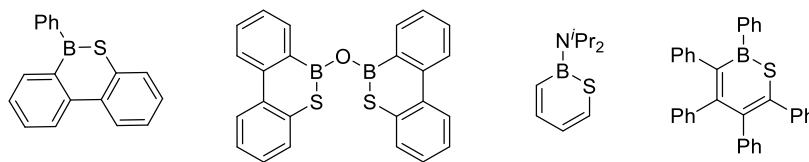
Figure 1.39 BS-thioborines.[72]

29

Although BS-thioborines show some similarities to the five-membered thiophene with applications in optoelectronic materials and medicine, there are only several BS-thioborines and analogues reported (Figure 1.39).[72] So far, there are no direct evidences of unique electronic properties.

1.3.3.3 Boron and Phosphine-Doped Aromatic Compounds

Surprisingly, the first 1,4-phosphaborine was reported to have a nonplanar phosphaborine ring, due to the pyramidalized sp^3-hybridized phosphorus.[73] Recently, Martin *et al* continued the methodology of ring expansion of boroles to synthesize 1,2-phosphaborines (Figure 1.40).[74] The difference with previous ring expansion of boroles is the insertion of the phosphorus atom driven by 254 nm light. The crystal structure of the 1,2-phosphaborine has a planar central ring with short bond lengths indicative of appreciable delocalization.
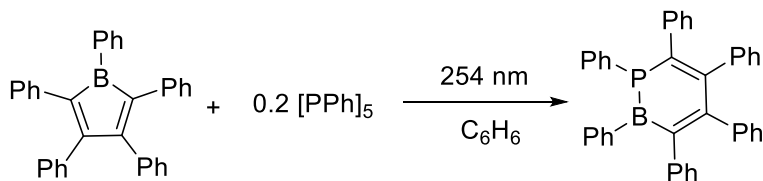
Figure 1.40 Synthesis of 1,2-phosphaborine.[74]

1.4 Photochemistry of Organoboron Compounds

Photochemical reactions are chemical reactions initiated by the absorption of energy in the form of light. As a consequence, a transient excited state of the molecule is generated. The chemical and physical properties of the excited molecules usually differ greatly from those of its ground state, which could cause the molecules to either decompose, transform to a new structure, polymerize with each other or react with other molecules. Because photochemical reactions often proceed differently compared to thermal reactions, they are valuable in organic and inorganic

chemistry. Furthermore, many thermal reactions have photochemical counterparts. Photochemical pathways offer the advantage over thermal methods of forming very often thermodynamically disfavored products, overcoming large activation barriers, and allowing reactivity otherwise inaccessible by thermal processes. In addition, photochemical pathways may proceed with high selectivity and clean conversion. Recently, the photochemistry of organoboron compounds has attracted much attention. However, compared to the extensive study on thermal reactions of boranes, the photoreaction of organoboron compounds has not been widely explored, because much more attention is paid to photophysical properties of boron compounds.[75]

1.4.1 Early Study of the Photochemistry of Organoboranes
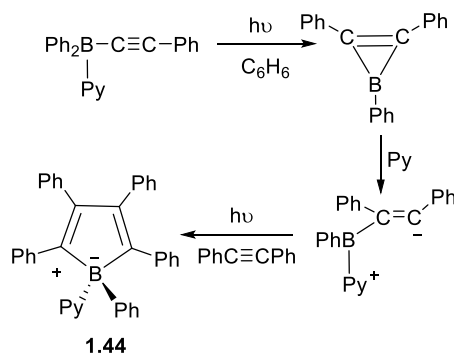
Figure 1.41 The photochemical synthesis of muti-substituted borole.[76]

The photochemistry of boron compounds can be dated back to the 1970s, when Williams and co-workers carried out the systematic work on photochemistry of sodium tetraphenyl borates.[75] In 1982, the Eisch group examined the photo-rearrangement of the diphenyl(phenylethynyl)borane-pyridine complex **1.44** (Figure 1.41).[76] Subsequently, in an attempt to prepare a solid borirene **1.45**, photolysis of the sterically hindered dimesityl(mesitylethynyl)borane was examined in a mixed solvent (Figure 1.42, top).[77] To disrupt the high symmetry of crystal trimesitylborirene, which prevented unambiguous differentiation between boron and carbon atoms in the central three-

31

membered ring, ((2,6-dimethylphenyl)ethynyl)dimesitylborane **1.46** was photolysed and the (2,6-dimethylphenyl)dimesitylborirene **1.47** was obtained and characterized by X-ray diffraction analysis (Figure 1.42, bottom).
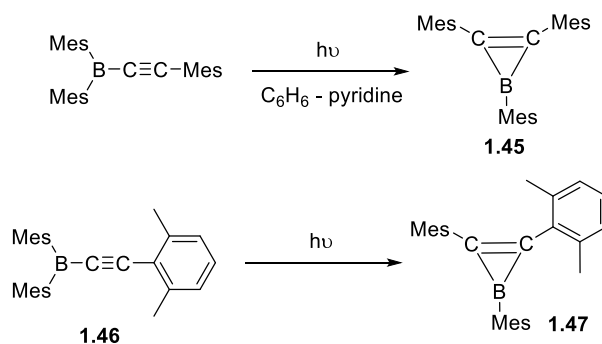
Figure 1.42 The photochemical synthesis of the borirene.[77]

1.4.2 Photoisomerization of Organoboron Compounds

Isomerization is a process in which one molecule is transformed into another molecule without the change of molecular formula but with structural changes, and is usually driven by external stimuli such as light, heat, or pressure, yielding different isomers that usually have distinct chemical and physical properties. The isomerization powered by light has been extensively exploited in biology and the development of advanced materials.[78] The photoisomerization of organoboranes often provides novel structures which are difficult to obtain via other synthetic methods, usually accompanied by distinct color change, thus photochromism.
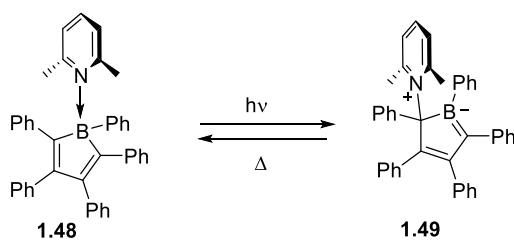
Figure 1.43 Photochromism based on a pentaphenylborole-2,6-lutidine adduct.[79]

32

In 2011, Braunschweig and co-workers reported a reversible photochromic four-coordinate boron system based on a pentaphenylborole-2,6-lutidine adduct (Figure 1.43).[79] Irradiation of a toluene solution of **1.48** at low temperature caused a shift of the base from boron to the adjacent carbon atom with the formation of a B=C bond in **1.49**, occurring with the significant color change from yellow to dark green.

Due to the special physical and optical features of substituted boroles, the application and synthesis of boroles have attracted considerable attention.[80] In 2012, Piers *et al.* reported the photochemical synthesis of a ladder diborole **1.51** (Figure 1.44).[81] Under reductive conditions, the bis-benzocycloborabutylidene **1.50** is formed which photochemically isomerizes to an air- and moisture-sensitive diborole ladder compound **1.51**. A photoinduced homolytic cleavage of the B–C bond between the boron atom and the phenyl group from the four-membered ring is proposed to allow the formation of the ladder diboroles **1.51**. The diborole **1.51** possesses 14 π electrons and exhibits Hückel aromaticity, which indicates the annulated aromatic benzene rings stabilize its antiaromatic core.
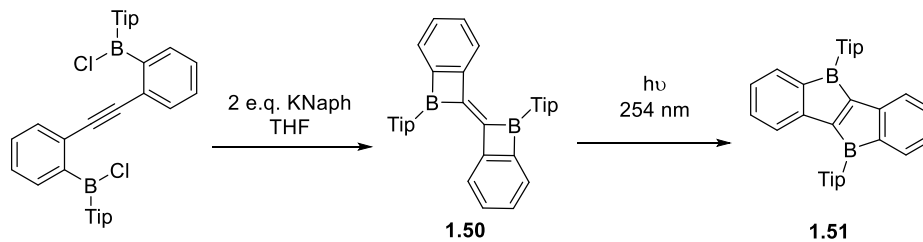
Figure 1.44 Synthesis of the ladder diborole by photoisomerization.[81]

Recently, when Yamaguchi and co-workers attempted to chemically synthesize a ladder diborole molecule, they unexpectedly obtained a boryl-substituted dibenzoborepin **1.52** from a diarylethene diboronic ester (Figure 1.45).[82] Interestingly, upon irradiation at 320 nm, the dimesitylboryl borepin **1.52** showed dramatically photochromic behavior with a color change from

colorless to deep blue, and the photoproduct **1.53** could be thermally reverted back to the starting borepin **1.52**, which can be explained as a bora-Nazarov cyclization. Notably, the B/C$^+$ isosterism is believed to be responsible for this unique reactivity and generates a product having an unusual electronic structure.
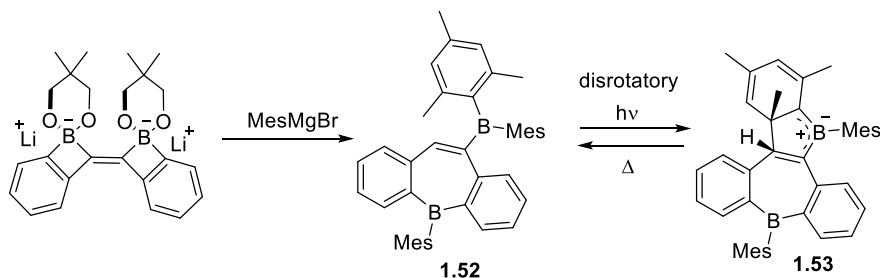
Figure 1.45 Synthesis of borylated dibenzoborepin and its photochromism.[82]

Our group has strong interests in the photo-transformation of organoboranes. In 2008, our group reported a reversible isomerization process which involves the formation/breaking of a C-C bond around the boron center (Figure 1.46).[83] The N,C-chelate ligand plays a critical role in this unusual photoisomerization phenomenon. This work motivated us to expand our investigation on the photoisomerization phenomenon to other ligands, such as N-heterocyclic carbenes (NHCs) and 2-phenylazolyl. Dimesitylboron chelates of NHCs[84] and 2-phenylazolyl[85] not only undergo highly efficient and clean photoisomerization in the same manner as the phenyl-pyridyl BMes$_2$ compounds do, they also undergo a sequential multi-structural transformation in response to light irradiation or heating.
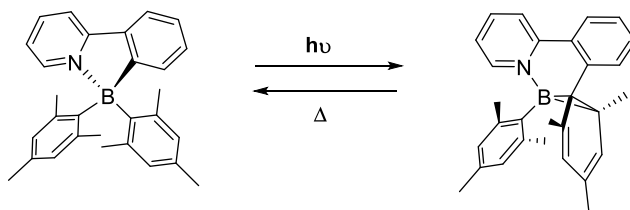
Figure 1.46 The reversible isomerization of N,C-chelate.[83]

Recently, as a continued interest in photochemistry, the dimesitylboron benzylimidazolyl chelate compound **1.54** was irradiated at 350 nm, and a new tricyclic 1,2-azaboratabisnorcaradiene molecules **1.55** was obtained, which can further transform into the first example of 1,2-azaborabenzotropilidenes **1.56** via a walk rearrangement (Figure 1.47).[86] 1,2-Azaborabenzotropilidene **1.56** contains a conjugated alkylideneborane unit with a B=C bond and can be fully reverted to tricyclic 1,2-azaboratabisnorcaradiene **1.55**, and subsequently to the starting material **1.54** upon heating.
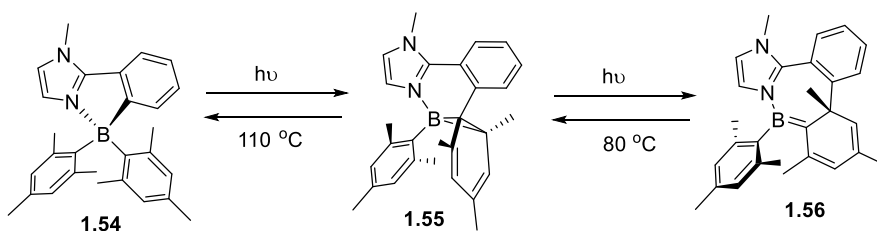
Figure 1.47 Photoisomerization involving "walk" rearrangement.[86]

Photochromic four-coordinated organoboron compounds discovered by our group open a novel opportunity in the research and development of thermal and photo-reactivity of BN-heterocycles, making them potentially useful and attractive as a new class of photochromic materials.

1.4.3 Photoelimination of BN-Heterocycles

Elimination reactions are a family of organic reactions in which two substituents are disconnected from the substrate molecule upon exposure to heat or light; usually at least one hydrogen atom is lost to form a double bond.[87] Photoelimination is much less studied than elimination driven by heat. Furthermore, compared to photoisomerization which has many potential applications in molecular switches, photoelimination appears to be less attractive until Wang and co-workers disclosed another type of BN-heterocycles that underwent an unprecedented

photoelimination to generate the fully conjugated and highly fluorescent 1,2-azaborine derivatives

with the removal of a hydrogen and a mesityl group, rather than photoisomerization (Figure 1.48).[88]

Unlike photoisomerization, this photoelimination is backbone-independent. This generality of the

photoelimination reaction was examined in a metal-containing system as well.[89]

Ar = pyridyl, benzothiazolyl
R = Me, Mes
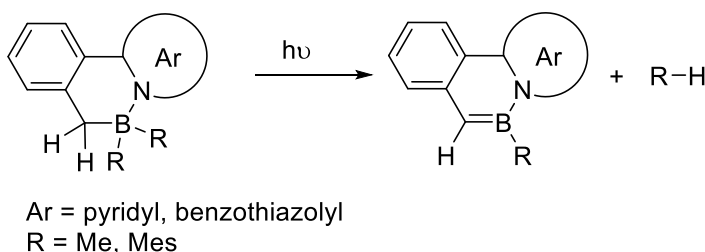
Figure 1.48 Generation of 1,2-azaborines via photoelimination of BN-heterocycles.[88]

R = Mes
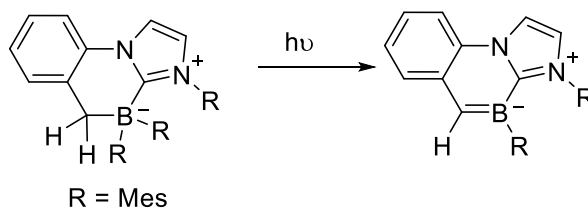
Figure 1.49 Generation of 1,3-azaborines via photoelimination of NHC-BN-heterocycles.[90]

Recently, we found that this unique photoelimination was also applicable to NHC–B,N-

heterocyclic compounds with the formation of rare blue fluorescent 1,3-azaborines which is

regarded as the least stable isomer among azaborine family (Figure 1.49).[90] This work indicates our

photoelimination is capable of generating several different BN-imbedded arenes.

1.4.4 Other Types of Photoreactions of Organoboron Compounds

In the past decade, visible-light photoredox catalysis has been spreading in many areas of

organic chemistry,[91] in particular, organoboron derivatives are qualified to photochemically

generate carbon radicals (Figure 1.50),[92] which tend to react with other components, forming highly

functionalized molecules. Generally, the visible-light photoredox reaction of organoboranes is a

mild and green alternative to conventional procedures. In addition, the incorporation of photoredox catalysis and cross-coupling has initiated new vistas in organic and organometallic chemistry, in return, it is believed that visible-light-driven dual catalysis will continue to fuel organoboron chemistry.
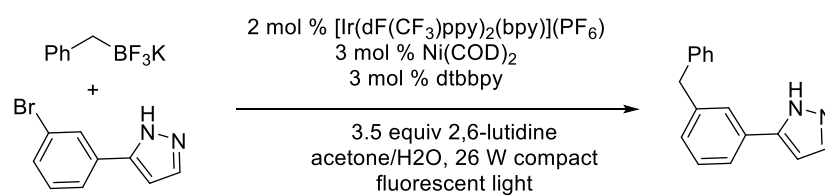
Figure 1.50. Single-electron transmetalation in organoboron cross-coupling by photoredox/nickel dual catalysis.[92]

1.5 Scope of this Thesis

The work described in the thesis focuses on the generation of BN-arenes with the aim to improve the quantum efficiency of photoreaction, and to develop of general methodology to generate BN-heterocycles which could be applied in optoelectronic devices, such as OFETs and OLEDs.

Chapter 2 demonstrates the thermal reactivity of BN-heterocycles and the novel 1,1-hydroboration which could be used to synthesize BN-heterocycles that usually are difficult to access by other methods. Investigation on the thermal reactivity of the BN heterocycles revealed that these molecules have two distinct and competitive thermal elimination pathways: HBR_2 elimination (or retro-hydroboration) versus R-H elimination, depending on the R group on the B atom and the chelate backbone.

Chapter 3 expands the investigation on the reactivity of pyrido[1,2-a]isoindole. A "one-pot" cycloaddition procedure of pyrido[1,2-a]isoindole with triarylboron functionalized acetylenes is demonstrated. The bulky boryl unit is found to greatly diminish intermolecular interactions, rendering these triarylboron-functionalized molecules highly fluorescent with good quantum efficiencies in both solution and the solid state.

Chapter 4 describes a series of poly-(BN)-heterocycles and their thermal and photo-reactivity. This work demonstrates that some of the BN-heterocycles are capable of undergoing elimination not only by heat and light, also by excitons generated electrically within electroluminescent (EL) devices, which further proves that the location and number of BN units in arenes provides BN-arenes unique photophysical properties.

Chapter 5 shows how the photoreactivity of BN-heterocycles can be tuned by internal factors. Both electronic and steric effects are found to have a significant and distinct impact on the

photoreaction pathways of BN-heterocycles. With bulky, electron-donating aryl rings on the B atom, the photoelimination efficiency is enhanced. In contrast, with sufficiently electron-withdrawing aryl groups on the B atom, bulky or not, photoisomerization occurs exclusively with high stereoselectivity.

1.6 References

(1) Boron Science New Technologies and Applications Hosmane, N. S., Ed.; CRC, Taylor & Francis, Boca Raton, **2012**.

(2) (a) Brown, H. C. *Tetrahedron* **1961**, *12*, 117. (b) R. M. Mikhailov, *Organoboron Compounds in Organic Synthesis*, Harwood Academic, **1984**. (c) H. C. Brown, *Boranes in Organic Chemistry*, Cornell University Press, Ithaca, **1972**.

(3) *Boronic acids*; Hall, D. G., Ed.; Wiley-VCH: Weinheim, **2005**.

(4) Miyaura, N.; Suzuki, A. *Chem. Rev.* **1995**, *95*, 2457.

(5) Boussonniàre, A.; Pan, X.; Geib, S. J.; Curran, D. P. *Organometallics* **2013**, *32*, 7445.

(6) (a) Al-Rafia, S. M. I.; McDonald, R.; Ferguson, M. J.; Rivard, E. *Chem. Eur. J.* **2012**, *18*, 13810. (b)Wang, T.; Stephan, D. W. *Chem. Eur. J.* **2014**, *20*, 3036.

(7) Shoji, Y.; Tanaka, N.; Muranaka, S.; Shigeno, N.; Sugiyama, H.; Takenouchi, K.; Hajjaj, F.; Fukushima, T. *Nat. Commun.* **2016**, *7*, 12704.

(8) Tanaka, N.; Shoji, Y.; Hashizume, D.; Sugimoto, M.; Fukushima, T. *Angew. Chem. Int. Ed.* **2017**, *56*, 5312.

(9) Sanzone, J. R.; Hu, C. T.; Woerpel, K. A. *J. Am. Chem. Soc.* **2017**, *139*, 8404.

(10) Wrackmeyer, B. *Coord. Chem. Rev.* **1995**, *145*, 125.

(11) Wrackmeyer, B. *Heteroatom Chem.* **2006**, *17*, 188.

(12) Ge, F.; Kehr, G.; Daniliuc, C. G.; Erker, G. *J. Am. Chem. Soc.* **2013**, *136*, 68.

(13) Chen, C.; Kehr, G.; Fröhlich, R.; Erker, G. *J. Am. Chem. Soc.* **2010**, *132*, 13594.

(14) Eller, C.; Kehr, G.; Daniliuc, C. G.; Stephan, D. W.; Erker, G. *Chem. Commun.* **2015**, *51*, 7226.

(15) Dierker, G.; Ugolotti, J.; Kehr, G.; Fröhlich, R.; Erker, G. *Adv. Synth. Catal.* **2009**, *351*, 1080.

(16) Möbus, J.; Bonnin, Q.; Ueda, K.; Fröhlich, R.; Itami, K.; Kehr, G.; Erker, G. *Angew. Chem. Int. Ed.* **2012**, *51*, 1954.

(17) Welch, G. C.; Juan, R. R. S.; Masuda, J. D.; Stephan, D. W. *Science* **2006**, *314*, 1124.

(18) (a) Hartwig, J. F. *J. Am. Chem. Soc.* **2016**, *138*, 2. (b) Ingleson, M. J. *Synlett* **2012**, 1411.

(19) (a) Oestreich, M. *Angew.Chem. Int. Ed.* **2016**, *55*,494. (b) Lipke, M. C.; Liberman-Martin, A. L.; Tilley, T. D. *Angew. Chem. Int. Ed.* **2017**, *56*, 2260

(20) Stephan, D. W.; Erker, G. *Angew. Chem. Int. Ed.* **2015**, *54*, 6400.

(21) Spies, P.; Erker, G.; Kehr, G.; Bergander, K.; Frohlich, R.; Grimme, S.; Stephan, D. W. *Chem. Commun.* **2007**, *47*, 5072.

(22) Parks, D. J.; Piers, W. E. *J. Am. Chem. Soc.* **1996**, *118*, 9440.

(23) Simonneau, A.; Oestreich, M. *Angew. Chem. Int. Ed.* **2013**, *52*, 11905

(24) Chatterjee, I.; Oestreich, M. *Angew. Chem. Int. Ed.* **2015**, *54*, 1965.

(25) Han, Y.; Zhang, S.; He, J.; Zhang, Y. *J. Am. Chem. Soc.* **2017**, *139*, 7399.

(26) Yin, Q.; Klare, H. F. T.; Oestreich, M. *Angew. Chem. Int. Ed.* **2017**, *56*, 3712.

(27) Légaré, M.-A.; Courtemanche, M.-A.; Rochette, E.; Fontaine, F.-G. *Science* **2015**, *349*, 513.

(28) Légaré, M.-A.; Rochette, É.; Lavergne, J. L.; Bouchard, N.; Fontaine, F.-G. *Chem. Commun.* **2016**, *52*, 5387.

(29) (a) Hudson, Z. M.; Wang, S. *Acc. Chem. Res.* **2009**, *42*, 1584. (b) Lorbach, A.; Hubner, A.; Wagner, M. *Dalton Trans.* **2012**, *41*, 6048. (c) Hudson, Z. M.; Wang, S. *Dalton Trans.* **2011**, *40*, 7805.

(30) (a) Wade, C. R.; Broomsgrove, A. E. J.; Aldridge, S.; Gabbaï, F. P. *Chem. Rev.* **2010**, *110*, 3958. (b) Zhao, H.; Leamer, L. A.; Gabbai, F. P. *Dalton Trans.* **2013**, *42*, 8164. (c) Bresner, C.; Haynes, C. J. E.; Addy, D. A.; Broomsgrove, A. E. J.; Fitzpatrick, P.; Vidovic, D.; Thompson, A. L.; Fallis, I. A.; Aldridge, S. *New J. Chem.* **2010**, *34*, 1652.

(31) Balzani, V.; Ceroni, P.; Juris, A. Photochemistry and Photophysics: Concepts, Research, Applications, *John Wiley & Sons*, 2014.

(32) Noda, T.; Shirota, Y. *J. Am. Chem. Soc.* **1998**, *120*, 9714.

(33) Shirota, Y.; Kinoshita, M.; Noda, T.; Okumoto, K.; Ohara, T. *J. Am. Chem. Soc.* **2000**, *122*, 11021.

(34) Kim, Y.; Gabbai, F. P. *J. Am. Chem. Soc.* **2009**, *131*, 3363.

(35) Yamaguchi, S.; Akiyama, S.; Tamao, K. *J. Am. Chem. Soc.* **2001**, *123*, 11372.

(36) Liu, X. Y.; Bai, D. R.; Wang, S. *Angew. Chem. Int. Ed.* **2006**, *45*, 5475.

(37) https://www.nobelprize.org/nobel_prizes/physics/laureates/2010/ (August 29th, 2017)

(38) (a) Liu, H.; Liu, Y.; Zhu, D. *J. Mater. Chem.* **2011**, *21*, 3335. (b) Wang, X.; Li, X.; Zhang, L.; Yoon, Y.; Weber, P. K.; Wang, H.; Guo, J.; Dai, H. *Science* **2009**, *324*, 768.

(39) (a) Tang, Y.-B.; Yin, L.-C.; Yang, Y.; Bo, X.-H.; Cao, Y.-L.; Wang, H.-E.; Zhang, W.-J. Bello, I.; Lee, S.-T.; Cheng, H.-M.; Lee, C.-S. *ACS Nano* **2012**, *6*, 1970. (b) Wu, Z.-S.; Ren, W.; Xu, L.; Li, F.; Cheng, H.-M. *ACS Nano* **2011**, *5*, 5463.

(40) (a) Saito, S.; Matsuo, K.; Yamaguchi, S. *J. Am. Chem. Soc.* **2012**, *134*, 9130. (b) Dou, C.; Saito, S.; Matsuo, K.; Hisaki, I.; Yamaguchi, S. *Angew. Chem. Int. Ed.* **2012**, *51*, 12206.

(41) Hertz, V. M.; Bolte, M.; Lerner, H.-W.; Wagner, M. *Angew. Chem. Int. Ed.* **2015**, *54*, 8800.

(42) John, A.; Bolte, M.; Lerner, H.-W.; Wagner, M. *Angew. Chem. Int. Ed.* **2017**, *56*, 5588.

(43) (a) Bosdet, M. J. D.; Piers, W. E. *Can. J. Chem.* **2009**, *87*, 8. (b) Campbell, P. G.; Marwitz, A. J. V.; Liu, S.-Y. *Angew. Chem. Int. Ed.* **2012**, *51*, 6074. (c) Wang, X.-Y.; Wang, J.-Y.; Pei, J. *Chem. Eur. J.* **2015**, *21*, 3528.

(44) Stock, A.; Pohland, E. *Ber. Dtsch. Chem. Ges.* **1926**, *59*, 2210.

(45) Ghosh, D.; Periyasamy, G.; Pati, P. K. *Phys. Chem. Chem. Phys.* **2011**, *13*, 20627.

(46) Dewar, M. J. S.; Kubba, V. P.; Pettit, R. *J. Chem. Soc.* **1958**, 3073.

(47) Ashe, A. J.; Fang, X. D. *Org. Lett.* **2000**, *2*, 2089.

(48) Marwitz, A. J. V.; Abbey, E. R.; Jenkins, J. T.; Zakharov, L. N.; Liu, S.-Y. *Org. Lett.* **2007**, *9*, 4905.

(49) Lamm, A. N.; Garner, E. B.; Dixon, D. A.; Liu, S.-Y. *Angew. Chem. Int. Ed.* **2011**, *50*, 8157.

(50) Braunschweig, H.; Geetharani, K.; Jimenez-Halla, J. O. C.; Schäfer, M. *Angew. Chem. Int. Ed.* **2014**, *53*, 3500.

(51) Braunschweig, H.; Hörl, C.; Mailänder, L.; Radacki, K.; Wahler, J. *Chem. Eur. J.* **2014**, *20*, 9858.

(52) (a) Bosdet, M. J. D.; Piers, W. E.; Sorensen, T. S.; Parvez, M. *Angew. Chem. Int. Ed.* **2007**, *46*, 4940. (b) Jaska, C. A.; Piers, W. E.; McDonald, R.; Parvez, M. *J. Org. Chem.* **2007**, *72*, 5234.

(53) (a) Dewar, M. J. S.; Kaneko, C.; Bhattacharjee, M. K. *J. Am. Chem. Soc.* **1962**, *84*, 4884. (b) Dewar, M. J. S.; Kubba, V. P.; Pettit, R. *J. Chem. Soc.* **1958**, 3073.

(54) Hatakeyama, T.; Hashimoto, S.; Seki, S.; Nakamura, M. J. *Am. Chem. Soc.* **2011**, *133*, 18614.

(55) Hatakeyama, T.; Hashimoto, S.; Oba, T.; Nakamura, M. *J. Am. Chem. Soc.* **2012**, *134*, 19600.

(56) Xu, S.; Zakharov, L. N.; Liu, S. Y. *J. Am. Chem. Soc.* **2011**, *133*, 20152.

(57) Braunschweig, H.; Damme, A.; Jimenez-Halla, O. C.; Pfaffinger, B.; Radacki, K.; Wolf, J. *Angew. Chem. Int. Ed.* **2012**, *51*, 10034.

(58) Liu, X.; Zhang, Y.; Li, B.; Zakharov, L. N.; Vasiliu, M.; Dixon, D. A.; Liu, S.-Y. *Angew.Chem. Int.Ed.* **2016**, *55*, 8333.

(59) (a) Agou, T.; Kobayashi, J.; Kawashima, T. *Org. Lett.* **2006**, *8*, 2241. (b) Agou, T.; Kobayashi, J.; Kawashima, T. *Chem. Commun.* **2007**, 3204. (c) Agou, T.; Sekine, M.; Kobayashi, J.; Kawashima, T.; *Chem. Eur. J.* **2009**, *15*, 5056. (d) Agou, T.; Sekine, M.; Kobayashi, J.; Kawashima, T. *Chem. Commun.* **2009**, 1894.

(60) Abbey, E. R.; Zakharov, L. N.; Liu, S.-Y. *J. Am. Chem. Soc.* **2010**, *132*, 16340.

(61) Ma, C.; Zhang, J.; Li, J.; Cui, C. *Chem. Commun.* **2015**, *51*, 5732.

(62) Wang, X.-Y.; Narita, A.; Feng, X.; Müllen, K. *J. Am. Chem. Soc.* **2015**, *137*, 7668.

(63) 2Wang, X.; Zhang, F.; Schellhammer, K. S.; Machata, P.; Ortmann, F.; Cuniberti, G.; Fu, Y.; Hunger, J.; Tang, R.; Popov, A. A.; Berger, R.; Müllen, K.; Feng, X. *J. Am. Chem. Soc.* **2016**, *138*, 11606.

(64) Numano, M.; Nagami, N.; Nakatsuka, S.; Katayama, T.; Nakajima, K.; Tatsumi, S.; Yasuda, N.; Hatakeyama, T. *Chem. Eur. J.* **2016**, *22*, 11574.

(65) Hatakeyama, T.; Shiren, K.; Nakajima, K.; Nomura, S.; Nakatsuka, S.; Kinoshita, K.; Ni, J.; Ono, Y.; Ikuta, T. *Adv. Mater.* **2016**, *28*, 2777.

(66) Letsinger, R. L.; Nazy, J. R. *J. Am. Chem. Soc.* **1959**, *81*, 3013.

(67) Chen, J.; Bajko, Z.; Kampf, J. W.; Ashe, A. J. *Organometallics* **2007**, *26*, 1563.

(68)   Yruegas, S.; Patterson, D. C.; Martin, C. D. *Chem. Commun.* **2016**, *52*, 6658.

(69)   Araneda, J. F.; Piers, W. E.; Sgro, M. J.; Parvez, M. *Organometallics* **2015**, *34*, 3408.

(70)   Katayama, T.; Nakatsuka, S.; Hirai, H.; Yasuda, N.; Kumar, J.; Kawai, T.; Hatakeyama, T. *J. Am. Chem. Soc.* **2016**, *138*, 5210.

(71)   Wang, X.-Y.; Narita, A.; Feng, X.; Müllen, K.; Zhang, W. *J. Am. Chem. Soc*. **2016**, *138*, 9021.

(72)   (a) Grisdale, P. J.; Williams, J. L. R.   *J. Org. Chem.* **1969**, *34*, 1675. (b) Davis, F. A.; Dewar, M. J. S. *J. Am. Chem. Soc.* **1968**, *90*, 3511. (c) Rohr, A. D.; Banaszak Holl, M. M.; Kampf, J. W.; Ashe III, A. J. *Organometallics* **2011**, *30*, 3698.

(73)   (a) Agou, T.; Kobayashi, J.; Kawashima, T. *Org. Lett.* **2005**, *7*, 4373. (b) Berger, H.-O.; Nçth, H. *J. Organomet. Chem.* **1983**, *250*, 33. (c) Ashe III, A. J.; Bajko, Z.; Carr, M. D.; Kampf, J. W. *Organometallics* **2003**, *22*, 910.

(74)   Barnard, J. H.; Brown, P. A.; Shuford, K. L.; Martin, C. D. *Angew. Chem., Int. Ed.* **2015**, *54*, 12083.

(75)   Pelter, A.; Pardasani, R. T.; Pardasani, P. *Tetrahedron* **2000**, *56*, 7339.

(76)   (a) Eisch, J. J.; Shen, F.; Tamao, K. *Heterocycles* **1982**, *18*, 245. (b) Eisch, J. J. *Adv. Organomet. Chem.* **1977**, *16*, 67. (c) Eisch, J. J. *Adv. Organomet. Chem.* **1996**, *39*, 375.

(77)   Eisch, J. J.; Shafii, B.; Odom, J. D.; Rheingold, A. L. *J. Am. Chem. Soc.* **1990**, *112*, 1847.

(78)   (a) Berkovic, G.; Krongauz, V.; Weiss, V. *Chem. Rev.* **2000**, *100*, 1741. and references therein. (b) Irie, M. *Chem. Rev.* **2000**, *100*, 1685. (c) Ko, C.-C.; Yam, V. W.-W. *J. Mater. Chem.* **2010**, *20*, 2063.

(79)   Ansorg, K.; Braunschweig, H.; Chiu, C.-W.; Engels, B.; Gamon, D.; Hügel, M.; Kupfer, T.; Radacki, K. *Angew. Chem. Int. Ed.* **2011**, *50*, 2833.

(80) Braunschweig, H.; Kupfer, T. *Chem. Commun.* **2011**, *47*, 10903.

(81) Araneda, J. F.; Neue, B.; Piers, W. E.; Parvez, M. *Angew. Chem. Int. Ed.* **2012**, *51*, 8546.

(82) Iida, A.; Saito, S.; Sasamori, T.; Yamaguchi, S. *Angew. Chem. Int. Ed.* **2013**, *52*, 3760.

(83) Rao, Y.-L.; Amarne, H.; Zhao, S.-B.; McCormick, T. M.; Martić, S.; Sun, Y.; Wang, R.-Y.; Wang, S. *J. Am. Chem. Soc.* **2008**, *130*, 12898.

(84) Rao, Y.-L.; Chen, L. D.; Mosey, N. J.; Wang, S. *J. Am. Chem. Soc.* **2012,** *134*, 11026.

(85) Rao, Y.-L.; Amarne, H.; Chen, L. D.; Brown, M. L.; Mosey, N. J.; Wang, S. *J. Am. Chem. Soc.* **2013**, *135*, 3407.

(86) Rao, Y.-L.; Hörl, C.; Braunschweig, H.; Wang, S. *Angew. Chem., Int. Ed.* **2014**, *53*, 9086.

(87) https://en.wikipedia.org/wiki/Elimination_reaction. (August 29th, 2017)

(88) Lu, J.-S.; Ko, S.-B.; Walters, N. R.; Kang, Y.; Sauriol, F.; Wang, S. *Angew. Chem., Int. Ed.* **2013**, *52*, 4544.

(89) Ko, S.-B.; Lu, J.-S.; Wang, S. *Org. Lett.* **2014**, *16*, 616.

(90) McDonald, S. M.; Mellerup, S. K.; Peng, J.; Yang, D.; Li, Q.- S.; Wang, S. *Chem. - Eur. J.* **2015**, *21*, 13961.

(91) Prier, C. K.; Rankic, D. A.; MacMillan, D. W. C. *Chem. Rev.* **2013**, *113*, 5322.

(92) (a) Molander, G. A. *J. Org. Chem.* **2015**, *80*, 7837. (b) Tellis, J. C.; Primer, D. N.; Molander, G. A. *Science* **2014**, *345*, 433.

Chapter 2

Investigation on Thermal Reactivity of BN-Heterocycles and 1,1-Hydroboration

2.1 Introduction

Boron and nitrogen containing compounds are known to display interesting thermal or photo-reactivity such as hydrogen storage,[1] polymerization,[2] hydroboration,[3] photoisomerization[4] and photoelimination.[5] Some members of this class of compounds are also known to be effective as fluorescent probes[6] or emitters/charge transport materials in organic devices such as organic light emitting diodes (OLEDs).[7] Fully conjugated BN-heterocycles such as azaborines and their polycyclic derivatives are especially appealing because of their unique electronic, photophysical and chemical properties.[8,9] Although various synthetic strategies have been devised for the construction of azaborines and related compounds, this class of compounds remains a synthetic challenge.[1a-c,8-10] We recently reported a photochemical process for the generation of highly emissive BN-phenanthrenes and related compounds (**2.2** in Figure 2.1) in solution and in a polymer matrix from unsaturated BN-heterocyclic molecules (**2.1**).[5a] Although the photochemical process allows the generation of BN-phenanthrenes exclusively, and in most instances nearly quantitatively, it can be slow and time-consuming when performed in solutions of high concentration (*e.g.* typical concentrations for recording an NMR spectrum) due to the low quantum efficiency of such reactions.[5] Computational studies for the thermal elimination of **2.1** to **2.2** revealed that it is a thermodynamically favored process but has a very large activation barrier (>50 kcal/mol), which is too high to overcome in common organic solvents. However, it is conceivable that this activation barrier may be overcome thermally in a solvent-free system as shown in Figure

2.1. To examine the possibility of producing BN-phenanthrenes (**2.2**) via thermal elimination, we set out to explore the thermal reactivity of BN-heterocycles (**2.1**) and developed a convenient protocol for high temperature thermal reactions. This investigation has led to several surprising and interesting discoveries on the thermal reactivity of BN-heterocycles, including competing thermal elimination pathways (Path I) and the unprecedented reversible borane insertion into a C-N bond (Path II, 1,1-hydroboration), as shown in Figure 2.2. The details of these studies on BN-heterocycles **2.1** (Ar = pyridyl) are presented in this chapter. All the compounds and intermediates of this project are outlined in Figure 2.2.
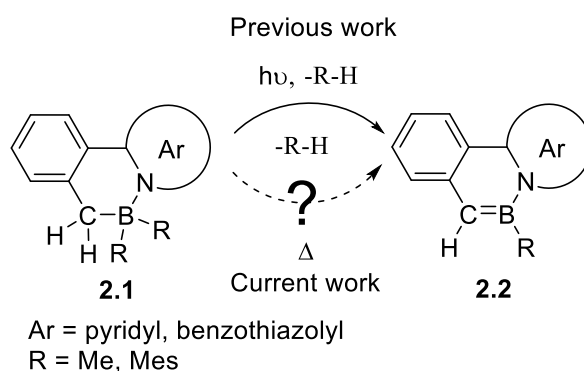
Figure 2.1 The previously reported photoelimination and the proposed thermal elimination of BN-heterocycles.
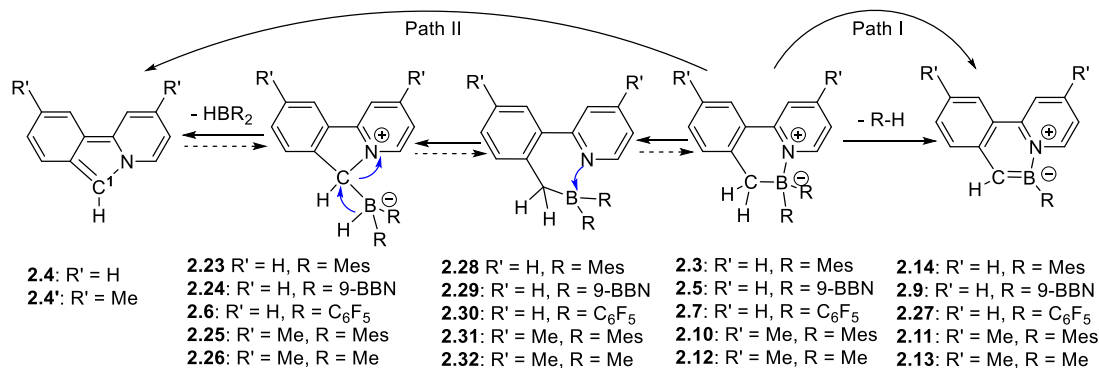
Figure 2.2. The compounds and intermediates investigated in this project.

48

2.2 Experimental Sections

2.2.1 General Procedure

All solvents were freshly distilled over sodium metal and stored under nitrogen prior to use. All starting materials were purchased from Sigma-Aldrich Chemicals Corp. except BMes$_2$F, which was purchased from TCI America Co. The mineral oil used in the thermal reaction was purchased from Sigma-Aldrich Corp. and was heated over sodium metal and stored under nitrogen prior to use. All reactions were carried out under nitrogen atmosphere, either using Schlenk/vacuum line techniques or in a glove box. The ^{1}H, ^{11}B, ^{13}C, ^{19}F, 2D-NOESY NMR spectra were recorded on a Bruker Avance 400, 500 or 600 MHz spectrometers. Boron chemical shift values are referenced to the external standard boron signal of BF$_3$·Et$_2$O. Data are presented as: chemical shift, multiplicity (s = singlet, d = doublet, t = triplet, q = quartet, quint = quintet, sext = sextet, sept = septet, m = multiplet and/or multiplet resonances, br = broad). UV-Vis spectra were obtained on Varian Cary 50 UV-Vis spectrophotometer. Fluorescence spectra were recorded on a Photon Technologies International Quanta Master Model C-60 spectrometer. High-resolution mass spectra (HRMS) were obtained from an Applied Biosystems Qstar XL spectrometer. Elemental analysis was conducted at Laboratorie d'Analyse Élémentaire de l'Université de Montréal. The thermal elimination reactions were performed in a sealed tube or high-pressure J-Young NMR Tube, while the photoelimination reactions were carried out in Norell quartz J-Young NMR tubes using a Rayonet Photochemical Reactor. Compounds **2.3**, **2.10** and **2.12** were prepared according to the previously reported procedure reported by us.[5a] HB(C$_6$F$_5$)$_2$ and HBMes$_2$ were prepared by literature methods.[11, 12] The independent synthesis of pyrido[1,2-a]isoindole (**2.4**) was carried out using the procedure reported by Kanemasa *et al.*[13]

2.2.2 Procedure of Photo- and Thermal Reactions

Monitoring the photolysis process via ^{1}H NMR spectra. Sample was prepared inside a glove box by dissolving approximately 5 mg of desired compound in dry C_6D_6, this was then subjected to UV irradiation (300 nm) inside a Rayonet photochemical reactor, followed by recording the ^{1}H and ^{11}B NMR spectra at different time intervals.

High temperature thermal reactions. In a glove box, 50 mg of BN-heterocycle was placed in a sealed tube containing a few drops of mineral oil. The reaction vessel was heated for 2 hrs at 280°C using a sand bath. The reaction mixture was subsequently washed with hexanes to remove the mineral oil and the product was recrystalized from benzene/THF.

2.2.2.1 Reversible 1,1-Hydroboration Reaction between **2.3** and **2.4**, Mes$_2$BH

Retro-hydroboration of 2.3. In a glove box, compound **2.3** (50 mg, 0.12 mmol) was placed in a sealed tube containing a few drops of mineral oil. The reaction vessel was heated for 2 hrs at 280 °C using a sand bath. The reaction mixture was subsequently washed with hexanes to remove the mineral oil, leaving behind compound **2.4** as a yellow powder which was recrystallized as yellow needles from benzene/THF (21 mg, 0.06 mmol, 80% yield). The ^{1}H NMR spectrum of **2.4** matched that reported in the literature. The same reaction was also performed in a J-Young NMR tube and monitored by NMR spectroscopy (Figure 2.3, and Figure 2.27 in Section 2.5).
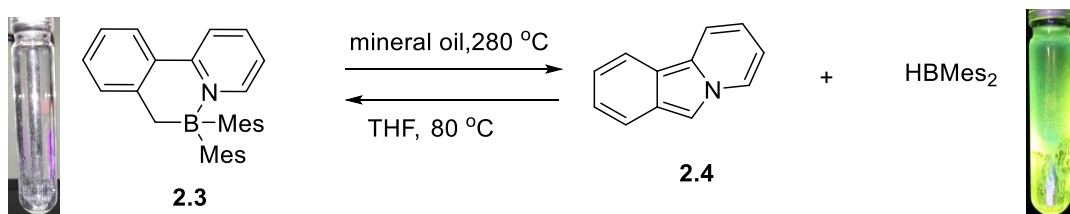
Figure 2.3 Reversible 1,1-hydroboration between **2.3** and **2.4**.

*1,1-Hydroboration of **2.4** with HBMes₂ (NMR Scale):* HBMes$_2$ (11 mg, 0.045 mmol) and **2.4** (5 mg, 0.03 mmol) were reacted in THF-d_8 (0.75 mL) at 80 °C for 3 days in a J-Young NMR tube. The NMR data were collected from the reaction mixture at room temperature every several hours.

*1,1-Hydroboration of **2.4** with HBMes₂ (Prep Scale):* HBMes$_2$ (220 mg, 0.9 mmol) and **2.4** (100 mg, 0.6 mmol) were reacted in THF (15 mL) at 80 °C for 3 days, at which point the volatiles were removed *in vacuo* and the product was isolated by column chromatography on silica gel using a solvent mixture of hexanes and ethyl acetate (10:1) as the eluent. The product **2.3** was obtained and isolated as a white solid (238 mg, 0.57 mmol, 95% yield) and its ^{1}H, ^{13}C and ^{11}B spectra match those reported previously for **2.3**.[5a]

2.2.2.2 1,1-Hydroboration of **2.4** with 9-BBN and Isolation of **2.5**

NMR Scale: 9-BBN (8 mg, 0.06 mmol) and **2.4** (5 mg, 0.03 mmol) were reacted in toluene-d_8 (0.75 mL) at 110 °C for 10 hrs in a J-Young NMR tube. The NMR data were collected from the reaction mixture at room temperature every several hours.

Prep Scale: 9-BBN (146 mg, 1.2 mmol) and **2.4** (100 mg, 0.6 mmol) were reacted in toluene (15 mL) at 110 °C in a flask for 10 hrs, at which point the volatiles were removed in *vacuo* and the product was isolated by column chromatography on silica gel using a solvent mixture of hexanes and ethyl acetate (10:1) as the eluent. The product **2.5** was isolated as a white solid (156 mg, 0.54 mmol, 90% yield) and fully characterized by NMR, MS, elemental analysis and X-ray diffraction analysis.
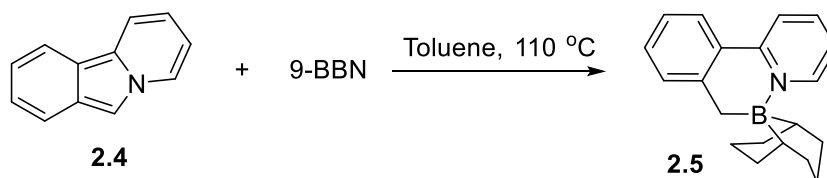
Figure 2.4 1,1-Hydroboration of **2.4** with 9-BBN.

^{1}H NMR data for **2.5** (400 MHz, C$_6$D$_6$): δ 8.82 – 8.63 (m, 1H), 7.40 (d, J = 7.4 Hz, 1H), 7.35 – 7.29 (m, 1H), 7.10 (t, J = 7.5 Hz, 1H), 7.04 (d, J = 7.6 Hz, 1H), 6.88 (td, J = 7.8, 1.5 Hz, 1H), 6.40 (ddd, J = 7.3, 6.0, 1.3 Hz, 1H), 2.53 (s, 2H), 2.46 – 2.21 (m, 4H), 2.13 (dd, J = 13.7, 6.5 Hz, 5H), 1.95 (s, 3H), 1.18 (s, 2H). ^{13}C NMR data (101 MHz, C$_6$D$_6$): δ 154.42, 147.17, 145.29, 138.35, 131.55, 131.12, 130.53, 128.05, 127.81, 127.56, 125.59, 124.38, 122.99, 121.31, 34.03, 31.53, 25.09, 24.49, 23.70. ^{11}B NMR (128 MHz, C$_6$D$_6$): δ -0.58. HR-EIMS (m/z): [M$^+$] calcd. for C$_{20}$H$_{24}$BN, 289.2002; found 289.2012. Anal. calcd. (%) for C$_{20}$H$_{24}$BN: C 83.06, H 8.36, N 4.84; found: C 82.89, H 8.37, N 4.86.

2.2.2.3 1,1-Hydroboration of **2.4** with HB(C$_6$F$_5$)$_2$ and Isolation of **2.7**.

NMR Scale: HB(C$_6$F$_5$)$_2$ (20 mg, 0.06 mmol) and **2.4** (5 mg, 0.03 mmol) were reacted in toluene-d_8 (0.75 mL) at room temperature in a J-Young NMR tube. The product **2.6** was obtained intermediately, which was characterized by NMR spectroscopy (Figure 2.4). After heating the solution of **2.6** in toluene-d_8 at 110 ºC for 1.5 hrs, product **2.7** was found to form quantitatively (Figure 2.5).
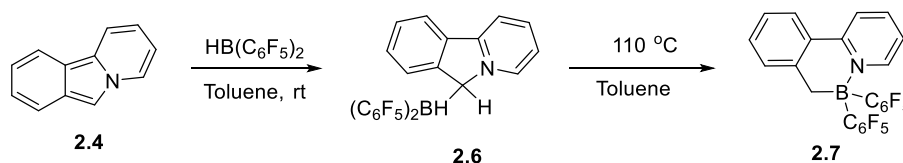
Figure 2.5 1,1-Hydroboration of **2.4** with HB(C$_6$F$_5$)$_2$ with the intermediate **2.6**.

^{1}H NMR data for **2.6** (400 MHz, toluene-d_8): δ 7.79 (d, J = 6.2 Hz, 1H), 7.60 (d, J = 7.9 Hz, 1H), 7.09 (dd, J = 7.9, 3.2 Hz, 2H), 6.93 (t, J = 7.6 Hz, 1H), 6.80 (t, J = 7.8 Hz, 1H), 6.72 (d, J = 8.2 Hz, 1H), 6.29 – 6.16 (m, 1H), 5.90 (s, 1H), 3.38 (dd, J = 190.1, 88.6 Hz, 2H). ^{13}C NMR (101 MHz, C$_6$D$_6$): δ 154.38, 150.67, 149.44, 147.33, 139.11, 138.76, 136.61, 133.90, 132.20, 126.37, 123.42, 120.91, 120.66, 117.29. The signals from the carbon atoms bound to boron were not

observed. ^{11}B NMR (128 MHz, toluene-d_8): δ -16 (d, 90 Hz). ^{19}F NMR (376 MHz, C$_6$D$_6$) δ -131.54 (d, J = 22.9 Hz), -132.46 (d, J = 23.8 Hz), -161.09 (t, J = 20.7 Hz), -165.44 (dd, J = 31.6, 13.3 Hz), -165.90 (dd, J = 31.3, 13.8 Hz).

Prep Scale: HB(C$_6$F$_5$)$_2$ (415 mg, 1.2 mmol) and **2.4** (100 mg, 0.6 mmol) were reacted in toluene (15 mL) at 110 ℃ in a flask until reaction completion, at which point the volatiles were removed *in vacuo* and the product was isolated by column chromatography on silica gel using a solvent mixture of hexane and ethyl acetate (10:1) as the eluent. The product **2.7** was isolated as a grey solid (203 mg, 0.588 mmol, 98% yield) and fully characterized by NMR, elemental analysis and X-ray diffraction analysis.

^{1}H NMR data for **2.7** (400 MHz, toluene-d_8) δ 7.94 (d, *J* = 5.8 Hz, 1H), 7.12 (d, *J* = 6.2 Hz, 1H), 7.07 – 6.95 (m, 4H), 6.82 (t, *J* = 7.5 Hz, 1H), 6.40 (td, *J* = 6.3, 2.3 Hz, 1H), 2.79 (s, 2H). ^{13}C NMR (101 MHz, CD$_2$Cl$_2$) δ 154.53, 149.49, 147.22, 145.63, 144.22, 142.44, 140.77, 138.30, 135.87, 131.86, 129.57, 126.76, 125.68, 124.10, 123.19, 25.58. ^{11}B NMR (128 MHz, C$_6$D$_6$) δ -2.78. 19F NMR (376 MHz, C6D6) δ -165.30 to -164.36 (m), -158.09 to -157.89 (m), -157.80 (t, J = 20.9 Hz), -133.72 (dd, J = 23.9, 8.5 Hz). Anal. calcd. (%) for C$_{24}$H$_{10}$BF$_{10}$N: C 56.18, H 1.96, N 2.73; found: C 55.71, H 2.16, N 2.78.

2.2.2.4 Reaction of **2.4** with B(C$_6$F$_5$)$_3$ and Isolation of **2.8**
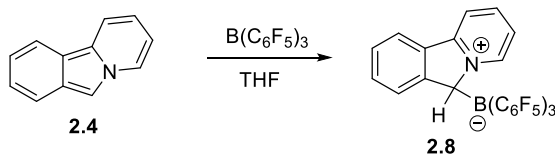
NMR Scale: B(C$_6$F$_5$)$_3$ (15 mg, 0.03 mmol) and **2.4** (5 mg, 0.03 mmol) in THF-d_8 (0.75 ml) were mixed at room temperature in a J-Young NMR tube. The product **2.8** was obtained intermediately and characterized by NMR spectroscopy.

Prep Scale: $B(C_6F_5)_3$ (307 mg, 0.6 mmol) and **2.4** (100 mg, 0.6 mmol) in THF (20 ml) were mixed at room temperature in a vial in the glovebox. The product **2.8** was obtained intermediately and the product **2.8** was isolated by recrystallization from THF (326 mg, 0.48 mmol, 80% yield), and fully characterized by NMR, MS, and X-ray diffraction analysis.

^{1}H NMR data for **2.8** (400 MHz, THF-d_8): δ 8.71 (d, J = 6.0 Hz, 1H), 8.41 – 8.22 (m, 2H), 7.95 (d, J = 7.7 Hz, 1H), 7.64 (t, J = 6.4 Hz, 1H), 7.53 (dd, J = 13.8, 6.4 Hz, 2H), 7.44 (t, J = 7.3 Hz, 1H), 7.33 (d, J = 6.3 Hz, 1H). ^{13}C NMR (101 MHz, THF-d8): δ 151.09, 147.20, 146.39, 144.76, 140.36, 139.78, 138.43, 137.26, 136.60, 134.12, 130.18, 127.83, 125.38, 121.86, 120.99, 119.37, 116.79, 114.08 (br). ^{11}B NMR (128 MHz, THF-d_8): δ -13.0. ^{19}F NMR (376 MHz, THF-d8): δ - 168.00 (t, J = 19.0 Hz), -161.21 (t, J = 20.0 Hz), -136.51 (d, J = 19.6 Hz). HR-ESIMS (m/z): $[M+Na]^+$ calcd. for $C_{30}H_9BF_{15}NNa$, 702.04807; found 702.04844; $[M+K]^+$ calcd. for $C_{30}H_9BF_{15}NK$, 718.02201; found 718.02245. The potassium and sodium ions are commonly found inside the MS spectrometer.

2.2.2.5 Photoelimination of **2.5** and Characterization of **2.9**
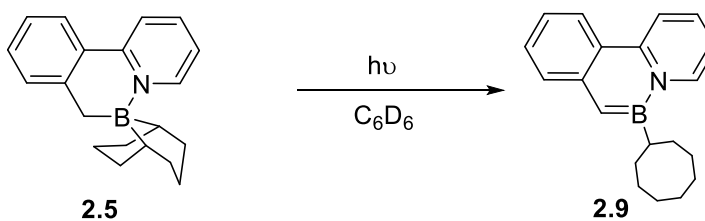
Figure 2.6 Photoelimination of **2.5**.

Compound **2.5** (5 mg) was dissolved in C_6D_6 (0.5 mL) in a quartz J-Young NMR tube and sealed under nitrogen. The NMR tube was then irradiated with 300 nm UV light and the progression of the reaction was monitored by ^{1}H and ^{11}B NMR spectra until it reached completion.

^{1}H NMR data for **2.9** (400 MHz, C$_6$D$_6$): δ 8.52 (d, J = 6.7 Hz, 1H), 8.21 (d, J = 8.7 Hz, 2H), 7.91 (d, J = 8.9 Hz, 1H), 7.46 – 7.41 (m, 1H), 7.41 (d, J = 4.1 Hz, 1H), 7.15 – 7.09 (m, 1H), 6.91 – 6.84 (m, 1H), 6.57 – 6.48 (m, 1H). 2.50-0.8 (m, 15H). ^{13}C NMR (101 MHz, C$_6$D$_6$): δ 145.32, 134.76, 128.74, 128.55, 128.41, 127.11, 124.65, 122.11, 119.48, 115.40, 115.29, 107.01, 31.65, 31.55, 31.08, 29.93, 28.12, 27.28, 27.25, 26.76. ^{11}B NMR (128 MHz, C$_6$D$_6$): δ 36.9. HR-EIMS (*m/z*): [M$^+$] calcd. for C$_{20}$H$_{24}$BN, 289.2002; found 289.1987.

2.2.2.6 Formation of BN-Phenanthrenes via Thermal Elimination
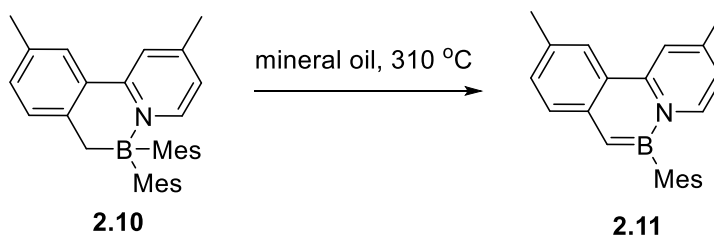
Figure 2.7 Thermal elimination of **2.10**.

In a glove box, compound **2.10** (5 mg, 0.011 mmol) was placed in a J-Young NMR tube containing a few drops of mineral oil. The reaction vessel was heated for 2 hrs at 310 ºC using a sand bath. C$_6$D$_6$ was added and the ^{1}H and ^{11}B NMR spectra were recorded. The elimination product was identified to be **2.11** based on the NMR data reported previously,[5a] and an 85% conversion of **2.10** to **2.11** was observed.
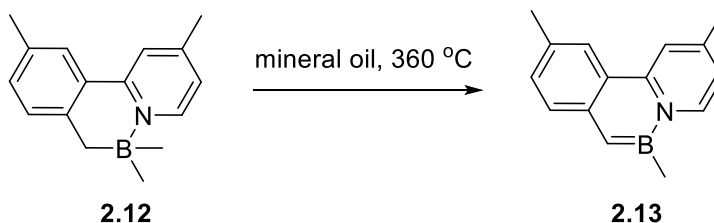
Figure 2.8 Thermal elimination of **2.12**.

In a glove box, compound **2.12** (5 mg, 0.022 mmol) was placed in a J-Young NMR tube containing a few drops of mineral oil. The reaction vessel was heated for 2 hrs at 360°C using a sand bath. C_6D_6 was added and the ^1H and ^{11}B NMR spectra were recorded. The elimination product was identified to be **2.13** based on the NMR data reported previously,[5a] and a 40% conversion of **2.12** to **2.13** was observed.

2.2.3 X-ray crystallographic analysis

Single crystals of compounds **2.4**, **2.5**, **2.7** and **2.8** were obtained by recrystallization from THF and hexanes at 298 K. Data were collected on a Bruker AXS Apex II single-crystal X-ray diffractometer with graphite-monochromated Mo Kα radiation, operating at 50 kV and 30 mA at 180 K. Data were processed on a PC with the aid of the Bruker SHELXTL software package (version 6.14)[14] and corrected for absorption effects. All structures were solved by direct methods. The crystals of **A** belong to the orthorhombic space group Pnma while those of **2.5**/**2.7** and **2.8** belong to the monoclinic space groups P2$_1$/n and P2$_1$/m, respectively. The molecules of **2.4** and **2.8** possess a crystallographically imposed mirror plane with 0.5 molecule in the asymmetric unit. As a consequence, the nitrogen atom (N(1)) and the carbon atom (C(2)) are disordered over the two symmetry related sites. All non-hydrogen atoms were refined anisotropically. The positions of hydrogen atoms were calculated, and their contributions in structural factor calculations were included. The details of crystallographic data can be found in the supporting information. Crystal data for all structures have been deposited to the Cambridge Crystal Data Center (CCDC No. 1035207 (**2.8**), 1035208 (**2.5**), 1035214 (**2.4**), 1043572 (**2.7**)).

2.2.4 DFT Calculations

All calculations were performed using the Gaussian 09 suite of programs[15] on the High Performance Computing Virtual Laboratory (HPCVL) at Queen's University. Initial input

coordinates were taken from the corresponding crystal structure data where applicable, while all others were generated from the optimized geometry of the (benzyl-pyridine)BMes$_2$ chelate reported previously. Modeling of the reaction pathway was accomplished using the CAMB3LYP5 level of theory and the 6-31g(d) basis set,[16] as this combination was found to accurately reproduce the experimentally determined UV-Vis spectrum of a reference compound in the same class considered here. All reactant, intermediate and product geometries were optimized without constraints and characterized as minima along the potential energy surfaces through vibrational frequency analysis. Transition state structures were located by employing the QST3 option in Gaussian and contained only one imaginary frequency. TD-DFT vertical excitations of **2.4**, **2.5** and **2.9** were performed using the B3LYP/6-311+g(d,p) method/basis set (following optimizations at this same level of theory) to allow for comparisons with previous computational work on similar compounds.

2.3 Results and Discussion

2.3.1 Thermal Elimination

R^1 = H, R^2 = Mes **2.3**
R^1 = Me, R^2 = Mes **2.10**
R^1 = Me, R^2 = Me **2.12**

R^1 = H, R^2 = Mes **2.14**
R^1 = Me, R^2 = Mes **2.11**
R^1 = Me, R^2 = Me **2.13**
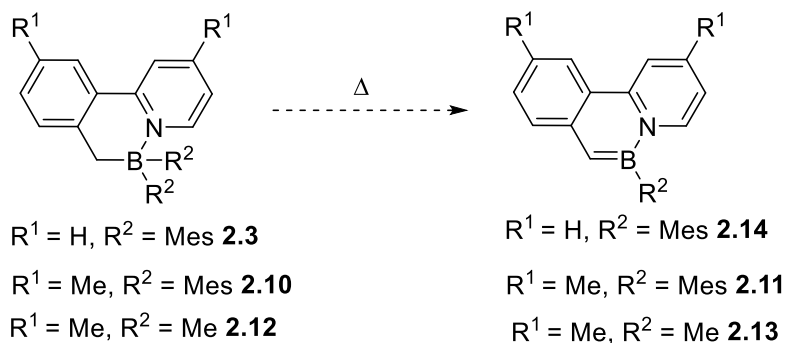
Figure 2.9 Proposed thermal eliminations.

Three previously reported[5a] BN-heterocyclic compounds **2.3**, **2.10** and **2.12** were examined for their thermal reactivity. Initial attempts involved placing powder samples of these compounds in a glass vessel that was kept under vacuum. Upon heating however, the BN-heterocycles sublimed

rapidly and no reaction was observed. To prevent sublimation, the same reaction was performed in a sealed glass tube under nitrogen. Upon heating to ~280 $^{\circ}$C or higher, yellow-green fluorescent products became readily visible on the wall of the glass tube for all these compounds, which are reminiscent of the BN-phenanthrenes **2.11**, **2.13** and **2.14** shown in Figure 2.9. Unfortunately, this method also resulted in decomposition of the sample and the formation of insoluble brown solids due to the temperature inhomogeneity of the solid inside the reaction vessel.

To improve the heat conductivity and homogeneity, a small amount of a high boiling mineral oil that was pre-dried over sodium metal was added to the solid sample in the glass tube. This approach was found to be far superior, as the unwanted decomposition of **2.3**, **2.10** and **2.12** were no longer observed. Employing this new method, heating of a reaction mixture of **2.3** at 280 $^{\circ}$C for less than 1 hr resulted in bright green-yellow fluorescent vapors which readily deposited as a green fluorescent solid film over the entire glass tube (Figure 2.3). Similarly, heating reaction mixtures of **2.10** and **2.12** at 310 $^{\circ}$C and 360 $^{\circ}$C respectively also resulted in the deposition of green fluorescent films. The products were subsequently isolated by washing away the mineral oil with hexanes. To monitor the thermal reaction, we also performed the same experiments using J-Young NMR tubes. After each heating period, the J-Young NMR tube was transferred inside a glove box and C_6D_6 was added to the reaction mixture to record the NMR spectrum. If the reaction was incomplete according to NMR data, the C_6D_6 solvent could be removed under reduced pressure and the heating process could be resumed. To our delight, NMR data for the isolated products of the bulk reactions and the NMR tube reactions showed that the BN-phenanthrenes **2.11** and **2.13** were obtained in good yields along with mesitylene and methane from the reactions of **2.10** and **2.12** respectively, which confirms that the BN-phenanthrenes are accessible thermally under our convenient reaction protocol. The relatively low yield of **2.13** is due to the low conversion of **2.12**,

58

since about 50-60% of **2.12** remained unchanged at the end of the reaction. Conversely, the green fluorescent product obtained from the thermal reaction of **2.3** was found to be an entirely new species, **2.4**, which was obtained in near quantitative yield (Figure 2.3).

Compound **2.4** was identified as pyrido[1,2-α]isoindole (or isocarbazole) and has been fully characterized by NMR, MS, and X-ray diffraction analysis (Figure 2.10). It is a brightly green fluorescent molecule with nearly 100% emission quantum efficiency (Figure 2.11) and can be prepared readily on a gram scale by independent procedures reported previously.[13] In addition to **2.4**, the borane molecule HBMes$_2$ was also found to form quantitatively in the thermal reaction of **2.3**. The transformation of **2.3** to **2.4** could therefore be described as a deborylation (retro-1,1-hydroboration) reaction. The BN-phenanthrene **2.14** is not an intermediate in the conversion of **2.3** to **2.4** as it remains unchanged when heated to 280°C in the presence of mesitylene under the same conditions used for the thermal reaction of **2.3**. Based on these observations it is evident that there are two competing thermal elimination pathways, namely, R-H elimination (path I) and retro-1,1-hydroboration (path II) for the BN-heterocyclic compounds **2.3, 2.10** and **2.12**.
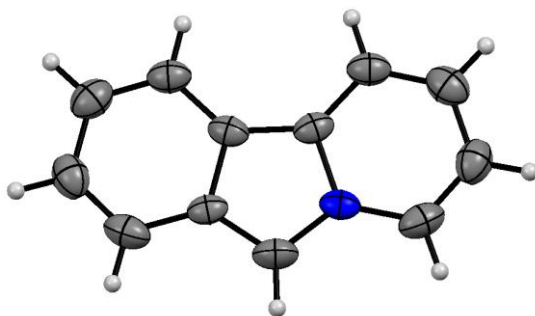
Figure 2.10 The crystal structure of **2.4**
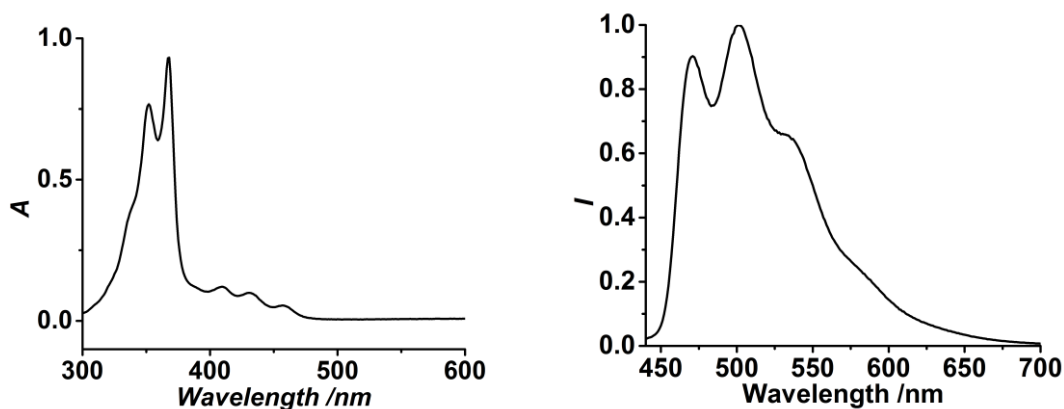
Figure 2.11 The UV-vis (left) and fluorescence (right) spectra of **2.4** in THF (1×10^{-5} M). The fluorescence spectrum was recorded at the excitation maximum.

2.3.2 1,1-Hydroboration of 2.4

To obtain mechanistic insights into the highly unusual retro-1,1-hydroboration reaction of **2.3**, we examined its reverse reaction, namely, the 1,1-hydroboration reaction of pyrido[1,2-*a*]isoindole (**2.4**). Surprisingly, **2.4** readily reacts with HBMes$_2$ in THF at 80°C, generating **2.3** in ~95% yield after 3 days (Figure 2.3 and Figure 2.12). No intermediate was observed in the ^{1}H NMR spectra of this reaction. The fact that the 1,1-hydroboration reaction of **2.4** occurs at a much lower temperature than the retro-1,1-hydroboration of **2.3** indicates that the activation barrier from **2.4** + HBMes$_2$ to **2.3** must be much lower than the retro-1,1-hydroboration of **2.3**. The apparent paradox that **2.4** and HBMes$_2$ can be obtained quantitatively from **2.3** at a temperature much higher than the temperature required to form **2.3** from **2.4** + HBMes$_2$ can be explained by the fact that in the retro-1,1-hydroboration reaction of **2.3**, the product **2.4** is continuously removed from the reaction medium due to its high volatility and deposited on the upper surface of the glass tube where the temperature is not high enough for the reverse 1,1-hydroboration reaction to occur. Recently, we have established that the 1,1-hydroboration of HBMes$_2$ is a general reactivity with other isoindole

derivatives (**2.4-1** – **2.4-3**) and can be used as a simple and effective method of preparing BN-heterocycles, as shown in Figure 2.12.
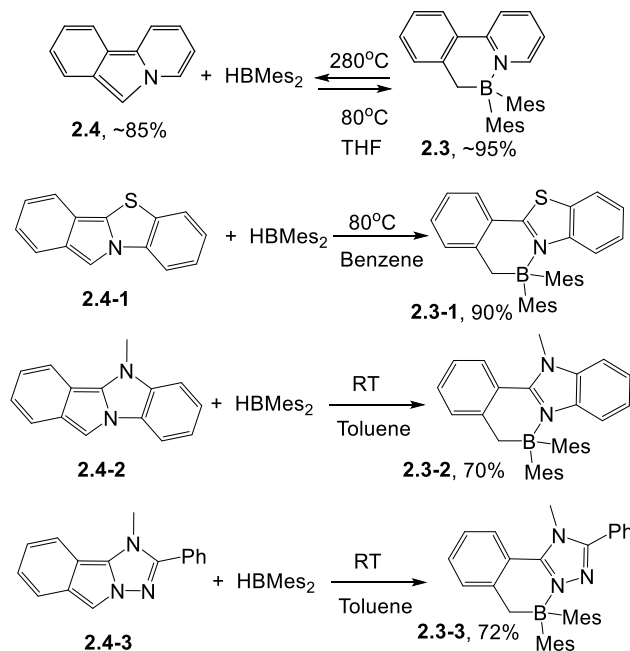
Figure 2.12. 1,1-Hydroboration of **2.4** and analogues with HBMes$_2$.

The molecule **2.4** was also found to react readily with 9-BBN in toluene at 110 °C, as shown in Figure 2.13, generating compound **2.5** in 90% yield which was confirmed by X-ray diffraction analysis (Figure 2.13). Again, no intermediate was observed in the NMR spectra (Figure 2.4 and Section 2.5). These 1,1-hydroboration reactions are highly unusual and unprecedented because hydrogen atom transfer, C-N bond cleavage, B-N and B-C bond formation are all involved in the process. Furthermore, these 1,1-hydroboration reactions provide a new and convenient method to synthesize the BN-heterocyclic compounds **2.3** and **2.5**, which is much simpler and cleaner than the previously reported procedure,[5] namely the selective lithiation of the tolyl-pyridine molecule, which is difficult to control and always produces mixed products.

61
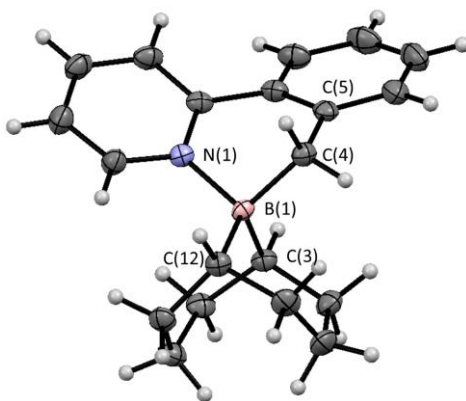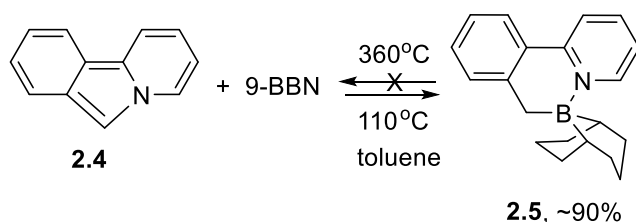
Figure 2.13 The crystal structure of **2.5**. Key bond lengths (Å) and angles (°): B(1) – C(4) 1.635(2), B(1) – N(1) 1.651(1), B(1) – C(3) 1.637(2), B(1) – C(12) 1.632(2); C(4) – B(1) – N(1) 100.33(8), C(3) – B(1) – C(12) 104.94(9).

To further understand this unusual 1,1-hydroboration reaction and establish its generality, the reaction of **2.4** with $HB(C_6F_5)_2$ was examined. As shown by the ^{1}H NMR spectra in Figure 2.14, the reaction of **2.4** with $HB(C_6F_5)_2$ occurred instantaneously at ambient temperature. Significantly, instead of forming the BN-heterocycle **2.7**, a new species **2.6** was obtained quantitatively. The ^{11}B NMR spectrum of **2.6** in toluene-d_8 shows a doublet at -16.0 ppm with a coupling constant of 90 Hz, which becomes a singlet in the [11]B{[1]H} spectrum (See Section 2.5). This is consistent with a tetrahedral boron center that has a B-H bond.[4b] Based on the ^{11}B and 2D NMR spectral data, the structure of **2.6** was determined to be an adduct of **2.4** and $HB(C_6F_5)_2$, as shown in Figure 2.4. Most significant is the observation that upon heating (80°C in benzene or 110°C in toluene), **2.6** converted quantitatively to compound **2.7**, a new member of the BN-heterocyclic compounds,

which was isolated in 98% and fully characterized by NMR, MS, elemental analysis, and X-ray diffraction analysis (Figure 2.15). This establishes that the adduct **2.6** is a key intermediate involved in the conversion of **2.4** + HB(C$_6$F$_5$)$_2$ to **2.7**. From this result, we expect that the analogous adducts of **2.4** + HBMes$_2$ or 9-BBN are likely involved in the conversion to **2.3** and **2.5**, respectively.
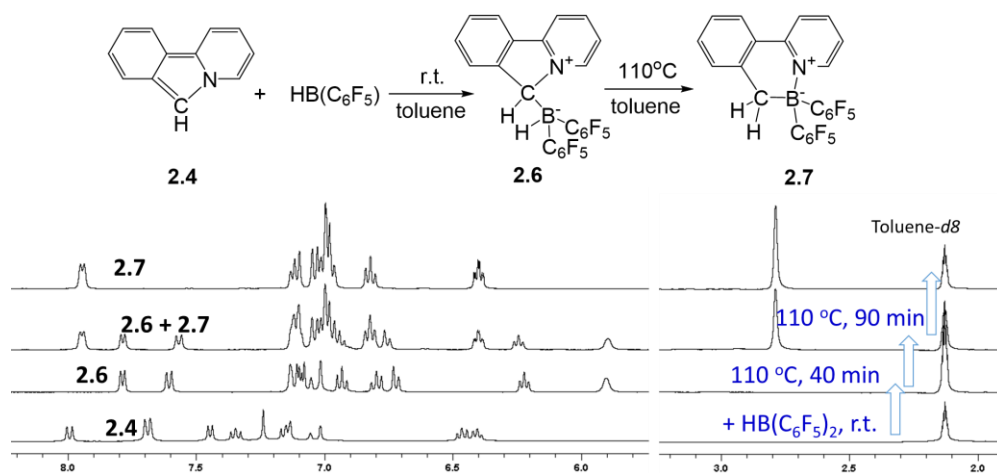
Figure 2.14 Bottom: The ^{1}H NMR spectra (the aliphatic region was omitted for clarity) showing the clean formation of **2.6** upon the mixing of **2.4** and HB(C$_6$F$_5$)$_2$ in toluene-d_8 at ambient temperature, and the subsequent clean transformation of **2.6** to **2.7**, upon heating at 110°C for 1.5 hrs. Top: A scheme showing the structure of the 1,1-hydroboration intermediate **2.6** and its conversion to the final product **2.7**.
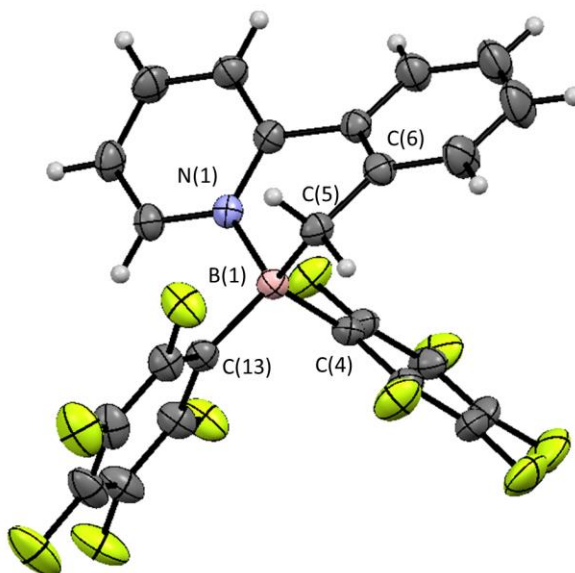
Figure 2.15 The crystal structure of **2.7**. Key bond lengths (Å) and angles (°): B(1)-N(1) 1.624(1), B(1)-C(5) 1.622(3), C(5)-C(6) 1.503(5), B(1)-C(13) 1.643(0), B(1)-C(4) 1.652(4); N(1)-B(1)-C(5) 103.1(2), C(13)-B(1)-C(4) 109.0(0).

2.3.3 Reaction of 2.4 with $B(C_6F_5)_3$ and Isolation of 2.8

To examine if isocarbazole **2.4** is capable of undergoing 1,1-carboboration with $B(C_6F_5)_3$, the reaction of **2.4** with $B(C_6F_5)_3$ was performed. Not surprisingly, the reaction of **2.4** with $B(C_6F_5)_3$ proceeded in the same manner as that of $HB(C_6F_5)_2$ at ambient temperature, forming an air-sensitive adduct **2.8** quantitatively. However, compound **2.8** displays a complex structural change upon heating rather than 1,1-carboboration, which is being investigated and will be reported in due course. The molecule **2.8** has a similar ^{11}B NMR signal to that of **2.6** (-13.0 ppm in THF-d_8). The crystal structure of **2.8** was determined by single-crystal X-ray diffraction analysis and is shown in Figure 2.16. The structure of **2.8** possesses a crystallographically imposed mirror plane that contains B(1), C(1) and C(8) atoms. As a consequence, the C(2) and N(1) atoms are disordered over the two mirror-plane related sites. The boron atom in **2.8** indeed

64

has a tetrahedral geometry, and the B(1)-C(1) bond between the **2.4** unit and the boron atom is 1.718(3) Å, considerably longer than the previously reported $(C_6F_5)_3$B-alkenyl bond lengths (~1.64 Å),[17,18a] but similar to that calculated for the related compound $\{B(C_6F_5)_3(Cp)\}^-$ by Erker and coworkers.[18b] The phenyl-pyridyl unit in **2.8** has π-stacking interactions with one of the perfluorophenyl rings as indicated by some of the short separation distances between the two units (2.92 Å - 3.21 Å).
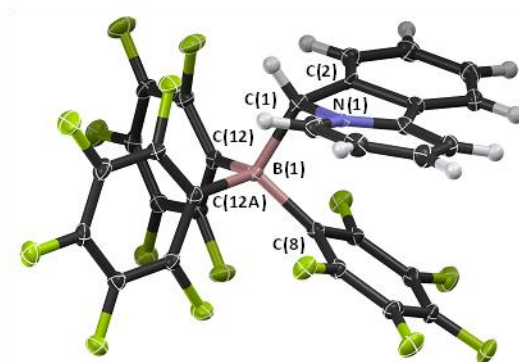
Figure 2.16 The crystal structure of **2.8**. Key bond lengths (Å) and angles (°): B(1) – C(1) 1.718(3), B(1) – C(8) 1.662(3), B(1) – C(12) 1.653(2), C(1)-C(2) 1.506(9), C(1) – N(1) 1.504(7); C(1) – B(1) – C(8) 102.8(2), C(1) – B(1) – C(12) 112.9(1), C(12) – B(1) – C(12A) 102.0(2), C(8) – B(1) – C(12) 113.4(1).

The structures of **2.6** and **2.8** establish that the pyrido[1,2-α]isoindole molecule **2.4** is a good nucleophile, capable of binding to a trivalent boron center via a carbon atom. This is in agreement with the previous work[19] and our computational studies, which have demonstrated that pyrido[1,2-α]isoindole is 1,3-dipolar with an overall negative charge on the C(1) atom. For less Lewis acidic and sterically encumbered boranes such as BPh$_3$, no reaction was observed with **2.4**.

2.3.4 Photo- and Thermal Reactivity of 2.5 and 2.7

Surprisingly, compound **2.5** was found to be thermally stable up to 280°C and no elimination product **2.4** or **2.9** was observed. At temperatures above 360°C, **2.5** decomposes producing unidentifiable species (Figure 2.17, top). To determine if the chelating cyclooctyl group prohibits the R-H elimination, the photoreactivity of **2.5** was examined (Figure 2.17). Interestingly, upon irradiation by UV light (300 nm) in C_6D_6, **2.5** was found to convert to the BN-phenanthrene **2.9** quantitatively *via* an intramolecular R-H elimination process (Figure 2.6 and Section 2.5 for the NMR data showing this clean photoelimination reaction). Compound **2.9** was fully characterized by MS and NMR spectroscopic analyses. It has a low energy absorption band with well resolved vibrational features at 400-500 nm and a fluorescent peak at $\lambda_{max} = 520$ nm, as shown in Figure 2.17, both of which are similar to those reported previously for **2.13**.[5a] This observation indicates that the activation barriers for both thermal elimination pathways of **2.5** are likely very high, thus not accessible via the thermal pathway. It further establishes the generality of the photoelimination reaction of the BN-heterocyclic compounds.

Heating up to 310°C or 300 nm UV irradiation of the new BN-heterocycle **2.7** did not produce **2.4** or corresponding BN-phenanthrene (Figure 2.17, top). Thus, the photoreactivity of this fluorinated BN-heterocycle does not appear to follow the pattern of generating the related BN-phenanthrene compounds. The photoreaction of **2.7** and impact of the C_6F_5 substituents on the photoreaction will be presented in Chapter 5.
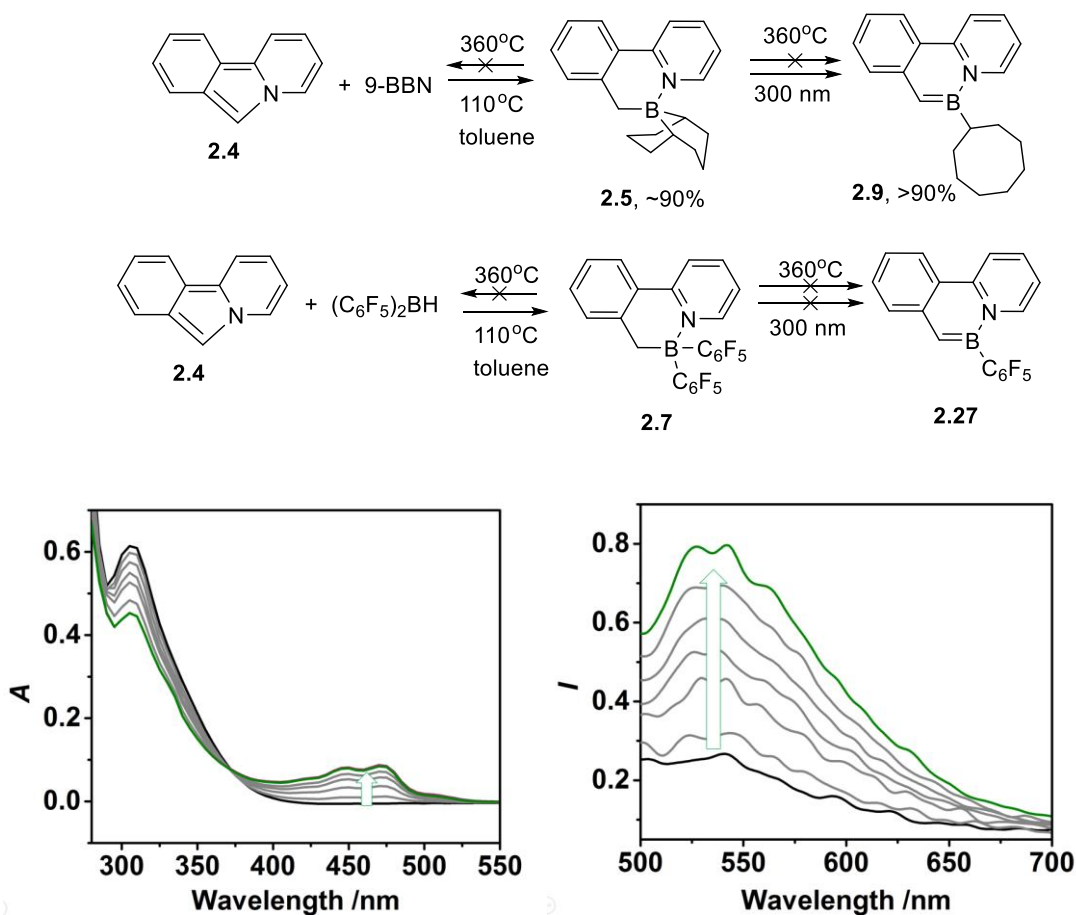
Figure 2.17 Top: Photo- and Thermal Reactivity of **2.5** and **2.7**. Bottom: The UV-vis (left) and fluorescence (right) spectral change of **2.5** in THF (1×10^{-4} M) with irradiation (300 nm) showing its conversion to **2.9**. The fluorescence spectra are recorded at the excitation maximum.

2.3.5 The Mechanism of the Reversible 1,1-Hydroboration

Boranes such as $HBMes_2$ and 9-BBN are well known for 1,2-hydroboration of alkenes and alkynes.[20] To the best of our knowledge, the hydrogen atom transfer from boron to α-carbon and concomitant insertion of BR_2 into a C-N bond as illustrated herein are quite remarkable and a previously unknown reactivity of boranes. The only relevant examples were reported by Erker and coworkers[18] as illustrated in Figure 2.18, in which the borane $B(C_6F_5)_2R$ reacts with an aminohydropentalene derivative **2.15** to give adduct **2.16**, which undergoes a 1,5-boron shift

ultimately producing **2.17**. Depending on the nature of the R group, molecule **2.17** either undergoes 1,1-carboboration[17b, 21] and insertion into a C-C bond (R = alkyl) forming **2.18**, or an H_2 elimination (R = H) forming **2.19**. There is a distinct difference between the reactivity of boranes in our system and that of Erker's system. First of all, there is no H_2 elimination in any of the 1,1-hydroboration reactions of HBR_2 with pyrido[1,2-α]isoindole **2.4** we examined, which supports that the 1,1-hydroboration and borane insertion into a C-N bond by the borane adduct are highly favoured in our system. Secondly, the 1,1-hydroboration in our system is not limited to the strongly Lewis acidic $HB(C_6F_5)_2$, an indication that the pyrido[1,2-α]isoindole molecule is much more reactive than the aminohydropentalene derivative **2.15**. Thirdly, the insertion reaction involves a C-N bond in our system, instead of a C-C bond as observed in Erker's system. Most significant is that the ,1-hydroboration and the C-N bond insertion reaction are reversible for $HBMes_2$ in our system, but are not known in Erker's system.
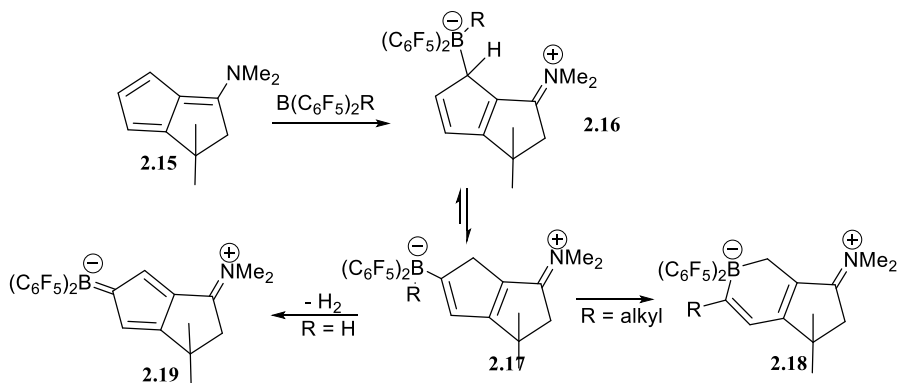
Figure 2.18 The reactivity of $B(C_6F_5)_2R$ with an aminodihydropentalene derivative reported by Erker and coworkers.

Having established that the species **2.20** is a key intermediate, the transformation of **2.4** + HBR_2 to **2.22** is proposed to involve the following sequence (Figure 2.19): (1) formation of the four-coordinated borane adduct **2.20**, (2) a hydride transfer from the boron atom to the carbon atom and

cleavage of the C-N bond in **2.20** resulting in the formation of intermediate **2.21**, which can be described as an olefin 1,1-hydroboration and is likely facilitated by the negatively charged borane and the positively charged nitrogen in **2.20**, (3) coordination of the nitrogen atom to the electron-deficient boron atom in **2.21**, forming the chelate product **2.22**. The fact that the borane adduct of **2.4** with $HBMes_2$ or 9-BBN was not observed at ambient temperature could be explained by the low Lewis acidity of $HBMes_2$ and 9-BBN that prevents adduct formation at ambient temperature. At elevated temperatures, the corresponding adduct intermediates could form, but they would be short-lived and undergo a rapid hydride transfer because of the low Lewis acidity of the boron center, leading to the formation of the BN-heterocycles **2.3** and **2.5** respectively. The retro-1,1-hydroboration reaction is proposed to follow the same mechanism but in the reverse direction.
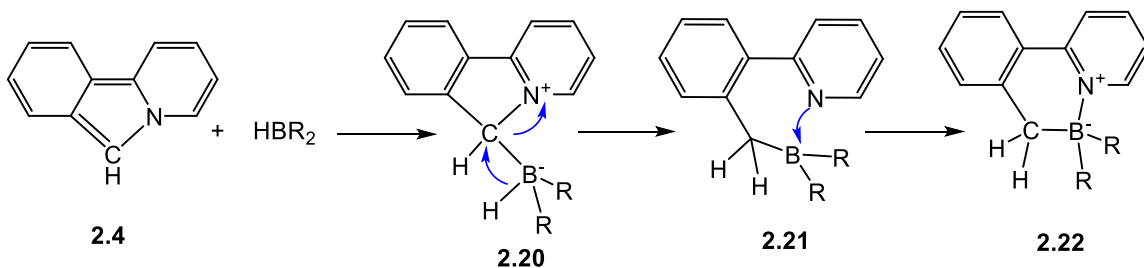
Figure 2.19 The proposed mechanism of the 1,1-hydroboration reaction.

2.3.6 Computational Studies

To further validate the proposed 1,1-hydroboration mechanism and to understand the distinct impact of the substituent groups on the boron atom and benzyl-pyridyl unit, the competing thermal reaction pathways of compounds **2.3**, **2.5**, **2.7**, **2.10** and **2.12** were modeled computationally using DFT methods.

Prior to modeling the reaction pathways, the nucleophilic nature of the C^1 atom in **2.4** was confirmed by Mulliken population analysis where it was found to be negatively charged (Figure 2.20) and contributing significantly to the HOMO level (Figure 2.21). The thermal reaction

69

pathways and energy profile for **2.3** are depicted in Figure 2.22, while those for the BN-heterocycles can be found in the Figures 2.23-2.26. The calculated mechanistic pathway is consistent with our proposed mechanism shown in Figure 2.19, where the calculated activation energy for the retro-hydroboration reaction (E_{a1}) is ~100 kJ/mol less than the corresponding mesitylene elimination activation energy (E_{a2}), which is in agreement with the fact that the HBMes$_2$ elimination is the preferred pathway for **2.3** (Figure 2.22). Furthermore, these modeling results support the observation that 1,1-hydroboration of **2.4** with HBMes$_2$ requires less energy to proceed than the retro-hydroboration due to the intermediate **2.23**, which resides much closer in energy and geometry to the transition state structure **2.28**[*]. The fact that this intermediate is not observed experimentally for this particular reaction is not surprising given the proximity of the intermediate and transition state energy levels. It is interesting to note that there is a large difference between the two product energies of each thermal elimination pathway for **2.3**, where the R-H elimination pathway produces the thermodynamically favored products. As argued before, we suspect that sublimation of **2.4** away from the reaction mixture as it forms allows for isolation of this kinetic product. Although we attempted to locate the transition states between **2.4** + HBMes$_2$ → **2.23** and **2.3** → **2.28**, they could not be found most likely because they reside very close in energy to the product of each transformation.
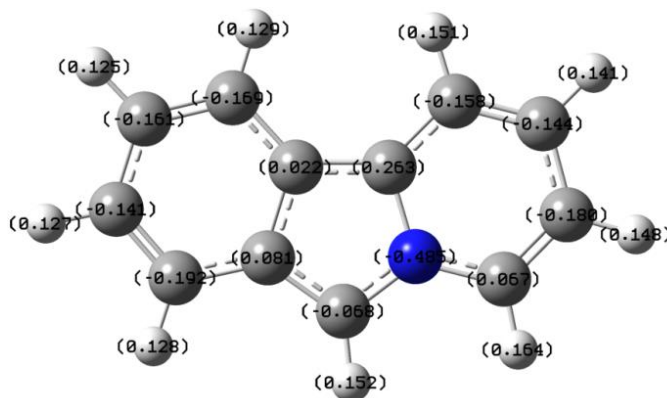
Figure 2.20 The calculated Mulliken charge population of pyrido[1,2-α]isoindole (**2.4**; B3LYP/6-311+g(d,p)).
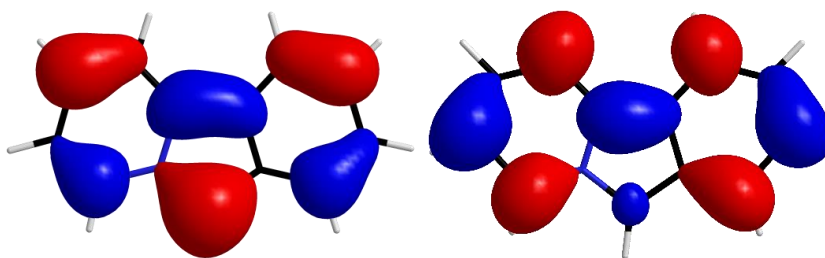
Figure 2.21 The calculated HOMO (left) and LUMO (right) of **2.4** (B3LYP/6-311+g(d,p); iso = 0.03).
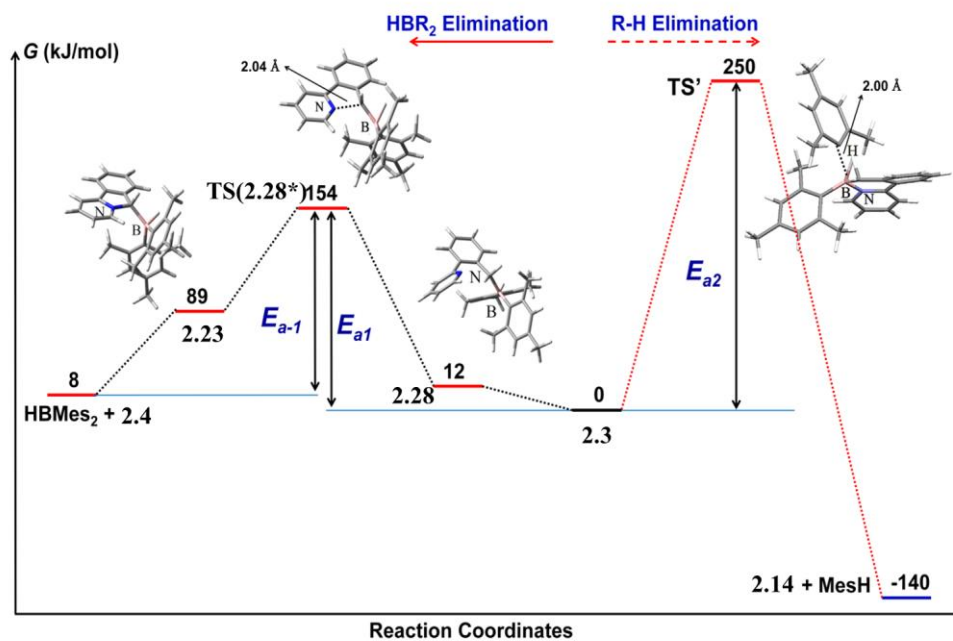
Figure 2.22 Relative ground state energies and structures calculated for the reactant, intermediates, transition states, and products involved in the two competing thermal pathways of **2.3**.

Table 2.1 Summary of activation barriers and pertinent ground state energies (kJ/mol) relative to the calculated energies of **2.3**, **2.5**, **2.7**, **2.10**, **2.12**.

Cmpd	2.4 (2.4') + HBR$_2$	E$_{a1}$	E$_{a-1}$	E$_{a2}$	2.20	2.21
2.3	8	154	146	250	89	-140
2.5	95	205	110	287	137	1
2.7	139	206	107	277	99	7
2.10	54	154	100	256	92	-142
2.12	118	227	109	288	145	-29

As is evident from the comparative data listed in Table 2.2 for the calculated pathways of the various **2.22**'s, the R group at the boron center and on the benzyl-pyridine backbone should lead to changes in the reactivity of the various compounds. In each other system, the calculated relative energies of the HBR$_2$ + **2.4** (or **2.4'**, 2,9-dimethylpyrido-[1,2-*a*]isoindole) molecules were found to be significantly higher in comparison to that of HBMes$_2$ + **2.4**. In the case of **2.10** and **2.12**, this is most likely the reason that the retro-hydroboration of **2.10** and **2.12** is not observed as the products are thermodynamically unstable. It is important to note that **2.4'** has not been synthesized to date, which further supports this claim. Given that these reactions were carried out at elevated temperatures, the excess kinetic energy of the system allows the E$_{a2}$ barrier to be crossed for **2.10** and **2.12**, leading the reaction to the "thermodynamic minimum" that is the R-H elimination products (Figure 2.25 and Figure 2.26). With respect to **2.5** and **2.7**, the predicted E$_{a-1}$ barrier is 36 and 39 kJ/mol less than that for **2.3**, respectively, which correlates nicely with the varying reaction times/temperatures of these three hydroboration reactions. In both cases, neither competing elimination pathway results in the formation of a thermodynamically stable product, which is most likely why heating of **2.5** and **2.7** does not induce either of these reactivities (Figure 2.23 and Figure 2.24). Lastly, it is interesting to note that the NMR spectroscopic observation of **2.6** is also in agreement with the calculation results, as the adduct **2.6** was found to be more thermodynamically stable than the mixture of **2.4** and HB(C$_6$F$_5$)$_2$. Subsequent heating of **2.6** gives the reaction mixture enough energy to traverse the activation barrier E$_{a-1}$, ultimately yielding **2.7**.
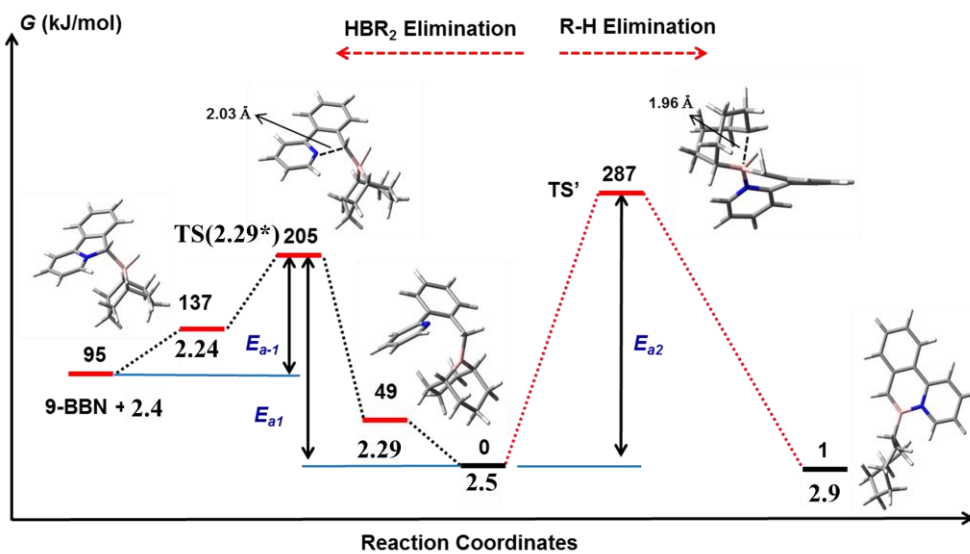
Figure 2.23 Relative ground state energies and structures calculated for the reactant, intermediates, transition states, and products involved in the two competing thermal pathways of **2.5**.
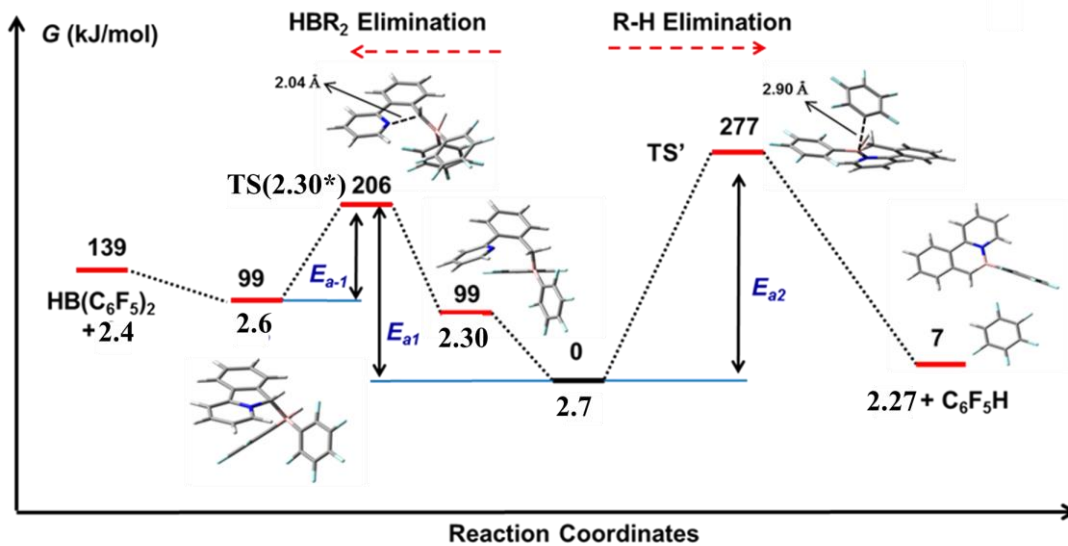
Figure 2.24 Relative ground state energies and structures calculated for the reactant, intermediates, transition states, and products involved in the two competing thermal pathways of **2.7**.
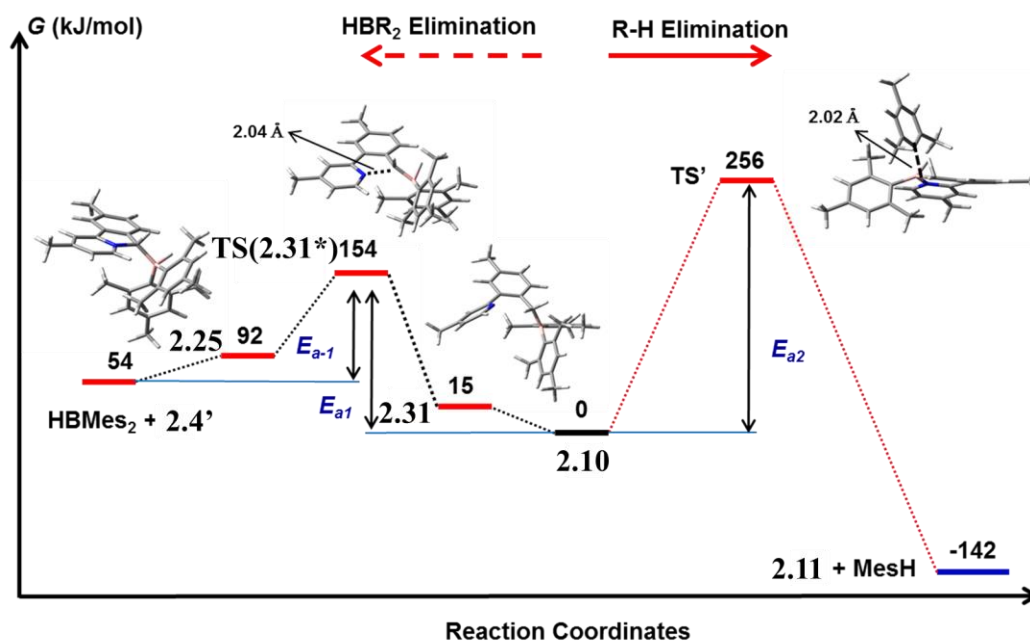
Figure 2.25 Relative ground state energies and structures calculated for the reactant, intermediates, transition states, and products involved in the two competing thermal pathways of **2.10**.
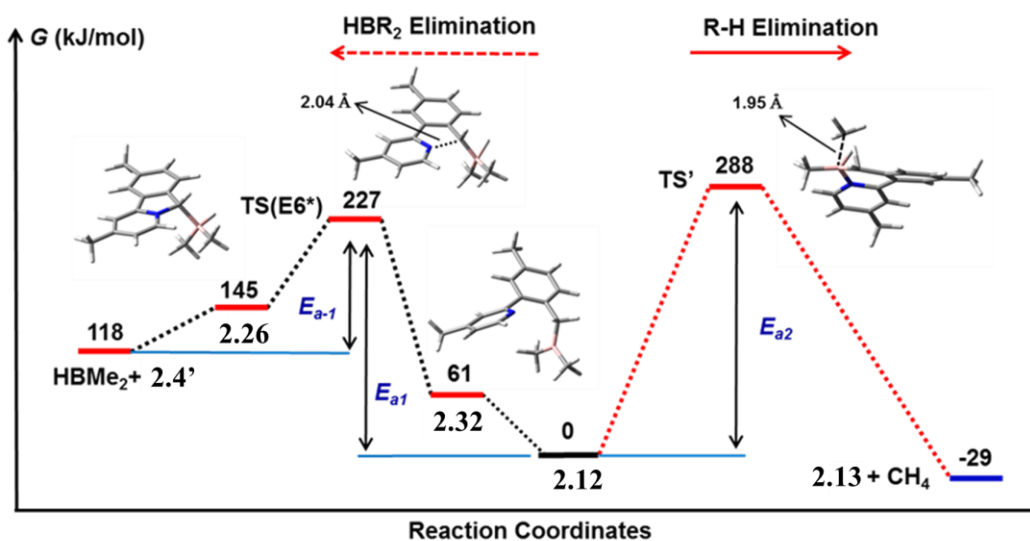
Figure 2.26 Relative ground state energies and structures calculated for the reactant, intermediates, transition states, and products involved in the two competing thermal pathways of **2.12**.

2.4 Conclusions

In summary, the thermal reactivity of N,C-chelated organoboron compounds with a benzyl-pyridyl backbone has been evaluated. Depending on the substitution pattern at boron and the benzyl-py ligand, different competing pathways are observed; *i.e.* retro-1,1-hydroboration to give HBR_2 and pyrido-[1,2-*a*]isoindole or R-H elimination to give mesitylene or methane and a BN-phenanthrene, which could also be obtained *via* photoelimination. Furthermore, the retro-1,1-hydroboration was found to be reversible *via* the insertion of an HBR_2 unit into pyrido-[1,2-*a*]isoindole. The 1,1-hydroboration reaction has been found to be a simple and convenient method for the synthesis of the N,C-chelate boron compounds, which led to the isolation of two new (benzyl-pyridyl)BR_2 compounds (R = C_6F_5, **2.7**; R_2 = 1,5-cyclooctyl, **2.5**). Compound **2.7** has been found to undergo an intramolecular R-H photoelimination, converting the 1,5-cyclooctyl to a 1-cyclooctyl ligand and generating a new BN-phenanthrene **2.9**. Mechanistic insight was obtained from the 1,1-hydroboration involving $HB(C_6F_5)_2$, as its adduct with pyrido-[1,2-*a*]isoindole, **2.6** was observed spectroscopically and its structure is supported by a closely related adduct **2.8** of $B(C_6F_5)_3$ with pyrido-[1,2-*a*]isoindole. Computational modeling of the competing reaction pathways in all five chelate systems described was found to be in agreement with experimental observations, further supporting our proposed mechanism of the reversible 1,1-hydroboration reactions.

2.5 Selected NMR Data
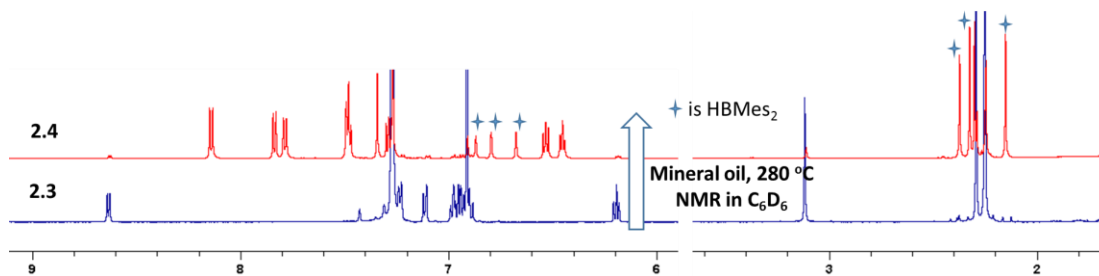
Figure 2.27 ^{1}H NMR spectra showing the clean conversion of **2.3** (bottom spectrum) to **2.4** (top spectrum) and the formation of HBMes$_2$ (monomer and dimer exist at the same time) in mineral oil at 280 °C.
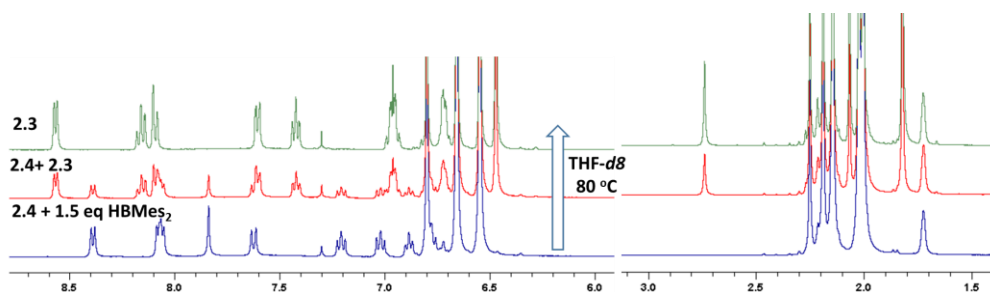
Figure 2.28 ^{1}H NMR spectra showing the clean conversion of **2.4** (bottom spectrum) to **2.3** (top spectrum) in THF-d_8 at 80 °C.
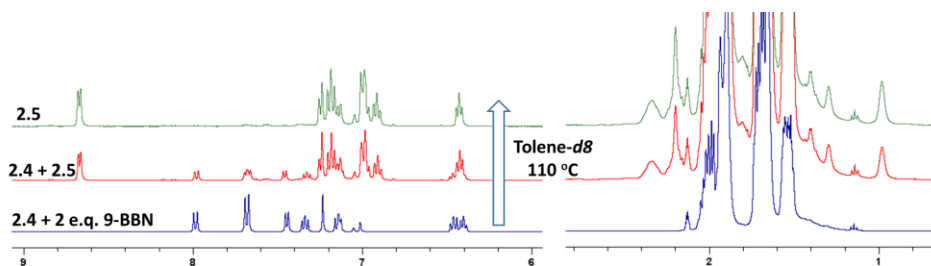
Figure 2.29 ^{1}H NMR spectra showing the clean conversion of **2.4** (bottom spectrum) to **2.5** (top spectrum) in toluene-d_8 at 110 °C.
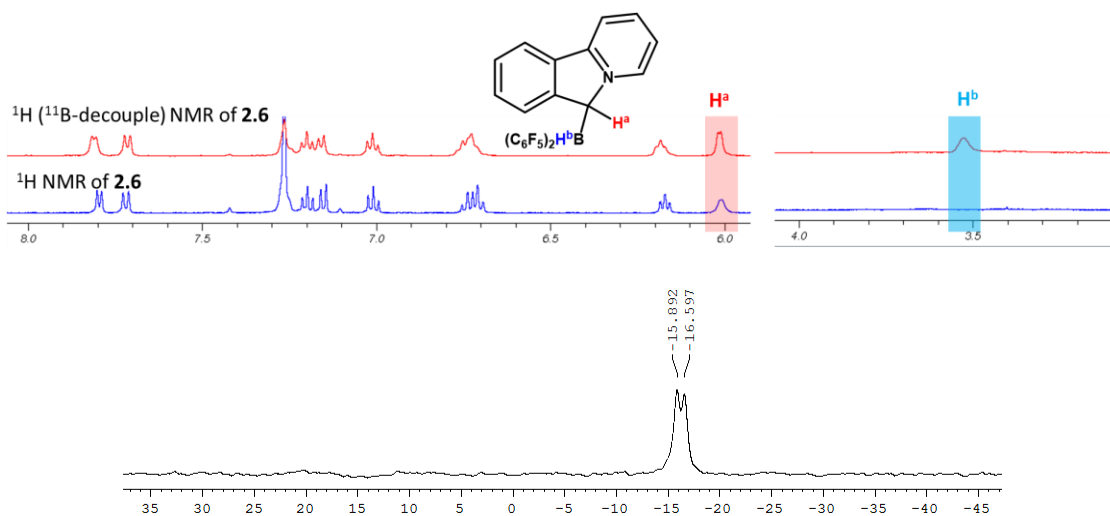
Figure 2.30 ^1H NMR spectra of **2.6** in C_6D_6 (top: ^1H (^{11}B-decouple) NMR spectrum), and ^{11}B NMR (bottom) of **2.6** in C_6D_6.
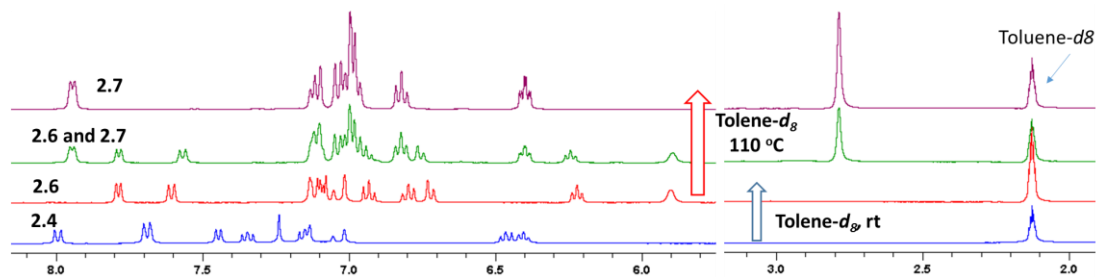
Figure 2.31 ^1H NMR spectra showing the clean conversion of **2.4** (bottom spectrum) to **2.7** (top spectrum) via **2.6** (middle) in toluene-d_8 from room temperature to 110 °C.
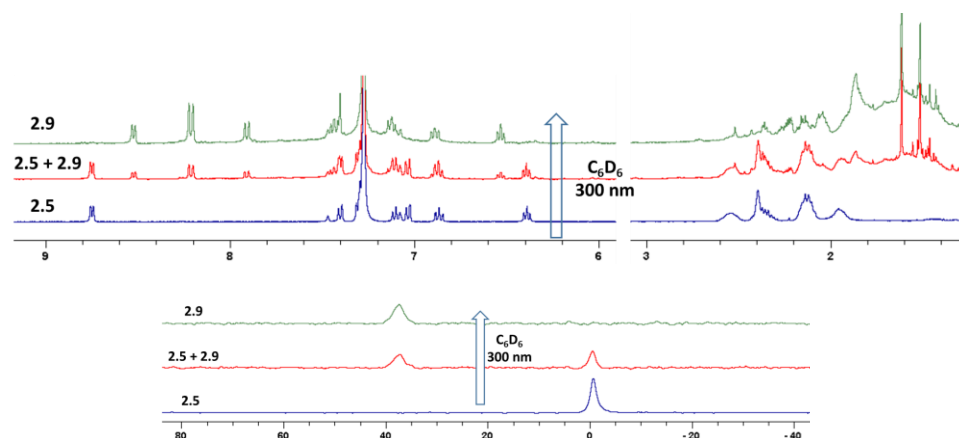
Figure 2.32 ^{1}H and ^{11}B NMR spectra showing the clean conversion of **2.5** (bottom spectrum) to **2.9** (top spectrum) in C_6D_6 at room temperature and 300 nm irradiation.
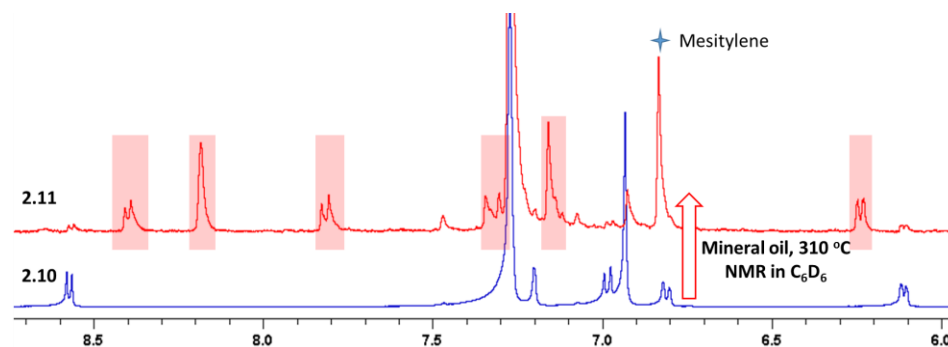
Figure 2.33 ^{1}H NMR spectra of the aromatic region showing the clean conversion of **2.10** (bottom spectrum) to **2.11** (top spectrum, red highlight) and the formation of mesitylene in mineral oil at 310 ^{o}C.
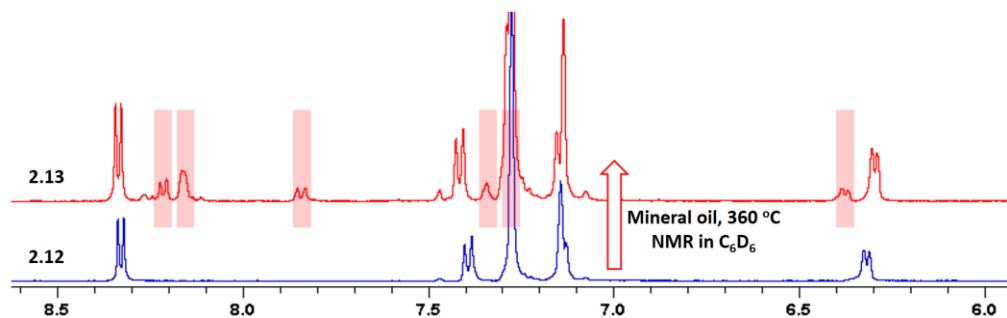
Figure 2.34 ^{1}H NMR spectra of the aromatic region showing the clean conversion of **2.12** (bottom spectrum) to **2.13** (top spectrum, red highlight) at 360 ^{o}C.

2.6 Notes and References

The work described in this chapter includes contributions from the following publications:

- Yang, D.-T.; Mellerup, S. K.; Wang, X.; Lu, J.-S.; Wang, S. * *Angew. Chem., Int. Ed.* **2015**, 54, 5498. (Selected as inside cover)

- Shi, Y-G[+]; Yang, D.-T.[+]; Mellerup, S. K.; Wang, N.; Peng, T.; Wang. S. * *Org. Lett.* **2016**, 18, 1626. ([+]Equal contribution, and this work was highlighted by *Synfacts*)

References:

(1) (a) Abbey, E. R.; Zakharov, L. N.; Liu, S.-Y. *J. Am. Chem. S*oc. **2008**, *130*, 7250. (b) Campbell, P. G.; Abbey, E. R.; Neiner, D.; Grant, D. J.; Dixon, D. A.; Liu, S.-Y. *J. Am. Chem. Soc.* **2010**, *132*, 18048. (c) Luo, W.; Campbell, P. G.; Zakharov, L. N.; Liu, S.-Y. *J. Am. Chem. Soc.* **2011**, *133*, 19326. (e) Hamilton, C.W.; Baker, R. T.; Staubitz, A.; Manners, I. *Chem. Soc. Rev.* **2009**, *38*, 279.

(2) (a) Staubitz, A.; Robertson, A. P. M.; Sloan, M. E.; Manners, I. *Chem. Rev.* **2010,** *110*, 4023. (b) Müller, Dipl.-Chem. M.; Maichle-Mössmer, C.; Bettinger, H. F. *Angew. Chem. Int. Ed*. **2014**, *53*, 9380.

(3) (a) Scheideman, M.; Wang, G.; Vedejs, E. *J. Am. Chem. Soc*. **2008**, 130, 8669. (b) Braunschweig, H.; Dewhurst, R. D.; Hörl, Dipl.-Chem. C.; Phukan, A. K.; Pinzner, F.; Ullrich, S. *Angew. Chem. Int. Ed.* **2014**, *53*, 324. (c) Braunschweig, H.; Hörl, C. *Chem. Commun.* **2014**, *50*, 10983. (d) Braunschweig, H.; Herbst, T.; Radacki, K.; Frenking, G.; Celik, M. A. *Chem. Eur. J.* **2009**, *15*, 12099.

(4) (a) Rao, Y.-L.; Amarne, H.; Zhao, S.-B.; McCormick, T. M.; Martić, S.; Sun, Y.; Wang, R.-Y.; Wang, S. *J. Am. Chem. Soc*. **2008**, *130*, 12898. (b) Rao, Y.-L.; Chen, L. D.; Mosey, N. J.; Wang, S. *J. Am. Chem. Soc.* **2012**, *134*, 11026. (c) Nagura, K.; Saito, S.; Fröhlich, R.;

Glorius, F.; Yamaguchi, S. *Angew. Chem. Int. Ed*. **2012**, *51*, 7762. (d) Rao, Y.-L.; Amarne, H.; Chen, L. D.; Brown, M. L.; Mosey, N. J.; Wang, S. *J. Am. Chem. Soc.* **2013**, *135*, 3407. (e) Rao, Y.-L.; Amarne, H.; Wang, S.; *Coord. Chem. Rev*. **2012**, *256*, 759.

(5) (a) Lu, J.-S.; Ko, S.-B.; Walters, N. R.; Kang, Y.; Sauriol, F.; Wang, S. *Angew. Chem. Int. Ed.* **2013**, *52*, 4544. (b) Ko, S.-B; Lu, J.-S.; Wang, S. *Org. Lett.* **2014**, *16*, 616.

(6) (a) Loudet, A.; Burgess, K. *Chem. Rev.* **2007**, *107***,** 4891. (b) Ulrich, G.; Ziessel, R.; Harriman, A. *Angew. Chem. Int. Ed.* **2008**, *47*, 1184. (c) Ziessel, R.; Ulrich, G.; Harriman, A. *New J. Chem*. **2007**, *31*, 496.

(7) (a) Entwistle, C. D.; Marder, T. B. *Angew. Chem. Int. Ed*. **2002**, *41*, 2927. (b) Entwistle, C. D.; Marder, T. B. *Chem. Mater*. **2004**, *16*, 4574. (c) Wakamiya, A.; Taniguchi, T.; Yamaguchi, S. *Angew. Chem. Int. Ed*. **2006**, *45*, 3170. (d) Fukazawa, A.; Yamaguchi, S. *Chem.—Asian J*. **2009**, *4*, 1386. (e) Job, A.; Wakamiya, A.; Kehr, G.; Erker, G.; Yamaguchi, S. *Org. Lett*. **2010**, *12*, 5470. (f) Rao, Y.-L.; Wang, S. *Inorg. Chem*., **2011**, *50*, 12263 and references therein. (g) Chen, P.; Lalancette, R. A.; Jäkle, F. *Angew. Chem. Int. Ed*. **2012**, *51*, 7994.

(8) (a) Maitlis, P. M. *Chem. Rev*. **1962**, *62*, 223. (b) Jaska, C. A.; Piers, W. E.; McDonald, R.; Parves, M. *J. Org. Chem.* **2007**, *72*, 5234. (c) Liu, Z.; Marder, T. B. *Angew. Chem. Int. Ed.* **2008**, *47*, 242. (d) Bosdet, M. J. D.; Piers, W. E. *Can. J. Chem.* **2009**, *87*, 8. (e) Campbell, P. G.; Marwitz, A. J. V.; Liu, S.-Y. *Angew. Chem. Int. Ed.* **2012**, *51*, 6074. (f) Braunschweig, H.; Damme, A.; Jimenez-Halla, J. O. C.; Pfaffinger, B.; Radacki, K.; Wolf, J. *Angew. Chem. Int. Ed.* **2012**, *51*, 10034. (g) Neue, B.; Araneda, J. F.; Piers, W. E.; Parvez, M. *Angew. Chem. Int. Ed.* **2013**, *52*, 9966.

(9) (a) Agou, T.; Kobayashi, J.; Kawashima, T. *Org. Lett.* **2006**, *8*, 2241. (b) Agou, T.; Sekine, M.; Kobayashi, J.; Kawashima, T. *Chem. Commun.* **2009**, 1894. (c) Campbell, P. G.; Abbey, E. R.; Neiner, D.; Grant, D. J.; Dixon, D. A.; Liu, S. -Y. *J. Am. Chem. Soc.* **2010**, *132*, 18048. (d) Lepeltier, M.; Lukoyanova, O.; Jacobson, A.; Jeeva, S.; Perepichka, D. F. *Chem. Commum.* **2010**, *46*, 7007. (e) Wang, X.-Y.; Lin, H.-R.; Lei, T.; Yang, D.-C.; Zhuang, F.-D.; Wang, J.-Y.; Yuan, S.-C.; Pei, J. *Angew. Chem. Int. Ed.* **2013**, *52*, 3117.

(10) (a) Dewar, M. J. S.; Kubba, V. P.; Pettit, R. *J. Chem. Soc.* **1958**, 3073. (b) Dewar, M. J. S.; Kaneko, C.; Bhattacharjee, M. K. *J. Am. Chem. Soc.* **1962**, *84*, 4884. (c) Ashe III, A. J.; Yang, H.; Fang, X.; Kampf, J. W. *Organometallics*, **2002**, *21*, 4578. (d) Bosdet, M. J. D.; Jaska, C. A.; Piers, W. E.; Sorensen, T. S.; Parves, M. *Org. Lett.* **2007**, *9*, 1395. (e) Fang, X.; Assoud, J. *Organometallics*, **2008**, *27*, 2408. (f) Rohr, A. D.; Kampf, J. W.; Ashe III, A. J. *Organometallics*, **2014**, *33*, 1318.

(11) Pelter, A.; Singaram, S.; Brown, H. *Tetrahedron. Lett.* **1983**, *24*, 1433.

(12) Parks, D. J.; Piers, W. E.; Yap, G. P. A. *Organometallics*, **1998**, 17, 5492.

(13) Kajigaeshi, S.; Mori, S.; Fujisaki, S.; Kanemasa, S. *Bull. Chem. Soc. Jpn.* **1985**, *58*, 3547.

(14) *SHELXTL Version 6.14*, Bruker AXS, Madison, WI, 2000-2003.

(15) Frisch, M. J.; Trucks, G. W.; Schlegel, H. B.; Scuseria, G. E.; Robb, M. A.; Cheeseman, J. R.; Scalmani, G.; Barone, V.; Mennucci, B.; Petersson, G. A. H.; Nakatsuji, M.; Caricato, X.; Li, H. P. F.; Hratchian, A.; Izmaylov, J.; Bloino, G.; Zheng, J. L.; Sonnenberg, M.; Hada, M.; Ehara, K.; Toyota, R.; Fukuda, J.; Hasegawa, M.; Ishida, T.; Nakajima, Y.; Honda, O.; Kitao, H.; Nakai, T.; Vreven, J. A.; Montgomery Jr., J. E.; Peralta, F.; Ogliaro, M.; Bearpark, J. J.; Heyd, E.; Brothers, K. N.; Kudin, V. N.; Staroverov, T.; Keith, R.; Kobayashi, J.; Normand, K.; Raghavachari, A.; Rendell, J. C.; Burant, S. S.; Iyengar, J.; Tomasi, M.; Cossi,

N.; Rega, J. M.; Millam, M.; Klene, J. E.; Knox, J. B.; Cross, V.; Bakken, C.; Adamo, J.; Jaramillo, R.; Gomperts, R. E.; Stratmann, O.; Yazyev, A. J.; Austin, R.; Cammi, C.; Pomelli, J. W.; Ochterski, R. L.; Martin, K.; Morokuma, V. G.; Zakrzewski, G. A.; Voth, P.; Salvador, J. J.; Dannenberg, S.; Dapprich, A. D.; Daniels, O.; Farkas, J. B.; Foresman, J. V.; Ortiz, J.; Cioslowski, J.; Fox, D. J. Gaussian 09 Revision C.01, 2010.

(16)   (a) Yanai, T.; Tew, D.; Handy, N. *Chem. Phys. Lett.* **2004**, *393*, 51. (b) Ditchfield, R.; Hehre, W.J.; Pople, J. A. *J. Chem. Phys.* **1971**, *54*, 724. (c) McLean, A. D.; Chandler, G. S. *J. Chem. Phys.* **1980**, *72*, 5639.

(17)   For examples, see: a) Dureen, M. A.; Stephan, D. W. *J. Am. Chem. Soc*. **2009**, *131*, 8396. (b) Dureen, M. A.; Brown, C. C.; Stephan, D. W. *Organometallics*, **2010**, *29*, 6594.

(18)   (a) Xu, B.-H.; Kehr, G.; Fröhlich, R.; Erker, G. *Chem. Eur. J*. **2010**, *16*, 12538. (b) Xu, B.-H, Kehr, G.; Fröhlich, R.; Grimme, S.; Erker, G. *J. Am. Chem. Soc*. **2011**, *133*, 3480.

(19)   (a) Fozard, A.; Bradsher, V. K. *J. Org. Chem*. **1967**, *32*, 2966. (b) Kajigaeshi, S.; Mori, S.; Fujisaki, S.; Kanemasa, S. *Bull. Chem. Soc. Jpn.* **1985**, *58*, 3547. (c) T. Mitsumori, M. Bendikov, O. Dautel, F. Wudl, T. Shioya, H. Sayo, Y. Sato. *J. Am. Chem. Soc*. **2004**, *126*, 16793.

(20)   (a) Brown, H. C. *Hydroboration*, W. A. Benjamin: New York, 1962. (b) Brown, H. C. *Boranes in Organic Chemistry*, Cornell University Press: Ithaca, NY, 1972. (c) Brown, C. A.; Coleman, R. A. *J. Org. Chem*., **1979**, *44*, 2328. (d) Pelter, A.; Singaram, S.; Brown, H. *Tetrahedron. Lett.* **1983**, *24*, 1433. (e) Pelter, A.; Smith, K.; Brown, H. C. *Borane Reagents*; Academic Press Ltd.: San Diego, 1988.

(21)   (a) Chen, C.; Kehr, G.; Fröhlich, R.; Erker, G. *J. Am. Chem. Soc*. **2010**, *132*, 13594. (b) Chen, C.; Fröhlich, R.; Kehr, G.; Erker, G. *Chem. Commun*. **2010**, *46*, 3580.

Chapter 3

Dimesitylboron-Functionalized Indolizine Derivatives

3.1 Introduction

Luminescent materials based on π-conjugated aromatic systems have long been studied for many different applications such as organic light emitting diodes (OLEDs),[1] organic field effect transistors (OFETs),[2] and fluorescent probes/sensors[3]. Within this vast family of organic compounds, two N-heterocycles, namely pyrido[2,1-*a*]isoindole and pyrrolo[1,2-*a*]pyridine, have started to attract some attention over the last decade due to their interesting electronic structure which allows them to undergo 1,3-dipolar cycloadditions with alkynes and ultimately expand their π-system through subsequent dehydrogenation yielding indolizino[3,4,5-*ab*]isoindole and pyrrolo[2,1,5-*cd*]indolizine derivatives, respectively.[4] This strategy has been employed to great effect with respect to purely organic fluorophores, where certain cycloaddition products obtained using electron poor alkynyl-dipolarophiles possessed good fluorescent quantum efficiencies and blue light emission.[4a] Aside from extending aromatic π-networks, incorporating three-coordinated organoboron moieties into such molecules can also have a dramatic effect on their electronic structure and photophysical properties[5] due to boron's empty p orbital which becomes part of the π-system. Previously it has been shown that triarylboron containing donor-acceptor systems tend to possess large electronic dipoles, which often results in enhanced donor-acceptor charge transfer (CT) upon photoexcitation and has shown significant promise as selective sensors for anions such as fluoride or cyanide.[6] Our interest in pyrido[2,1-*a*]isoindole arose as part of our recent work with BN-heterocycles in Chapter 2, where pyrido[2,1-*a*]isoindole was found to be a product of their *retro*-1,1-hydroboration.[7] Given the potential of electron rich pyrido[2,1-*a*]isoindole / pyrrolo[1,2-

a]pyridine to act as suitable donors, we set out to create new boron appended fluorophores through the cycloaddition of pyrido[2,1-*a*]isoindole / pyrrolo[1,2-*a*]pyridine with dimesitylboron functionalized alkynes in the hopes of generating new CT fluorescent molecules (**3.1** – **3.4**, Figure 3.1). Much to our surprise, these new species do not exhibit CT emission but rather intense $\pi \rightarrow \pi^*$ transitions which emit either blue or blue-green light as discussed in further detail below.
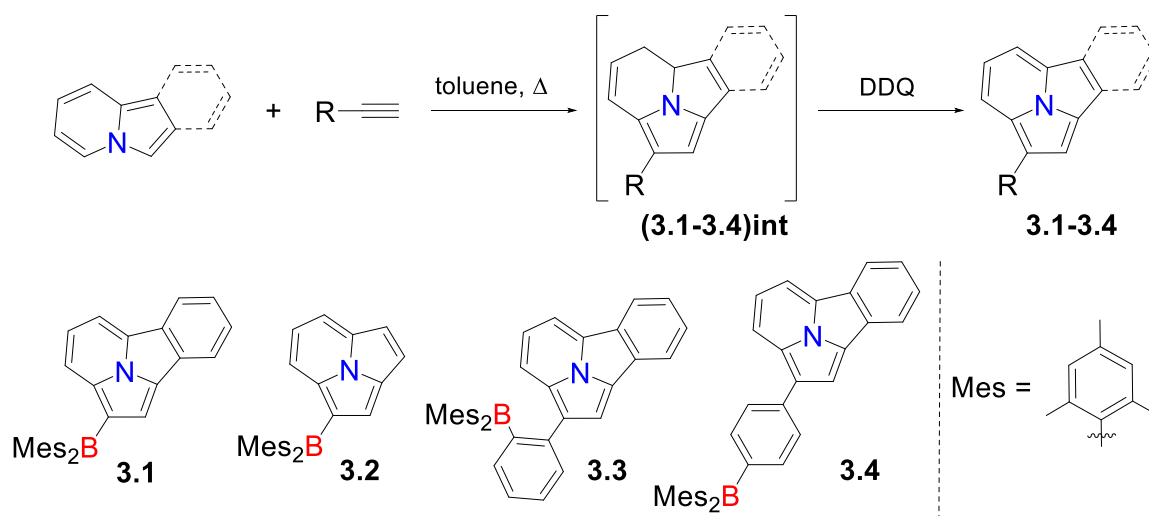
Figure 3.1 Synthetic Procedures of Mes₂B-Functionalized Indolizine Derivatives.

3.2 Experimental Sections

3.2.1 General Procedure

Experimental techniques for synthesis, the uses of instrumentation are as described in Chapter 2.2.1. Solution quantum yields were calculated using optically dilute solutions (A ≈ 0.1) relative to 9,10-diphenylanthracene, and solid-state quantum yields were measured using an integration sphere. Cyclic voltammetry experiments were conducted on a BAS CV-50W analyzer with a scan rate of 100 mVs^{-1}.

3.2.2 Synthetic Procedure

3.2.2.1 Synthesis of **3.1**
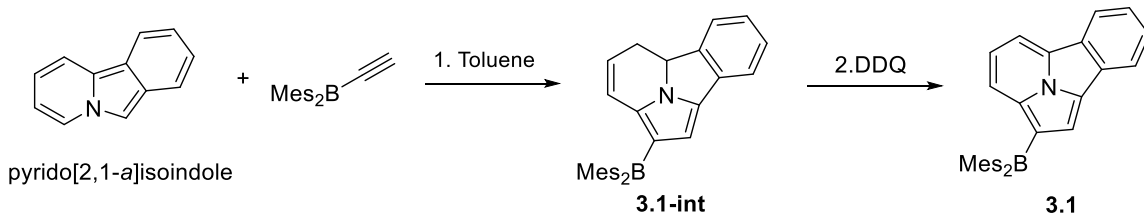
Step by step procedure: Dimesitylboronacetylene (165 mg, 0.6 mmol) and pyrido[2,1-a]isoindole (100 mg, 0.6 mmol) were reacted in toluene (15 mL) at room temperature in a 50 mL flask for 30 min, at which point the volatiles were removed *in vacuo* and the product was isolated by column chromatography on silica gel using a solvent mixture of hexanes and ethyl acetate (10:1) as the eluent. The product **3.1-int** was isolated as a yellow solid (238 mg, 0.54 mmol, 90% yield) and fully characterized by NMR, MS, and X-ray diffraction analysis.

^{1}H NMR (400 MHz, CDCl$_3$) δ 7.37 (d, J = 7.6 Hz, 1H), 7.26 (dd, J = 16.5, 7.9 Hz, 2H), 7.14 – 7.04 (m, 1H), 6.72 (s, 4H), 6.27 (s, 1H), 5.74 (dd, J = 9.8, 2.8 Hz, 1H), 5.65 – 5.53 (m, 1H), 4.77 (dd, J = 16.0, 6.5 Hz, 1H), 2.85 – 2.54 (m, 1H), 2.32 – 2.27 (m, 1H), 2.23 (s, 6H), 2.11 (s, 12H).^{13}C NMR (101 MHz, CDCl$_3$) δ 145.19, 142.71, 140.65, 137.32, 135.94, 134.67, 134.06, 131.07, 128.46, 127.88, 125.27, 123.10, 122.06, 121.82, 120.05, 108.98, 53.73, 27.14, 23.33, 21.20. HRMS (TOF MS EI$^+$): Calcd. for C$_{32}$H$_{32}$BN: 441.2634; Found: 441.2639.

Compound **3.1-int** (50 mg, 0.11 mmol) was placed in a 50 mL flask containing 10 mL toluene, and 2,3-dichloro-5,6-dicyano-1,4-benzoquinone (DDQ) (30 mg, 0.13 mmol) was added at room temperature. After reacting 30 min, the volatiles were removed *in vacuo* and the product was isolated by column chromatography on silica gel using a solvent mixture of hexanes and ethyl

acetate (10:1) as the eluent. The product **3.1** was isolated as a yellow solid (45 mg, 0.10 mmol, 90% yield) and fully characterized by NMR, MS, and X-ray diffraction analysis.

^{1}H NMR (400 MHz, CDCl$_3$) δ 8.38 (d, J = 7.9 Hz, 1H), 8.16 (d, J = 8.0 Hz, 1H), 8.06 (d, J = 7.3 Hz, 1H), 7.81 (s, 1H), 7.72 (t, J = 7.6 Hz, 1H), 7.67 (t, J = 7.8 Hz, 1H), 7.57 (t, J = 7.6 Hz, 1H), 7.36 (d, J = 8.3 Hz, 1H), 6.93 (s, 4H), 2.41 (s, 6H), 2.24 (s, 6H), 2.17 (s, 6H). ^{13}C NMR (101 MHz, CDCl$_3$) δ 142.73, 140.95, 140.43, 137.54, 135.25, 130.62, 129.96, 129.70, 128.55, 128.10, 125.56, 123.98, 123.78, 122.76, 122.49, 120.33, 117.21, 108.75, 23.80, 23.18, 21.26. HRMS (TOF MS EI$^+$): Calcd. for C$_{32}$H$_{30}$BN: 439.2477; Found: 439.2483.
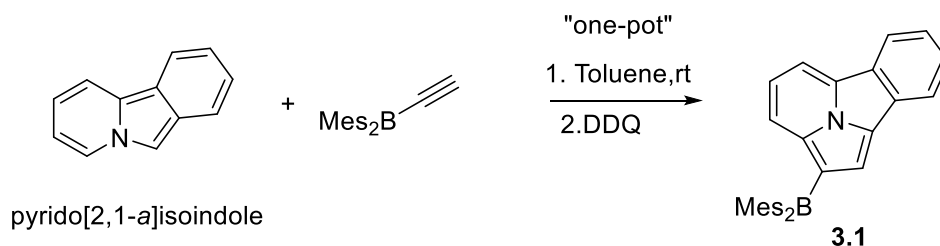
pyrido[2,1-*a*]isoindole

"one-pot" procedure: Dimesitylboronacetylene (165 mg, 0.6 mmol) and pyrido[2,1-*a*]isoindole (100 mg, 0.6 mmol) were reacted in toluene (15 mL) at room temperature in a 50 mL flask for 30 min, and then DDQ (164 mg, 0.72 mmol) was added at room temperature. After reacting 30 min, the volatiles were removed in *vacuo* and the product was isolated by column chromatography on silica gel using a solvent mixture of hexanes and ethyl acetate (10:1) as the eluent. The product **3.1** was isolated as a yellow solid (234 mg, 0.53 mmol, 89% yield). Recrystallization from CH$_2$Cl$_2$/hexane afforded yellow crystals (206 mg, 0.47 mmol) in 78% yield.

3.2.2.2 Synthesis of **3.2**

"one-pot"
1. Toluene, Δ
2. DDQ

pyrrolo[1,2-*a*]pyridine

Mes$_2$B

3.2
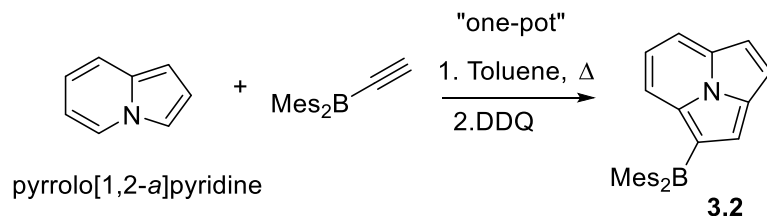
"one-pot" procedure: Dimesitylboronacetylene (118 mg, 0.43 mmol) and pyrrolo[1,2-*a*]pyridine (50 mg, 0.43 mmol) were reacted in toluene (12 mL) at 110 ºC in a 50 mL flask for 3 days, after the mixture was cooled to room temperature, DDQ (117 mg, 0.52 mmol) was added at room temperature. After reacting 30 min, the volatiles were removed in *vacuo* and the product was isolated by column chromatography on silica gel using a solvent mixture of hexanes and ethyl acetate (10:1) as the eluent. The product **2** was isolated as a yellow solid (92 mg, 0.24 mmol, 55% yield), recrystallized by CH$_2$Cl$_2$/hexane as yellow crystals (59 mg, 0.15 mmol) in 36% yield, and fully characterized by NMR and MS.

^{1}H NMR (400 MHz, CDCl$_3$) δ 7.90 (d, *J* = 7.7 Hz, 1H), 7.78 (s, 1H), 7.64 (t, *J* = 7.8 Hz, 1H), 7.61 (d, *J* = 4.6 Hz, 1H), 7.36 (d, *J* = 4.6 Hz, 1H), 7.26 (d, *J* = 7.9 Hz, 1H), 6.89 (s, 4H), 2.38 (s, 6H), 2.15 (s, 12H). ^{13}C NMR (101 MHz, CDCl$_3$) δ 141.43, 139.67, 136.70, 134.37, 130.56, 130.19, 128.33, 127.03, 127.00, 122.68, 117.84, 113.77, 112.66, 111.72, 22.50, 20.21. HRMS (TOF MS EI[+]): Calcd. for C$_{28}$H$_{28}$BN: 389.2320; Found: 389.2328.

3.2.2.3 Synthesis of **3.3**

pyrido[2,1-*a*]isoindole

3.3
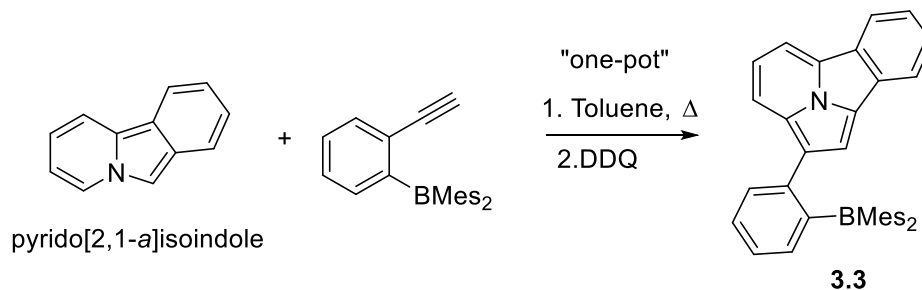
"one-pot" procedure: (2-Ethynylphenyl)dimesitylborane (210 mg, 0.6 mmol) and pyrido[2,1-*a*]isoindole (100 mg, 0.6 mmol) were reacted in toluene (15 mL) at 110 °C in a 50 mL flask for 3 days, after the mixture was cooled to room temperature, DDQ (164 mg, 0.72 mmol) was added at room temperature. After reacting 30 min, the volatiles were removed in *vacuo* and the product was isolated by column chromatography on silica gel using a solvent mixture of hexanes and ethyl acetate (10:1) as the eluent. The product **3.3** was isolated as a yellow solid (231 mg, 0.45 mmol, 75% yield), recrystallized by CH_2Cl_2/hexane as yellow crystals (188 mg, 0.366 mmol) in 61% yield, and fully characterized by NMR, MS, and X-ray diffraction analysis.

^{1}H NMR (500 MHz, CDCl$_3$) δ 8.40 (d, *J* = 7.7 Hz, 1H), 8.09 (d, *J* = 7.7 Hz, 1H), 7.98 (d, *J* = 7.1 Hz, 1H), 7.90 (d, *J* = 8.1 Hz, 1H), 7.77 (d, *J* = 7.0 Hz, 1H), 7.70 (t, *J* = 7.1 Hz, 1H), 7.62 (t, *J* = 7.5 Hz, 2H), 7.52 (d, *J* = 5.0 Hz, 2H), 7.40 (s, 2H), 6.19 (s, 4H), 1.94 (s, 16H). ^{13}C NMR (101 MHz, CDCl$_3$) δ 149.54, 142.60, 141.97, 139.73, 137.45, 135.83, 130.82, 130.23, 129.61, 128.53, 127.63, 127.54, 127.38, 126.57, 126.27, 125.12, 122.20, 122.10, 121.58, 119.39, 119.11, 114.65, 114.02, 107.96, 23.26, 20.73. HRMS (TOF MS EI$^+$): Calcd. for $C_{38}H_{34}BN$: 515.2791; Found: 515.2783.

3.2.2.4 Synthesis of **3.4**

"one-pot"
1. Toluene, Δ
2. DDQ

pyrido[2,1-*a*]isoindole

Mes₂B

3.4
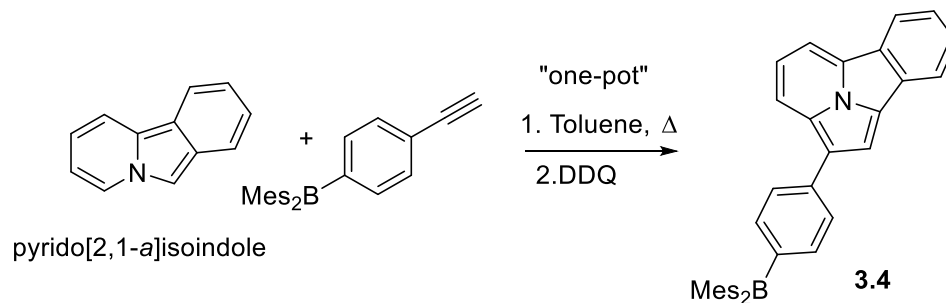
"one-pot" procedure: (4-Ethynylphenyl)dimesitylborane (210 mg, 0.6 mmol) and pyrido[2,1-*a*]isoindole (100 mg, 0.6 mmol) were reacted in toluene (15 mL) at 110 °C in a 50 mL flask for 3 days, after the mixture was cooled to room temperature, DDQ (164 mg, 0.72 mmol) was added at room temperature. After reacting 30 min, the volatiles were removed in *vacuo* and the product was isolated by column chromatography on silica gel using a solvent mixture of hexanes and ethyl acetate (10:1) as the eluent. The product **3.4** was isolated as a yellow solid (256 mg, 0.5 mmol, 83% yield), recrystallized by CH_2Cl_2/hexane as yellow powder (230 mg, 0.45 mmol) in 75% yield, and fully characterized by NMR and MS.

^{1}H NMR (500 MHz, CD_2Cl_2) δ 8.50 (d, *J* = 7.7 Hz, 1H), 8.46 (d, *J* = 8.0 Hz, 1H), 8.28 (d, *J* = 7.5 Hz, 1H), 8.21 (d, *J* = 6.9 Hz, 1H), 8.05 (s, 1H), 7.99 (d, *J* = 7.3 Hz, 2H), 7.90 – 7.81 (m, 1H), 7.77 (d, *J* = 7.0 Hz, 1H), 7.66 (d, *J* = 7.4 Hz, 2H), 7.61 (d, *J* = 7.3 Hz, 1H), 6.90 (s, 4H), 2.36 (s, 6H), 2.13 (s, 12H). ^{13}C NMR (101 MHz, CD_2Cl_2) δ 143.11, 142.26, 141.15, 140.87, 138.87, 138.09, 130.02, 129.51, 129.37, 128.73, 128.50, 126.71, 126.47, 123.68, 123.19, 122.91, 121.63, 121.49, 120.03, 116.31, 110.86, 109.17, 23.64, 21.32. HRMS (TOF MS EI+): Calcd. for $C_{38}H_{34}BN$: 515.2791; Found: 515.2799.

3.2.3 X-ray crystallographic analysis

Single crystals of **3.1**, **3.1-int**, and **3.3** were obtained from CH_2Cl_2 and hexanes by slow evaporation of the solvent. The crystals were mounted on glass fibers and the data were collected on a Bruker Apex II single-crystal X-ray diffractometer with graphite-monochromated Mo Kα radiation, operating at 50 kV and 30 mA, and at 180 K. Data were processed on a PC with the aid of the Bruker SHELXTL software package (version 6.14) and corrected for absorption effects. All structures were solved using direct methods. The crystals of **3.1** and **3.1-int** belong to the monoclinic space group $P2_1/c$, while that of **3.3** belongs to the triclinic space group P-1. All non-hydrogen atoms were refined anisotropically. Complete crystal structural data have been deposited at the Cambridge Crystallographic Data Centre [CCDC No. 1058108 (**3.1**), 1058109 (**3.1-int**), 1058110 (**3.3**)]. These data can be obtained free of charge from The Cambridge Crystallographic Data Centre via www.ccdc.cam.ac.uk/data_request/cif.].

Table 3.1 Crystal data and structure refinement for **3.1**, **3.1-int**, **3.3**.

	3.1	3.1-int	3.3
Empirical formula	C32 H30 B N	C32 H32 B N	C38 H34 B N
Formula weight	439.38	441.40	515.47
Crystal system	Monoclinic	Monoclinic	Triclinic
Space group	P2(1)/c	P2(1)/c	P-1
a/Å	10.2671(2)	10.0993(2)	8.8087(5)
b/Å	10.1236(2)	10.2609(2)	11.1753(6)
c/Å	23.3329(6)	23.8794(5)	16.1219(9)
α, deg	90	90	72.148(4)
β, deg	98.876(2)	97.3582(11)	78.052(4)
γ, deg	90	90	74.662(4)
V/Å^3	2396.18(9)	2454.19(9)	1443.04(14)
Z	4	4	2
Density (calculated)	1.218 Mg/m^3	1.195 Mg/m^3	1.186 Mg/m^3
Absorption coefficient	0.069 mm^{-1}	0.068 mm^{-1}	0.067 mm^{-1}
Reflections collected	13974	14049	24920
Completeness to theta	99.7 % (26.00º)	99.9 % (25.50º)	98.8 % (27.67º)
Goodness-of-fit on F^2	1.024	1.154	1.053
Final R indices [I>2sigma(I)]	R1 = 0.0550, wR2 = 0.1212	R1 = 0.0783, wR2 = 0.1621	R1 = 0.0575, wR2 = 0.1344
R indices (all data)	R1 = 0.1202, wR2 = 0.1506	R1 = 0.1085, wR2 = 0.1772	R1 = 0.1254, wR2 = 0.1636

Table 3.2 Selected bond lengths [Å] and angles [°] for **3.1**.

N(1)-C(14)	1.366(3)	C(3)-N(1)-C(10)	115.7(2)
N(1)-C(3)	1.379(3)	C(1)-B(1)-C(24)	118.2(2)
N(1)-C(10)	1.382(3)	C(1)-B(1)-C(15)	119.9(2)
B(1)-C(1)	1.520(3)	C(24)-B(1)-C(15)	122.0(2)
B(1)-C(24)	1.588(4)	C(14)-C(1)-C(2)	105.37(19)
B(1)-C(15)	1.596(3)	C(14)-C(1)-B(1)	129.1(2)
C(1)-C(14)	1.440(3)	C(2)-C(1)-B(1)	125.5(2)
C(1)-C(2)	1.441(3)	C(3)-C(2)-C(1)	110.2(2)
C(14)-N(1)-C(3)	113.80(19)	N(1)-C(3)-C(2)	105.1(2)
C(14)-N(1)-C(10)	130.5(2)	N(1)-C(3)-C(4)	104.31(19)
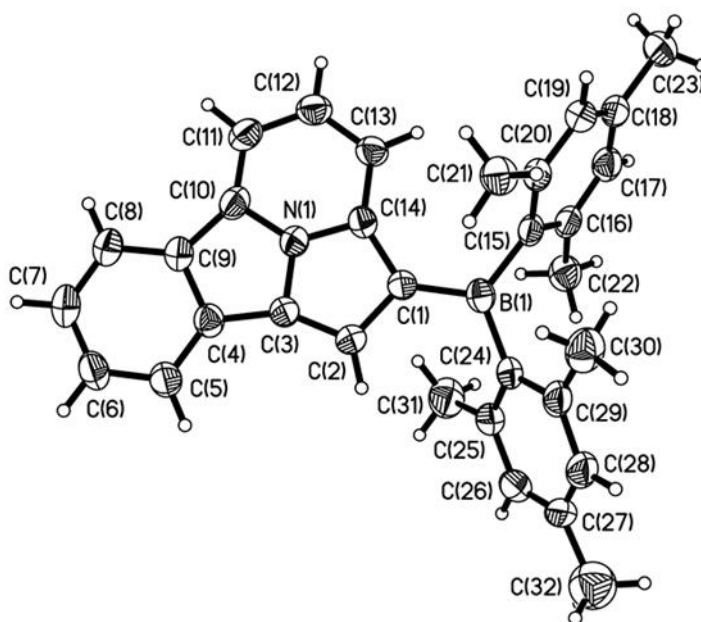
Figure 3.2 The crystal structure with labeling schemes of **3.1**.

Table 3.3 Selected bond lengths [Å] and angles [°] for **3.1-int**.

N(1)-C(14)	1.342(4)	C(14)-N(1)-C(3)	113.3(2)
N(1)-C(3)	1.370(4)	C(14)-N(1)-C(10)	130.9(3)
N(1)-C(10)	1.454(4)	C(3)-N(1)-C(10)	115.8(3)
B(1)-C(1)	1.535(4)	C(1)-B(1)-C(24)	117.8(3)
B(1)-C(24)	1.583(4)	C(1)-B(1)-C(15)	120.1(3)
B(1)-C(15)	1.593(4)	C(24)-B(1)-C(15)	122.1(2)
C(1)-C(14)	1.420(4)	C(14)-C(1)-C(2)	105.4(2)
C(1)-C(2)	1.444(4)	C(14)-C(1)-B(1)	129.2(3)
C(10)-C(11)	1.387(5)	C(2)-C(1)-B(1)	125.3(3)
C(11)-C(12)	1.513(5)	C(3)-C(2)-C(1)	108.9(3)
N(1)-C(3)-C(4)	105.0(2)	C(2)-C(3)-N(1)	105.9(2)
C(11)-C(10)-N(1)	111.2(4)	C(10)-C(11)-C(12)	114.7(3)
C(11)-C(10)-C(9)	133.5(4)	N(1)-C(14)-C(1)	106.4(3)
N(1)-C(10)-C(9)	99.7(3)	N(1)-C(14)-C(13)	113.3(3)
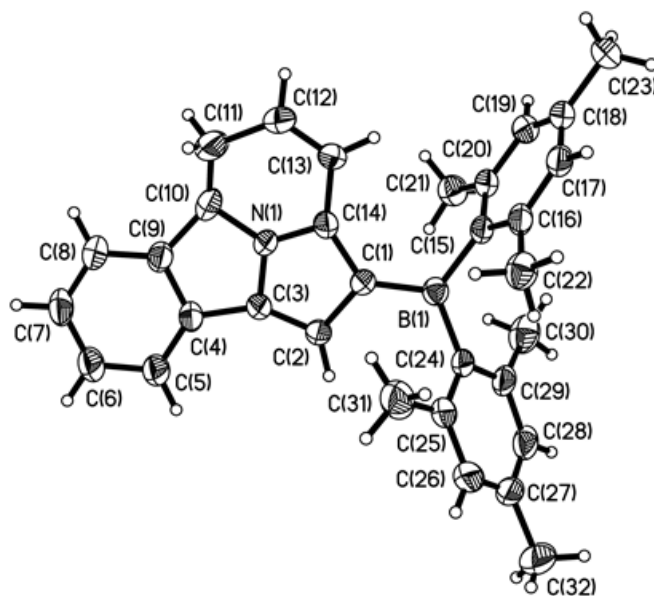
Figure 3.3 Crystal structure of **3.1-int** with labeling schemes.

Table 3.4 Selected bond lengths [Å] and angles [°] for **3.3**.

B(1)-C(20)	1.572(3)	C(20)-B(1)-C(21)	121.40(17)
B(1)-C(21)	1.576(3)	C(20)-B(1)-C(30)	116.20(17)
B(1)-C(30)	1.580(3)	C(21)-B(1)-C(30)	122.26(18)
N(1)-C(3)	1.357(2)	C(3)-N(1)-C(10)	116.54(18)
N(1)-C(10)	1.370(2)	C(3)-N(1)-C(14)	113.70(17)
N(1)-C(14)	1.373(2)	C(10)-N(1)-C(14)	129.63(18)
C(1)-C(2)	1.403(3)	C(2)-C(1)-C(14)	107.45(17)
C(1)-C(14)	1.421(3)	C(2)-C(1)-C(15)	128.51(18)
C(1)-C(15)	1.467(3)	C(14)-C(1)-C(15)	123.92(19)
C(1)-C(2)-C(3)	108.97(18)	N(1)-C(3)-C(2)	105.02(18)
C(1)-C(2)-H(2A)	125.5	N(1)-C(3)-C(4)	104.26(17)
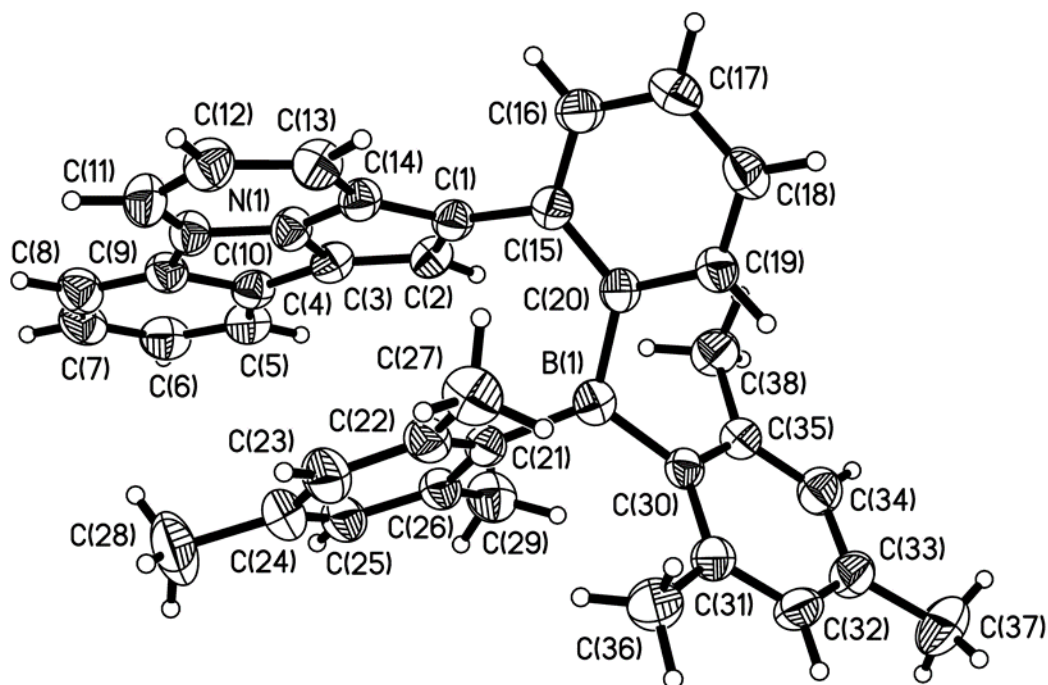
Figure 3.4 Crystal structure of **3.3** with labeling schemes.

3.2.4 DFT calculations

All calculations were performed using the Gaussian 09 suite of programs[8] on the High Performance Computing Virtual Laboratory (HPCVL) at Queen's University. Initial input coordinates were taken from the corresponding crystal structure data where applicable, while all others were generated from the optimized geometries of pyrido[2,1-*a*]isoindole or pyrrolo[1,2-*a*]pyridine. All ground state geometry optimizations and TD-DFT vertical excitations were performed at the B3LYP[9] level of theory employing the 6-311+g(d,p)[10] Pople-style basis set for all atoms.

3.3 Results and Discussion

3.3.1 Synthesis and Structural Analysis

Pyrido[2,1-*a*]isoindole[11a] and the alkyne starting materials $BMes_2$-acetylene,[11b] *o*-$BMes_2$-C_6H_4-acetylene,[11c] and *p*-$BMes_2$-C_6H_4-acetylene[11d] were prepared according to literature methods. The cycloaddition reactions of the alkyne compounds with pyrido[2,1-*a*]isoindole / pyrrolo[1,2-*a*]pyridine were carried out in toluene under nitrogen according to the procedure shown in Figure 3.1. The cycloaddition between pyrido[2,1-*a*]isoindole and $BMes_2$-acetylene proceeded rapidly, yielding **3.1-int** quantitatively after 1 hour at room temperature. Although **3.1-int** can be isolated and purified prior to dehydrogenation, the subsequent addition of 2,3-dichloro-5,6-dicyano-1,4-benzoquinone (DDQ, 1.2 eq.), a well-known reagent for oxidative dehydrogenation,[12] to the reaction mixture was found to be the most efficient method of generating compound **3.1** in excellent yield (*i.e.* a one-pot synthesis). With respect to the synthesis of **3.2** - **3.4**, their initial cycloaddition reactions required refluxing the N-heterocycles and the corresponding alkyne starting material in toluene for several days due to the relatively low reactivity of pyrrolo[1,2-*a*]pyridine and $BMes_2$-C_6H_4-alkynes. Under these harsher reaction conditions, both the intermediates (**int**) and the fully

dehydrogenated products **3.2** – **3.4** were observed. Therefore, no attempts to isolate the intermediates were performed as it would have resulted in a loss of potential yield. Once again, addition of DDQ to each reaction mixture resulted in quantitative conversion to the desired products **3.2** – **3.4** in decent to good yield. In the previously reported cycloaddition reactions of pyrido[2,1-*a*]isoindole with alkynes, the most commonly used dehydrogenation reagent is sulfur,[4a] which requires the isolation of the intermediate first. Our attempts employing sulfur powder as the oxidant for converting the intermediate **3.1-int** to **3.1** required much longer reaction times and elevated temperatures compared to DDQ. Furthermore, we were unable to fully remove the excess sulfur from the final products *via* recrystallization or column/thin-layer chromatography. The one-pot procedure employing DDQ as the oxidant not only greatly simplifies the reaction, but also allows us to isolate the fully conjugated products in high purity and good yield. Compounds **3.1** - **3.4** and **3.1-int** were fully characterized by ^{1}H and ^{13}C NMR as well as HRMS. Attempts to record the ^{11}B NMR spectra for these compounds at various temperatures have not been successful.
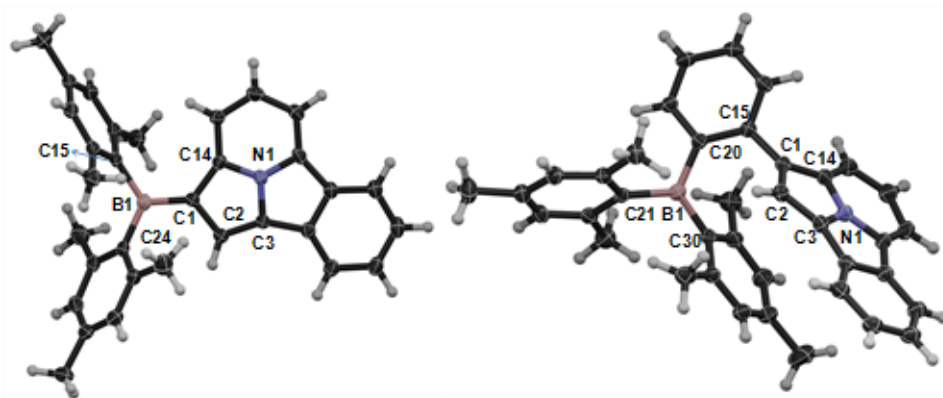
Figure 3.5 Crystal structure of **3.1** (left) and **3.3** (right). Important bond lengths (Å) for 1: B(1)-C(1) 1.520(3), B(1)-C(15) 1.596(3), B(1)-C(24) 1.588(4), C(1)-C(2) 1.441(3), C(1)-C(14) 1.440(3), C(2)-C(3) 1.379(3), N(1)-C(3) 1.379(3), N(1)-C(14) 1.366(3); for 2: B(1)-C(20) 1.572(3), B(1)-C(21) 1.576(3), B(1)-C(30) 1.580(3), C(1)-C(2) 1.403(3), C(1)-C(14) 1.421(3), C(2)-C(3) 1.406(3), N(1)-C(3) 1.357(2), N(1)-C(14) 1.373(2).

^{1}H NMR data reveals that only one regioisomer is formed for **3.1** – **3.4**, in which the carbon atom of the alkyne that is attached to the boron unit forms a bond with a pyridyl carbon atom. The regioselectivity of the cycloaddition reaction is further supported by the single-crystal X-ray diffraction data of compounds **3.1**, **3.1-int**, and **3.3**. The crystal structures of **3.1** and **3.3** are shown in Figure 3.5. The observed regioselectivity of the 1,3-dipolar cycloaddition is in agreement with the frontier molecular orbital theory,[13] which rationalizes that the dominant electronic interaction is the combination of the largest HOMO and LUMO orbital contributions from the 1,3-dipole and dipolarophiles, respectively. From our computational analysis, the C(6) position of pyrido[2,1-*a*]isoindole (labeled as C(3) in the crystal structure) and C(3) position of pyrrolo[1,2-*a*]pyridine were found to possess the largest HOMO contribution, while the terminal alkyne carbon of all three dipolarophiles were found to possess the largest LUMO contribution which ultimately leads to the formation of only one regioisomer.
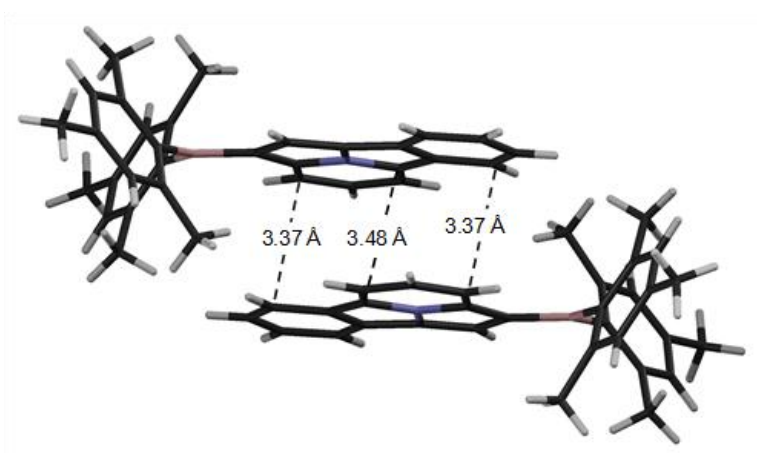
Figure 3.6 The π-stacked dimer of **3.1**.

Although molecules of **3.1** form discrete π-stacked dimers between each indolizino[3,4,5-*ab*]isoindole ring in the crystal lattice (Figure 3.6), no extended π-stacking interactions were observed. This is in sharp contrast to previously reported indolizino[3,4,5-*ab*]isoindole derivatives,

97

which display strong and extended π-stacking interactions in the solid state.[4a] The bulky BMes$_2$ group is clearly responsible for the significant reduction in intermolecular π-stacking interactions of molecule **3.1**. It is conceivable that similar π-stacking interactions are also possible for molecules **3.2** and **3.3** due to their structural similarity to **3.1**. Molecules of **3.3** display intramolecular π-stacking interactions between the five-membered ring containing the C(1), C(2), C(3) and C(14) atoms and the benzene ring of a mesityl with atomic separation distances of 3.10 (C(1)···C(30)) to 3.90 Å (Figure 3.5), which is attributed to steric congestion. Intermolecular π-stacking interactions similar to that of **3.1** were not observed for **3.3**.

3.3.2 Electrochemical and Photophysical Properties
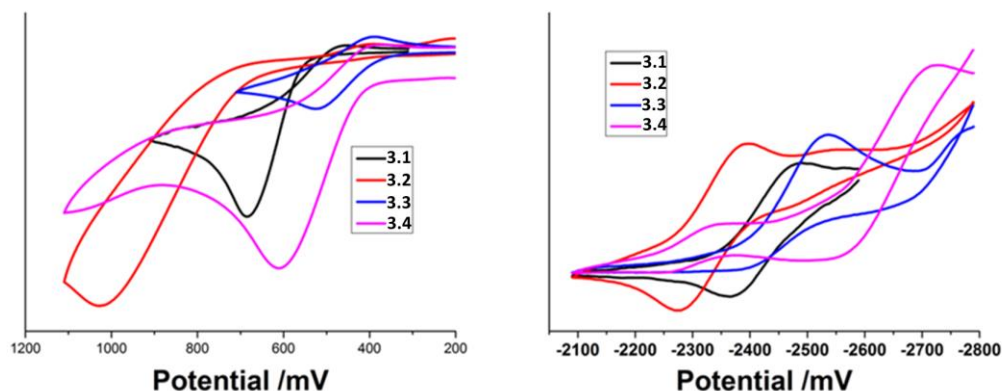
Figure 3.7 Cyclic voltammetry of compounds **3.1**-**3.4** (Left: oxidation; Right: Reduction). CV diagrams of compounds recorded in DMF:THF(1:1) with NBu$_4$PF$_6$ as the electrolyte, scan rate 75 mV/s.

The attachment of the BMes$_2$ group to indolizino[3,4,5-*ab*]isoindole has a distinct impact on the electronic and photophysical properties of the molecule. Molecules **3.1** - **3.4** display pseudo reversible reduction peaks between -2.34 V (**3.2**) and -2.55 V (**3.3**) (Figure 3.7 and Table 3.5), which are characteristic of the boron unit but somewhat more negative than those of BMes$_2$Ar (Ar

= phenyl or substituted phenyl)[14] due to the electron-rich nature of the indolizino[3,4,5-*ab*]isoindole or pyrrolo[2,1,5-*cd*]indolizine N-heterocycle. An irreversible oxidation peak is also observed for all four compounds between 0.53 (**3.3**) and 1.00 (**3.2**) V, which is characteristic of the N-heterocyclic unit.[4a]

Table 3.5 Electrochemical data

Compounds	E_{pa}^{ox} (V)[a]	$E_{1/2}^{red}$ (V)[a]
3.1	0.69	-2.44
3.2	1.00	-2.34
3.3	0.53	-2.55
3.4	0.61	-2.48

[a] Relative to Cp_2Fe/Cp_2Fe^+.
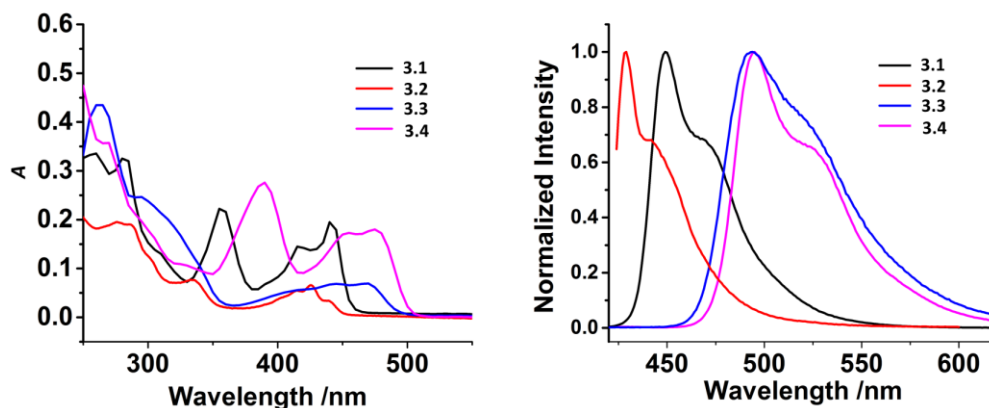
Figure 3.8 UV−vis (left) and emission (right) spectra of compounds **3.1** – **3.4** in CH_2Cl_2 (1.0 × 10^{-5} M).

Much like the non-boron containing parent molecules, **3.1** – **3.4** all possess strong absorption bands between 400-500 nm as shown in Figure 3.8 and Table 3.6. As one might expect, the absorption bands of **3.1** and **3.2** are hypsochromically shifted by ~40 nm compared to **3.3** and **3.4**

which is most likely due to the increased π-conjugation in the latter. Compared to **3.4**, the absorption band of **3.3** is weaker and at a slightly higher energy, which is likely caused by the steric congestion in **3.3** that results in poor π-conjugation between the phenyl-BMes$_2$ and indolizino[3,4,5-*ab*]isoindolyl ring.

Table 3.6 Absorption and fluorescence data

compd	λ_{abs}, nm (ε,M^{-1}cm^{-1})[a]	λ_{em}, nm[b]	Φ[c]
3.1	355, 415, 440 (1.95 x 10^4)	448/468	0.64/0.51
3.2	335, 415, 425 (1.80 x 10^4)	428/440, 505	0.27/0.31
3.3	445, 468 (0.692 x 10^4)	494/494	0.33/0.97
3.4	389, 455, 475 (0.656 x 10^4)	495/505	0.68/0.60

[a] 10^{-5} M in CH$_2$Cl$_2$ at 298 K. [b] CH$_2$Cl$_2$/PMMA film (10 wt %). [c]The solution QY was determined in CH$_2$Cl$_2$ using 9,10-diphenylanthracene as the reference under N$_2$. The solid state QY was measured using an integration sphere.

To investigate the origin of the low energy absorption bands and electronic properties of these new molecules, TD-DFT calculations were performed on the computationally optimized geometries of **3.1** - **3.4** and **3.1**'s parent molecule (**3.1-no B**). For **3.1** - **3.4**, the predicted UV-Vis spectra were found to be in good agreement with the experiment data. For **3.1**, **3.2**, and **3.4**, the low energy absorption band is likely from the S$_0$→S$_1$ electronic transition which primarily involves HOMO → LUMO (> 90%, large oscillator strengths). As shown in Figure 3.9, the HOMO is concentrated on the N-heterocylic ring, while the LUMO is dominated by the empty p$_\pi$ orbital of the boron atom and the π*-orbitals of the N-heterocyclic ring. Therefore, these absorption bands appear to be π → π* transitions. With respect to **3.3**, its low energy absorption band is predicted to be comprised of transitions to S$_1$ and S$_2$, which involve HOMO→LUMO and HOMO→LUMO+1,

respectively. As with the other three compounds, the HOMO of **3.3** is comprised of the π-orbitals from the N-heterocyclic ring system. Although the vacant p-orbital on the boron atom also dominates the LUMO of compound **3.3**, it possesses almost no contribution from the N-heterocyclic ring system. Rather, the remaining contributions to the LUMO of **3.3** are the π^*-orbitals of both the phenyl linker and mesityls. Therefore, the $S_0 \rightarrow S_1$ transition of **3.3** appears to have CT character. However, close in energy (5 nm difference) and with a greater oscillator strength is the $S_0 \rightarrow S_2$ transition that can be characterized as π(HOMO) $\rightarrow \pi^*$(LUMO+1) localized on the N-heterocycle and likely is the predominant excitation of **3.3**. The attachment of the BMes$_2$ unit to the parent molecule (**3.1-no B**) appears to stabilize both the HOMO and LUMO without significantly changing the HOMO-LUMO gap. The calculated trend of HOMO and LUMO energies agree with our electrochemical data.

All four compounds are brightly fluorescent with the emission energy following the same trend as the absorption spectra (Figure 3.8). The emission maxima of **3.1** - **3.4** in CH$_2$Cl$_2$ were found to be at 448, 428, 494, and 495 nm respectively, with **3.1** and **3.4** having the most impressive emission quantum efficiencies (0.64 and 0.68, respectively). This indicates that both the N-heterocyclic π-system and appended organoboron moiety play a pivotal role in the electronic structure of these compounds. For **3.1**, **3.2** and **3.4**, the emission peaks were found to be unaffected by solvents of varying polarity, which is in agreement with the $\pi \rightarrow \pi^*$ transition localized on the N-heterocycle being the first excited state (Figure 3.10 and Figure 3.20). For compound **3.3**, although the emission λ_{max} was not affected by solvent polarity, its shoulder peak at ~540 nm experiences broadening and a red-shift with increasing solvent polarity which is consistent with the involvement of both $\pi \rightarrow \pi^*$ and CT transitions for **3.3**, as shown in Figure 3.10.
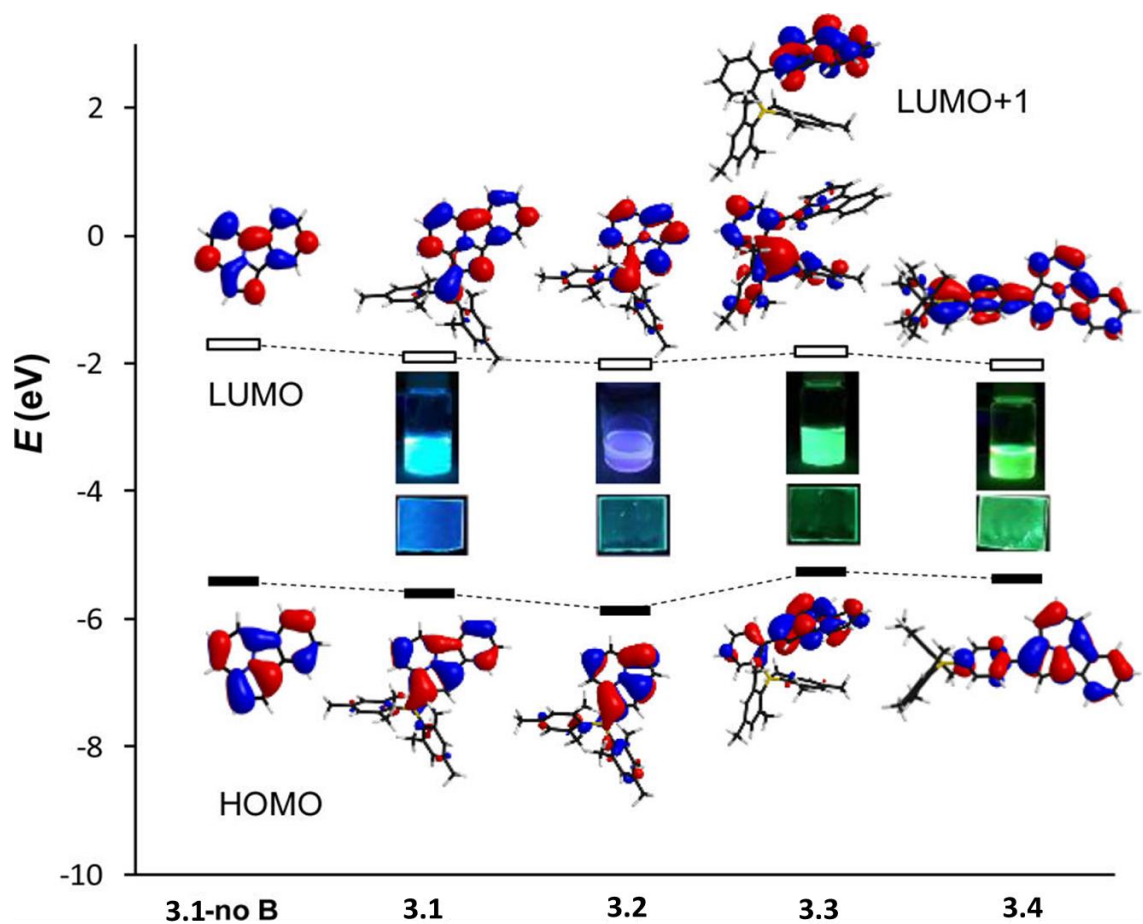
Figure 3.9 Energies and diagrams of HOMO and LUMO (LUMO+1) for the parent molecule (**3.1-no B**) and **3.1 – 3.4**. Inset: photographs showing the fluorescent colors of **3.1 – 3.4** in CH_2Cl_2 (top) and PMMA films (10 wt %).
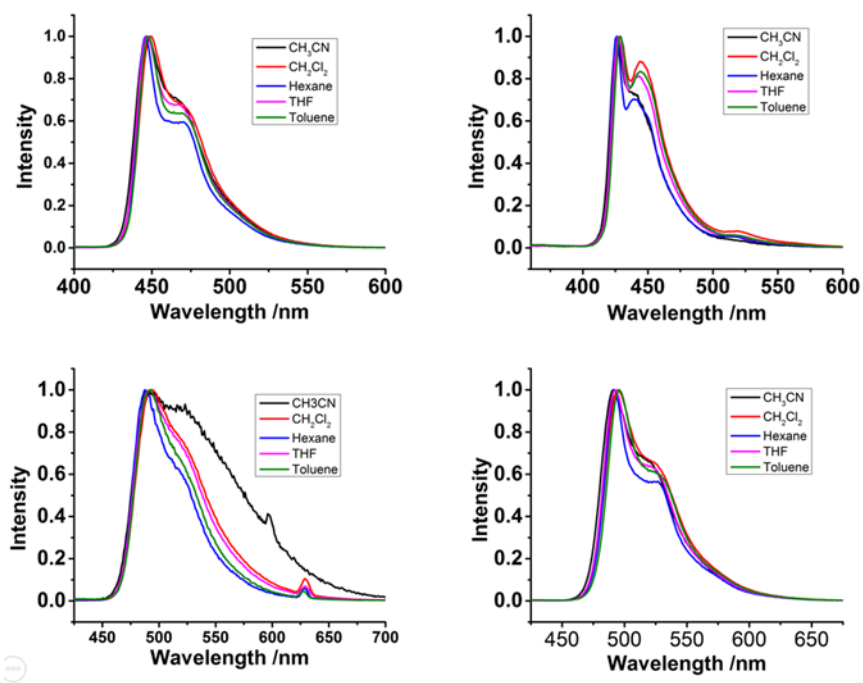
Figure 3.10 Fluorescence spectra of compounds **3.1**- **3.4** in different solvents. (Top-left: **3.1**. Top-right: **3.2**. Bottom-left: **3.3**. Bottom-right: **3.4**)

The emission profile of **3.1** - **3.4** do not change significantly at the concentration range of 10^{-6} M to 10^{-4} M (Figure 3.11). At concentrations $>10^{-4}$ M, the emission spectra of **3.1**, **3.2** and **3.4** broaden and red-shift indicating the presence of intermolecular interactions. In contrast, similar concentration dependent-change was not observed for **3.3**. In the solid state, compounds **3.1**, **3.3** and **3.4** display an emission color similar to that observed in solution and have high quantum yields (Table 3.6 and Figure 3.8). For **3.1** and **3.4**, the solid-state emission spectra are broader and red-shifted by ~10-20 nm compared to their spectra in solution, while the spectrum of **3.3** experiences no change (Figure 3.12). Unlike its purple emission in solution, **3.2** emits a greenish blue color in the solid state with two distinct emission peaks at ~440 and ~500 nm respectively, where the latter is attributed to the formation of excimers. These observations are consistent with the presence of greater intermolecular interactions for **3.1**, **3.2** and **3.4**, compared to **3.3**.
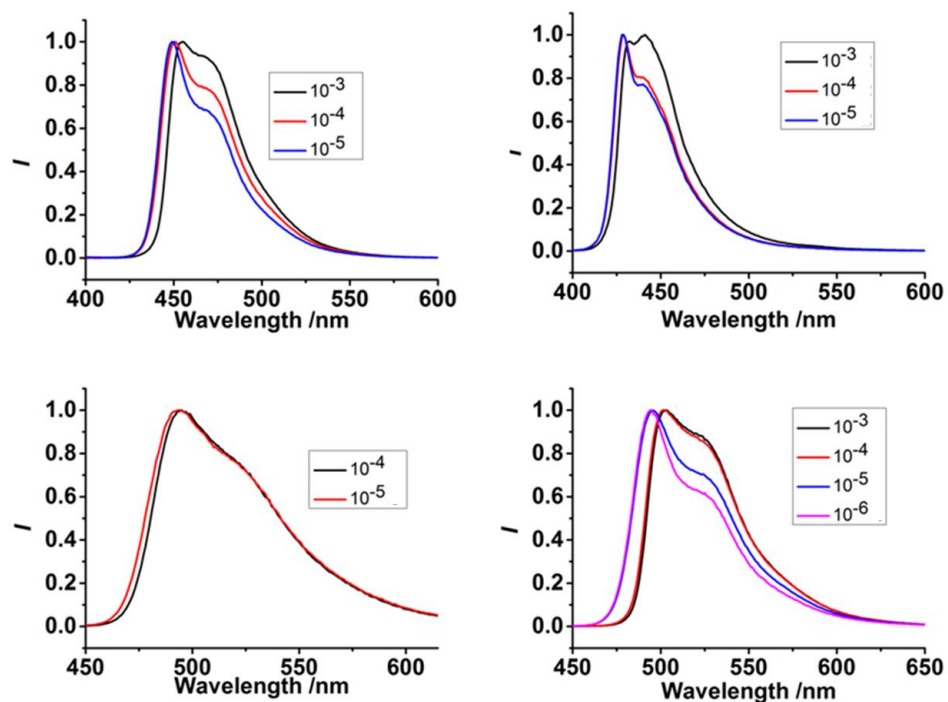
Figure 3.11 Fluorescence of compounds **3.1**- **3.4** in different concentrations CH_2Cl_2 solution. (Top-left: **3.1**. Top-right: **3.2**. Bottom-left: **3.3**. Bottom-right: **3.4**)
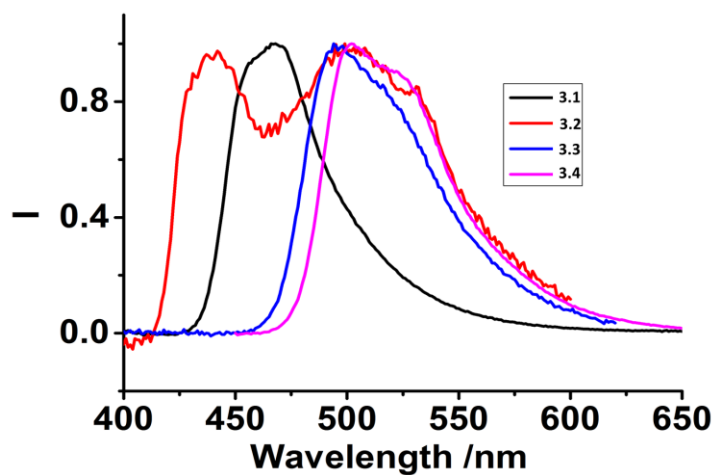
Figure 3.12 Normalized emission of compounds **3.1**- **3.4** in PMMA (10%) with background correction.

3.3.1 Fluoride Titration
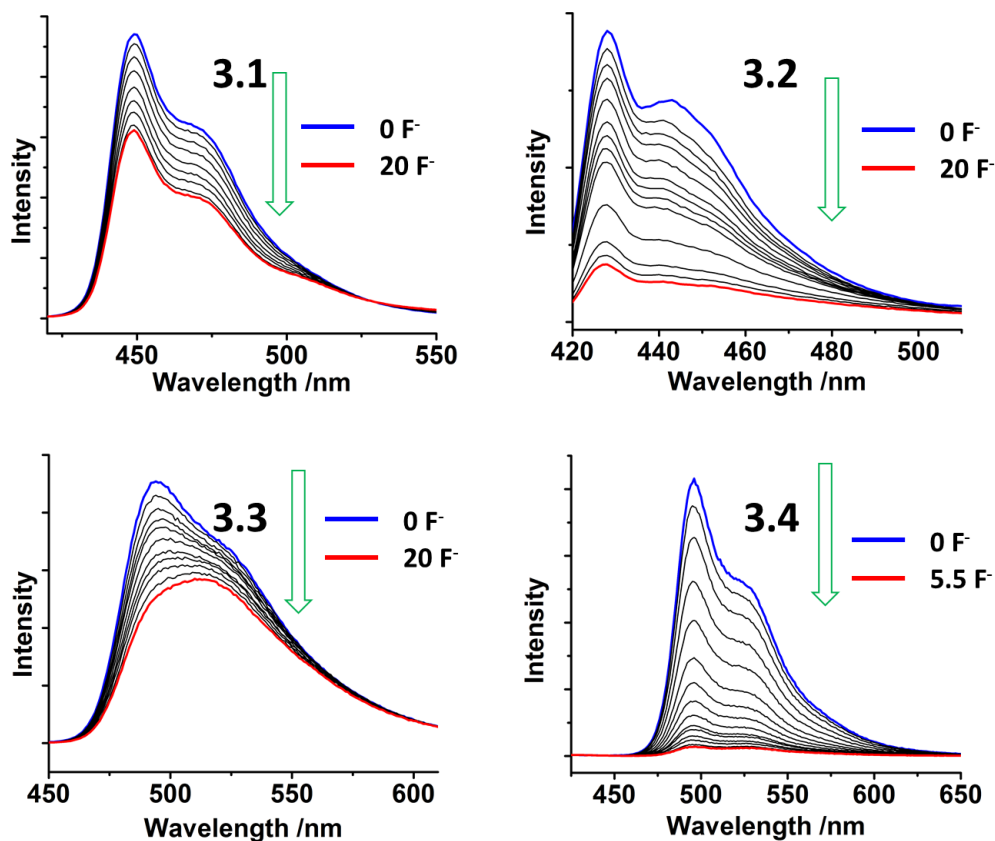
Figure 3.13 Fluorescent titration of **3.1** – **3.4** (10^{-5} M) with TBAF in CH_2Cl_2 at 298 K.

To further understand the fluorescent properties of **3.1** – **3.4**, fluoride titrations employing NBu_4F (TBAF) in CH_2Cl_2 were performed (Figure 3.13). For compounds **3.1**, **3.2**, and **3.4**, a uniform decrease in both the primary absorption bands (Figure) and emission peaks was observed. This is in agreement with the predicted electronic transitions, as the empty p-orbital of the boron atom is the largest contributor to most of the unoccupied orbitals. Interestingly, the fluorescence of **3.4** was quenched with fewer equivalents of fluoride compared to **3.1** and **3.2**. This may be attributed to the greater steric congestion around the boron atom in **3.1** and **3.2** relative to **3.4**, which is evident in their NMR spectra (Figure 3.24). As expected from the TD-DFT data, the addition of

TBAF to a solution of **3.3** did not result in complete quenching of the emission peak. Instead, the emission peak is only partially quenched, where the remaining emission peak is likely the result of a localized π→π* transition on the indolizino[3,4,5-*ab*]isoindole backbone of **3.3**.

3.4 Conclusions

In conclusion, a "one-pot" cycloaddition procedure has been successfully developed for the synthesis of a series of BMes$_2$ functionalized N-heterocycles. The boryl unit has been found to greatly diminish intermolecular interactions, rendering the molecules highly fluorescent with good quantum efficiencies in both solution and the solid state.

3.5 Appendix

3.5.1 DFT Calculation Data
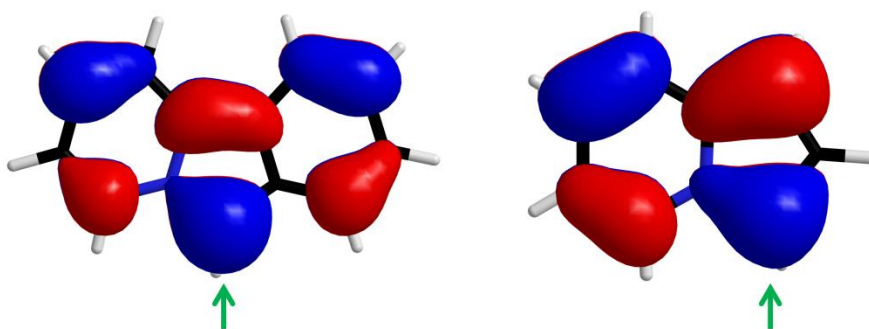
Figure 3.14 HOMO of pyrido[2,1-*a*]isoindole (left) and pyrrolo[1,2-*a*]pyridine (right); green arrows indicate the more electron rich carbon atoms of the 1,3-dipole (iso = 0.03).
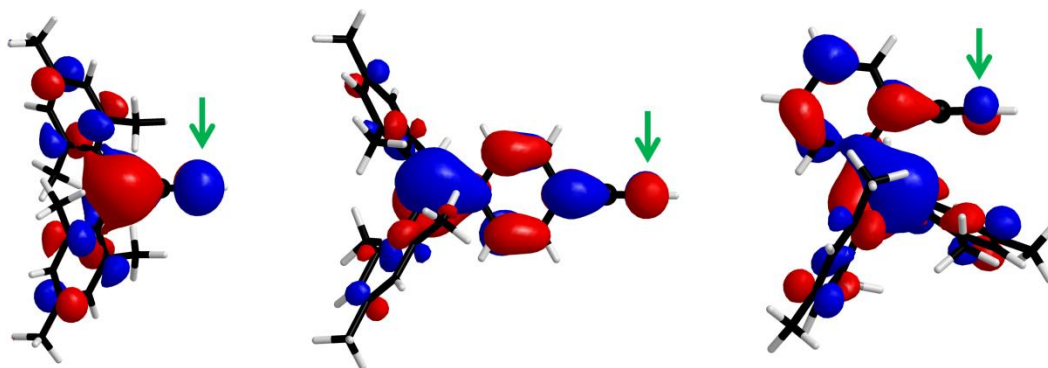
Figure 3.15 LUMO of organoboron functionalized alkynes; green arrows indicate the more electron rich carbon atoms of the dipolarophile (iso = 0.03).

Table 3.7 TD-DFT calculated electronic transition configurations for **3.1** along with their corresponding excitation energies and oscillator strengths.

Compound	Spin State	Transition Configuration	Excitation Energy (nm, eV)	Oscillator Strength
3.1	S_1	HOMO → LUMO (93%)	399.20 (3.11)	0.2343
		HOMO → LUMO+1 (3%)		
	S_2	HOMO-3 → LUMO (10%)	345.30 (3.59)	0.2204
		HOMO-2 → LUMO (5%)		
		HOMO → LUMO (3%)		
		HOMO → LUMO+1 (78%)		
	S_3	HOMO-1 → LUMO (90%)	341.85 (3.63)	0.0380
		HOMO-1 → LUMO+1 (8%)		
	S_4	HOMO-3 → LUMO (4%)	329.67 (3.76)	0.0089
		HOMO-2 → LUMO (87%)		
		HOMO-2 → LUMO+1 (5%)		
		HOMO → LUMO+1 (3%)		
	S_5	HOMO-3 → LUMO (76%)	323.64 (3.83)	0.0343
		HOMO → LUMO+1 (13%)		
		HOMO → LUMO+2 (4%)		
	S_6	HOMO-5 → LUMO (4%)	320.16 (3.87)	0.0024
		HOMO-4 → LUMO (80%)		
		HOMO-4 → LUMO+1 (4%)		
		HOMO → LUMO+2 (10%)		
	S_7	HOMO-5 → LUMO (39%)	316.69 (3.91)	0.0049
		HOMO-4 → LUMO (13%)		
		HOMO → LUMO+2 (43%)		
	S_8	HOMO-3 → LUMO+1 (3%)	300.55 (4.13)	0.0322
		HOMO-1 → LUMO (8%)		
		HOMO-1 → LUMO+1 (85%)		
	S_9	HOMO-4 → LUMO+1 (3%)	292.85 (4.23)	0.0013
		HOMO-3 → LUMO+1 (6%)		
		HOMO-2 → LUMO (4%)		
		HOMO-2 → LUMO+1 (79%)		
		HOMO-1 → LUMO+1 (2%)		
	S_{10}	HOMO-3 → LUMO (3%)	289.93 (4.28)	0.0163
		HOMO-3 → LUMO+1 (80%)		
		HOMO-2 → LUMO+1 (6%)		

Table 3.8 TD-DFT calculated electronic transition configurations for **3.2** along with their corresponding excitation energies and oscillator strengths.

Compound	Spin State	Transition Configuration	Excitation Energy (nm, eV)	Oscillator Strength
3.2	S_1	HOMO → LUMO (93%)	377.44 (3.28)	0.2376
	S_2	HOMO-1 → LUMO (96%)	352.94 (3.51)	0.0448
		HOMO-1 → LUMO+1 (3%)		
	S_3	HOMO-2 → LUMO (92%)	339.42 (3.65)	0.0009
		HOMO → LUMO+1 (5%)		
	S_4	HOMO-3 → LUMO (79%)	332.80 (3.73)	0.0160
		HOMO → LUMO+1 (14%)		
	S_5	HOMO-4 → LUMO (97%)	326.73 (3.79)	0.0037
	S_6	HOMO-5 → LUMO (22%)	315.38 (3.93)	0.1044
		HOMO-3 → LUMO (10%)		
		HOMO → LUMO (2%)		
		HOMO → LUMO+1 (63%)		
	S_7	HOMO-5 → LUMO (65%)	299.98 (4.13)	0.0488
		HOMO-5 → LUMO+1 (5%)		
		HOMO-3 → LUMO (6%)		
		HOMO → LUMO+1 (14%)		
		HOMO → LUMO+2 (5%)		
	S_8	HOMO-1 → LUMO (3%)	292.93 (4.23)	0.0464
		HOMO-1 → LUMO+1 (93%)		
	S_9	HOMO-4 → LUMO+1 (4%)	284.40 (4.36)	0.0030
		HOMO-2 → LUMO+1 (87%)		
	S_{10}	HOMO-4 → LUMO+1 (5%)	280.26 (4.42)	0.0365
		HOMO-3 → LUMO+1 (87%)		
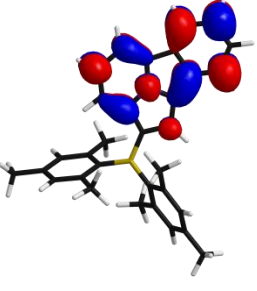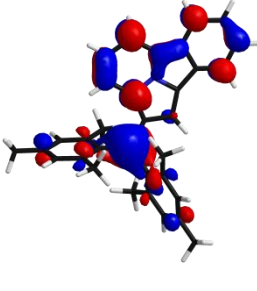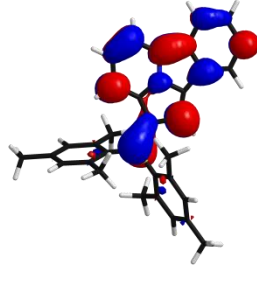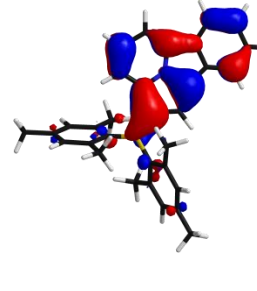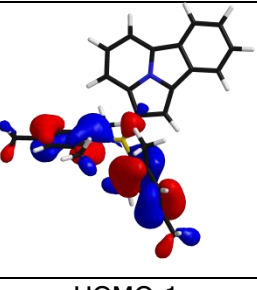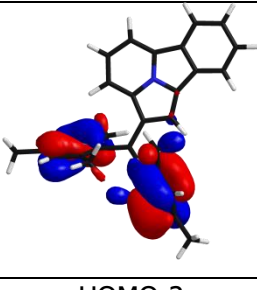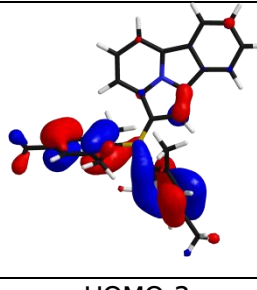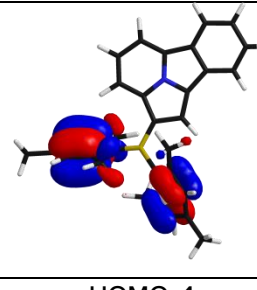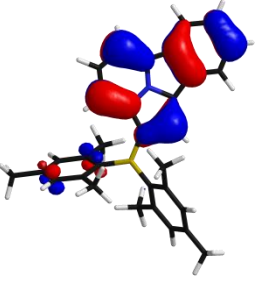
Table 3.9 TD-DFT calculated electronic transition configurations for **3.3** along with their corresponding excitation energies and oscillator strengths.

Compound	Spin State	Transition Configuration	Excitation Energy (nm, eV)	Oscillator Strength
3.3	S_1	HOMO → LUMO (98%)	432.11 (2.87)	0.0655
	S_2	HOMO → LUMO+1 (96%)	426.99 (2.90)	0.1073
	S_3	HOMO-2 → LUMO (4%)	347.24 (3.57)	0.0674
		HOMO-1 → LUMO (91%)		
	S_4	HOMO-5 → LUMO+1 (4%)	331.48 (3.74)	0.0479
		HOMO-2 → LUMO (6%)		
		HOMO-1 → LUMO+1 (22%)		
		HOMO → LUMO+2 (60%)		
	S_5	HOMO-3 → LUMO (5%)	328.65 (3.77)	0.0462
		HOMO-2 → LUMO (82%)		
		HOMO-1 → LUMO (3%)		
		HOMO-1 → LUMO+1 (2%)		
		HOMO → LUMO+2 (3%)		
	S_6	HOMO-3 → LUMO (90%)	325.05 (3.81)	0.0544
		HOMO-2 → LUMO (3%)		
	S_7	HOMO-5 → LUMO+1 (4%)	320.18 (3.87)	0.0231
		HOMO-1 → LUMO+1 (60%)		
		HOMO → LUMO+2 (18%)		
		HOMO → LUMO+3 (10%)		
	S_8	HOMO-5 → LUMO (23%)	315.99 (3.92)	0.0098
		HOMO-4 → LUMO (75%)		
	S_9	HOMO-7 → LUMO (3%)	310.13 (4.00)	0.0154
		HOMO-5 → LUMO (20%)		
		HOMO-5 → LUMO+1 (7%)		
		HOMO-4 → LUMO (5%)		
		HOMO-4 → LUMO+1 (2%)		
		HOMO-2 → LUMO+1 (3%)		
		HOMO-1 → LUMO+1 (9%)		
		HOMO → LUMO+3 (42%)		
		HOMO → LUMO+4 (2%)		
	S_{10}	HOMO-3 → LUMO+1 (68%)	305.16 (4.06)	0.0034
		HOMO-2 → LUMO+1 (26%)		

Table 3.10 TD-DFT calculated electronic transition configurations for **3.4** along with their corresponding excitation energies and oscillator strengths.

Compound	Spin State	Transition Configuration	Excitation Energy (nm, eV)	Oscillator Strength
3.4	S_1	HOMO → LUMO (85%)	437.88 (2.83)	0.4208
		HOMO → LUMO+1 (13%)		
	S_2	HOMO → LUMO (13%)	393.27 (3.15)	0.3460
		HOMO → LUMO+1 (84%)		
	S_3	HOMO-1 → LUMO (77%)	350.57 (3.54)	0.723
		HOMO-1 → LUMO+1 (21%)		
	S_4	HOMO-2 → LUMO (78%)	337.58 (3.67)	0.0042
		HOMO-2 → LUMO+1 (16%)		
	S_5	HOMO-5 → LUMO (11%)	331.93 (3.74)	0.0047
		HOMO-5 → LUMO+1 (4%)		
		HOMO-3 → LUMO (24%)		
		HOMO-3 → LUMO+1 (3%)		
		HOMO → LUMO+2 (50%)		
	S_6	HOMO-5 → LUMO (9%)	330.78 (3.75)	0.0345
		HOMO-3 → LUMO (51%)		
		HOMO-3 → LUMO+1 (14%)		
		HOMO → LUMO+2 (20%)		
	S_7	HOMO-4 → LUMO (79%)	325.70 (3.81)	0.0104
		HOMO-4 → LUMO+1 (18%)		
	S_8	HOMO-1 → LUMO (21%)	303.38 (4.09)	0.0079
		HOMO-1 → LUMO+1 (75%)		
	S_9	HOMO-6 → LUMO (5%)	302.05 (4.10)	0.0703
		HOMO-6 → LUMO+1 (2%)		
		HOMO-5 → LUMO (20%)		
		HOMO-3 → LUMO+1 (4%)		
		HOMO-2 → LUMO (6%)		
		HOMO-2 → LUMO+1 (23%)		
		HOMO → LUMO+2 (9%)		
		HOMO → LUMO+3 (23%)		
	S_{10}	HOMO-5 → LUMO (38%)	299.08 (4.15)	0.0984
		HOMO-5 → LUMO+1 (13%)		
		HOMO-2 → LUMO (5%)		
		HOMO-2 → LUMO+1 (35%)		
		HOMO → LUMO+2 (3%)		

Table 3.11 The major contributing orbitals to the calculated transitions of **3.1** (iso = 0.03).

LUMO+2	LUMO+1	LUMO	HOMO
HOMO-1	HOMO-2	HOMO-3	HOMO-4
HOMO-5			

HOMO and LUMO diagrams for 1-no B
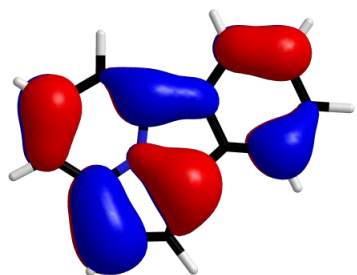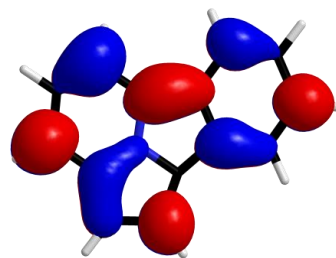
HOMO   **(-5.41 eV)**   **LUMO (-1.70 eV)**

Table 3.12 The major contributing orbitals to the calculated transitions of **3.2** (iso = 0.03).

LUMO+2	LUMO+1	LUMO	HOMO
HOMO-1	HOMO-2	HOMO-3	HOMO-4
HOMO-5			
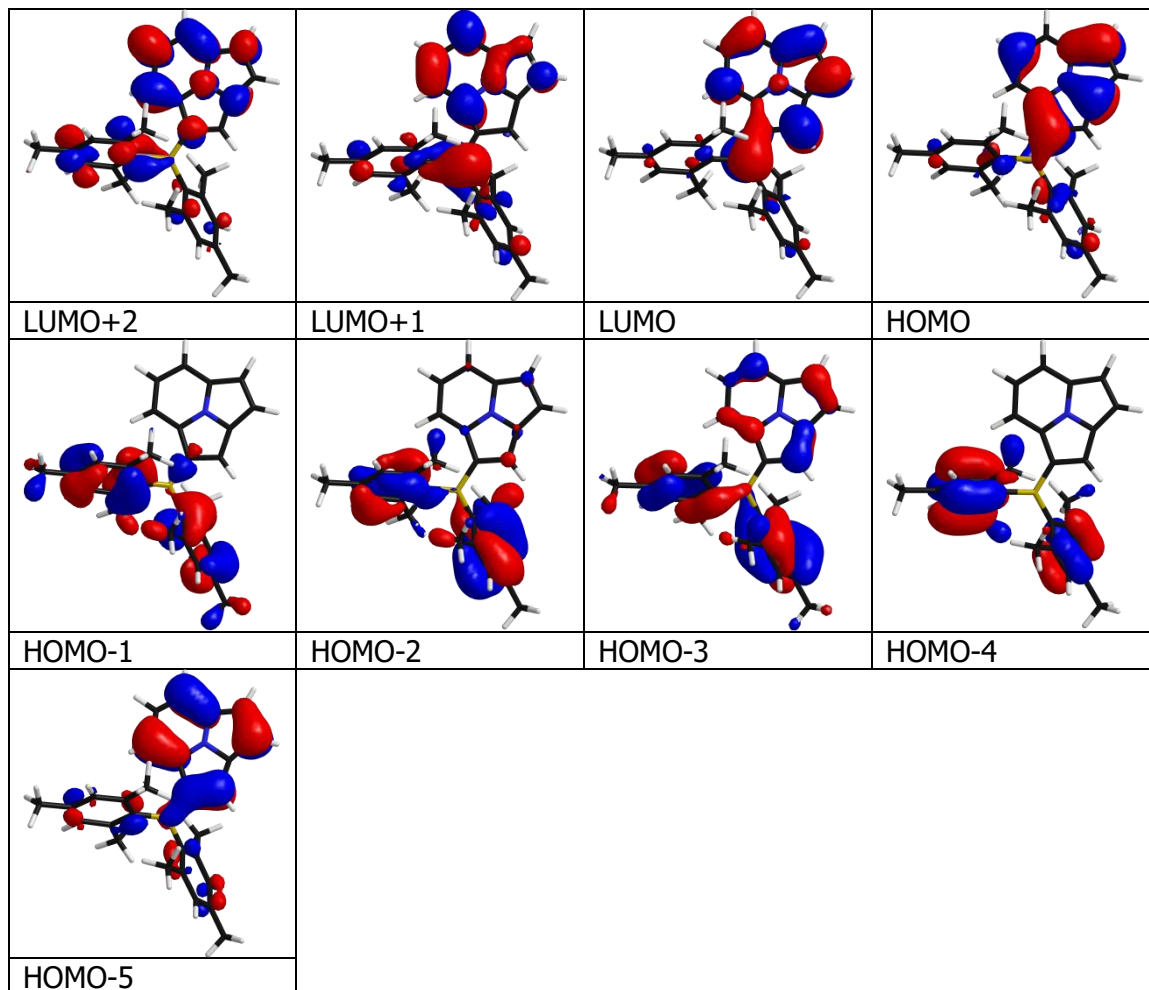
Table 3.13 The major contributing orbitals to the calculated transitions of **3.3** (iso = 0.03).

LUMO+4	LUMO+3	LUMO+2	LUMO+1
LUMO	HOMO	HOMO-1	HOMO-2
HOMO-3	HOMO-4	HOMO-5	HOMO-6
HOMO-7			
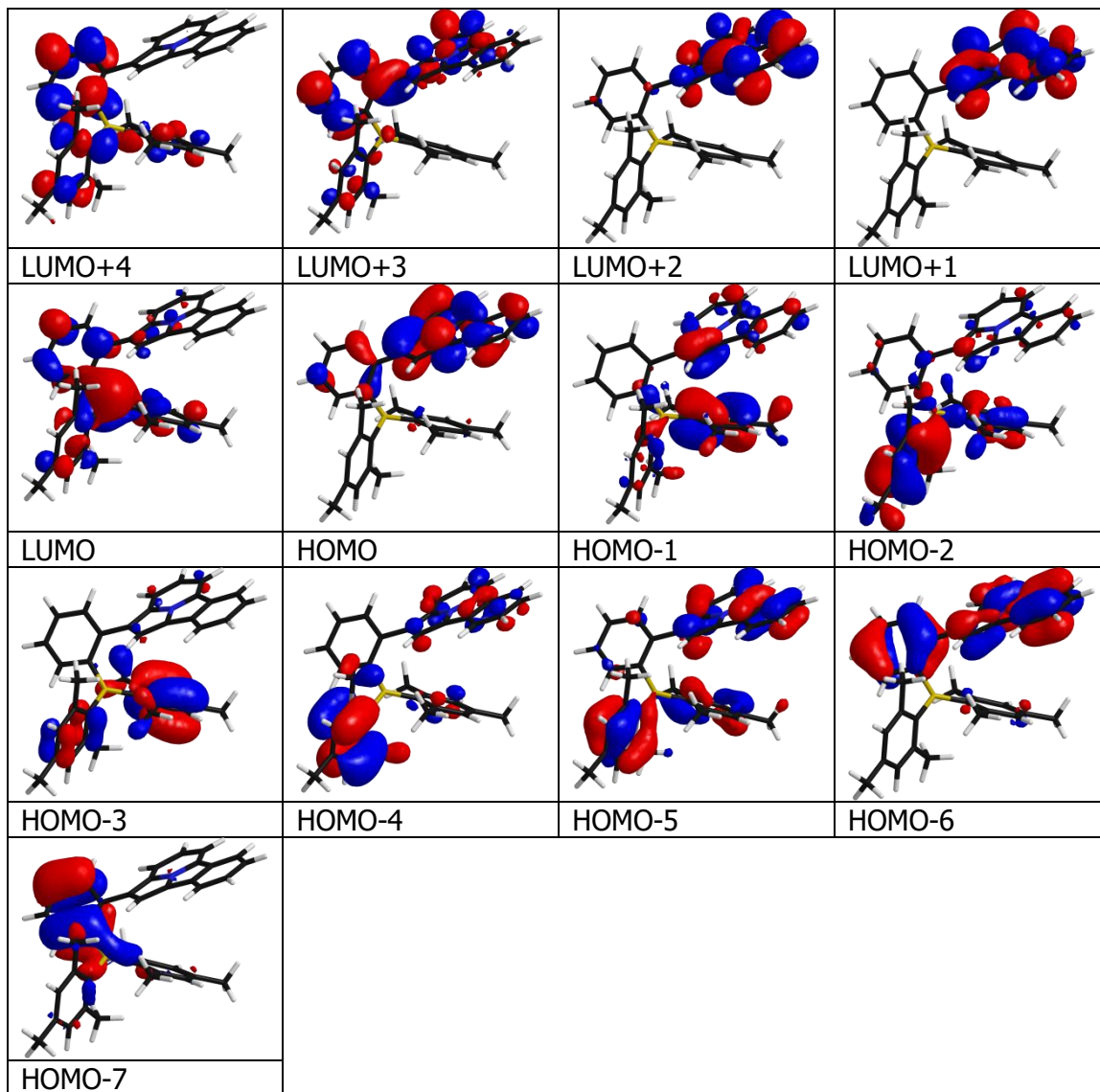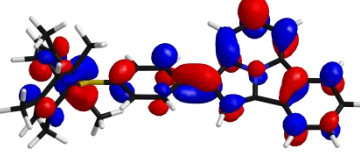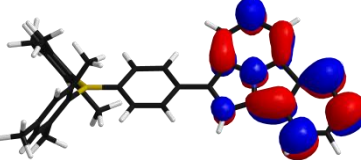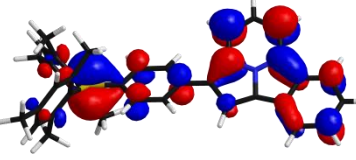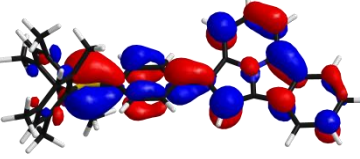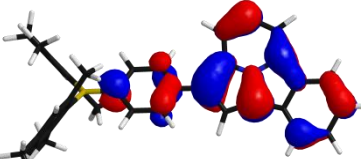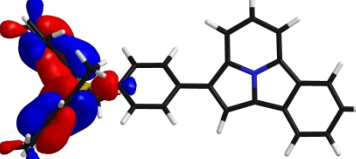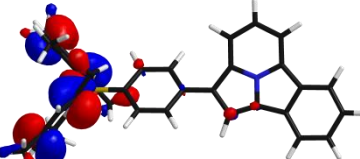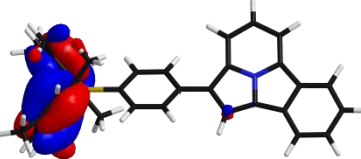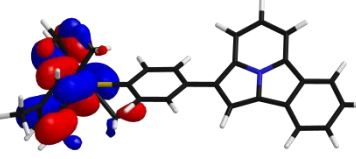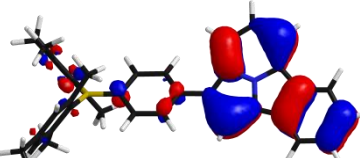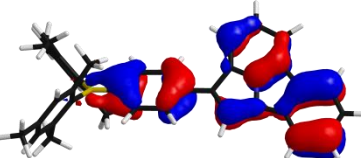
Table 3.14 The major contributing orbitals to the calculated transitions of **3.4** (iso = 0.03).

LUMO+3	**LUMO+2**	**LUMO+1**
LUMO	**HOMO**	**HOMO-1**
HOMO-2	**HOMO-3**	**HOMO-4**
HOMO-5	**HOMO-6**	

Figure 3.16 Predicted UV/Vis spectrum of **3.1** (first 10 excited states); B3LYP/6-311+g(d,p).
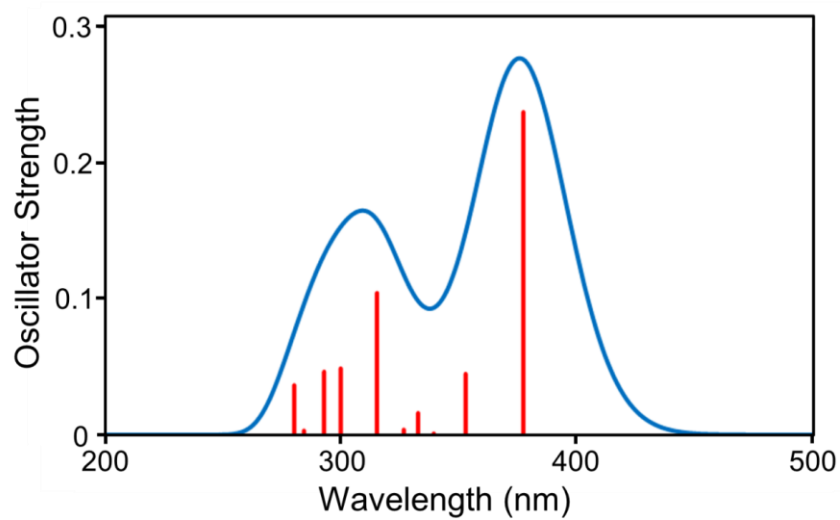
Figure 3.17 Predicted UV/Vis spectrum of **3.2** (first 10 excited states); B3LYP/6-311+g(d,p).
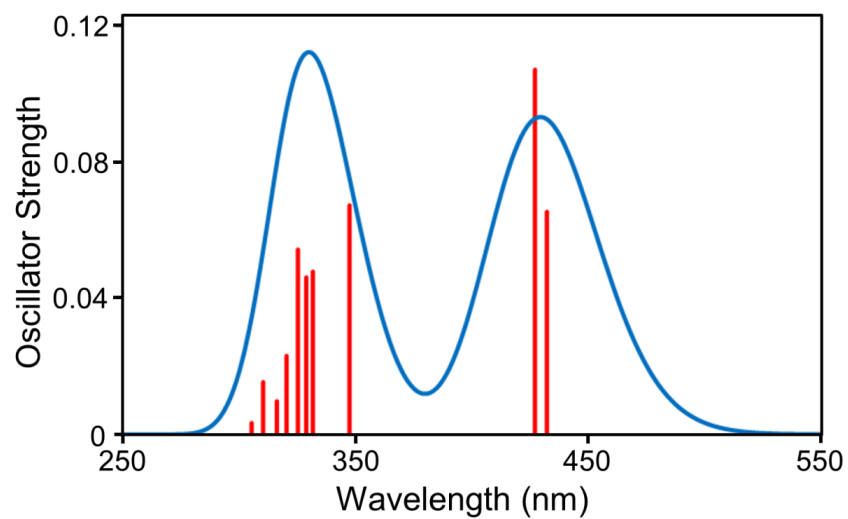
Figure 3.18 Predicted UV/Vis spectrum of **3.3** (first 10 excited states); B3LYP/6-311+g(d,p).
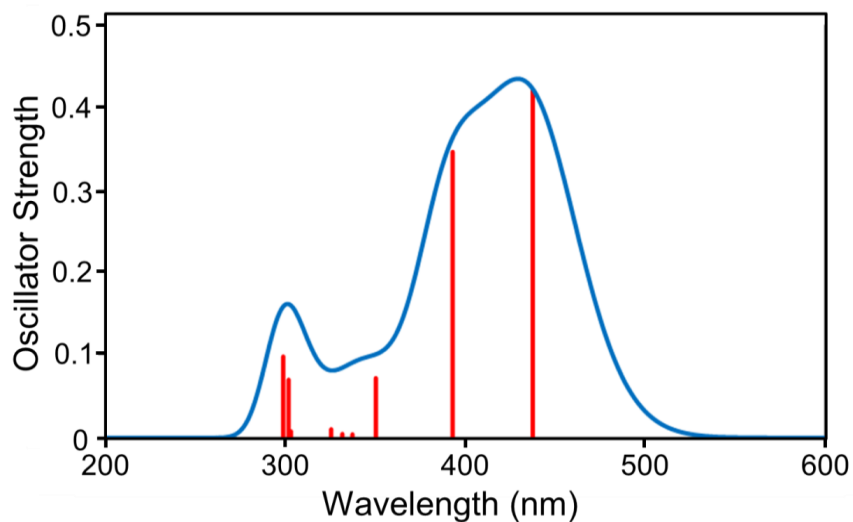
Figure 3.19 Predicted UV/Vis spectrum of **3.4** (first 10 excited states); B3LYP/6-311+g(d,p).

117

3.5.2 Selected Supporting Information
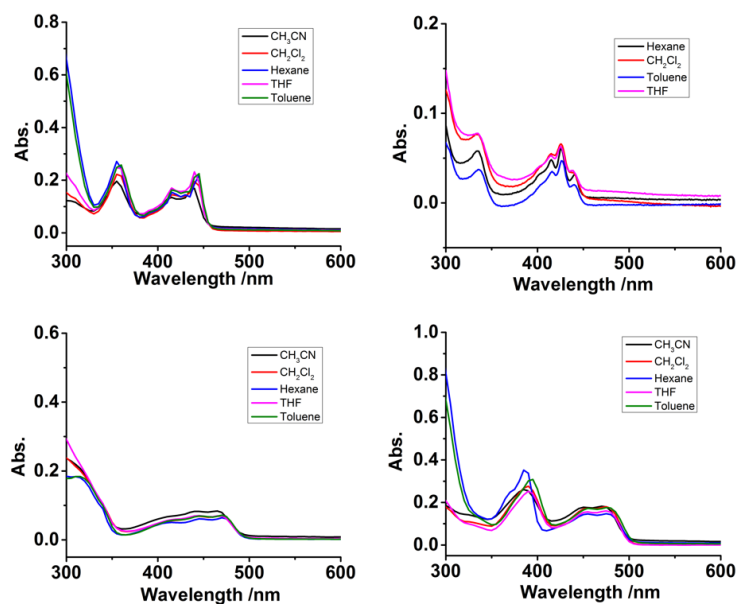
Figure 3.20 UV-vis spectra of compounds **3.1**-**3.4** in different solvents (c= 1×10^{-5} mol/L) (Top-left: **3.1**. Top-right: **3.2**. Bottom-left: **3.3**. Bottom-right: **3.4**).
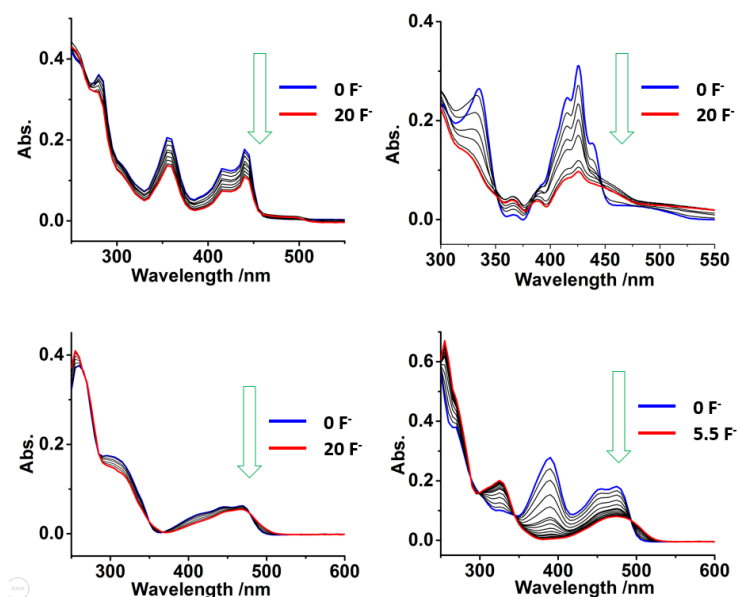
Figure 3.21 The UV-Vis absorption titration of **3.1** – **3.4** (1×10^{-5} M) by TBAF in CH_2Cl_2 at 298 K (Top-left: **3.1**. Top-right: **3.2**. Bottom-left: **3.3**. Bottom-right: **3.4**).
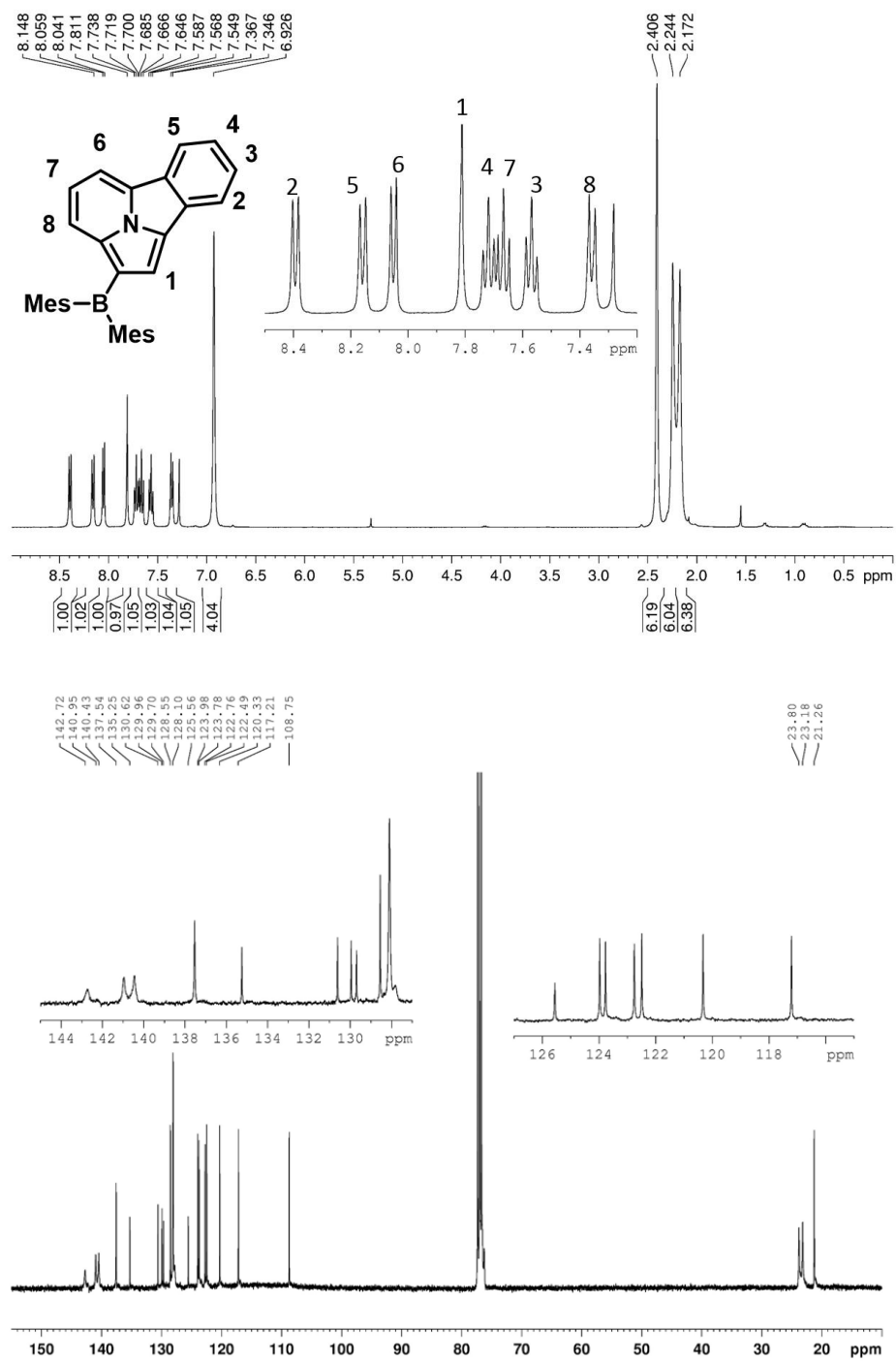
Figure 3.22 ^{1}H and ^{13}C NMR Spectra of Compound **3.1** in CDCl$_3$.

119
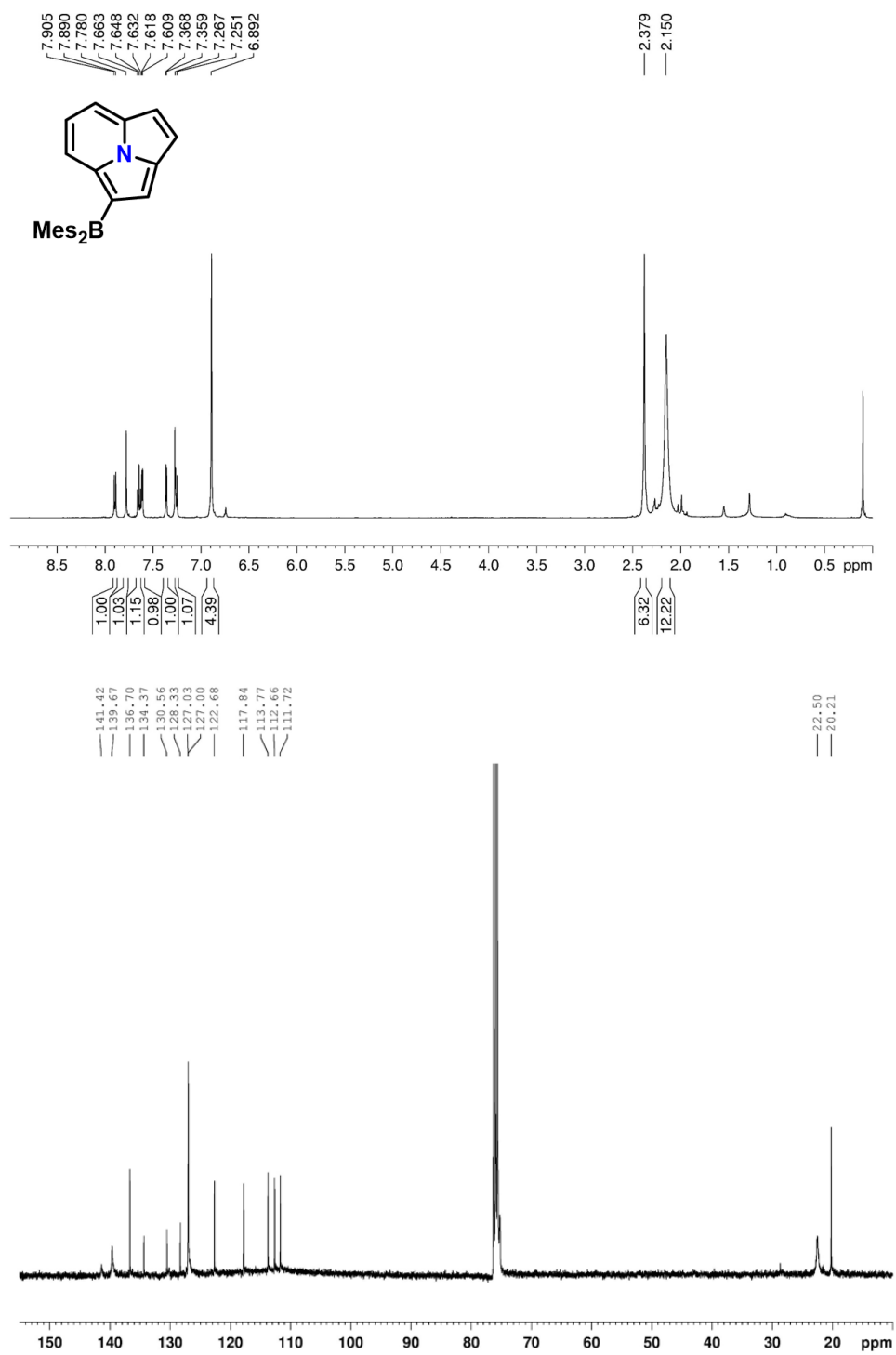
Figure 3.23 ^{1}H and ^{13}C NMR Spectra of Compound **3.2** in CDCl$_3$.
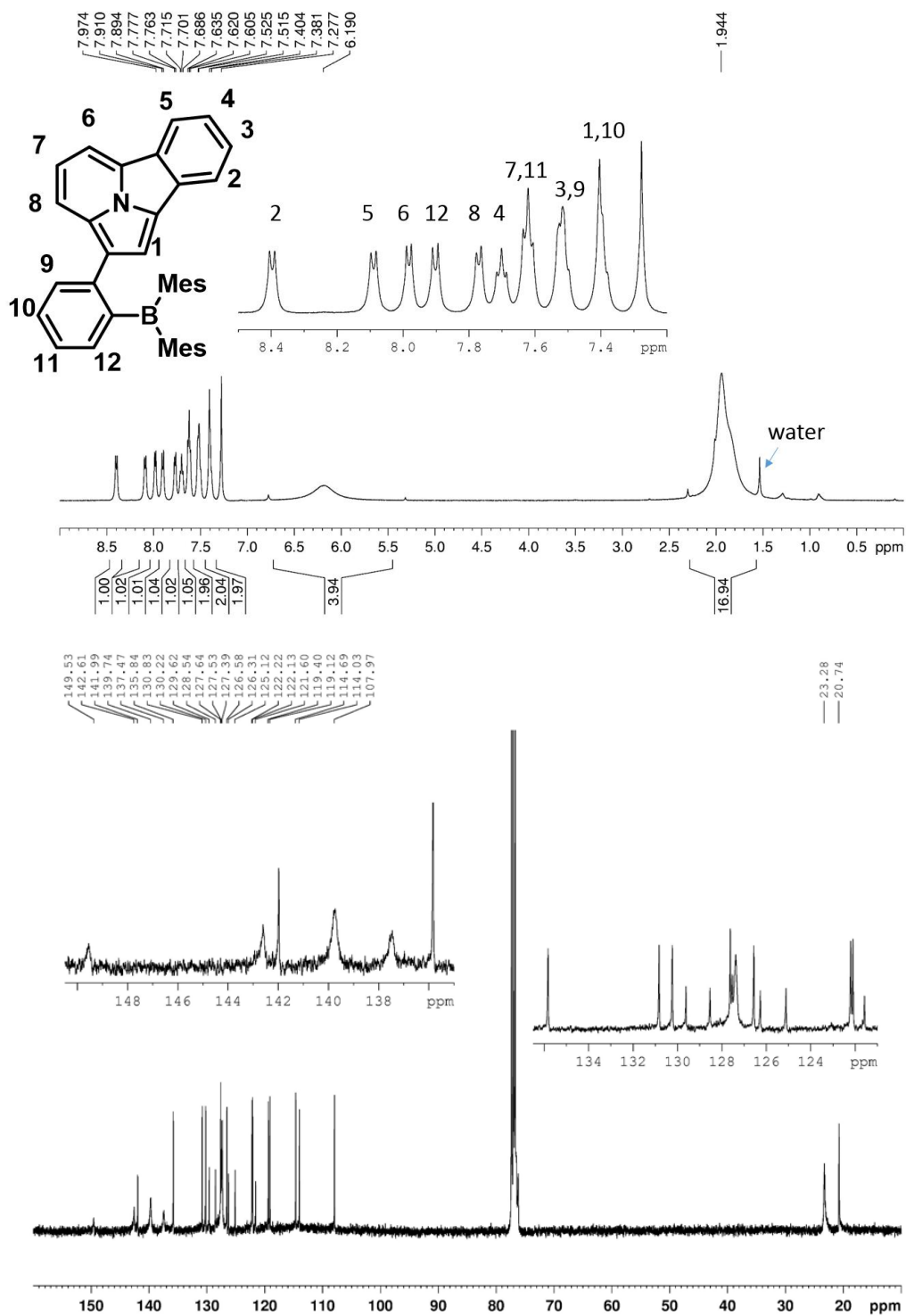
Figure 3.24 ^{1}H and ^{13}C NMR Spectra of Compound **3.3** in CDCl$_3$.
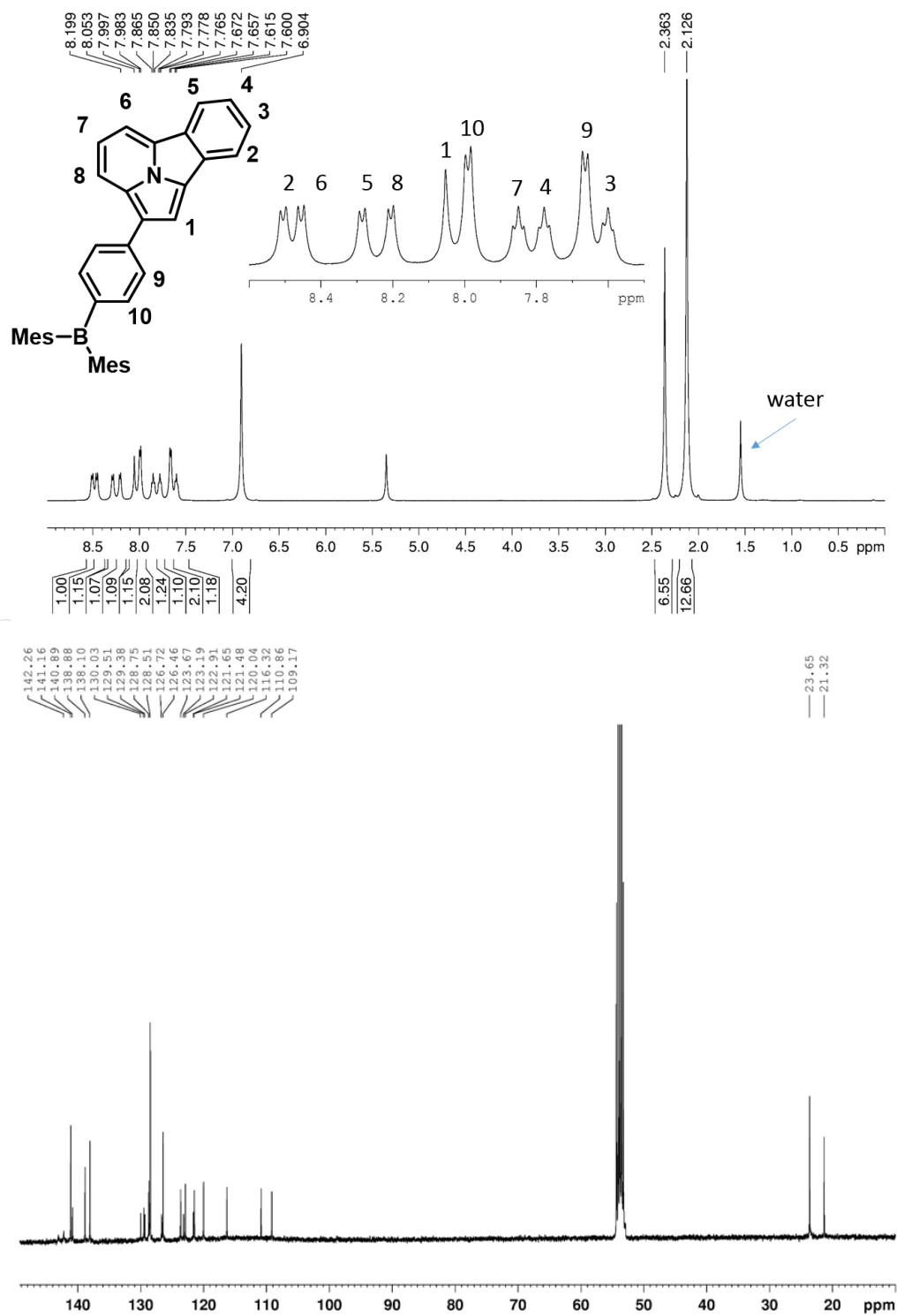
Figure 3.25 ^{1}H and ^{13}C NMR Spectra of Compound **3.4** in CD_2Cl_2.

3.6 Notes and References

The work described in this chapter includes contributions from the following publications:

- Yang, D.-T.; Radtke, J.; Mellerup, S. K.; Yuan, K.; Wang, X.; Wagner, M.; Wang, S. * *Org. Lett.* **2015**, *17*, 2486.

References:

(1) (a) Anthony, J. E. *Chem. Rev.* **2006**, *106*, 5028. (b) Tao, Y.; Yang, C.; Qin, J. *Chem. Soc. Rev.* **2011**, *40*, 2943. (c) Miteva, T.; Meisel, A.; Knoll, W.; Nothofer, H.G.; Scherf, U.; Muller, D.C.; Meerholz, K.; Yasuda, A.; Neher, D. *Adv. Mater.* **2001**, *13*, 565. (d) Burroughes, J. H.; Bradley, D.D.C.; Brown, A.R.; Marks, R.N.; Mackay, K.; Friend, R. H.; Burns, P.L.; Holmes, A.B. *Nature*, **1990**, *347*, 539. (e) He, G.; Pfeiffer, M.; Leo, K.; Hofmann, M.; Birnstock, J.; Pudzich, R.; Salbeck, J. *Appl. Phys. Lett.* **2004**, *85*, 3911.

(2) (a) Wang, C.; Dong, H.; Hu, W.; Liu, Y.; Zhu, D. *Chem. Rev.* **2012**, *112*, 2208. (b) Wu, W.; Liu, Y. Zhu, D. *Chem. Soc. Rev.* **2010**, *39*, 1489. (c) Mas-Torrent, M.; Rovira, C. *Chem. Soc. Rev.* **2008**, *37*, 827. (d) Zaumseil, J.; Sirringhaus, H. *Chem. Rev.* **2007**, *107*, 1296. (e) Coropceanu, V.; Cornil, J.; da Silva Filho, D. A.; Olivier, Y.; Silbey, R.; Brédas, J.-L. *Chem. Rev.* **2007**, *107*, 926. (f) Arias, A. C.; MacKenzie, J. D.; McCulloch, I.; Rivnay, J.; Salleo, A. *Chem. Rev.* **2010**, *110*, 3.

(3) (a) Thomas III, S. W.; Joly, G. D.; Swager, T. M. *Chem. Rev.* **2007**, *107*, 1339. (b) Chen, X.; Pradhan, T.; Wang, F.; Kim, J. S.; Yoon, J. *Chem. Rev.* **2012**, *112*, 1910. (c) Peng, H.; Chen, W.; Cheng, Y.; Hakuna, L.; Strongin, R.; Wang, B. *Sensors* **2012**, *12*, 15907. (d) Kim, J. S.; Quang, D. T. *Chem. Rev.* **2007**, *107*, 3780. (e) Carter, K. P.; Young, A. M.; Palmer, A. E. *Chem. Rev.* **2014**, *114*, 4564.

(4) (a) Mitsumori, T.; Bendikov, M.; Dautel, O.; Wudl, F.; Shioya, T.; Sato, H.; Sato, Y. *J. Am. Chem. Soc.* **2004**, *126*, 16793. (b) Hu, H.; Li, G.; Hu, W.; Liu, Y.; Wang, X.; Kan, Y.; Ji, M. *Org. Lett.* **2015**, *17*, 1114. (c) Matsuda, Y.; Gotou, H.; Katou, K.; Matsumoto, H.; Yamashita, M.; Takahashi, K.; Ide, S. *Heterocycles*, **1990**, *31*, 983. (d) Liu, Y.; Hu, H.-Y.; Zhang, Y.; Hu, H.-W.; Xu, J.-H. *Org. Biomol. Chem.* **2010**, *8*, 4921. (e) Tominaga, Y.; Shiroshita, Y.; Hosomi, A. *Heterocycles* **1988**, *27*, 2251.

(5) (a) Hudson, Z. M.; Wang, S. *Acc. Chem. Res.* **2009**, 42, 1584. (b) Jäkle, F. *Chem. Rev.* **2010**, *110*, 3985. (c) Bissinger, P.; Steffen, A.; Vargas, A.; Dewhurst, R.D.; Damme, A.; Braunschweig, H. *Angew. Chem. Int. Ed.* **2015**, *54*, 4362. (d) Marwitz, A.J.V.; Jenkins, J.T.; Zakharov, L.N.; Liu, S.Y. *Angew. Chem. Int. Ed.* **2010**, *49*, 7444. (e) Matsuo, K.; Saito, S.; Yamaguchi, S. *J. Am. Chem. Soc.* **2014**, *136*, 12580. (f) Kushida, T.; Camacho, C.; Shuto, A.; Irle, S.; Muramatsu, M.; Katayama, T.; Ito, S.; Nagasawa, Y.; Miyasaka, H.; Sakuda, E.; Kitamura, N.; Zhou, Z.; Wakamiya, A.; Yamaguchi, S. *Chem. Sci.* **2014**, *5*, 1296. (g) Entwistle, C. D.; Marder, T. B. *Angew. Chem. Int. Ed*. **2002**, 41, 2927. (h) Entwistle, C. D.; Marder, T. B. *Chem. Mater.* **2004**, 16, 4574. (i) Ji, L.; Edkins, R. M.; Sewell, L. J.; Beeby, A.; Batsanov, A. S.; Fucke, K.; Drafz, M.; Howard, J. A. K.; Moutounet, O.; Ibersiene, F.; Boucekkine, A.; Furet, E.; Liu, Z.; Halet, J.-F.; Katan, C.; Marder, T. B. *Chem. Eur. J.* **2014**, 20, 13618. (j) Yin, X.; Chen, J.; Lalancette, R. A.; Marder, T. B.; Jäkle, F.; *Angew. Chem. Int. Ed.* **2014**, 53, 9761. (k) Zhang, Z.; Edkins, R. M.; Nitsch, J.; Fucke, K.; Eichhorn, A.; Steffen, A.; Wang, Y.; Marder, T. B. *Chem. Eur. J.* **2015**, 21, 177.

(6) (a) Wade, C. R.; Broomsgrove, A. E. J.; Aldridge, S.; Gabbaï, F. P. *Chem. Rev.* **2010**, *110*, 3958. (b) Zhao, H.; Leamer, L. A.; Gabbaï, F. P. *Dalton Trans.* **2013**, *42*, 8164. (c) Bresner,

C.; Haynes, C.J. E.; Addy, D. A.; Broomsgrove, A. E. J.; Fitzpatrick, P.; Vidovic, D.; Thompson, A. L.; Fallisb, I. A.; Aldridge, S. *New J. Chem.* **2010**, *34*, 1652.

(7) Yang, D.-T.; Mellerup, S. K.; Wang, X.; Lu, J.-S.; Wang, S. *Angew. Chem. Int. Ed.* **2015,** 54, 5498.

(8) Frisch, M. J.; Trucks, G. W.; Schlegel, H. B.; Scuseria, G. E.; Robb, M. A.; Cheeseman, J. R.; Scalmani, G.; Barone, V.; Mennucci, B.; Petersson, G. A. H.; Nakatsuji, M.; Caricato, X.; Li, H. P. F.; Hratchian, A.; Izmaylov, J.; Bloino, G.; Zheng, J. L.; Sonnenberg, M.; Hada, M.; Ehara, K.; Toyota, R.; Fukuda, J.; Hasegawa, M.; Ishida, T.; Nakajima, Y.; Honda, O.; Kitao, H.; Nakai, T.; Vreven, J. A.; Montgomery Jr., J. E.; Peralta, F.; Ogliaro, M.; Bearpark, J. J.; Heyd, E.; Brothers, K. N.; Kudin, V. N.; Staroverov, T.; Keith, R.; Kobayashi, J.; Normand, K.; Raghavachari, A.; Rendell, J. C.; Burant, S. S.; Iyengar, J.; Tomasi, M.; Cossi, N.; Rega, J. M.; Millam, M.; Klene, J. E.; Knox, J. B.; Cross, V.; Bakken, C.; Adamo, J.; Jaramillo, R.; Gomperts, R. E.; Stratmann, O.; Yazyev, A. J.; Austin, R.; Cammi, C.; Pomelli, J. W.; Ochterski, R. L.; Martin, K.; Morokuma, V. G.; Zakrzewski, G. A.; Voth, P.; Salvador, J. J.; Dannenberg, S.; Dapprich, A. D.; Daniels, O.; Farkas, J. B.; Foresman, J. V.; Ortiz, J.; Cioslowski, J.; Fox, D. J. Gaussian 09, revision C.01; Gaussian, Inc.: Wallingford, CT, 2010.

(9) (a) Becke, A. D. *Phys. Rev. A* **1988**, *38*, 3098. (b) Becke, A. D. *J. Chem. Phys*. **1993**, *98*, 1372. (c) Lee, C.; Yang, W.; Par, R. G. *Phys. Rev. B* **1988**, *37*, 785.

(10) (a) Ditchfield, R.; Hehre, W. J.; Pople, J. A. *J. Chem. Phys*. **1971**, *54*, 724. (b) McLean, A. D.; Chandler, G. S. *J. Chem. Phys*. **1980**, *72*, 5639.

(11) (a) Kajigaeshi, S.; Mori, S.; Fujisaki, S.; Kanemasa, S. *Bull. Chem. Soc. Jpn.* **1985**, *58*, 3547. (b) Bertermann, R.; Braunschweig, H.; Brown, C. K. L.; Damme, A.; Dewhurst, R.

D.; Hörl, C.; Kramer, T. Krummenacher, I.; Pfaffinger, B.; Radacki, K. *Chem. Commun.* **2014**, *50*, 97. (c) Fukazawa, A.; Yamada, H.; Yamaguchi S. *Angew. Chem. Int. Ed.* **2008**, *47*, 5582. (d) An, Z.; Odom, S. A.; Kelley, R. F.; Huang, C.; Zhang, X.; Barlow, S.; Padilha, L. A.; Fu, J.; Webster, S.; Hagan, D. J.; Van Stryland, E. W.; Wasielewski, M. R.; Marder, S. R. *J. Phys. Chem. A* **2009**, *113*, 5585.

(12) Li, X.; Li, C.; Yin, B.; Li, C.; Liu, P.; Li, J.; Shi, Z. *Chem. Asian J.* **2013**, *8*, 1408, and references therein.

(13) (a) Caramella, P.; Houk, K.N. *J. Am. Chem. Soc.* **1976**, *98*, 6397. (b) Caramella, P.; Gandour, R.W.; Hall, J.A.; Deville, C.G.; Houk, K.N. *J. Am. Chem. Soc.* **1977**, *99*, 385.

(14) Zhao, S. B.; Wucher, S. B.; Hudson, Z. M.; McCormick, T. M.; Liu, X. Y.; Wang, S.; Feng, X. D.; Lu, Z. H., *Organometallics*, **2008**, *27*, 6446.

Chapter 4

Investigation of Poly-BN-Arenes and Electroluminescent Devices

4.1 Introduction

The incorporation of BN units into arenes has attracted growing attention[1] due to the unique optical and electronic properties of the resulting BN-arenes which have a number of potential applications such as optoelectronic materials[2] and sensors.[3] Particularly, replacing a C−C unit by a BN unit in conjugated systems can lead to a lower LUMO energy and improved electron affinity, which enhances electron transport.[4,5] Following the pioneering work of Dewar and co-workers more than 50 years ago,[6] many entries in this class of compounds have been shown to display unique photophysical and/or electronic properties, and several BN-arenes have been shown to be highly effective and often superior, compared to their all carbon analogues, as components in devices such as organic field-effect transistors (OFETs) and OLEDs.[2, 7] These recent findings have inspired intense research efforts in the development of new synthetic methodologies for BN-arenes, leading to an increasing number of diverse examples appearing throughout the literature.[1-8] Despite these successes, however, the practical implementation of such species has proven to be quite challenging owing to various issues associated with extended π-conjugated materials such as stability and processability. Furthermore, many interesting and rare BN-arene compounds are not accessible by conventional synthetic approaches.

We recently succeeded synthesizing a number of BN-phenanthrenes (**4.1a** in Figure 4.1 and derivatives) *via* photolytic or thermal elimination reactions[8] of benzylpyridyl BR$_2$ chelate compounds (BN-heterocycles, for example, **4.1**), in addition, the BN-heterocyclic precursor compounds are important and interesting in their own right because a number of closely related

compounds have been demonstrated to be good electron acceptors in devices such as organic photovoltaics (OPV).[4,5] Therefore, we envisioned that it may be possible to study new BN-heterocycles **4.2** – **4.7** (Figure 4.1) that contain two BN units and investigated their thermal and phototransformations. The aim of this work is to determine the influence of the location and the number of BN units within the heterocyclic skeleton on the electronic structures and the photophysical/photochemical properties of this class of compounds as well as their applications in electroluminescent (EL) devices.
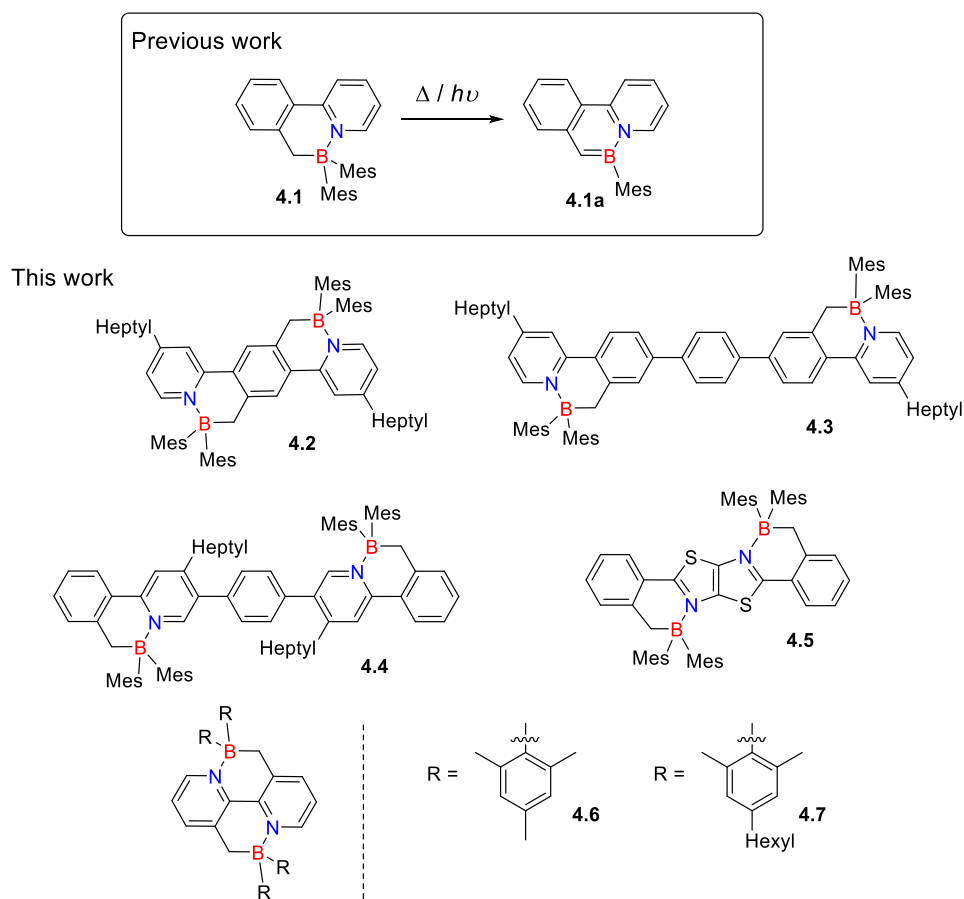
Figure 4.1 Examples of BN-heterocycles investigated for elimination reactions.

4.2 Experimental

4.2.1 General procedure

Experimental techniques for synthesis, the uses of instrumentation are as described in Chapter 2.2.1. Cyclic voltammetry experiments were conducted on a BAS CV-50W analyzer with a scan rate of 100 mVs^{-1}. Thermogravimetric analysis (TGA) was performed on a SHIMADZU TGA-50 apparatus. Melting points (m. p.) were measured on a Yanaco Micro Melting Point Apparatus. The fluorescent quantum efficiency of **4.7a** was determined using Ir(ppy)$_3$ as a standard in THF under nitrogen.[9] The crystal structure of **4.6** was collected on a synchrotron X-ray diffraction facility in Japan.

4.2.2 Synthetic Procedure

4.2.2.1 Synthesis of **4.2**
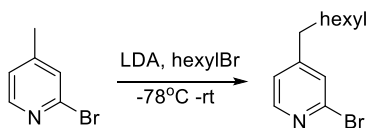
Synthesis of 2-bromo-4-heptylpyridine: 2-Bromo-4-methylpyridine (1.0 g, 5.8 mmol) and dry THF (40 ml) were cooled to -78°C. Corresponding to this solution, lithium diisopropylamide (LDA, 8.8 mmol) was added dropwise using a syringe. The mixture was then stirred for 1.5 hours at -78°C. To this mixture, 1-bromohexane (hexylBr, 1.95g, 6.4 mmol) was slowly added. Then the reaction was warmed up to room temperature and stirred overnight. Water was added and the mixture was extracted with ethyl acetate. The organic extract was purified by column chromatography on silica gel to afford the product (1.18 g, 4.64 mmol, 80% yield) as a light-yellow oil. ^{1}H NMR (400 MHz, CDCl$_3$) δ 8.13 (d, J = 5.1 Hz, 1H), 7.21 (s, 1H), 6.97 (d, J = 5.0 Hz, 1H), 2.51 – 2.43 (m, 2H), 1.52

(tt, J = 9.6, 7.8, 3.6 Hz, 3H), 1.28 – 1.16 (m, 11H), 0.78 (d, J = 7.3 Hz, 4H). ^{13}C NMR (101 MHz, CDCl$_3$) δ 154.92, 149.70, 142.29, 127.87, 123.03, 34.84, 31.62, 30.07, 29.02, 28.95, 22.55, 14.00.
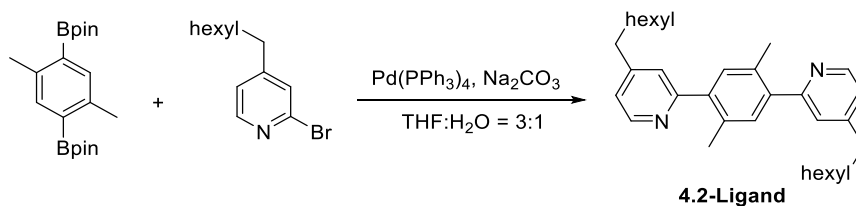
4.2-Ligand

*Synthesis of **4.2-Ligand**:* This compound was synthesized using a modified Suzuki coupling procedure. A mixture of THF (60 mL) and water (20 mL) was stirred and purged by nitrogen for 1 h. Diboron esters (2.1 g, 5.9 mmol), 2-bromo-4-heptylpyridine (3 g, 11.8 mmol), Pd(PPh$_3$)$_4$ (410 mg, 0.354 mmol), and Na$_2$CO$_3$ (3.7 g, 35.4 mmol) were added to the mixed solvents. The mixture was stirred and reflux for 24 hours. The organic solvents were removed under vacuum. The water layer was separated and extracted with CH$_2$Cl$_2$ (3 x 50 mL). The combined organic layers were washed by brine and dried over magnesium sulfate, and the solvents were evaporated under reduced pressure. Purification of the crude product by column chromatography afforded the product **4.2-Ligand** as a white solid in 45% yield (1.2 g). ^{1}H NMR (400 MHz, CDCl$_3$) δ 8.60 (d, *J* = 5.0 Hz, 2H), 7.36 (s, 2H), 7.26 (d, *J* = 1.6 Hz, 2H), 7.09 (dd, *J* = 5.1, 1.7 Hz, 2H), 2.68 (t, *J* = 7.7 Hz, 4H), 2.39 (s, 6H), 1.76 – 1.62 (m, 4H), 1.42 – 1.27 (m, 16H), 0.95 – 0.85 (m, 6H). ^{13}C NMR (101 MHz, CDCl$_3$) δ 159.57, 151.74, 149.10, 140.35, 132.99, 131.98, 124.35, 121.89, 35.38, 31.75, 30.40, 29.19, 29.08, 22.63, 19.78, 14.08. HR-ESIMS (m/z): [M+1]$^+$ calcd. for C$_{32}$H$_{45}$N$_2$: 457.35773; found: 457.35591.
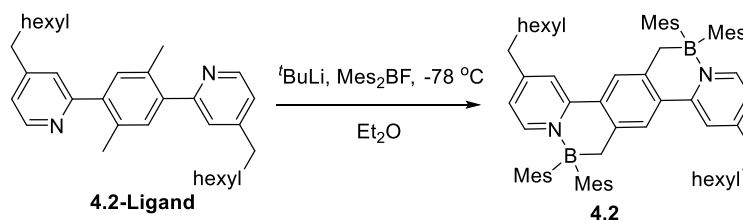
4.2-Ligand → **4.2**

Synthesis of 4.2: ^{t}BuLi (4.0 mL, 1.7 M in hexane, 6.78 mmol) was added to a solution of compound **4.2-Ligand** (700mg, 1.54 mmol) in Et$_2$O (25 mL) at −78 °C. After stirring at this temperature for 1 hr, the precooled boron reagent Mes$_2$BF (1.23g, 4.62mmol) in THF was added via cannula transfer with vigorous stirring at −78 °C. The mixture was stirred for another hour at −78 °C, then allowed to warm slowly to room temperature and stirred overnight. The solution was extracted with CH$_2$Cl$_2$ and water. The organic phase was dried over magnesium sulfate and filtered. The filtrate was purified by column chromatography on silica gel to afford product **4.2** (514 mg, 0.54 mmol, 35% yield) as a yellow solid. ^{1}H NMR (400 MHz, CD$_2$Cl$_2$) δ 8.38 (d, J = 6.2 Hz, 2H, py), 7.59 (s, 2H, py), 7.16−7.07 (m, 2H, py), 7.03 (s, 2H, benzene ring), 6.59 (s, 8H, Mes), 2.79 (t, J = 7.8 Hz, 4H, CH2), 2.69 (s, 4H, B-CH2), 2.16 (s, 12H, Me), 1.84 (m, 24H, Mes), 1.74 (br, 4H, CH2), 1.42−1.31 (m, 16H, CH2), 0.93 (t, J = 6.6 Hz, 6H, Me in heptyl). ^{13}C NMR (101 MHz, CD$_2$Cl$_2$) δ157.98, 154.95, 147.28, 142.89, 141.59, 133.18, 132.37, 129.55, 126.00, 123.45, 123.20, 35.32, 31.64, 29.77, 29.66, 29.05, 28.95, 24.56, 22.58, 20.28, 13.81. ^{11}B NMR (128 MHz, CD2Cl2) δ 2.6. HR-ESIMS (m/z): [M + 1]$^{+}$ calcd for C$_{68}$H$_{87}$B$_2$N$_2$: 953.70499; found: 953.70893.

4.2.2.2 Synthesis of **4.3**
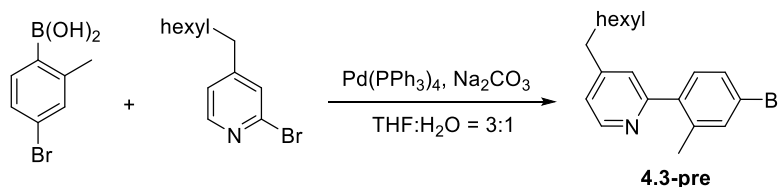
4.3-pre

*Synthesis of **4.3-pre***: A mixture of THF (40 mL) and water (14 mL) was stirred and purged with nitrogen for 1 h. Boronic acid (0.85 g, 4.0 mmol), 2-bromo-4-heptylpyridine (1 g, 3.9 mmol), Pd(PPh$_3$)$_4$ (140 mg, 0.118 mmol), and Na$_2$CO$_3$ (1.25 g, 11.7 mmol) were added to the mixed solvents. The mixture was stirred and reflux for 24 hours. The organic solvents were removed under vacuum. The water layer was separated and extracted with CH$_2$Cl$_2$ (3 x 40 mL). The combined organic layers were washed by brine and dried over magnesium sulfate, and the solvents were evaporated under reduced pressure. Purification of the crude product by column chromatography afforded the product **4.3-pre** as a colorless oil in 67% yield (900 mg, 2.6 mmol). ^{1}H NMR (400 MHz, CDCl$_3$) δ 8.58 (d, J = 5.1 Hz, 1H), 7.46 (d, J = 2.0 Hz, 1H), 7.44 – 7.38 (m, 1H), 7.31 (d, J = 8.1 Hz, 1H), 7.15 (d, J = 1.6 Hz, 1H), 7.06 (dd, J = 5.1, 1.7 Hz, 1H), 2.35 (s, 3H), 1.68 (ddd, J = 13.6, 10.4, 5.4 Hz, 2H), 1.58 (tdd, J = 14.0, 9.6, 5.0 Hz, 2H), 1.27 – 1.17 (m, 8H), 0.87 (t, J = 6.8 Hz, 3H). ^{13}C NMR (101 MHz, CDCl$_3$) δ 158.59, 155.80, 149.25, 139.72, 138.00, 133.37, 131.22, 128.89, 123.61, 122.07, 121.56, 45.73, 36.25, 31.70, 29.30, 27.44, 22.60, 20.18, 14.06.
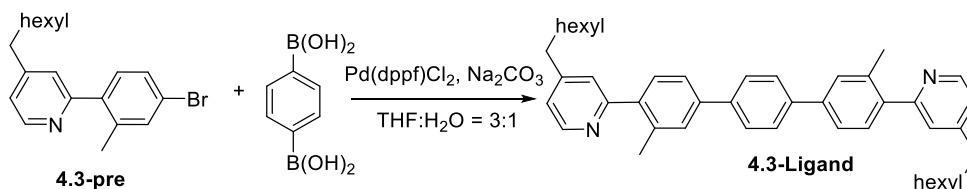
*Synthesis of **4.3-Ligand***: A mixture of THF (30 mL) and water (10 mL) was stirred and and purged by nitrogen for 1h. Boronic acid (204 mg, 1.23 mmol), compound **4.3-pre** (870 mg, 2.5 mmol), Pd(dppf)Cl$_2$ (18 mg, 0.024 mmol), and Na$_2$CO$_3$ (782 mg, 7.37 mmol) were added to the mixed solvents. The mixture was stirred and reflux for 24 hours. The organic solvents were removed under vacuum. The water layer was separated and extracted with CH$_2$Cl$_2$ (3 x 40 mL). The combined organic layers were washed by brine and dried over magnesium sulfate, and the solvents were evaporated under reduced pressure. Purification of the crude product by column

chromatography afforded the product **4.3-Ligand** as a colorless oil in 78% yield (590 mg, 0.97 mmol). ^{1}H NMR (400 MHz, CDCl$_3$) δ 8.65 (d, J = 5.1 Hz, 2H), 7.79 (d, J = 3.8 Hz, 4H), 7.68 – 7.57 (m, 6H), 7.29 (s, 2H), 7.09 (dd, J = 5.1, 1.5 Hz, 2H), 2.52 (s, 6H), 1.79 – 1.57 (m, 8H), 1.30 (d, J = 15.2 Hz, 16H), 0.91 (t, J = 6.7 Hz, 6H). ^{13}C NMR (101 MHz, CDCl$_3$) δ 159.40, 155.57, 149.24, 140.48, 139.91, 136.21, 130.29, 129.42, 127.53, 127.40, 124.57, 13.77, 121.38, 45.79, 36.34, 31.77, 29.37, 27.51, 22.66, 20.63, 14.12. HR-ESIMS (m/z): [M+1]$^+$ calcd. for C$_{44}$H$_{53}$N$_2$: 609.42033; found: 609.41839.
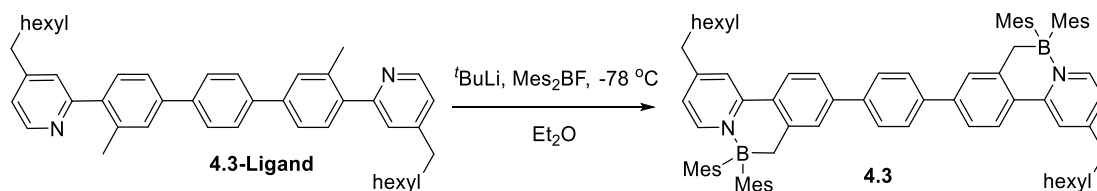
Synthesis of 4.3: The compound **4.3** was synthesized using the same synthetic protocol as for compound **4.2.** The mixture was recrystallized in ethyl acetate and hexanes to afford product **4.3** (632 mg, 0.57 mmol, 60% yield) as a yellow solid, which was confirmed by X-ray diffraction analysis. ^{1}H NMR (400 MHz, CD$_2$Cl$_2$) δ 8.44 (d, J = 6.2 Hz, 2H, py), 7.83 (d, J = 2.0 Hz, 2H, py), 7.69 (d, J = 8.1 Hz, 2H, ph), 7.56 (s, 4H, benzene linker), 7.36 (dd, J = 8.0, 1.9 Hz, 2H, ph), 7.17 (dd, J = 6.2,1.9 Hz, 2H, py), 7.09 (d, J = 1.9 Hz, 2H, ph), 6.60 (s, 8H, Mes), 2.83 (br, 8H, CH$_2$ and B-CH$_2$), 2.15 (s, 12H, Mes), 1.90 (s, 24H, Mes), 1.78 (br, 4H, CH$_2$), 1.44−1.32 (m, 16H, CH$_2$), 0.94 (t, J = 6.7 Hz, 6H, Me in heptyl). ^{13}C NMR (101 MHz, CD$_2$Cl$_2$) δ 158.19, 155.25, 148.36, 147.23, 142.27, 141.63, 139.66, 133.38, 129.78, 129.57, 127.18, 126.72, 126.48, 123.27, 123.18, 122.74, 35.42, 31.68, 30.41, 29.88, 29.04, 28.98, 24.62, 22.59, 20.27, 13.84. ^{11}B NMR (128 MHz, CD$_2$Cl$_2$) δ 1.6. HR-ESIMS (m/z): [M+1]$^+$ calcd. for C$_{80}$H$_{95}$B$_2$N$_2$: 1105.76759; found: 1105.77307.

4.2.2.3 Synthesis of **4.4**
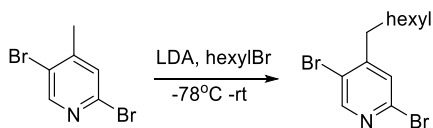
Synthesis of 2,5-dibromo-4-heptylpyridine: 2,5-Dibromo-4-methylpyridine (2.51 g, 10 mmol) and dry THF (40 mL) were cooled to -78 °C. Corresponding to this solution, lithium diisopropylamide (LDA, 7.5 mL, 2M, 15 mmol) was added dropwise using a syringe. The mixture was then stirred for 1.5 hours at -78°C. To this mixture, 1-bromohexane (hexylBr, 2.86 mL, 11 mmol) was slowly added. Then the reaction was warmed up to room temperature and stirred overnight. Water was added and the mixture was extracted with ethyl acetate. The filtrate was purified by column chromatography on silica gel to afford 2,5-dibromo-4-heptylpyridine (2.35 g, 7.0 mmol, 70% yield) as a light-yellow oil. ^{1}H NMR (499 MHz, CDCl$_3$) δ 8.41 (s, 1H), 7.34 (s, 1H), 2.72 – 2.63 (m, 2H), 1.62 (h, *J* = 6.6, 6.0 Hz, 2H), 1.41 – 1.22 (m, 8H), 0.90 (t, *J* = 6.8 Hz, 3H). ^{13}C NMR (125 MHz, CDCl$_3$) δ 153.84, 151.61, 140.70, 129.00, 122.38, 35.30, 31.67, 29.21, 28.96, 28.71, 22.62, 14.09.
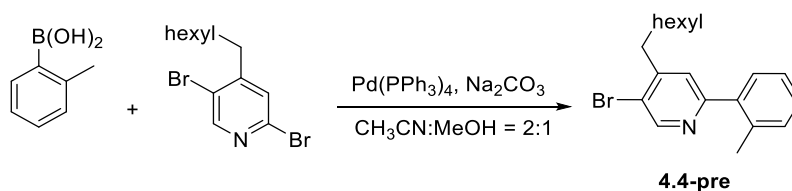
4.4-pre

*Synthesis of **4.4-pre**:* A mixture of CH$_3$CN (30 mL) and MeOH (15 mL) was stirred and purged with nitrogen for 1h. Boronic acid (830 mg, 6.1 mmol), 2,5-dibromo-4-heptylpyridine (1.85 g, 5.5 mmol), Pd(PPh$_3$)$_4$ (320 mg, 0.28 mmol), and Na$_2$CO$_3$ (2.3 g, 16.7 mmol) were added to the mixed solvents. The mixture was stirred and reflux for 24 hours. The organic solvents were removed under vacuum. The water layer was separated and extracted with CH$_2$Cl$_2$ (3 x 40 mL). The combined organic layers were washed by brine and dried over magnesium sulfate, and the solvents were evaporated under reduced pressure. Purification of the crude product by column chromatography

134

afforded the product **4.4-pre** as a colorless oil in 62% yield (1.18 g, 3.41 mmol). ^{1}H NMR (499

MHz, CDCl$_3$) δ 8.76 (s, 1H), 7.43 (d, J = 7.3 Hz, 1H), 7.37 – 7.28 (m, 4H), 2.80 (t, J = 7.9 Hz, 2H),

2.42 (s, 3H), 1.72 (d, J = 7.4 Hz, 2H), 1.49 – 1.33 (m, 8H), 0.95 (t, J = 6.8 Hz, 3H). ^{13}C NMR (125

MHz, CDCl$_3$) δ 158.80, 151.09, 150.77, 139.46, 135.76, 130.87, 129.53, 128.48, 125.96, 125.52,

121.35, 35.56, 31.80, 29.34, 29.11, 29.00, 22.70, 20.39, 14.16.
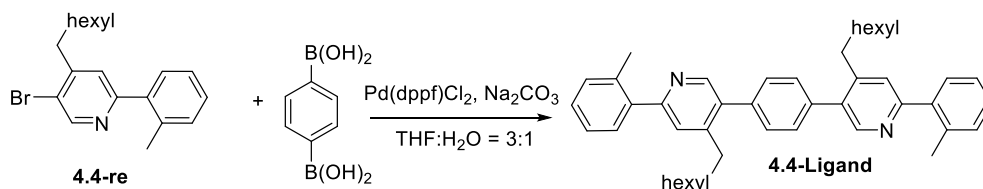
*Synthesis of **4.4-Ligand***: Compound **4.4-Ligand** was synthesized using the same procedure of

synthesis of compound **4.3-Ligand** as a colorless oil in 60% yield (600 mg, 0.99 mmol). ^{1}H NMR

(499 MHz, CDCl$_3$) δ 8.61 (s, 2H), 7.52 (m, 6H), 7.40 (s, 2H), 7.34 (p, J = 3.7 Hz, 6H), 2.79 – 2.70

(m, 4H), 2.48 (s, 6H), 1.61 (td, J = 7.9, 3.9 Hz, 4H), 1.32 – 1.23 (m, 16H), 0.88 (t, J = 6.8 Hz, 6H).

^{13}C NMR (125 MHz, CDCl$_3$) δ 158.88, 149.67, 149.24, 140.43, 137.33, 135.84, 135.08, 130.78,

129.69, 129.53, 128.23, 125.90, 124.34, 32.58, 31.68, 30.36, 29.34, 28.96, 22.61, 20.45, 14.09.

HR-ESIMS (m/z): [M+1]$^+$ calcd. for C$_{44}$H$_{53}$N$_2$: 609.42033; found: 609.41840.
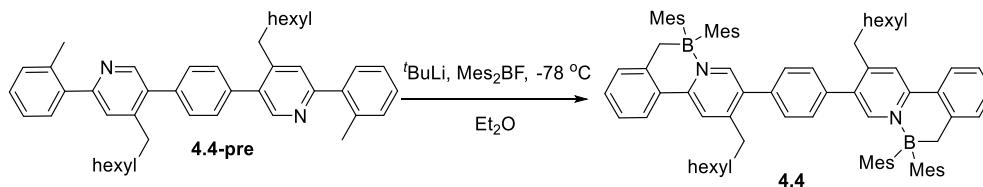
*Synthesis of **4.4***: Compound **4.4** was synthesized using the same procedure of synthesis of

compound **4.2** to provide product **4.4** (497 mg, 0.45 mmol, 50% yield) as a yellow solid, which

was confirmed by X-ray diffraction analysis. ^{1}H NMR (400 MHz, CD$_2$Cl$_2$) δ 8.43 (s, 2H, py), 7.91

(s, 2H, py), 7.67 (br, 2H, ph), 7.26 (br, 4H, ph), 7.13 (br, 4H, ph), 6.91 (br, 2H, ph), 6.57 (s, 8H,

Mes), 2.83 (br, 8H, CH$_2$ and B-CH$_2$), 2.15 (s, 12H, Mes), 1.90 (s, 24H, Mes), 1.71−1.59 (m, 4H, CH$_2$), 1.29 (br, 16H, CH$_2$), 0.90 (t, J = 6.5 Hz, 6H, Me in heptyl). ^{13}C NMR (101 MHz, CD$_2$Cl$_2$) δ 155.59, 154.46, 147.82, 147.64, 146.81, 141.66, 136.17, 135.95, 133.37, 130.62, 130.32, 129.63, 129.54, 128.51, 125.99, 124.24, 123.77, 32.74, 31.59, 29.91, 29.12, 28.85, 24.68, 22.53, 20.26, 13.82. ^{11}B NMR (128 MHz, CD$_2$Cl$_2$) δ 1.8. HR-ESIMS (m/z): [M + 1]$^+$ calcd for C$_{80}$H$_{95}$B$_2$N$_2$: 1105.76759; found: 1105.76845.

4.2.2.4 Synthesis of **4.5**
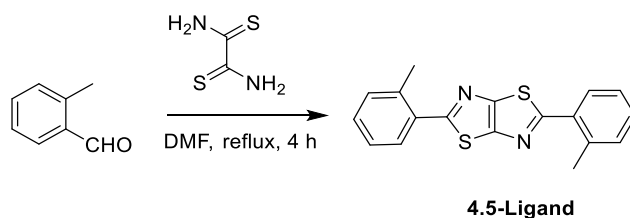
4.5-Ligand

*Synthesis of **4.5-Ligand**:* A solution of ethanebis(thioamide) (0.454 g, 3.7 mmol) and 2-methylbenzaldehyde (1.0 g, 8.3 mmol) in DMF (10 mL) was refluxed for 4 hours. After being cooled to room temperature, the solvents were then removed under reduced pressure. The crude product was purified by silica gel chromatography (petroleum ether/CH$_2$Cl$_2$ = 1/1). Compound **4.5-Ligand** was obtained as a pale yellow solid in 64% yield (0.768 g, 2.38 mmol); ^{1}H NMR (400 MHz, CDCl$_3$) δ 7.76 (d, *J* = 7.5 Hz, 2H), 7.43 – 7.28 (m, 6H), 2.69 (s, 6H). ^{13}C NMR (101 MHz, CDCl$_3$) δ 168.98, 151.03, 137.09, 133.37, 131.87, 130.16, 126.41, 21.70. HR-ESIMS (m/z): [M+H]$^+$ calcd. for C$_{18}$H$_{15}$N$_2$S$_2$, 323.06766; found 323.06415.

4.5-Ligand

4.5
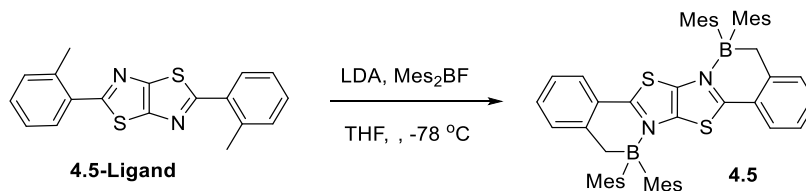
Synthesis of 4.5: To a solution of **4.5-Ligand** (0.1 g, 0.31 mmol) in anhydrous THF (10 mL) a solution of LDA in THF (1 mL, 2M, 0.78 mmol) was added dropwise in a N_2 atmosphere at -78 °C. The mixture was stirred at -78 °C for 2 hrs and Mes_2BF (0.195 g, 0.78 mmol) in anhydrous THF (10 mL) was added. The mixture solution was warmed up to room temperature and stirred for 12 hrs. After removal of the solvent under the reduced pressure, the resulting crude product **4.5** was purified by silica gel chromatography (petroleum ether/CH_2Cl_2 = 3:1) as a yellow solid in 4% yield (0.011 g, 0.013 mmol). ^1H NMR (400 MHz, C_6D_6) δ 6.91 (d, J = 7.6 Hz, 2H, ph), 6.82 (s, 8H, Mes), 6.74 (d, J = 7.6 Hz, 2H, ph), 6.62 (t, J = 7.5 Hz, 2H, ph), 6.33 (t, J = 7.5 Hz, 2H, ph), 2.96 (s, 4H, B-CH_2), 2.17 (br, 36H, Me). ^{13}C NMR (176 MHz, C_6D_6) δ 172.71, 147.94, 143.62, 133.74, 130.88, 126.40, 126.06, 125.13, 20.94. ^{11}B NMR (128 MHz, C_6D_6): δ 2.3. HR-ESIMS (m/z): $[M + 1]^+$ calcd for $C_{54}H_{57}B_2N_2S_2$, 819.41438; found 819.41334.

4.2.2.5 Synthesis of **4.6**

3,3'-dimethyl-2,2'-bipyridine

a) ^{n}BuLi / TMEDA
-78 °C, THF

b) Mes_2BF

4.6
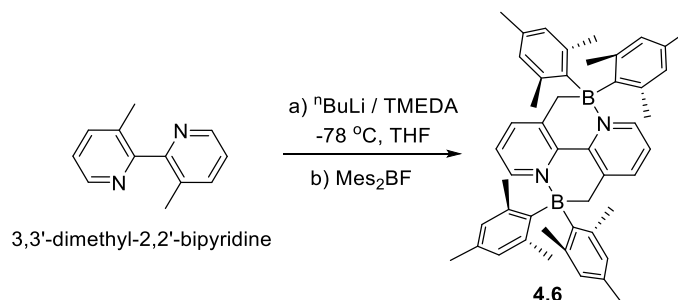
^{n}BuLi (1.6 mL, 2.5 M, 2.5 mmol) was added to a mixture of 3,3'-dimethyl-2,2'-bipyridine (184 mg, 1 mmol) and tetramethylethylenediamine (TMEDA) (0.57 mL, 4.0 mmol) in THF (25 mL) at -78 °C. After stirring at the temperature for 2 hrs, Mes_2BF (590 mg, 2.2 mmol) was added. The mixture was stirred for 1 h at -78 °C, then allowed to warm slowly to room temperature and stirred for 16 hrs. After removal of the solvent, the residue was extracted with $CHCl_3$ and water. The organic phase was dried over $MgSO_4$ and filtered. The filtrate was purified by column

chromatography on silica gel to afford dimer **4.6** as a white solid (136 mg, 20% yield). **4.6** sublimed/decomposed over 286 °C; ^{1}H NMR (400 MHz, CDCl$_3$): δ 8.46 (d, *J* = 5.9 Hz, 2H), 7.64 (d, *J* = 7.8 Hz, 2H), 7.15 – 7.02 (m, 2H), 6.67 (s, 8H), 2.96 (s, 4H), 2.21 (s, 12H), 1.77 (s, 24H); ^{11}B NMR (128 MHz, CDCl$_3$): δ 3.70; HR-EIMS (*m/z*): [M$^+$] calcd. for C$_{48}$H$_{54}$B$_2$N$_2$, 680.4489; found, 680.4457.

4.2.2.6 Synthesis of **4.7**

3,3'-dimethyl-2,2'-bipyridine

4.7
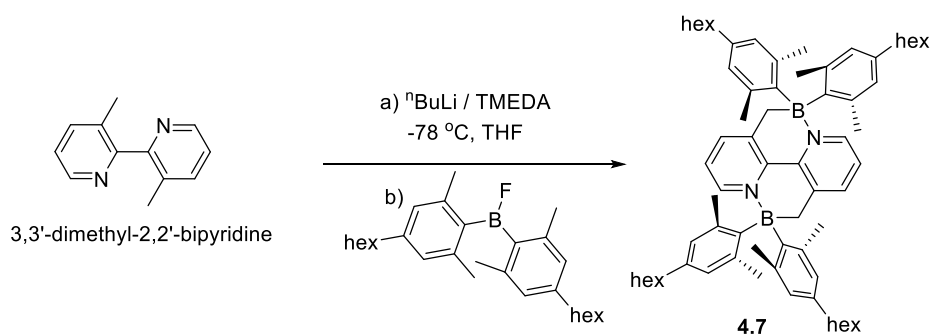
To a solution of 3,3'-dimethyl-2,2'-bipyridine (97.2 mg, 0.528 mmol) and TMEDA (0.315 mL, 2.11 mmol) in THF (5 mL) at –78 °C, ^{n}BuLi (1.22 M in hexane, 0.950 mL, 1.16 mmol) was added dropwise. After warmed to room temperature for 1 h, the mixture was cooled to –78 ºC again, and then a solution of diarylboronfluoride (642 mg, 1.57 mmol) in THF (5 mL) was added to the mixture at –78 °C. The mixture was gradually warmed to room temperature with stirring. After removing the solvent, the crude product was purified by silica gel column chromatography (hexane/CH$_2$Cl$_2$ = 4/1) to give 282 mg (0.293 mmol) of **4.7** in 56% yield as yellow solid. mp:184-185 °C; ^{1}H NMR (400 MHz, CD$_2$Cl$_2$): δ 8.43 (dd, *J* = 5.8, 1.3 Hz, 2H), 7.73 – 7.54 (m, 2H), 7.09 (dd, *J* = 7.6, 5.9 Hz, 2H), 6.67 (s, 8H), 2.98 (s, 4H), 2.47 (t, *J* = 7.7 Hz, 8H), 1.80 (s, 24H), 1.57 (d, *J* = 7.6 Hz, CH$_2$, 8H), 1.32 (m, CH$_2$, 24H), 0.92 (dd, *J* = 9.1, 4.3 Hz, CH$_3$, 12H); ^{13}C NMR (101 MHz, CD$_2$Cl$_2$): δ 146.66, 146.49, 146.05, 144.08, 142.21, 141.21, 138.92, 129.38, 124.76, 35.03,

31.63, 31.10, 28.92, 27.87, 25.34, 22.51, 13.72; ^{11}B NMR (128 MHz, CD$_2$Cl$_2$): δ 1.18; HRMS (APCI) (*m/z*): [M$^-$] calcd. for C$_{68}$H$_{94}$B$_2$N$_2$, 960.7624; found, 960.7654.

4.2.3 Fabrication of Electroluminescent Device

The hole-injection material MoO$_3$ and electron-injection material LiF were purchased from Sigma-Aldrich and used as received. The hole-transporting material and host CBP, electron transport material TPBi were purchased from Luminescence Technology Corporation and used as received. All devices were fabricated in a Kurt J. Lesker LUMINOS cluster tool with a base pressure of 10^{-8} Torr without interrupting vacuum. The ITO anode is commercially patterned and coated on glass substrates with a thickness of 120 nm. Prior to loading, the substrate was degreased with a standard regiment of Alconox, acetone, and methanol, blow-dried using a N$_2$ gun, and treated in an UV−ozone chamber for 15 minutes. All doping concentrations used in this work are by weight percentage. The active area for all devices was 2 mm^2. Prior to removing the devices from vacuum for characterization, an encapsulation layer of 300 nm thick SiO$_2$ was deposited by thermal evaporation. Luminance−voltage measurements were carried out using a Minolta LS-110 Luminance meter. Current−voltage characteristics were measured using an HP4140B pA meter. The EL spectra were measured using an Ocean Optics USB4000 spectrometer calibrated with a standard halogen lamp. Spectral power of the devices were recorded by applying a constant bias voltage of 5 V for 60 s, and each spectrum was recorded under 1 s of a constant bias voltage by taking the average of 3 scans with 0.3 s integration time. Photos of the device illumination were taken under a constant bias voltage of 5 V after the first 30 s. All the measurements were conducted in ambient air. Additional details regarding device fabrication and characterization measurements have been described elsewhere.[10]

4.2.4 X-ray Crystallography Analysis

Single crystals of **4.3**, **4.4**, **4.5** and **4.6** suitable for X-ray analysis were obtained by slow diffusion of hexane to CH_2Cl_2. Intensity data of **4.6** were collected at 100 K using a diffractometer equipped with an ADSC Quantun315 CCD detector with synchrotron radiation at a wavelength of 0.75 Å at the SPring-8 beam line BL38B1. A total of 23085 reflections were measured with a maximum 2θ angle of 56.0°, of which 3620 were independent reflections (R_{int} = 0.0484). The collected diffraction data were processed with the HKL2000 software program. The crystal data of **4.3** and **4.4** were collected on a Bruker Apex II X-ray diffractometer with Mo-target ($\lambda = 0.71073$ Å) at 180 K while the crystal structure of **4.5** was determined on a Bruker D8-Venture diffractometer with Mo-target at 180 K. The structures were solved by direct methods (SHELXTL, version 6.14)[11a] and refined by the full-matrix least-squares on F^2 (SHELXL-97[11]). All non-hydrogen atoms were refined anisotropically. All hydrogen atoms were placed using AFIX instructions. All non-hydrogen atoms were refined anisotropically. The molecule of **4.6** has a crystallographically imposed C_2 symmetry. The crystals of **4.6** contain disordered CH_2Cl_2 solvent molecules (~one per molecule), which could not be modelled and refined properly. As a result, the solvent molecules were removed by using the Squeeze routine of the Platon software[11b] to improve the accuracy of the structural parameters. Complete crystal structural data have been deposited at the Cambridge Crystallographic Data Centre [CCDC No. 1542183 **4.3**, 1542182 **4.4**, 1542181 **4.5,** 1414974 **4.6**]. These data can be obtained free of charge from the Cambridge Crystallographic Data Centre via www.ccdc.cam.ac.uk/ data_request/cif].

4.2.5 DFT Calculations

The TD-DFT computational work of **4.6**, **4.7** and their corresponding analogues were performed using the Gaussian 09[12] suite of programs on High Performance Computing Virtual

Laboratory (HPCVL) at Queen's University. All computations were performed at the B3LYP level of theory using 6-311++g(d,p)[13] basis set for all atoms.

All calculations of **4.2** - **4.5** and their corresponding analogues were performed using the Gaussian 09 suite of programs on the High-Performance Computing Virtual Laboratory (HPCVL) at Queen's University. Initial input coordinates were taken from the corresponding crystal structure data where applicable, while all others were generated in Gaussian 09. DFT and TD-DFT calculations were performed using the B3LYP/6-31G(d) level of theory.[13]

4.3 Results and Discussion

4.3.1 Synthesis and Structural Analysis

Molecules **4.2** - **4.4**, **4.6** and **4.7** were prepared *via* double lithiation of corresponding ligands, followed by the addition of the appropriate BAr_2F reagents. The double lithiation/borylation synthesis of **4.2** - **4.4** only succeeded when $^{t}BuLi$ was used as lithiation reagent in diethyl ether solution rather than $^{n}BuLi$/Tetramethylethylenediamine (TEMDA) in THF solution. The heptyl and hexyl groups were introduced to improve the solubility of the ligands as well as of the final $(BN)_2$-heterocycles. Compound **4.5** can only be obtained in low yield from the reaction of **4.5-Ligand** with 2.5 equiv of LDA at -78 °C, followed by the addition of 2.5 equiv of Mes_2BF. All $(BN)_2$-heterocycles **4.2** - **4.7** were fully identified and characterized by ^{1}H, ^{13}C, ^{11}B NMR, and HRMS. Furthermore, single crystals suitable for X-ray diffraction analysis were obtained for **4.3**, **4.4**, **4.5** and **4.6**.

Table 4.1 Selected bond length (Å)

Compounds	B-N	B-CH$_2$	B-Mes
4.3	1.646(6)	1.657(6)	1.655(6)/1.666(7)
4.4	1.683(3)	1.641(3)	1.654(3)/1.655(3)
4.5	1.653(2)	1.645(2)	1.651(2)/1.656(2)
4.6	1.678(3)	1.641(4)	1.660(4)/ 1.659(4)

The crystal structures of **4.3** - **4.6** are shown in Figures 4.2 – 4.5 and Table 4.1, respectively. All four compounds possess a crytallographically imposed inversion center. Compounds **4.3**, **4.4** are isomers. For **4.3**, the pyridyl rings are the outer-most ring while for **4.4** the benzyl rings are the outer-most. As a result of the location difference of the pyridyl, benzyl ring and the heptyl substituents, **4.4** is sterically much more congested than **4.3**. As shown by the side view in Figure 4.2 and 4.3, the five aryl rings in the backbone of **4.3** are essentially coplanar with the largest torsion angle between these rings being 20°. In contrast, the five aryl rings in **4.4** are significantly out of coplanarity with the torsion angle between the central benzene ring and the pyridyl ring being 44°. In addition, the B – N bond in **4.4** (1.683(3) Å) is much longer than that in **4.3** (1.646(6) Å), again a consequence of the greater steric congestion in **4.4**. This structural difference has a significant impact on the electronic properties of these two isomeric molecules, which will be discussed in the next section. The aryl rings of the backbone in **4.5** have a good coplanarity with the torsion angle between the benzene ring and the fused bis-thiazole ring being 18°.
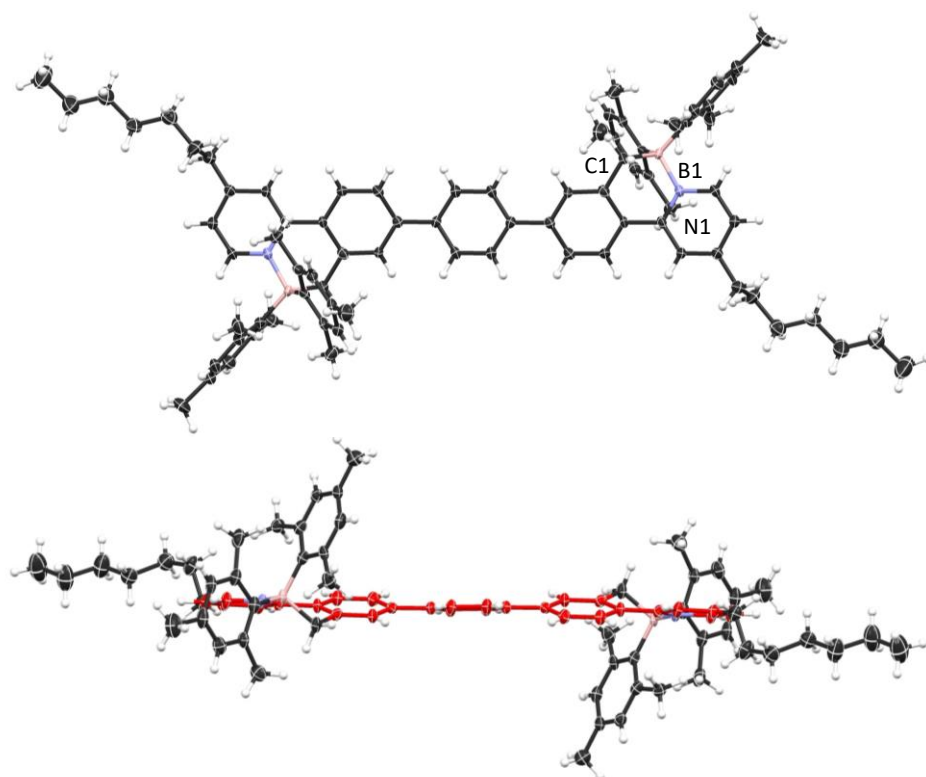
Figure 4.2 Crystal structure of **4.3**: top view and side view (the 5 linked aryl rings are shown in red).
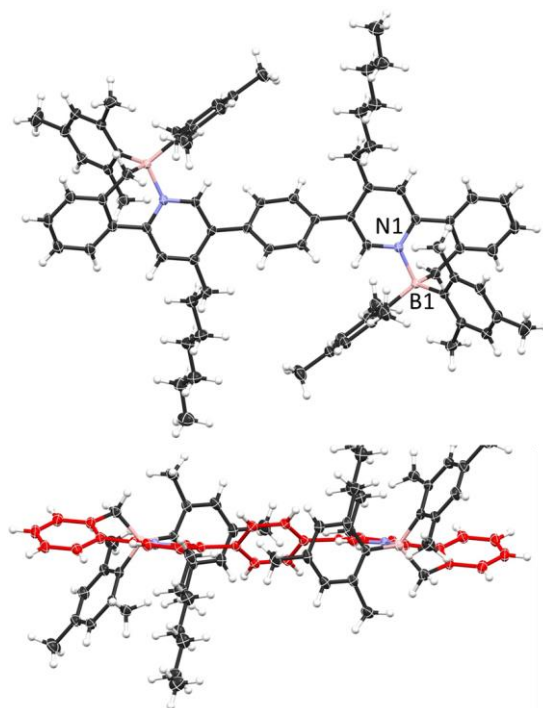
Figure 4.3 Crystal structure of **4.4**: top view and side view (the 5 linked aryl rings are shown in red).
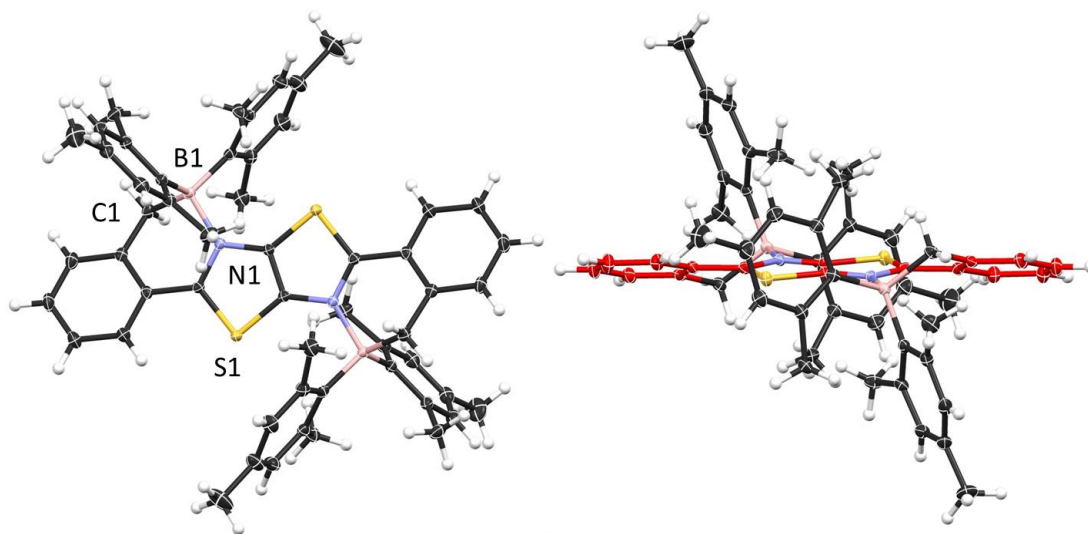
Figure 4.4 Crystal structure of **4.5**: top view and side view (the 5 linked aryl rings are shown in red).
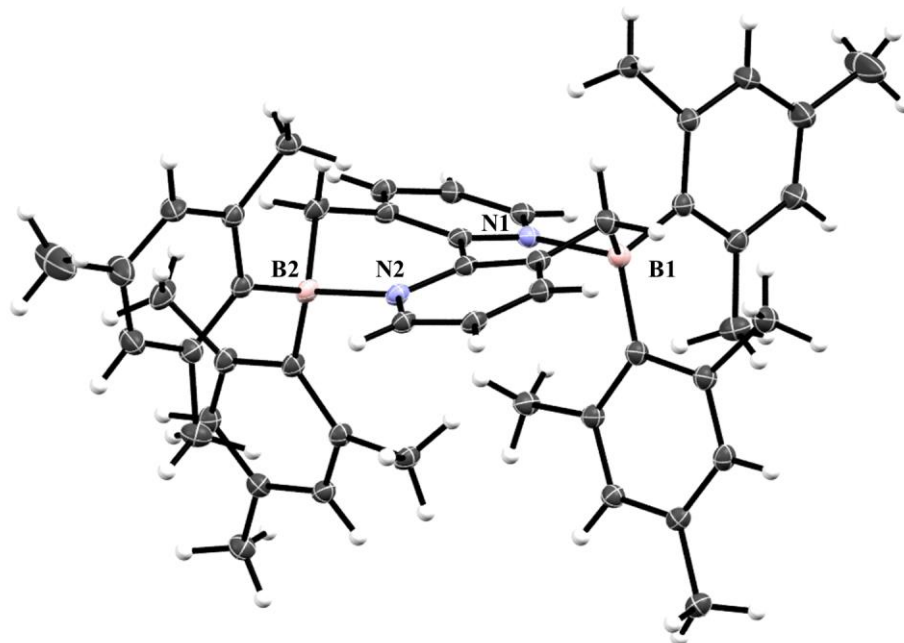
Figure 4.5 A diagram showing the crystal structure of **4.6** with labeling schemes.

4.3.2 Electrochemical and Photophysical Properties of 4.2-4.7
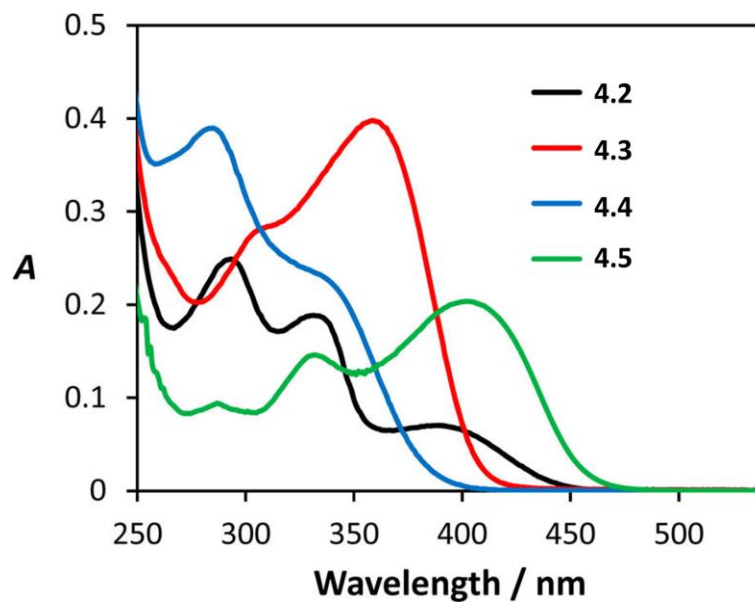
Figure 4.6 UV/Vis spectra of **4.2** – **4.5** in THF (1.0×10^{-5} M).

Table 4.2 Electronic and Photophysical Properties of (BN)$_2$-Heterocycles.

Compounds	E_{red} (V)^a	λ_{abs} / ε (nm)^b / (x 10^4 M^{-1} cm^{-1})	Absorp. Edge/DFT (nm)	HOMO (eV) Exp^c / DFT^d	LUMO (eV) Exp^e / DFT^d
4.2	-2.11	394/0.70	450/454	-5.48/-5.19	-2.69 /-2.15
4.3	-2.18	359/3.98	420/445	-5.64/-5.26	-2.62 /-1.94
4.4	-2.33	340/2.21	400/445	-5.69/-5.33	-2.47/-1.99
4.5	-1.68	402/2.03	475/470	-5.73/-5.18	-3.12/-2.59
4.6	N.A.	350/5.60	445/N.A.	N.A.	N.A.
4.7	N.A.	350/5.60	445/N.A.	N.A.	N.A.

^{a}Relative to [FeCp$_2$]$^+$/[FeCp$_2$] recorded in THF for **4.2** – **4.4** and in DMF for **4.5** with [Bu$_4$N][PF$_6$] as the electrolyte. ^{b}10^{-5} M in THF at 298 K. ^{c}The experimental value is from the absorption edge, and the DFT value is from the first symmetry allowed vertical excitation. ^{d}Calculated using to absorption edge and reduction potential. ^{e}Estimated from the reduction potential.

All six (BN)$_2$-heterocycles **4.2** - **4.7** possess strong absorption bands between 300 and 470 nm as shown in Figure 4.6 (Figures 4.21 and 4.22 in Section 4.5.2 for **4.6** and **4.7**, respectively) and Table 4.2. Compound **4.2** has a low energy absorption band at ~394 nm. As structural isomers, the absorption bands of **4.4** are hypsochromically shifted by ~20 nm compared to **4.3**, which agrees with the greater coplanarity, hence better extended π-conjugation of the backbone in **4.3** as revealed by the crystal structures. Furthermore, **4.3** has a much bigger extinction coefficient at the low energy absorption band (ε = 3.98 × 10^4 M^{-1}cm^{-1}, λ = 359 nm) than that of **4.4** (ε = 2.21 × 10^4 M^{-1}cm^{-1} at 340 nm). These all support that the location of the BMes$_2$ chelate units has a great impact on the electronic properties of isomeric structures. Among the six BN-heterocycles, **4.5** has the most bathochromically shifted absorption band with absorption edge at ~470 nm, followed by **4.2** that has the absorption edge at ~450 nm and **4.6** and **4.7** that have the absorption edges at ~445 nm. The sharing of the same central chelate unit by the two BMes$_2$ units in **4.2** and **4.5** - **4.7** clearly is

146

more effective in lowering the energy of the absorption edge than the insertion of the benzene linker to extend the π-conjugation in **4.3** and **4.4**, which can be attributed to the effective conjugation and better coplanarity of the backbone in the former. Compounds **4.2** – **4.7** are not fluorescent or have very week emission lower than 400 nm.

The electrochemical data revealed that the four $(BN)_2$-heterocycles **4.2** – **4.5** display the characteristic one electron reduction peak at $E_{red} = -2.11, -2.18, -2.33,$ and -1.68 V, respectively (relative to $[FeCp_2]^+/[FeCp_2]$, Table 4.2 and Section 4.5.2). The electrochemical data indicates that compound **4.5** is likely a good electron acceptor for organic devices such as photovoltaics due to its deep LUMO (−3.12 eV), which will be examined in a future study. To understand UV-vis spectral difference and electrochemical data, TD-DFT calculations were performed at the B3LYP/6-31g(d) level of theory on the optimized geometries of all four $(BN)_2$-heterocycles. In addition, we also performed DFT calculations for **4.2-pre** - **4.4-pre** in order to compare the change of HOMO/LUMO energy levels between ligands **4.2-pre** - **4.4-pre** and corresponding **4.2** - **4.4**. After boron chelation, the HOMO levels of these three BN-heterocycles are raised by about 0.57 eV, while their LUMO levels are stabilized by up to 1.09 eV, supporting the idea that embedding the boron chelate units into heterocycles can enhance the electron affinity of the molecule and reduce the HOMO-LUMO gap, in agreement with the general trend observed for previously reported boron chelate compounds.[4,5] On the basis of the DFT data, the low energy absorption band of **4.2** - **4.5** can be assigned to a mesityl → backbone charge transfer (CT) transition. The calculated absorption spectral patterns and the trend of the first symmetry allowed vertical excitation energy for **4.2** - **4.5** match approximately with the experimental data as shown in Table 4.2 (and Section 4.5). The main deviation is the HOMO and LUMO energies of **4.5** that are much higher than the experimental values. Since the reduction potential of **4.5** was determined in DMF due to its low

147

solubility, the inconsistency between the experimentally observed redox trend and the calculated one may be due to solvent effects which were not accounted for in TD-DFT calculations. For **4.3** and **4.4**, the TD-DFT calculated values change significantly with the dihedral angles between the central benzene ring and its neighboring rings in the backbone. The data shown in Table 4.2 for these two molecules are based on crystal structural parameters which were further optimized by DFT. In the optimized structure of **4.3**, the central benzene ring has a much larger dihedral angle with its neighboring rings than that observed in the crystal structure, leading to its calculated optical energy gap being similar to that of **4.3**.

4.3.3 Photo- and Thermal Reactions

To establish if (BN)$_2$-heterocycles **4.2** - **4.7** can act as precursors for the generation of double BN-doped fully π-conjugated systems, their thermal and photoreactivities were examined and summarized in Figure 4.7. Upon irradiation with 350 nm UV light, the C$_6$D$_6$ solution of all six compounds gradually become fluorescent and displayed distinct fluorescent colors (Figure 4.7). However, when these photoreactions were monitored by ^{1}H and ^{11}B NMR spectroscopy, only **4.4** and **4.7** eliminates two mesitylene molecules cleanly and produces a new diazaborine, **4.4a** and **4.7a** in ∼90% yield, respectively. Compound **4.3** only undergoes partial conversion (∼56%) to **4.3a** along with the formation of an unidentified product under 350 nm. Irradiation of **4.2** generated unidentifiable species with orange color and bright yellow emission. **4.5**'s behavior appears to be similar to that of **4.2**. Although ^{11}B NMR data indicated that **4.5** may partially form the double-eliminated product **4.5a**, upon irradiation at either 300 or 365 nm, the chemical shifts of the aromatic protons are mostly absent or very broad in the ^{1}H NMR spectrum with unidentifiable peaks in the aliphatic region (see Section 4.5.2). Furthermore, both **4.2** and **4.5** only display detectable changes by NMR after a long exposure to UV light. Perhaps the rigid structures imposed

by the two boron units sharing the central linker unit in **4.2** and **4.5** make the elimination reaction difficult, although the details are not understood yet. The different photoreactivities of **4.3** and **4.4** are probably caused by the different locations of the two BN units and heptyl groups, which led to a highly congested structure for **4.4**, compared to that of **4.3**. The steric congestion likely makes the photoelimination of **4.4** more efficient and is responsible for its relatively clean double elimination.
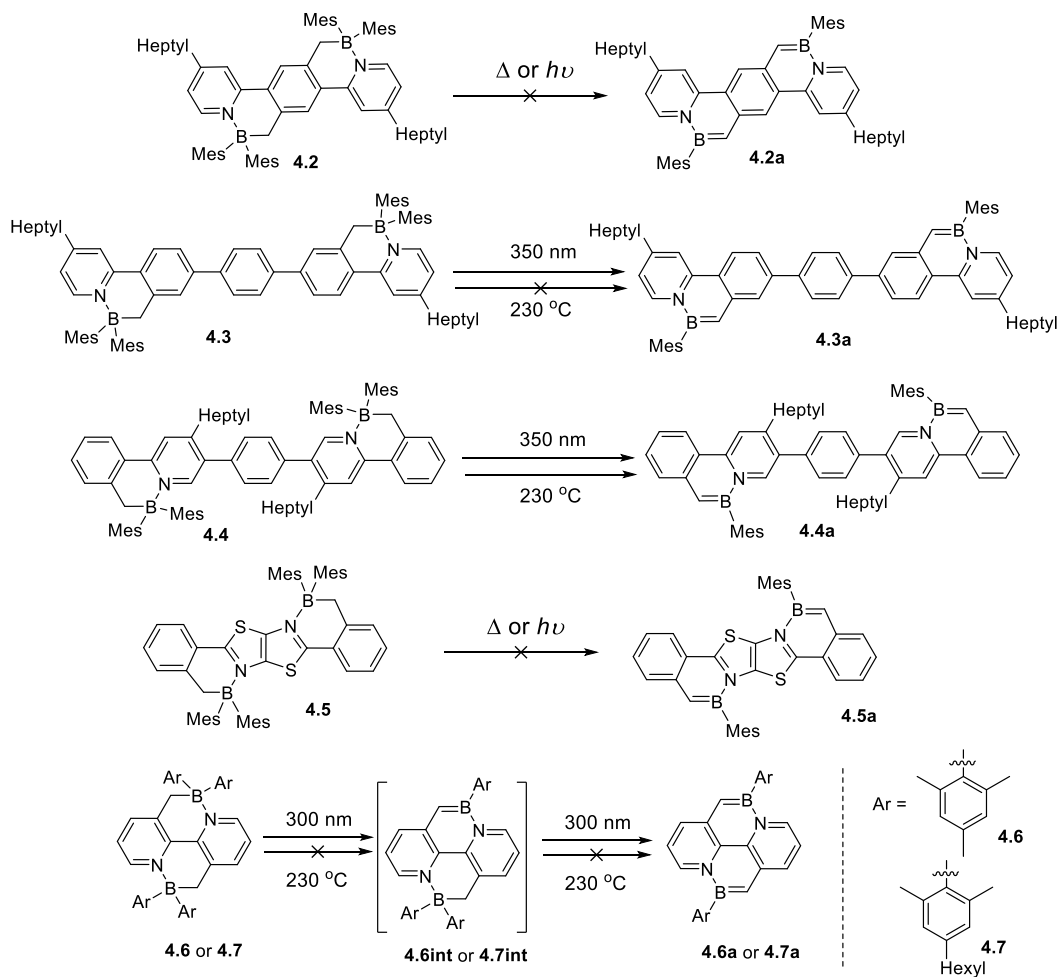
Figure 4.7 Thermal and photoreactivities of **4.2** – **4.7**.

With respect to compound **4.6** and **4.7**, their expected elimination products-BN-pyrenes are attractive target molecules because of their extended conjugated structure as well as the highly fluorescent nature of pyrene analogues.[14] However, only three examples of BN-pyrenes have been reported to date, namely **(BN)-pyrene-1**,[6e] **(BN)-pyrene-2**,[1j,k] and **(BN)₂-pyrene-1**[6a,f] (Figure 4.8), of which only **(BN)-pyrene-2** and its derivatives were shown to be fluorescent. Computational data of the analogues shown in Figure 4.8 suggests that the location and number of BN units within the pyrene skeleton dramatically affects the electronic structure of these molecules, and consequently, their photophysical properties as well. Among the BN-pyrenes described in Figure 4.8, **(BN)₂-pyrene-2** and **(BN)₂-pyrene-3** are most interesting as they possess small HOMO – LUMO gaps and stabilized LUMO levels according to the DFT data (see Section 4.6 for details). However, our attempts to synthesize the precursor compound for the **(BN)₂-pyrene-3** derivatives failed, only the precursors for **(BN)₂-pyrene-2** derivatives (**4.6** and **4.7**) were successfully obtained.

	(BN)-Pyrene-1	(BN)-Pyrene-2	(BN)-Pyrene-3
LUMO (eV)	-1.7	-2.0	-2.3
HOMO (eV)	-5.8	-5.6	-5.1

	(BN)₂-Pyrene-1	(BN)₂-Pyrene-2	(BN)₂-Pyrene-3
LUMO (eV)	-1.5	-2.6	-2.9
HOMO (eV)	-6.0	-5.1	-5.0
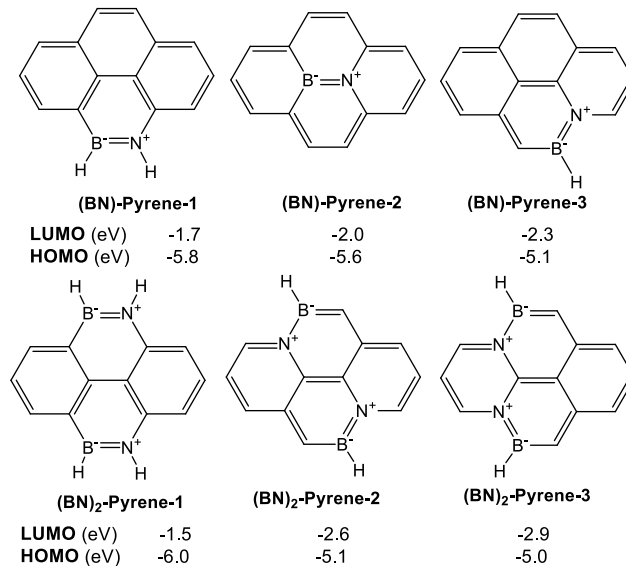
Figure 4.8 DFT calculated HOMO-LUMO energy levels of selected BN-pyrenes.

150
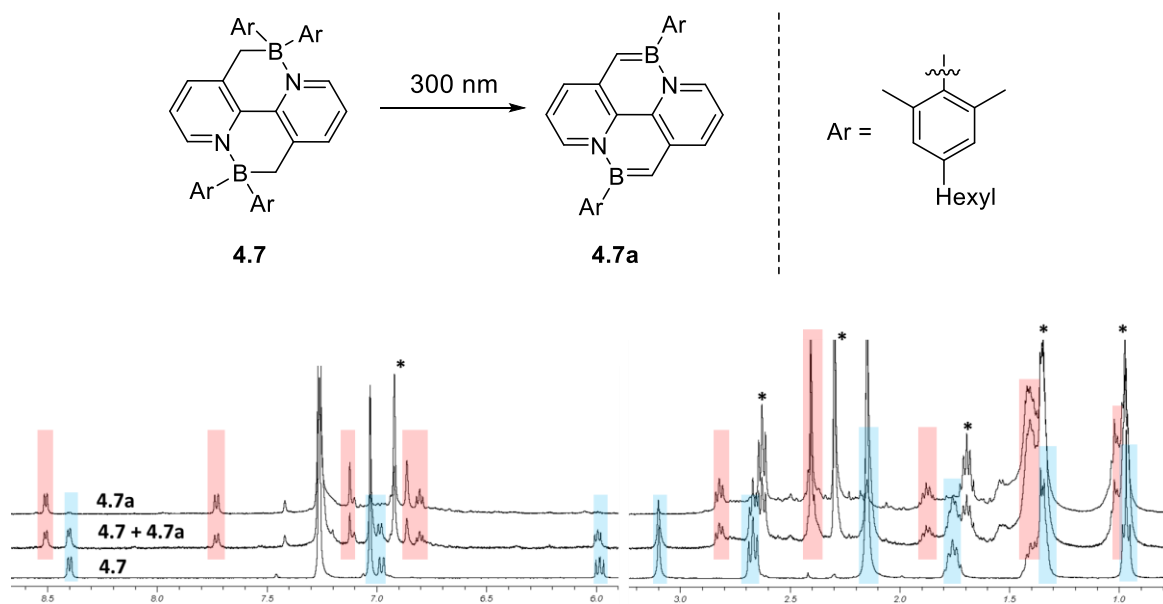
Figure 4.9 ^{1}H NMR spectra showing the clean conversion of **4.7** (blue highlight) to **4.7a** (red highlight) in C_6D_6 at room temperature under 300 nm irradiation (1-hexyl-3,5-dimethylbenzene shown by asterisks (*)).

Upon irradiation at 350 nm, the light-yellow solution of **4.6** or **4.7** gradually becomes red–orange with a new absorption band appearing in the 400–600 nm region (Figure 4.21 and Figure 4.23, respectively), which is attributed to the BN-pyrene species **4.6a**/**4.7a**. HRMS analysis (see Section 4.5.2) confirmed the formation of both single-elimination (**4.6int**) and double-elimination products (**4.6a**) from the photoreaction shown in Figure **4.7**. However, the fluorescence of **4.6int**/**4.7int** was not detected. **4.6a** could not be characterized by NMR spectroscopy because it is insoluble in common NMR solvents. Due to the solubility enhancing hexyl groups in **4.7**, it was possible to monitor the double-photoelimination process by ^{1}H NMR spectroscopy, which established unequivocally the clean transformation of **4.7** to **4.7a** over a period of several days at the typical NMR concentration scale (Figure 4.9). Interestingly, the single elimination product **4.7int** was not observed in the NMR spectra, indicating that it may be short-lived and transforms

readily to **4.7a** upon its formation in solution. Compared to **4.1**, the photoelimination of **4.4**, **4.6** and **4.7** are much slower and less efficient under the same conditions, which is likely caused by their highly congested structures (see the crystal structures of **4.4** and **4.6** in Figure 4.3 and Figure 4.5, respectively), leading to an unstable transition state[8b, c] in the reaction pathway toward single elimination products. The stepwise elimination process was also confirmed by DFT computations, as shown in Section 4.5.1.3.

Besides phototransformations, previously we have also shown that related BN-chelate compounds can display either retro-1,1-hydroboration (deborylation) or mesitylene elimination upon heating.[8c] To determine if the new BN-heterocycles display similar reactivities, their thermal reactions were examined. Molecules **4.2**, **4.3**, **4.5**, **4.6** and **4.7** produced unidentifiable products in mineral oil at 230 °C. In contrast, only compound **4.4** underwent a clean thermal elimination upon heating at 230 °C, producing **4.4a** nearly quantitatively (see the Section 4.5.2).

4.3.4 Electrochemical and Photophysical Properties of 4.4a, 4.6a and 4.7a
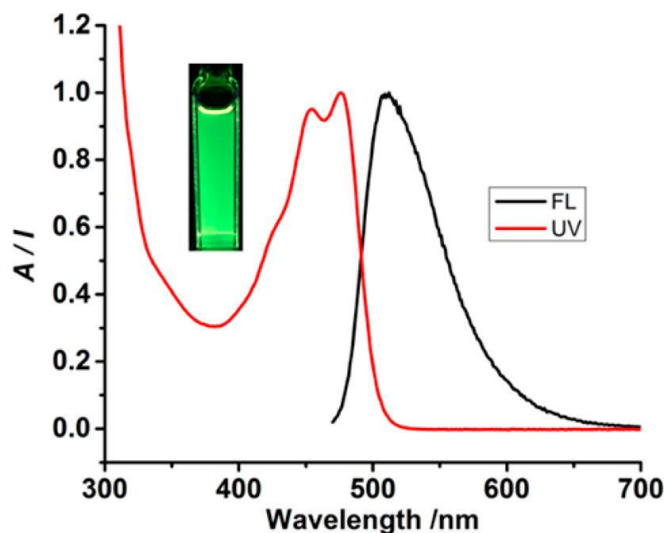
Figure 4.10 Absorption (red) and fluorescence (black) spectra of **4.4a** in THF. Inset: photograph showing the emission color of **4.4a** in THF.

Compound **4.4a** was fully characterized by NMR and HRMS. The [11]B chemical shift of **4.4a** (36 ppm) is consistent with that of azaborines.[8] **4.4a** has a low-energy absorption band at ~476 nm with well-resolved vibrational features and bright green-yellow fluorescent emission (λ_{em} = 510 nm, Φ_{FL} = 0.14; Figure 4.10), which is similar to that of the corresponding mono-BN-phenanthrene reported previously.[8] This suggests that increasing π conjugation *via* a phenyl linker does not significantly change the absorption and fluorescent properties of BN-phenanthrene. The most stable form of **4.4a** has an approximate *syn*-conformation with the two BMes units on the same side as shown in Figure 4.11, based on DFT structural optimization. The central benzene ring has a torsion angle of ~58° with the two neighboring BN-phenanthrene rings. This confirms the poor conjugation between these three units in **4.4a** and explains the lack of the influence of the central benzene linker on the electronic properties of the bis-BN-phenanthrene molecule **4.4a**.
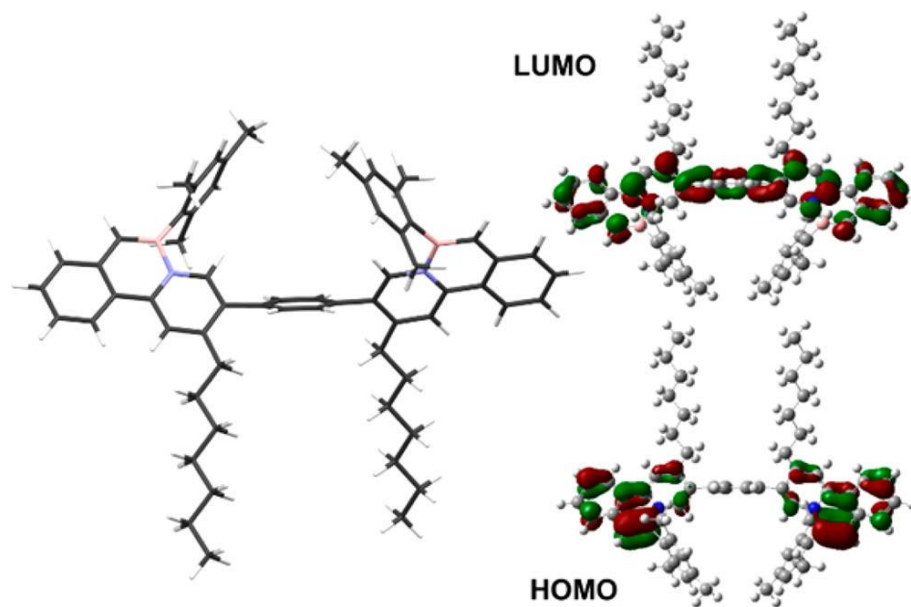
Figure 4.11 Left: DFT-optimized structure of **4.4a**. Right: HOMO and LUMO diagrams of **4.4a**.

TD-DFT computation studies (see Section 4.5.1 for details) confirmed that the $S_0 \rightarrow S_1$ transition of **4.4a** involves primarily the HOMO and LUMO orbitals (83%), localized

predominantly on the BN-phenanthrene units with a very high oscillator strength (0.168, Figure 4.11). This transition is believed to be responsible for the green fluorescence of **4.4a**. Compound **4.4a** displays two pseudoreversible reduction waves in the CV diagram (in THF) at −2.22 and −2.47 V, respectively, and an irreversible oxidation at 0.64 V (vs $[FeCp_2]^+/[FeCp_2]$, see Section 4.5.2), which correspond to approximately LUMO, LUMO+1, and HOMO levels of −2.58, −2.33, and −5.44 eV, respectively.
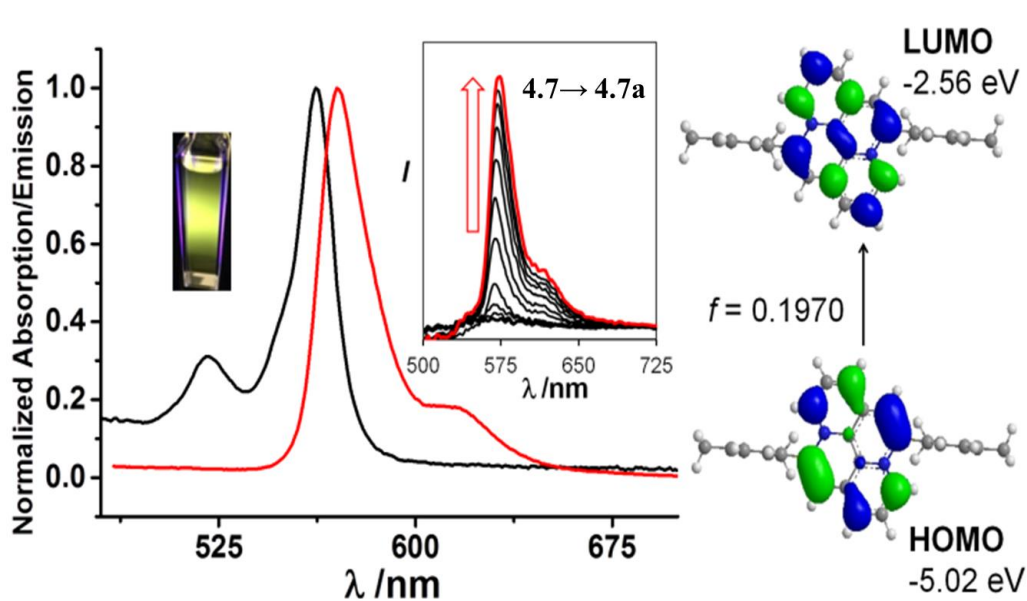
Figure 4.12 Left: The absorption (black) and fluorescence (red) spectra of **4.7a** in THF. Inset: a photograph showing the emission color of **4.7a** in THF and the change in the fluorescence spectrum of **4.7** in a PMMA film (20 wt%) with 350 nm irradiation. Right: The MO diagrams of **4.7a** involved in the $S_0 \rightarrow S_1$ transition.

Both **4.6a** and **4.7a** display bright yellow fluorescence in solution and in the solid state ($\lambda_{max}= 570$ nm, Figure 4.12, and see Section 4.5.2 for details) and their fluorescent spectra have well-resolved vibrational features. The fluorescence quantum efficiency of **4.7a** was determined to be 0.27 in THF (using $[Ir(ppy)_3]$ as the reference [9]). Interestingly, the absorption and fluorescent peaks of **4.6a**

154

and **4.7a** have very small Stokes shifts (*ca.*10 nm) as shown in Figure 4.12, which is clearly due to their rigid structure and the symmetry-allowed $S_0 \rightarrow S_1$ transitions in these BN-pyrenes. In contrast to pyrene which is highly prone to excimer emission,[15] **4.6a** and **4.7a** do not display excimer emission, which is credited to the bulky aryl group on each boron atom. Compared to the green-emissive BN-phenanthrene **4.1a** which has an emission peak at around 495 nm,[8] the maxima of the absorption and fluorescent bands of **4.6a** and **4.7a** are red-shifted by ca. 70 nm, which is consistent with the greater π-conjugation in **4.6a** and **4.7a**.

TD-DFT computational studies (see Section 4.5.1) confirmed that the $S_0 \rightarrow S_1$ transitions of **4.6a** and **4.7a** involve primarily the HOMO and LUMO orbitals (97%), which are localized on the BN-pyrene ring with a very high oscillator strength (0.1970, Figure 4.12) and believed to be responsible for the yellow fluorescence of these molecules. The optical energy gap (*ca.* 2.06 eV) of **4.6a** and **4.7a** is about 1.5 eV smaller than that of pyrene. Compared to the previously reported **(BN)-pyrene-2** and its derivatives, [1j,k] the absorption band of **4.6a**/**4.7a** is red-shifted by about 120 nm while the fluorescent band is red-shifted by approximately 70 - 90 nm, which is consistent with the general trend predicted by DFT data. **4.7a** displays a reversible one-electron reduction in THF at -2.10 V, a potential about 0.40 V more positive than that of **4.1a**, and an irreversible oxidation at 0.35 V (vs. $[FeCp_2]^+/[FeCp_2]$), corresponding to approximate HOMO and LUMO levels of -5.15 and -2.70 eV, respectively. These properties make **4.6a** and **4.7a** promising candidates for use as yellow emitters in EL devices.

4.3.5 Electroluminescent Devices

Due to the slow, inefficient photoelimination of **4.6**/**4.7** and air-sensitive nature of **4.6a**/**4.7a**, it is difficult to synthesize large quantities of the BN-pyrenes for applications in electroluminescent (EL) devices using the photochemical procedure. We therefore postulated that perhaps the

precursor species **4.6**/**4.7** could be directly converted to **4.6a**/**4.7a** using excitons within the EL devices, namely, the aforementioned *in situ* exciton-driven elimination (EDE) procedure. Since EL devices employ materials in the solid state, it was necessary to first establish if the double photoelimination of **4.6**/**4.7** could occur in the condensed phase. Indeed, we found that compounds **4.6** and **4.7** underwent double photoelimination in PMMA films (20 wt%), forming **4.6** and **4.7** as evidenced by the fluorescence spectra shown in Figure 4.12 and Section 4.5.2. Next, an EL device incorporating **4.6** was fabricated using vacuum deposition. To demonstrate the generality of the EDE method, EL devices incorporating compounds **4.1**, **4.8**, **4.9** and **2.5** were also fabricated (Figure 4.13). **2.5** is not suitable for EL device fabrication *via* vacuum deposition because of its high molecular weight and relatively low melting point.
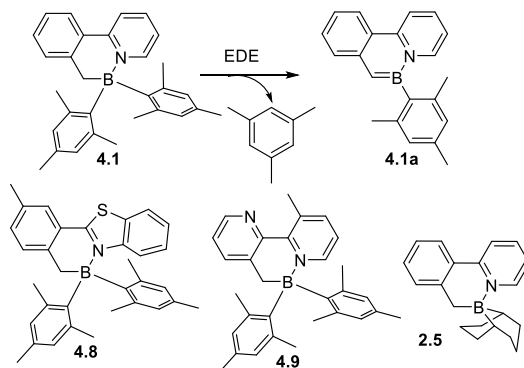
Figure 4.13 The EDE reactions of **4.1**, **4.8**, **4.9** and **2.5**.

The details of the EL work based on **4.1** and **4.6** are presented here. The device data for other compounds are provided in Section 4.5.2. A standard EL device structure was adopted (Figure 4.14a) for all compounds in which MoO_3 and LiF serve as hole- and electron-injection layers, respectively; 4,4'-bis(carbazol-9-yl)-biphenyl (CBP) and 1,3,5-tris(N-4-phenylbenzimidazol-2-yl)-benzene (TPBi) act as hole- and electron-transport layers, respectively; the BN-heterocycles were doped into CBP as the emissive layer. The vacuum deposition temperature was 105 °C and

208 °C for **4.1** and **4.6**, respectively, temperatures far below their melting points (218 °C for **4.1**) and thermal decomposition temperatures (>280 °C for both **4.1** and **4.6**,). It is important to note that the processability of the BN-heterocycles is one major advantage of our *in situ* strategy, as their BN-arene counterparts tend to possess poorer solubility and stability, which complicates their incorporation into optoelectronic devices and diminishes their potential value as organic materials.
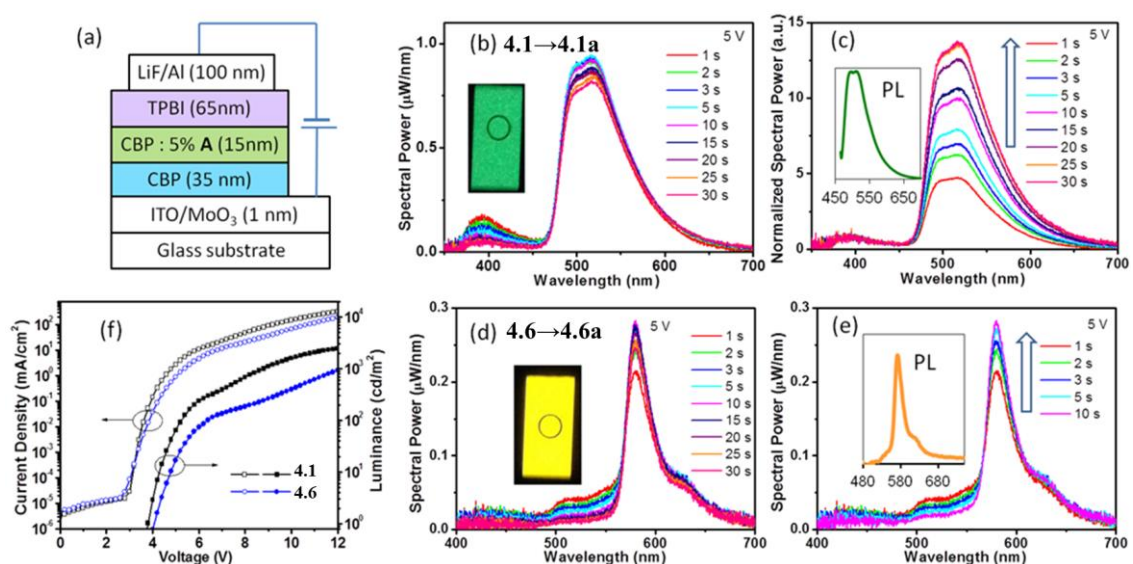
Figure 4.14 a) The structure of the EL device used for investigating the EDE process. b) EL spectra (spectral power versus wavelength) of the **4.1→4.1a** device. c) Normalized EL spectra of the **4.1→4.1a** device. d) The EL spectra of the **4.6→4.6a** device. e) The EL spectral change of the **4.6→4.6a** device during the first 10 s drive. Both devices were operated at a constant driving voltage of 5 V for 30 s. Each spectrum was recorded under 1 s of the constant driving voltage by taking the average of three scans with 0.3 s integration time. Insets: PL spectra of **4.1a** and **4.6a** films, and photographs showing the emission colors of the in situ fabricated EL devices. f) The current density–luminance–voltage diagrams for **4.1**- and **4.6**-based devices.

To monitor the elimination process of **4.1** or **4.6** driven by excitons in the EL devices, the EL spectral power versus time was recorded for the device at a constant driving voltage of 5 V (Figure 4.14b, c). The EL peaks, at roughly 498 and 518 nm, from the **4.1**-based device match the PL

spectrum of **4.1a**, indicating that the mesitylene elimination from **4.1** can indeed be driven by excitons in EL devices. Assuming that the emission intensity of the CBP host at 392 nm is constant, the EDE process can be tracked by monitoring the emission intensity of the main peak. As shown in Figure 4.14b, the emission intensity of the peaks at 498 and 518 nm quickly rises to the maximum within the first 25 s of applied driving voltage, suggesting that the EDE process of **4.1** to **4.1a** in an EL device occurs on a timescale of a few seconds under electrical bias. Based on these observations, the rate of the EDE process is estimated to be at least five orders of magnitude faster than the photoelimination process, which generally takes several hours of UV exposure for doped PMMA films.[8a] This extremely quick and efficient conversion of the BN-heterocyclic precursor to its BN-phenanthrene within the EL device is surprising; it is also the first example of a desirable chemical transformation proceeding within a normal EL device under standard operating conditions. The elimination reaction within the EL device likely proceeds through an excited-state pathway similar to photoelimination discussed in other publications,[8] where the electronic transitions to the relevant excited states of the BN-heterocycle are facilitated by the efficient and highly localized exciton generation within the device.

The **4.6**-based device also displayed fast conversion to the BN-pyrene compound **4.6a** at a constant driving voltage of 5 V, with the EL intensity reaching its maximum within about 10 s (Figure 4.14d, e). The **4.6a**-based device has a distinct yellow EL peak at 575 nm, which matches the photoluminescence properties of **4.6a**. This finding indicates that the double-elimination reaction can also be effectively driven to completion using electrically generated excitons. The weak EL peak at about 520 nm which decreases in intensity with driving time may be from the single-elimination product **4.6int**. The rapid conversion of **4.6** to **4.6a** in the EL device is truly remarkable, particularly given the fact that the double photoelimination of **4.6** is even slower and

158

less efficient than the single photoelimination of **4.1**. The turn-on voltages for the **4.1**- and **4.6**-based devices are 3.8 and 4.2 V, respectively. Both devices demonstrate modest brightness (Figure 4.14f) and current efficiencies (max.≈ 2.4 cdA^{-1}, and 1.9 cdA^{-1} for **4.1** and **4.6**, respectively, see Section 4.5.2), which is mainly a result of the modest photoluminescence quantum efficiency of **4.1a** and **4.6a** (Φ = 0.27). Despite its low volatility (b.p. 165 $^{\circ}$C), the eliminated mesitylene could diffuse rapidly to the hole- and electron-transport layers with an overall concentration of about 0.5%; however, because of its very large HOMO–LUMO gap it is unlikely to trap charges or excitons and thus has little to no influence on the EL device performance.

Compounds **4.8** and **4.9** were also found to undergo rapid EDE, producing the corresponding BN-phenanthrenes[8] and their green EL devices, in analogy to the reactions of **4.1** (see Section 4.5.2). EDE in an EL device does not work well for BN-heterocycles that have alkyl substituents on the B atom such as 1,5-cyclooctyl (**2.5**, see Section 4.5.2)[8c] and the B(CH$_3$)$_2$ analogue (m.p. 120 $^{\circ}$C)[8a] due to the low phase-transition temperature of the precursors and products.

4.4 Conclusions

Six new (BN)$_2$-heterocycles with extended conjugated backbones have been synthesized. The impact of the linker unit and the location of the boron chelate unit on the electronic properties and photoreactivity of this class of compounds have been examined. The experimental and computational data suggests that the location of BN units, the steric congestion, and the linker unit within the π-conjugated backbone can greatly affect the electronic structure of these molecules as well as their photophysical/photochemical properties. Diboron BN-heterocycles that share the central linker unit appear to be either unstable or have a poor reactivity toward light while those that do not share the central linker can undergo double photoelimination with the sterically congested one being more effective. Two BN-pyrene derivatives and one bis-BN-phenanthrene

159

have been achieved *via* a double mesitylene-elimination reaction. Furthermore, we have established that the photoelimination reaction can be extended to/and efficiently driven for several representative members of BN-heterocycles *in situ* through the unprecedented EDE within an EL device. The discovery of the EDE phenomenon has a number of important synthetic and practical implications, as it provides a new approach for the design and preparation of novel organic materials as well as their implementation within optoelectronic device architectures. We envision that this strategy will be most valuable for the *in situ* conversion/processing of stable, soluble, and readily accessible poly-BN-heterocyclic systems with high thermal stability to less stable, less soluble, and not directly accessible but highly functional poly-BN-aromatic hydrocarbons for OFETs or OLEDs. We are currently investigating the scope and applications of this unusual phenomenon.

4.5 Appendix

4.5.1 DFT Calculation Data

4.5.1.1 Computation Data for **4.2** - **4.5** and **4.4a**

The calculations of **4.2** - **4.5** and **4.2a** - **4.5a** were performed using the Gaussian 09 suite[13] of programs on the High Performance Computing Virtual Laboratory (HPCVL) at Queen's University. Initial input coordinates were taken from the corresponding crystal structure data where applicable. All ground state geometry optimizations and TD-DFT vertical excitations were performed at the B3LYP level of theory employing the 6-31g(d) basis set[14] for all atoms.

Table 4.3 HOMO and LUMO energy levels.

Compounds	LUMO /eV	HOMO /eV
4.2-Ligand	-1.06	-5.76
4.2	-2.15	-5.19
4.3-Ligand	-1.26	-5.49
4.3	-1.89	-5.21
4.4-Ligand	-1.28	-5.89
4.4	-2.08	-5.32

Table 4.4 TD-DFT calculated electronic transitions for **4.2** along with their corresponding excitation energies and oscillator strengths (iso = 0.03).

Compd	Spin State	Transition Configuration	Excitation Energy (nm, eV)	Oscillator Strength
4.2	S_1	HOMO->LUMO (98%)	497.26 nm (2.49 eV)	0.0000
	S_2	H-1->LUMO (98%)	491.03 nm (2.52 eV)	0.0005
	S_3	H-2->LUMO (99%)	453.92 nm (2.73 eV)	0.0039
	S_4	H-3->LUMO (99%)	453.31 nm (2.85 eV)	0.0004

LUMO -2.15 eV	HOMO -5.19 eV	HOMO-1 5.22 eV
HOMO-2 5.40 eV	HOMO-3 -5.51 eV	
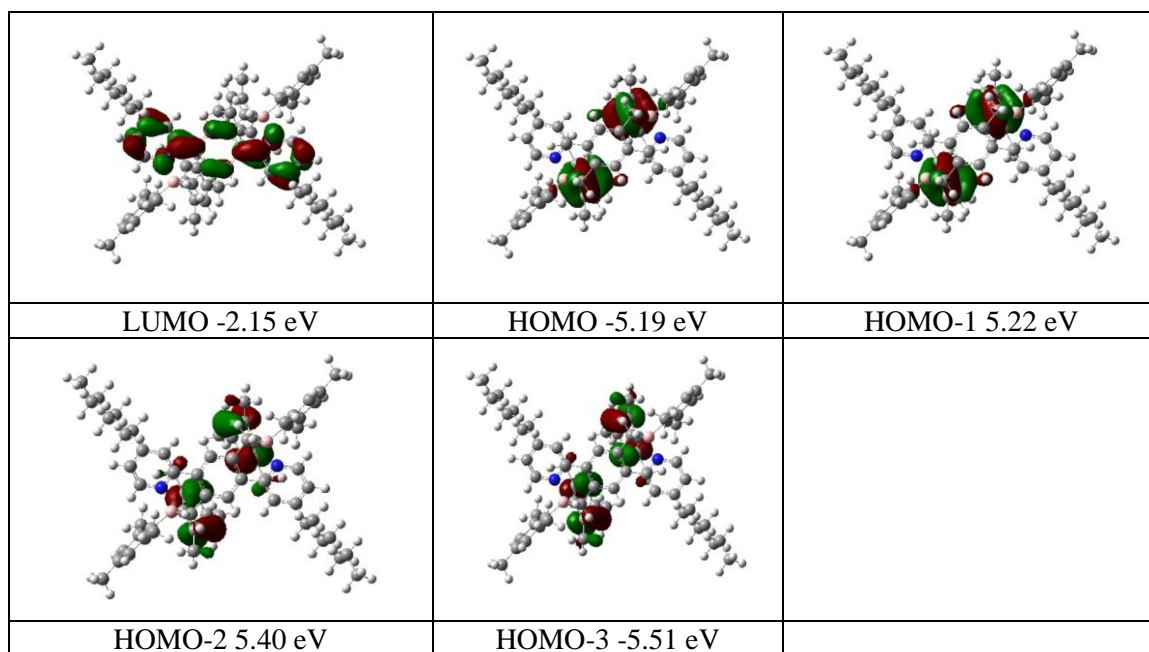
Table 4.5 TD-DFT calculated electronic transitions for **4.3** along with their corresponding excitation energies and oscillator strengths (iso = 0.03).

Compound	Spin State	Transition Configuration	Excitation Energy (nm, eV)	Oscillator Strength
4.3	S$_1$	HOMO->LUMO (72%), HOMO->L+1 (27%)	443.67 nm (2.79 eV)	0.0032
	S$_2$	H-1->LUMO (74%), H-1->L+1 (25%)	438.34 nm (2.83 eV)	0.001
	S$_3$	H-2->LUMO (75%), H-2->L+1 (22%)	401.84 nm (3.08 eV)	0.0435

LUMO+1 -1.69 eV	LUMO -1.89 eV	HOMO -5.21 eV
HOMO-1 -5.25 eV	HOMO-2 -5.46 eV	
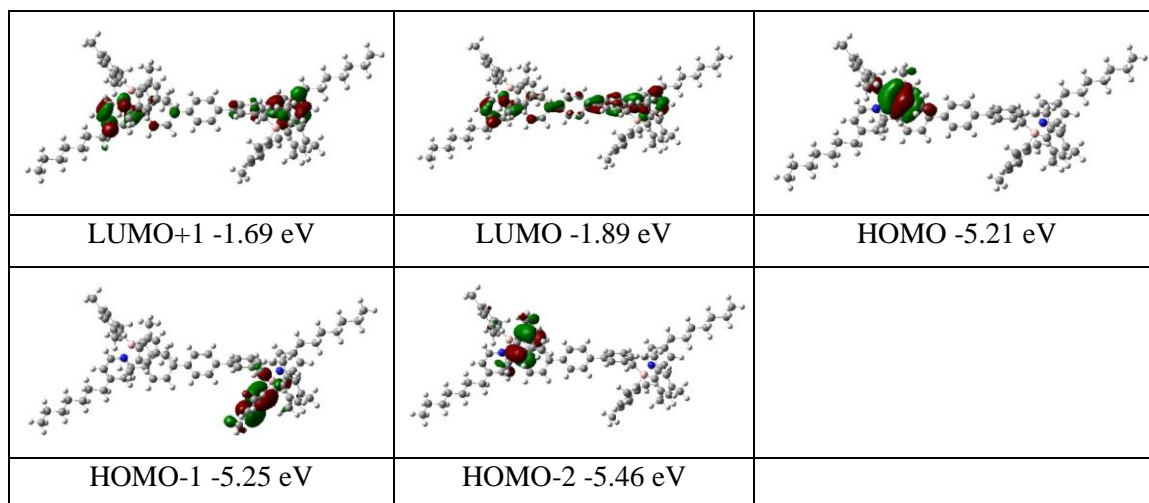
Table 4.6 TD-DFT calculated electronic transitions for **4.4** along with their corresponding excitation energies and oscillator strengths (iso = 0.03).

Compound	Spin State	Transition Configuration	Excitation Energy (nm, eV)	Oscillator Strength
4.4	S_1	HOMO->LUMO (76%), HOMO->L+1 (14%) H-1->L+1 (7%)	450.72 nm (2.75 eV)	0.0027
	S_2	H-1->LUMO (76%), H-1->L+1 (14%) HOMO->L+1 (7%)	450.70 nm (2.75 eV)	0.0005
	S_3	H-3->L+1 (18%), H-2->LUMO (81%)	408.03 nm (3.04 eV)	0.0212

LUMO+1 -1.82 eV	LUMO -2.08 eV	HOMO -5.33 eV
HOMO-1 -5.33 eV	HOMO-2 -5.58 eV	HOMO-3 -5.58 eV
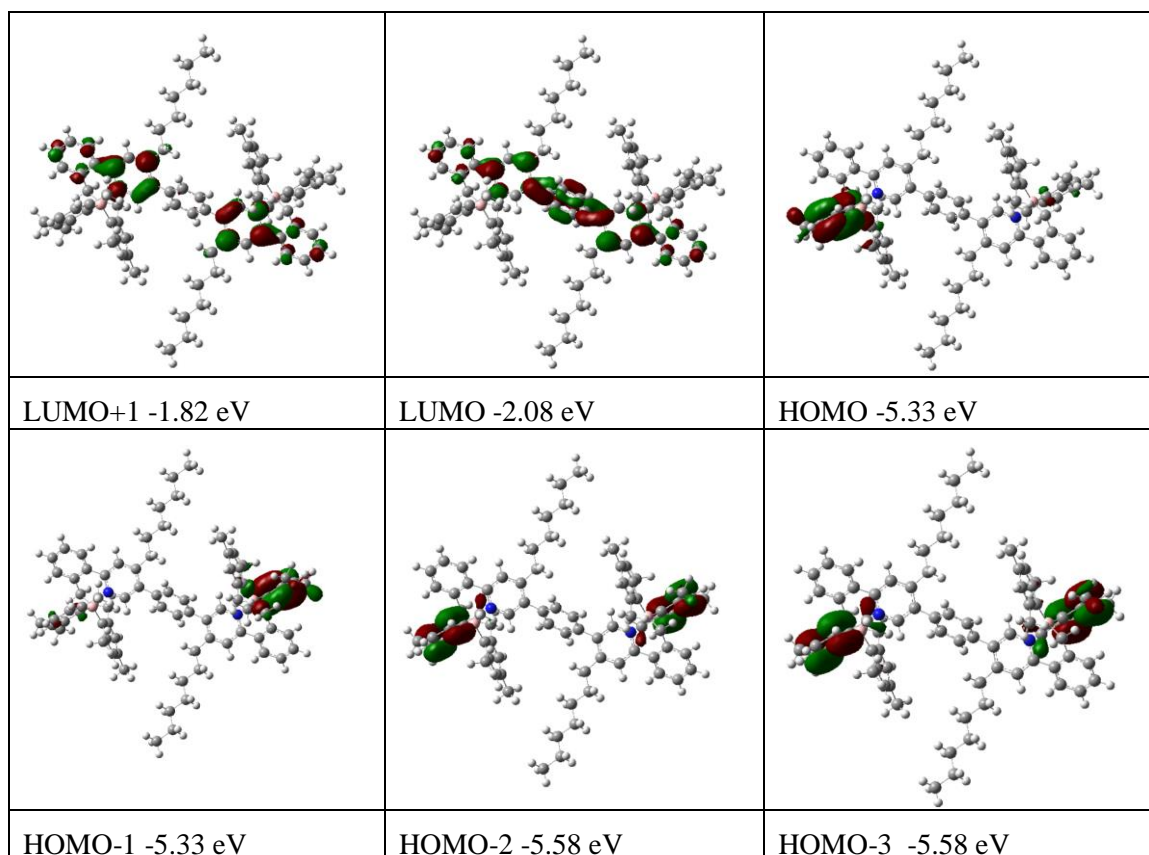
Table 4.7 TD-DFT calculated electronic transitions for **4.5** along with their corresponding excitation energies and oscillator strengths (iso = 0.03).

Compound	Spin State	Transition Configuration	Excitation Energy (nm, eV)	Oscillator Strength
4.5	S$_2$	H-1->LUMO (98%)	521.31 nm (2.38 eV)	0.0009
	S$_3$	H-2->LUMO (97%)	470.26 nm (2.64 eV)	0.0118
	S$_5$	H-4->LUMO (95%)	454.95 nm (2.72 eV)	0.0851

LUMO -2.59 eV	HOMO -5.18 eV	HOMO-1 -5.51 eV
HOMO-2 -5.74 eV	HOMO-4 -5.87 eV	
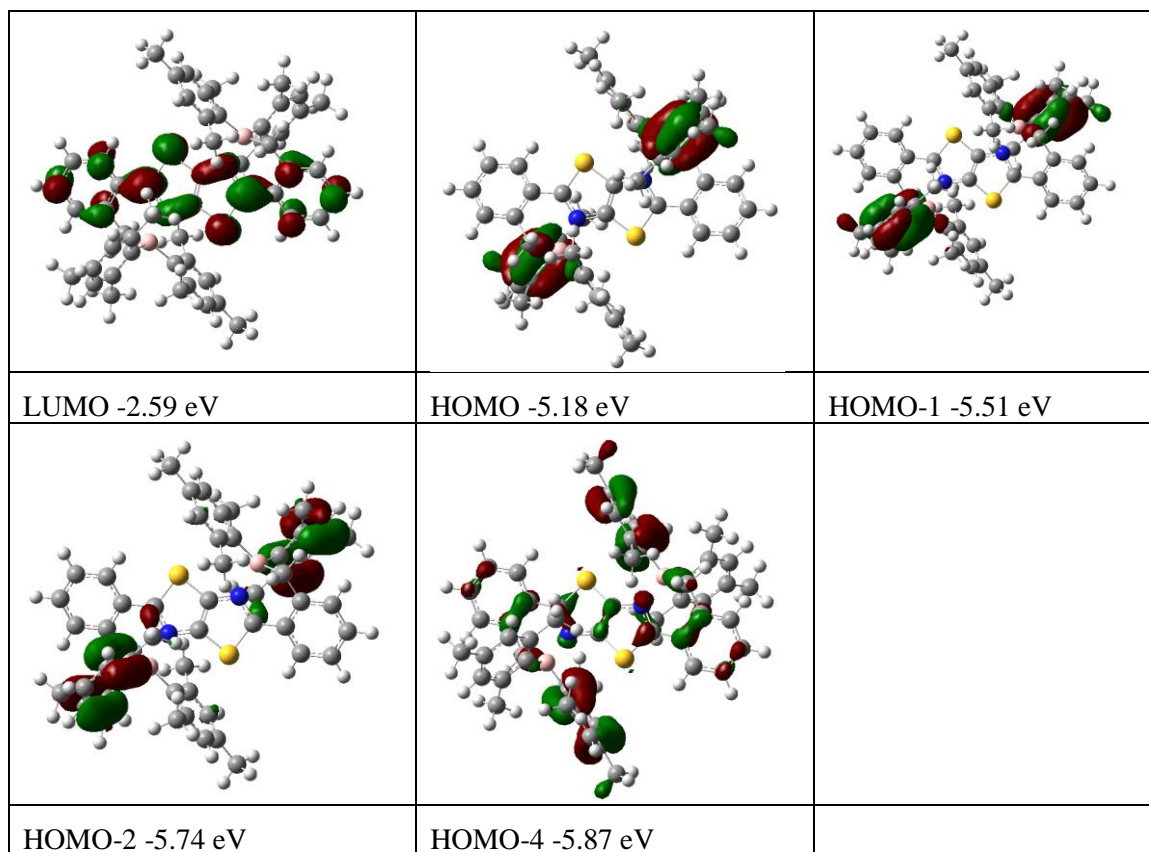
Table 4.8 TD-DFT calculated electronic transitions for **4.4a** along with their corresponding excitation energies and oscillator strengths (iso = 0.03).

Compound	Spin State	Transition Configuration	Excitation Energy (nm, eV)	Oscillator Strength
4.4a	S$_1$	HOMO->LUMO (83%), HOMO->L+2 (10%) H-1->L+3 (5%)	446.38 nm (2.78 eV)	0.168
	S$_2$	H-1->LUMO (78%), H-1->L+2 (14%) HOMO->L+3 (7%)	439.55 nm (2.82 eV)	0.0606
	S$_3$	H-1->L+2 (13%), HOMO->L+1 (76%) H-1->LUMO (4%), HOMO->L+3 (6%)	404.48 nm (3.06 eV)	0.0368

LUMO+3 -0.99 eV	LUMO+2 -1.20 eV	LUMO+1 -1.45 eV
LUMO -1.62 eV	HOMO -4.75 eV	HOMO-1 -4.77 eV
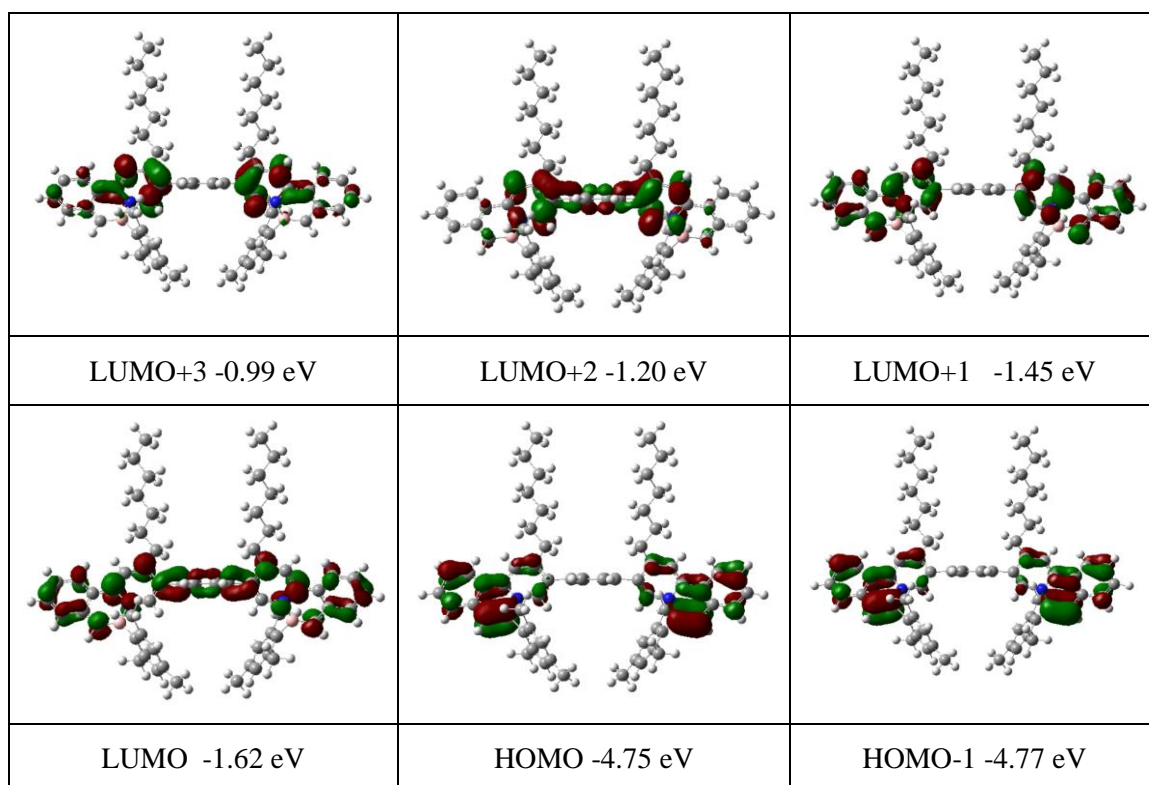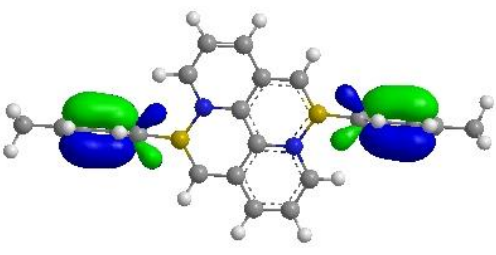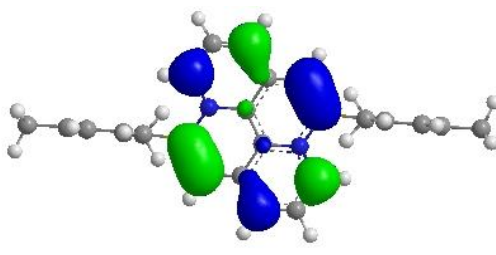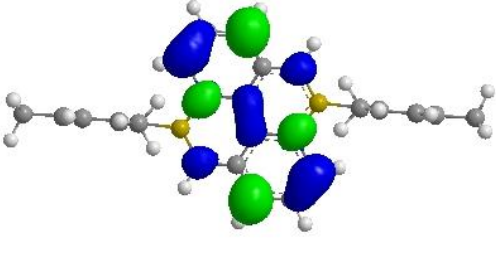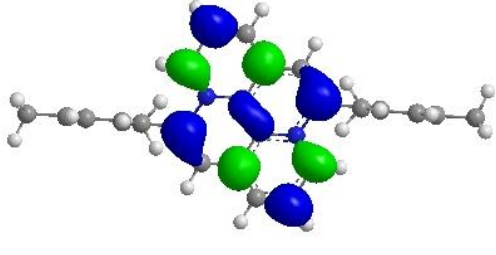
4.5.1.2 TD-DFT calculations on electronic transitions of BN-pyrenes.

The computational calculations were performed using Gaussian 09 software package and the High Performance Computing Virtual Laboratory (HPCVL) at Queen's University. All computations were performed at the B3LYP level of theory using 6-311++g(d,p) basis set[12] for all atoms.

Table 4.9 TD-DFT calculated electronic transitions for **4.6a** along with their corresponding excitation energies and oscillator strengths (iso = 0.03).

Compound	Excited State	Transition configuration	Transition Energy	Oscillator strength
4.6a	S_1	H→L 97%	515.43 nm (2.41 eV)	0.1970
	S_5	H→L +1 86%	378.47 nm (3.28 eV)	0.2144
	S_7	H-4→L 98%	371.78 nm (3.33 eV)	0.0075

HOMO-4	-6.39 eV	HOMO	-5.02 eV
LUMO	-2.56 eV	LUMO+1	-1.24 eV

4.5.1.3 DFT Calculation on the double elimination pathway of **4.6**.

The calculations of **4.6** were performed using the Gaussian 09 suite of programs[13] on the High Performance Computing Virtual Laboratory (HPCVL) at Queen's University. Initial input coordinates were taken from the corresponding crystal structure data where applicable, while all others were generated from the optimized geometry of **4.6**. Modeling of the reaction pathway was accomplished using the B3LYP level of theory and the 6-31g(d) basis set,[14] as this combination was found to accurately reproduce the experimentally determined UV-Vis spectrum of a reference compound in the same class considered here. All reactant, intermediate and product geometries were optimized without constraints and characterized as minima along the potential energy surfaces through vibrational frequency analysis. Transition state structures were located by employing the QST3 option in Gaussian and contained only one imaginary frequency. Subsequent single point energy calculations were performed for each structure at the B3LYP/6-31+g(d,p) level of theory, where the implicit solvent effects of benzene were accounted for with the conducting polarizable continuum model (C-PCM).[18] Due to convergence issues of **TS2** as a result of free mesitylene translational motion, this transition state structure was first optimized without the free mesitylene, after which the total energy was calculated from the coordinates described below.
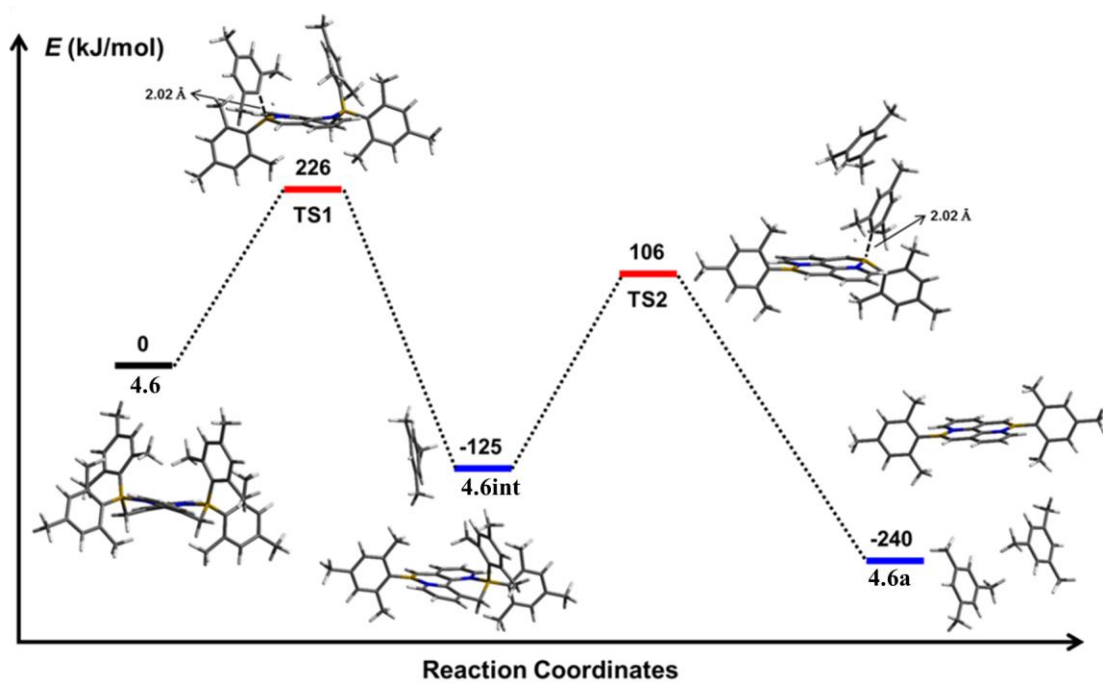
Figure 4.15 Relative ground state energies and structures calculated for the reactant, intermediate, transition states, and product involved in the stepwise meistylene elimination pathway of **4.6**.

4.5.2 Selected Supporting Information
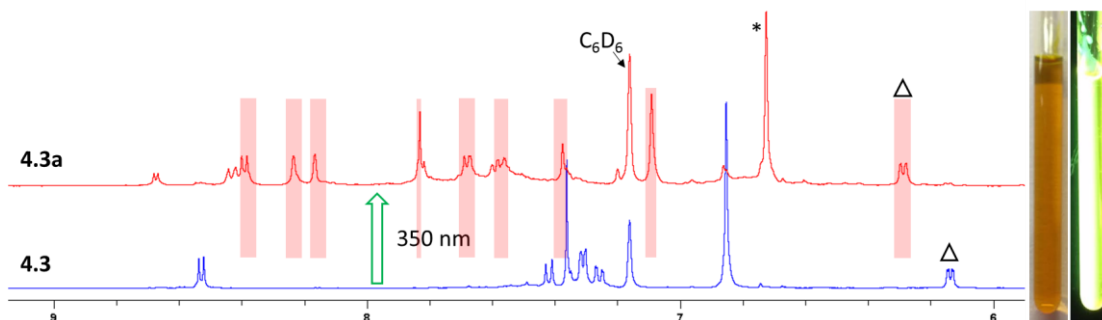
Figure 4.16 ^{1}H NMR spectra showing the partial conversion of **4.3** (bottom) to **4.3a** (top, red highlight) in C_6D_6 under 350 nm irradiation at room temperature. The mesitylene produced is marked with an asterisk and the peaks used for calculating conversion yield relative to the solvent peak are marked with Δ. The aliphatic region is not shown because it is mostly obscured by the heptyl peaks.
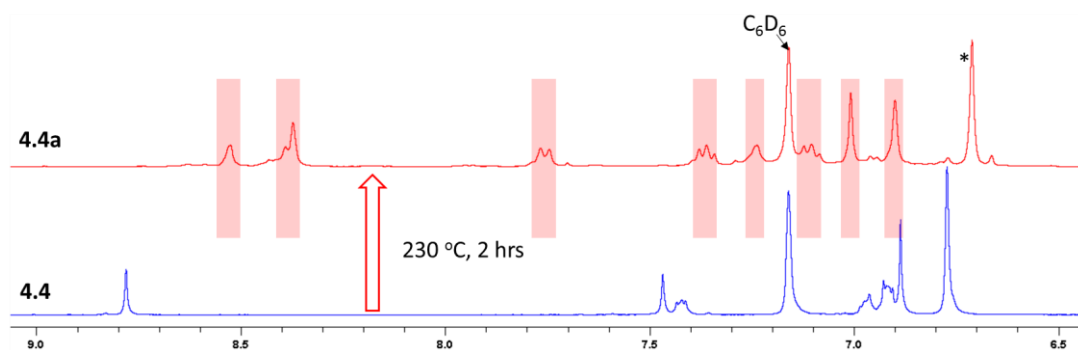
Figure 4.17 ^{1}H NMR spectra showing the clean conversion of **4.4** (bottom, recorded in C_6D_6.) to **4.4a** (top, red highlight, recorded in C_6D_6 in the presence of ~0.1 mL of mineral oil used in heating) after heating in mineral oil at 230 °C. The mesitylene peak was marked with an asterisk. The broad peaks were caused by mineral oil.
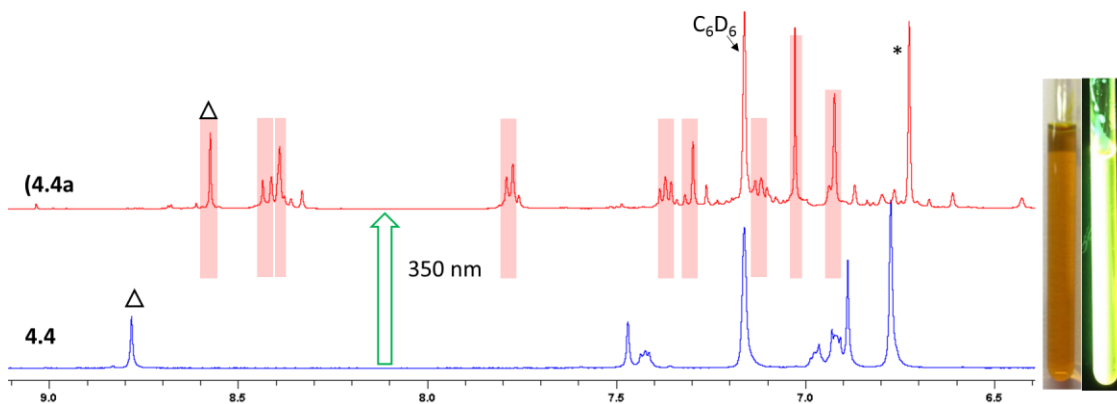
Figure 4.18 ^{1}H NMR spectra showing the clean conversion of **4.4** (bottom) to **4.4a** (top, red highlight) in C$_6$D$_6$ under 350 nm irradiation at room temperature. The mesitylene produced is marked with an asterisk and the peaks used for calculating conversion yield relative to the solvent peak are marked with Δ. The aliphatic region is not shown because it is mostly obscured by the heptyl peaks.
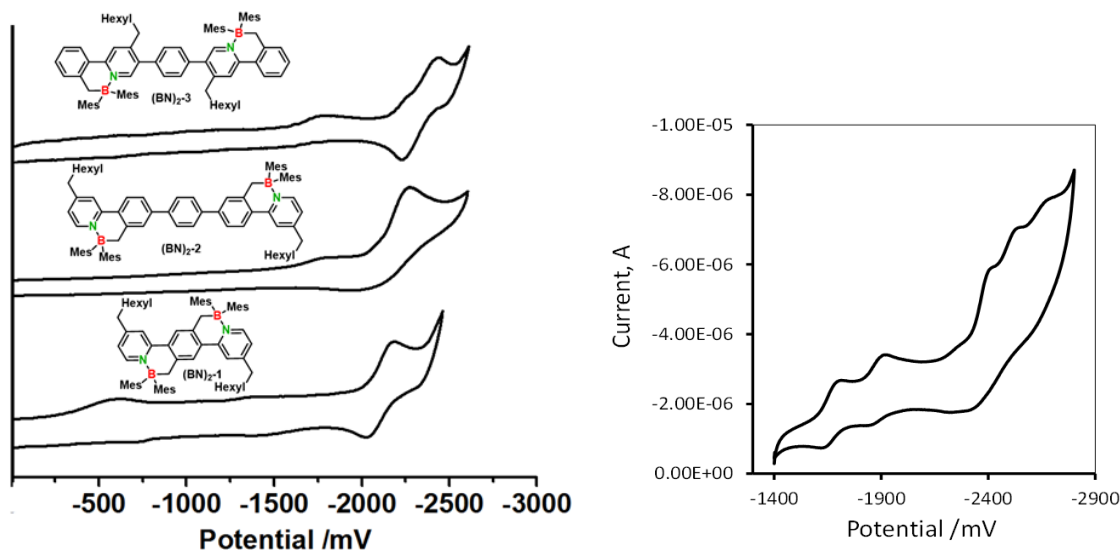
Figure 4.19 CV diagrams of **4.2** - **4.5** (*vs* Fc/FcH$^+$) showing the reduction waves at a 100 mV/s scan rate with [Bu$_4$N]$^+$[PF$_6$]$^-$ as the electrolyte (**4.2** - **4.4**, left) in THF and (**4.5**, right) in DMF.

170
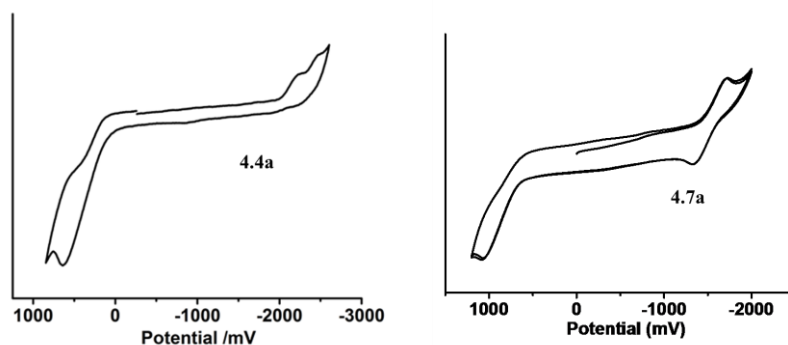
Figure 4.20 CV diagrams of **4.4a** and **4.7a** (vs [FeCp$_2$]$^+$/[FeCp$_2$]) showing the reduction and oxidation waves at a 100 mV/s scan rate with [Bu$_4$N]$^+$[PF$_6$]$^-$ as the electrolyte in THF.
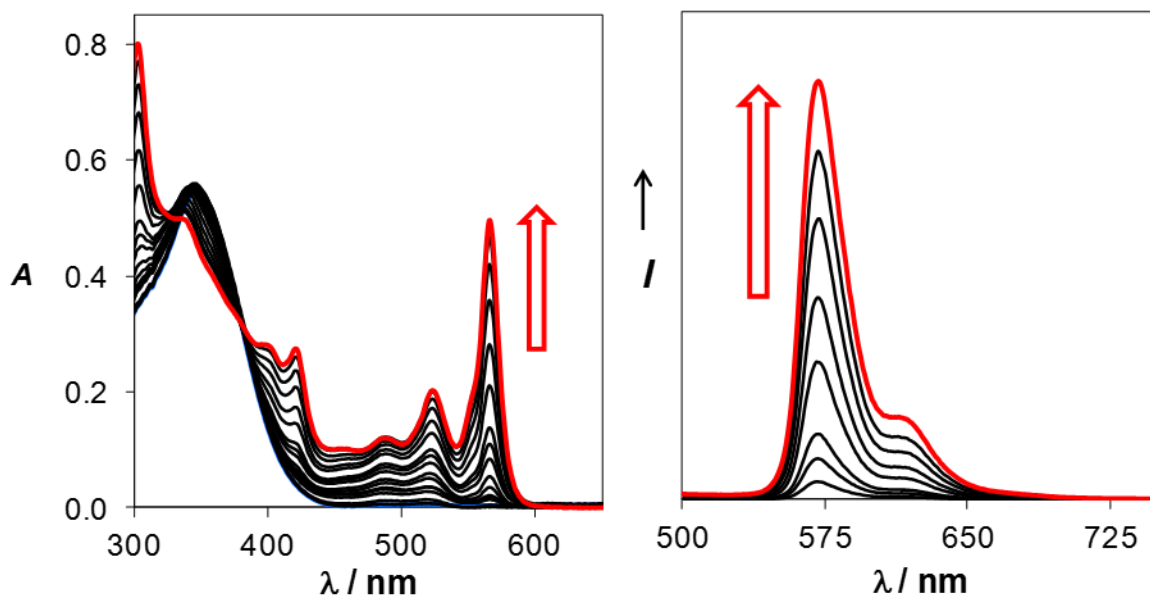
Figure 4.21 The Spectral tracking of the **4.6**→**4.6a** conversion. Left: the absorption spectral change. Right: the fluorescence change (λ_{ex} = 420 nm) spectral change of **4.6** in THF upon irradiation at 350 nm. The absorption and fluorescence spectra were recorded under nitrogen at about 10-20 minutes intervals during which time the cuvette that contains the sample was kept inside an UV-reactor equipped with 350 nm light bulbs.
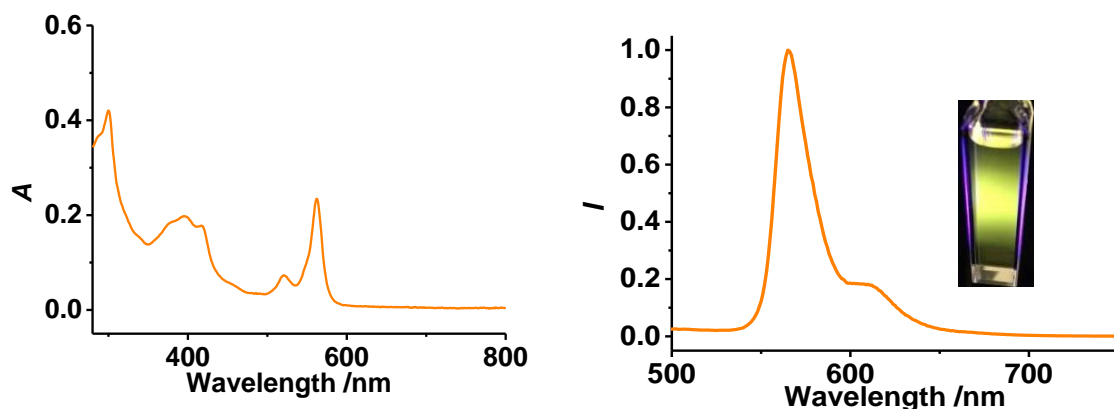
Figure 4.22 The absorption (left) and fluorescence (right) spectra of **4.7a** in THF. The fluorescence spectra are recorded at the λ_{ex} = 420 nm. The full time-lapsed spectra of conversion **4.7** → **4.7a** could not be obtained. The UV-Vis and fluorescence of **4.7a** were measured by using the photoelimination product of **4.7**. The concentration of **4.7a** was about 10^{-5} M.
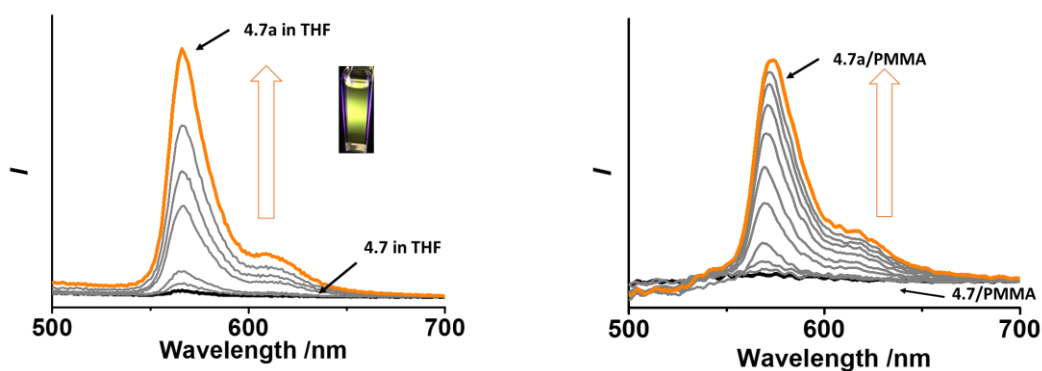
Figure 4.23 The fluorescence spectral change of **4.7** in THF (left) and in PMMA film (20 wt%) with irradiation (300 nm) time. The fluorescence spectra are recorded at the λ_{ex} = 420 nm. The procedure of solid-state conversion of compound **4.7** in PMMA films is as follow: About 10 mg of the purified PMMA powder and 2 mg of **4.7** were mixed and dissolved in 2 mL of dry THF in a glove box. The solution was used to cast a thin film on a quartz J-Young NMR tube. After the film was dried, it was subjected to UV irradiation at 300 nm.
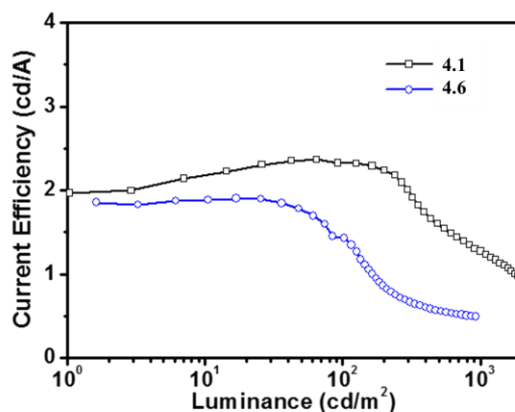
Figure 4.24 The current efficiency versus luminance curves for **4.1** and **4.6**-based devices.
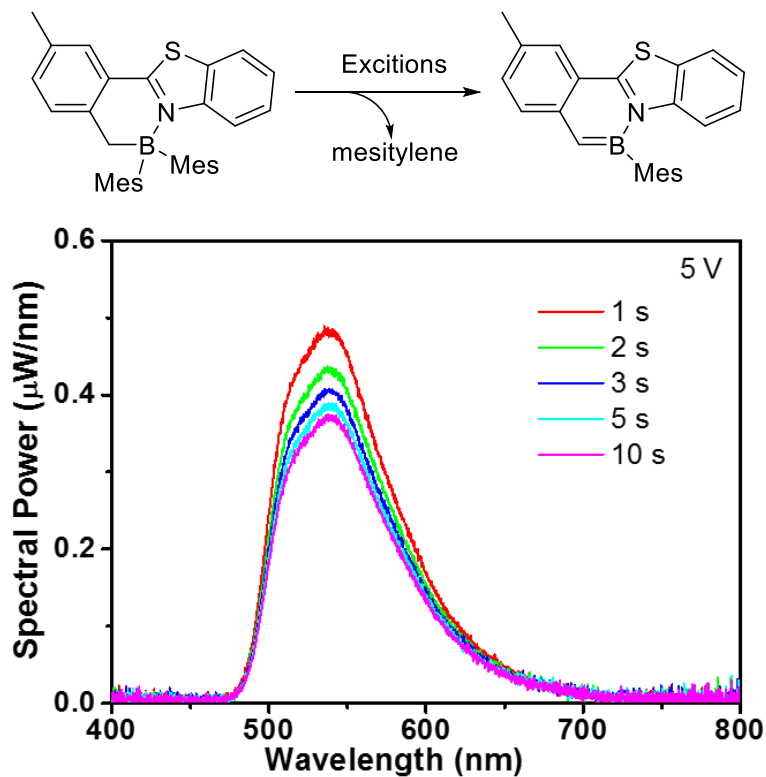
Figure 4.25 The spectral power of the device based on **4.8** at a constant driving voltage of 5 V for the first 10 s. Each spectrum was recorded under 1 s of the constant driving voltage by taking the average of 3 scans with 0.3 s integration time.
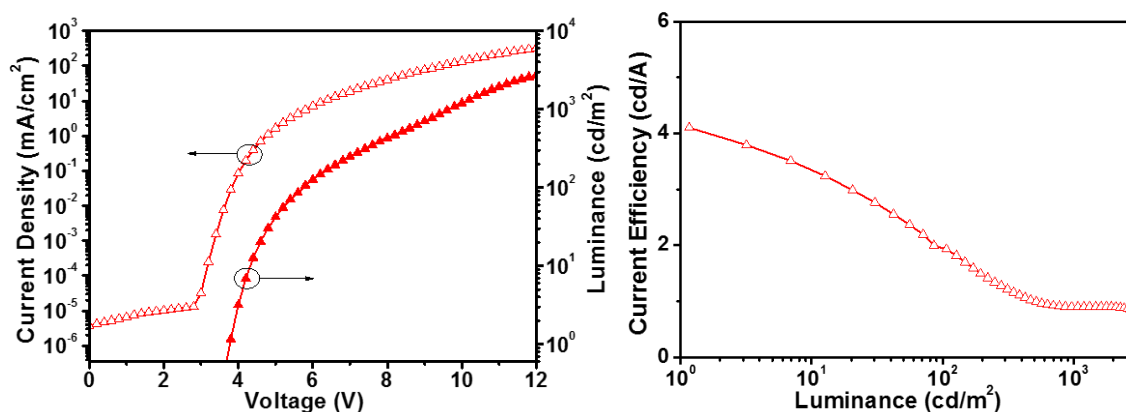
Figure 4.26 The current density-luminance-voltage diagrams (Left) and the current efficiency versus luminance curves (Right) for **4.8**-based device.
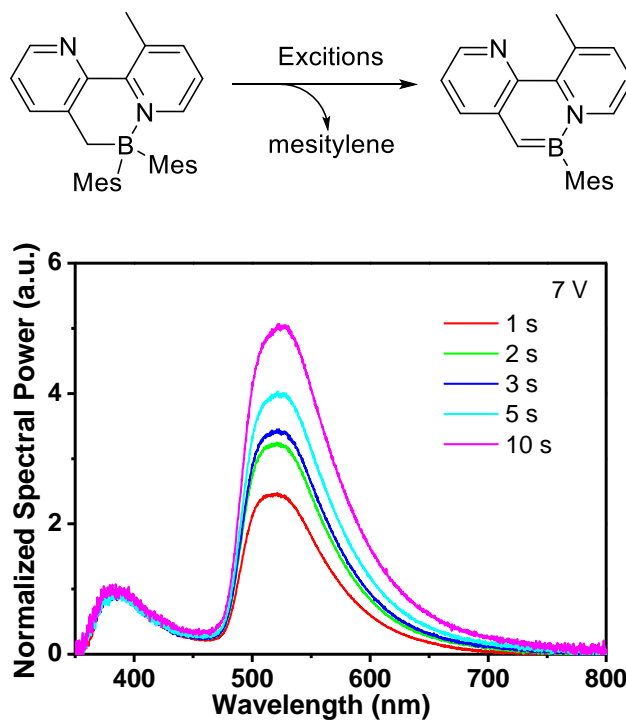
Figure 4.27 The normalized spectral power of the device based on **4.9** at a constant driving voltage of 7 V for the first 10 s. Each spectrum was recorded under 1 s of the constant driving voltage by taking the average of 3 scans with 0.3 s integration time. The shoulder peak is from the CBP host.
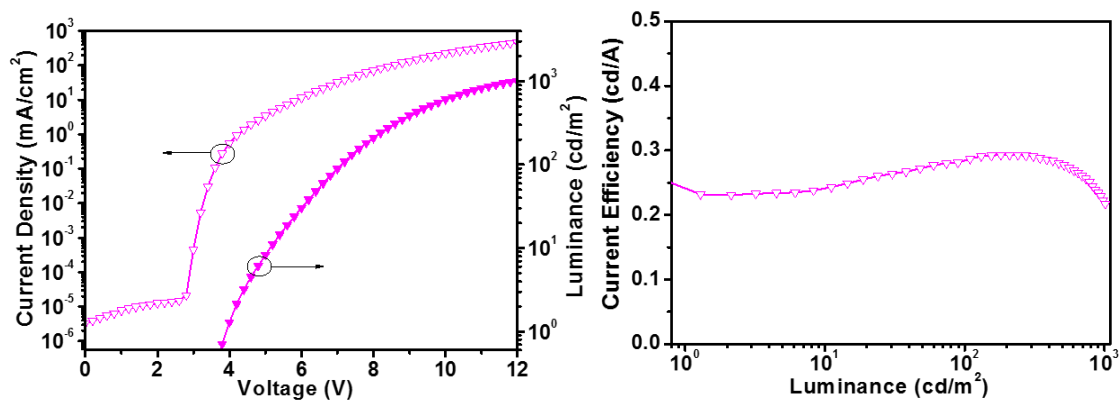
Figure 4.28 The current density-luminance-voltage diagrams (Left) and the current efficiency versus luminance curves (Right) for **4.9**-based device.
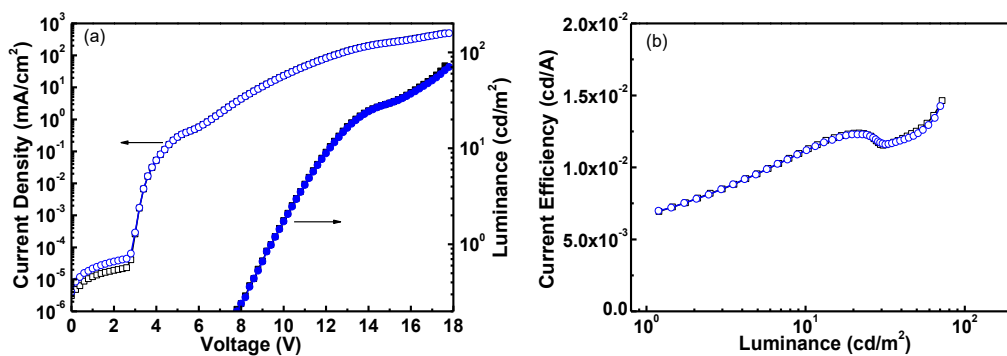
Figure 4.29 Left: Current density-voltage-luminance characteristics (*J-V-L*). Right: current efficiency versus luminance curves for the devices based on **2.5**. Due to the poor performance of this device, EL spectra were too weak to be recorded.

4.6 Notes and References

The work described in this chapter includes contributions from the following publications:

- Wang, S.; * Yang, D.-T.; Lu, J.; Shimogawa, H.; Gong, S.; Wang, X.; Mellerup, S. K.; Wakamiya, A.; Chang, Y.-L.; Yang, C.; Lu, Z. H. *Angew. Chem., Int. Ed.* **2015**, *54*, 15074.

- Yang, D.-T.; Shi, Y.; Peng, T.; Wang, S.* *Organometallics* **2017**, *36*, 2654.

References:

(1) (a) Liu, Z.; Marder, T. B. *Angew. Chem. Int. Ed.* **2008**, *47*, 242. (b) Bosdet, M. J. D.; Piers, W. E. *Can. J. Chem.* **2009**, *87*, 8. c) Campbell, P. G.; Marwitz, A. J. V.; Liu, S.-Y. *Angew. Chem. Int. Ed.* **2012**, *51*, 6074. (d) Wang, X.-Y.; Wang, J.-Y. Pei, J. *Chem. Eur. J.* **2015**, *21*, 3528. (e) Narita, A.; Wang, X.-Y.; Feng, X.; Müllen, K. *Chem. Soc. Rev.* **2015**, *44*, 6616. (f) Stępień, M. Gońka, E.; Żyła, M.; Sprutta, N. *Chem. Rev.*, **2017**, *117*, 3479. (g) Schäfer, M.; Beattie, N. A.; Geetharani, K.; Schäfer, J.; Ewing, W. C.; Krahfuß, M.; Hörl, C.; Dewhurst, R. D.; Macgregor, S. A.; Lambert, C.; Braunschweig, H. *J. Am. Chem. Soc.* **2016**, *138*, 8212. (h) Chen, P.; Lalancette, R. A.; Jäkle, F. *Angew. Chem. Int. Ed.* **2012**, *51*, 7994. (i) Wakamiya, A.; Taniguchi, T.; Yamaguchi, S. *Angew. Chem. Int. Ed.* **2006**, *45*, 3170. (j) Bosdet, M. J. D.; Piers, W. E.; Sorensen, T. S.; Parvez, M. *Angew. Chem. Int. Ed.* **2007**, *46*, 4940. (k) Jaska, C. A.; Piers, W. E.; McDonald, R.; Parvez, M. *J. Org. Chem.* **2007**, *72*, 5234.

(2) (a) Hatakeyama, T.; Hashimoto, S.; Seki, S.; Nakamura, M. *J. Am. Chem. Soc.* **2011**, *133*, 18614. (b) Wang, X.-Y.; Lin, H.-R.; Lei, T.; Yang, D.-C.; Zhuang, F.-D.; Wang, J.-Y.; Yuan, S.-C.; Pei, J. *Angew. Chem. Int. Ed.* **2013**, *52*, 3117. (c) Katayama, T.; Nakatsuka, S.; Hirai, H.; Yasuda, N.; Kumar, J.; Kawai, T.; Hatakeyama, T. *J. Am. Chem. Soc.* **2016**, *138*, 5210.

(3) Wade, C. R.; Broomsgrove, A. E. J.; Aldridge, S.; Gabbäi, F. P. *Chem. Rev.* **2010**, *110*, 3958.

(4) (a) Crossley, D. L.; Cid, J.; Curless, L. D.; Turner, M. L.; Ingleson, M. J. *Organometallics* **2015**, *34*, 5767. (b) Grandl, M.; Rudolf, B.; Sun, Y.; Bechtel, D. F.; Pierik, A. J.; Pammer, F. *Organometallics* DOI: 10.1021/acs.organomet.6b00916.

(5) (a) Dou, C.; Ding, Z.; Zhang, Z.; Xie, Z.; Liu, J.; Wang, L. *Angew. Chem. Int. Ed.* **2015**, *54*, 3648. (b) Zhao, R.; Dou, C.; Xie, Z.; Liu, J.; Wang, L. *Angew. Chem. Int. Ed.* **2016**, *55*, 5313. (c) Long, X.; Ding, Z.; Dou, C.; Zhang, J.; Liu, J.; Wang, L. *Adv. Mater.* **2016**, *28*, 6504.

(6) (a) Dewar, M. J. S. *Tetrahedron* **1959**, *7*, 213; (b) Dewar, M. J. S.; Dietz, R. *J. Chem. Soc.* **1959**, 2728; (c) Dewar, M. J. S.; Marr, P. A. *J. Am. Chem. Soc.* **1962**, *84*, 3782; (d) White ,D. G., *J. Am. Chem. Soc.* **1963**, 85, 3634; (e) Dewar, M. J. S.; Poesche, W. H. *J. Org. Chem.* **1964**, *29*, 1757. (f) Chissick, S. S.; Dewar, M. J. S. Maitlis, P.W. *Tetrahedron Lett.* **1960**, *23*, 8.

(7) Hatakeyama, T.; Shiren, K.; Nakajima, K.; Nomura, S.; Nakatsuka, S.; Kinoshita, K.; Ni, J.; Ono, Y.; Ikuta, T. *Adv. Mater.* **2016**, *28*, 2777.

(8) (a) Lu, J. S.; Ko, S. B.; Walters, N. R.; Kang, Y.; Sauriol, F.; Wang, S. *Angew. Chem. Int. Ed.* **2013**, *52*, 4544; (b) Ko, S.-B.; Lu, J.-S.; Wang, S. *Org. Lett.* **2014**, *16*, 616; (c) Yang, D.-T.; Mellerup, S. M.; Wang, X.; Lu, J.-S.; Wang, S. *Angew. Chem. Int. Ed.* **2015**, *54*, 5498.

(9) Sajoto, T.; Djurovich, P. I.; Tamayo, A. B.; Oxgaard, J.; Goddard III, W. A.; Thompson, M. E.; J. *Am. Chem. Soc.* **2009**, *131*, 9813.

(10)   Yanai, T.; Tew, D.; Handy, N. *Chem. Phys. Lett.* **2004**, *393*, 51.

(11)   (a) SHELXTL *Version 6.14* (Bruker Analytical X-ray Systems, copyright 2000–2003). (b) PLATON, 1980-2014, Spek, A. L., Utrecht University, Padualaan 8, 3584 CH Utrecht, The Netherlands, reference: Spek, A. L. *Acta Cryst.* **2009**, *D65,* 148.

(12) Gaussian 09, Revision E.01, Frisch, M. J.; Trucks, G. W.; Schlegel, H. B.; Scuseria, G. E.;

Robb, M. A.; Cheeseman, J. R.; Scalmani, G.; Barone, V.; Mennucci, B.; Petersson, G. A.;

Nakatsuji, H.; Caricato, M.; Li, X.; Hratchian, H. P.; Izmaylov, A. F.; Bloino, J.; Zheng, G.;

Sonnenberg, J. L.; Hada, M.; Ehara, M.; Toyota, K.; Fukuda, R.; Hasegawa, J.; Ishida, M.;

Nakajima, T.; Honda, Y.; Kitao, O.; Nakai, H.; Vreven, T.; Montgomery, Jr., J. A.; Peralta,

J. E.; Ogliaro, F.; Bearpark, M.; Heyd, J. J.; Brothers, E.; Kudin, K. N.; Staroverov, V. N.;

Keith, T.; Kobayashi, R.; Normand, J.; Raghavachari, K.; Rendell, A.; Burant, J. C.; Iyengar,

S. S.; Tomasi, J.; Cossi, M.; Rega, N.; Millam, J. M.; Klene, M.; Knox, J. E.; Cross, J. B.;

Bakken, V.; Adamo, C.; Jaramillo, J.; Gomperts, R.; Stratmann, R. E.; Yazyev, O.; Austin,

A. J.; Cammi, R.; Pomelli, C.; Ochterski, J. W.; Martin, R. L.; Morokuma, K.; Zakrzewski,

V. G.; Voth, G. A.; Salvador, P.; Dannenberg, J. J.; Dapprich, S.; Daniels, A. D.; Farkas, O.;

Foresman, J. B.; Ortiz, J. V.; Cioslowski, J.; Fox, D. J. Gaussian, Inc., Wallingford CT, 2013.

(13) (a) Ditchfield, R.; Hehre, W.J.; Pople, J. A. *J. Chem. Phys.* **1971**, *54*, 724. (b) McLean, A.

D.; Chandler, G. S. *J. Chem. Phys.* **1980**, *72*, 5639. (c) Lee, C.; Yang, W.; Parr, R. G. *Phys.

Rev. B: Condens. Matter Mater. Phys.* **1988**, *37*, 785.

(14) Turro, N. J.; Ramamurthy, V.; Scaiano, J. C. Principles of Molecular Photochemistry: An

Introduction, University Science Books, Sausalito, 2009.

(15) Liao, L.-Y.; Kong, X.-R.; Duan, X.-F. *J. Org. Chem.* **2014**, *79*, 777.

178

Chapter 5

Investigation on the Effect of Substituents on the Photorectivity of BN-Heterocycles

5.1 Introduction

Controlling the fate of chemical transformations is one of the cornerstones of modern chemistry and biology. Although nature has achieved this feat by employing molecular architectures (*e.g.*, enzymes),[1] chemists rely heavily on manipulating the steric and electronic factors of small molecules/complexes[2] to promote desired reaction outcomes. For example, steric/electronic considerations have proven highly effective in both the stabilization of rare chemical entities[3] as well as the facilitation of unique molecular transformations.[4] Recently, similar strategies have been applied to organoboron systems, which has demonstrated the remarkable breadth of varying reactivity and functions available to these species[5] (*e.g.,* optoelectronics,[5b,h] catalytic components,[5i,l] organic synthons, [5m,q] etc.). We have had a long-standing interest in the photoresponsive properties of organoboron compounds[6,7] and have previously shown that BN-heterocycles such as **2.3** (R =Me, X = H; Figure 5.1) are capable of undergoing photoelimination of mesitylene to produce fully conjugated and highly luminescent BN-phenanthrenes **2.3a**.[6d] Although this transformation does provide a new method of preparing these BN-phenanthrene isomers and allow for the *in situ* generation of optoelectronic devices such as OLEDs based on such BN systems,[7] the low quantum efficiency of the photoreaction ($\Phi_{PE} \leq 0.044$) severely limits its synthetic and practical usefulness. Inspection of the DFT-calculated transition state for this reaction revealed that B−C_{Ar} bond breaking is likely the rate-limiting step.[6f] Therefore, we postulated that weakening the B−C_{Ar} bond through either greater steric encumberment, i.e., replacing the Mes groups in **2.3** with 2,4,6-

triisopropylphenyl (tipp, **5.1**) or bulky/strongly electron-withdrawing groups such as 2,4,6-trifluoromethylphenyl (MesF, **5.2**), could improve the efficiency of the photoelimination. Indeed, this strategy proved successful with respect to **5.1**, which eliminated much more efficiently than **2.3**. However, instead of elimination, **5.2** exhibited an unprecedented photochromic switching around the boron core, generating an intensely colored and previously unknown BN-1,3,5-cyclooctatriene (COT). Further investigation revealed that the photochemical formation of BN-1,3,5-COT is a general phenomenon for BN-heterocycles with electron-deficient aryl groups on boron, establishing the possibility to control such molecular transformations by tuning the steric and electronic properties of the molecule. The details of the two distinct phototransformations and mechanistic insights are presented herein.
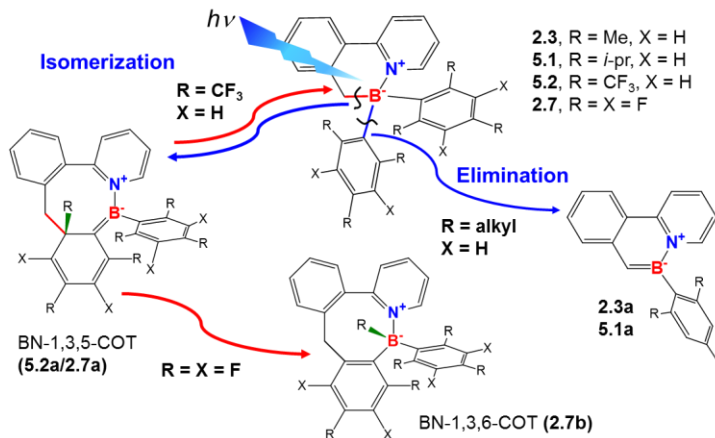
Figure 5.1 Substituent-directed transformations of BN-heterocycles.

5.2 Experimental

5.2.1 General Procedure

Experimental techniques for synthesis, the uses of instrumentation are as described in Chapter 2.2.1.

5.2.2 Synthetic Procedure

5.2.2.1 Synthesis of **5.1**
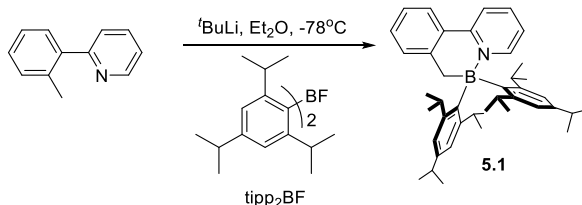
Preparation of tipp$_2$BF:[8] According to the modified literature procedure, a two-necked, 50 mL round-bottomed flask equipped with reflux condenser was charged with magnesium turnings (158 mg, 6.6 mmol), tripyl bromide (1.86 g, 6.6 mmol) in THF and one crystal of iodine. The mixture was warmed up to initiate reaction by a heat gun, the reaction was heated under reflux overnight, then allowed to cool to room temperature. And then freshly distilled BF$_3$.OEt$_2$ (393 uL, 3.2 mmol) was added to the pre-cool Grignard solution of tippMgBr at -78ºC. Once addition was completed the coolant was removed and the mixture fast stirred at room temperature for 30 min., then under reflux for 3 hrs, then for 2 hrs at room temperature. This solution of TIP$_2$BF was used directly for next step.

^{t}BuLi (2.7 mL, 1.7 M in hexane, 4.66 mmol) was added to a mixture solution of 2-(*o*-tolyl)pyridine (358 mg, 2.12 mmol) in Et$_2$O (15 mL) at -78 ºC. After stirring at this temperature for 1 h, the pre-cooled borane reagent tipp$_2$BF was added using a double-ended needle and with vigorous stirring at -78 ºC. The mixture was stirred for another hour at -78 ºC, then allowed to warm slowly to room temperature and stirred overnight. The solution was extracted with CH$_2$Cl$_2$ and water. The organic phase was dried over magnesium sulfate and filtered. The filtrate was purified by column chromatography on silica gel to afford product **5.1** (509 mg, 0.87 mmol, 41% yield) as a white solid, which was confirmed by X-ray diffraction analysis. ^{1}H NMR (400 MHz, C$_6$D$_6$, 298K) δ 9.01 (d, *J* = 6.0 Hz, 1H), 7.24 (d, *J* = 7.7 Hz, 1H), 7.13 (d, *J* = 8.0 Hz, 1H), 7.08 (s,

4H), 6.98 (d, J = 7.4 Hz, 1H), 6.84 (dt, J = 11.8, 7.7 Hz, 2H), 6.76 (t, J = 7.4 Hz, 1H), 6.28 (t, J = 6.7 Hz, 1H), 3.19 (s, 6H), 2.83 (p, J = 6.9 Hz, 3H), 1.28 (d, J = 6.9 Hz, 12H), 1.06 (s, 24H). ^{13}C NMR (101 MHz, C$_6$D$_6$, 298K) δ 156.30, 152.18, 148.75, 147.01, 146.21, 145.42, 140.05, 131.52, 130.72, 129.92, 127.32, 123.98, 122.67, 121.85, 121.55, 34.14, 32.77, 31.99, 25.37, 24.15. ^{11}B NMR (128 MHz, C$_6$D$_6$, 298K) δ 5.75. HR-EIMS (m/z): [M]$^+$ calcd. for C$_{42}$H$_{56}$BN, 585.4506; found 585.4511.

5.2.2.2 Synthesis of **5.2**
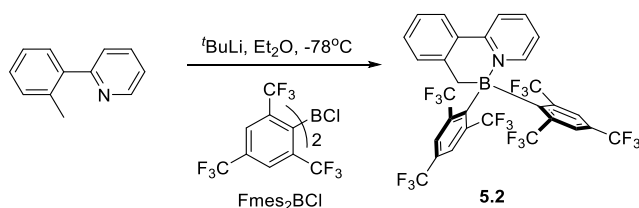
Preparation of Fmes$_2$BCl: 1,3,5-Tris(trifluoromethyl)benzene (1.45 g, 5.12 mmol) was dissolved in 20 mL dry Et$_2$O, the solution was cooled to –78ºC in an acetone/dry ice bath for over 30 min. ^{n}BuLi (2.05 mL, 2.5 M in hexane, 5.12 mmol) was added dropwise to the reaction mixture at –78ºC, then allowed to warm up to room temperature. After stirring at room temperature for 3 hrs, BCl$_3$ (2.5 mL, 1.0 M in hexane, 2.5 mmol) was added at -78 ºC, and the solution was stirred at –78ºC for 30 min and then room temperature for 2 h. This solution of Fmes$_2$BCl was used directly for next step.

An oven-dried Schlenk flask was added 2-(*o*-tolyl)pyridine (0.338 g, 2.0 mmol) and dry Et$_2$O (20 mL) and cooled to –78 ºC in an acetone/dry ice bath for over 10 min. ^{t}BuLi (2.6 mL, 1.7 M in hexane, 4.4 mmol) was added dropwise to the reaction mixture at –78 ºC. After stirring at –78 ºC for 1 h, pre-cooled Fmes$_2$BCl solution was added using cannula to the reaction mixture at –78 ºC. The mixture was allowed to warm to room temperature and stirred 24 hours. The mixture was

extracted with CH_2Cl_2 and water. The filtrate was purified by column chromatography on silica gel to afford product **5.2** (148 mg, 0.20 mmol, 10% yield) as a white solid, which was confirmed by X-ray diffraction analysis. ^{1}H NMR (499 MHz, C_6D_6, 298K) δ 8.20 (s, 2H), 8.11 (d, J = 6.3 Hz, 1H), 7.93 (s, 1H), 7.59 (s, 1H), 6.97 – 6.77 (m, 3H), 6.66 (dt, $J^4_{H\text{-}F}$ = 22.9, $J^3_{H\text{-}H}$ = 7.3 Hz, 2H), 6.44 (d, J = 7.4 Hz, 1H), 6.31 – 6.19 (m, 1H), 3.09 (s, 1H), 2.08 (s, 1H). ^{1}H NMR (499 MHz, C_6D_6, 278K) δ 8.20 (d, J = 10.0 Hz, 2H), 8.06 (d, J = 6.3 Hz, 1H), 7.94 (s, 1H), 7.60 (s, 1H), 6.90 (d, J = 7.7 Hz, 1H), 6.85 – 6.72 (m, 2H), 6.67 (t, J = 7.6 Hz, 1H), 6.62 (t, J = 7.5 Hz, 1H), 6.43 (d, J = 7.5 Hz, 1H), 6.20 (t, J = 6.5 Hz, 1H), 3.11 (d, J = 15.6 Hz, 1H), 2.09 (d, J = 15.6 Hz, 1H). ^{1}H NMR (400 MHz, $CDCl_3$, 298K) δ 8.60 (d, J = 6.1 Hz, 1H), 8.32 – 8.00 (m, 3H), 7.97 (dd, J = 8.2, 1.4 Hz, 1H), 7.76 (s, 1H), 7.56 – 7.31 (m, 3H), 7.07 (td, J = 7.6, 1.3 Hz, 1H), 6.99 (td, J = 7.5, 1.4 Hz, 1H), 6.58 (dd, J = 7.5, 1.3 Hz, 1H), 2.98 (s, 1H), 1.91 (s, 1H). ^{13}C NMR (101 MHz, $CDCl_3$, 298K) δ 155.67, 150.21, 142.73, 142.61, 131.52, 130.06, 128.38, 128.11, 127.38, 127.01, 125.35, 123.87, 123.00(-CF3, q, J = 274 Hz, 124.33, 121.62),122.22, 30.79. ^{13}C NMR (126 MHz, $CDCl_3$, 278K) δ 155.50, 150.23, 142.73, 142.67, 138.47 - 135.12 ($-C\text{-}CF_3$), 131.52, 130.02, 130.00 – 121.00 ($-C\text{-}CF_3$, $-CF_3$), 128.34, 128.04, 127.42, 127.21, 126.90, 125.39, 123.93, 122.33, 30.71. ^{19}F NMR (376 MHz, C_6D_6, 298K) δ -51.58, -52.15, -52.87 – -53.94 (m), -63.96, -64.39. ^{11}B NMR (128 MHz, C_6D_6, 298K) δ -0.03. ^{19}F NMR (376 MHz, C_6D_6, 298K) δ -51.58, -52.15, -53.45, -53.51, -63.96, -64.39. HR-EIMS (m/z): [M]$^+$ calcd. for $C_{30}H_{14}BNF_{18}$, 741.0932; found 741.0932.

5.2.2.3 Synthesis of **5.3**
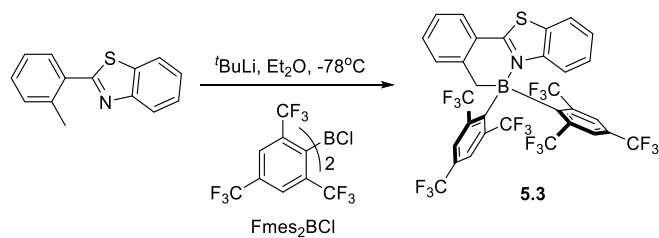
To an oven-dried Schlenk flask was added 2-(*o*-tolyl)benzo[*d*]thiazole (340 mg, 1.51 mmol) and dry Et_2O (20 mL) and cooled to –78ºC in an acetone/dry ice bath for over 10 minutes. ^{t}BuLi (2.0 mL, 1.7 M in hexane, 3.24 mmol) was added dropwise to the reaction mixture at –78ºC. After stirring at –78ºC for 1 h, pre-cooled $Fmes_2BCl$ (1.5 eq) solution was added using cannula to the reaction mixture at –78ºC. The mixture was allowed to warm to room temperature and stirred 24 hours. The mixture was extracted with CH_2Cl_2 and water. The filtrate was purified by column chromatography on silica gel to afford product **5.3** (217 mg, 0.27 mmol, 18% yield) as a white solid. ^{1}H NMR (400 MHz, C_6D_6, 298K) δ 8.32 (s, 1H), 8.17 (s, 1H), 7.92 (s, 1H), 7.67 (d, *J* = 8.7 Hz, 1H), 7.59 (s, 1H), 7.03 (d, *J* = 7.5 Hz, 1H), 6.97 (dd, *J* = 8.0, 1.4 Hz, 1H), 6.72 – 6.65 (m, 1H), 6.63 (ddt, *J* = 6.4, 3.0, 1.4 Hz, 2H), 6.60 – 6.49 (m, 2H), 3.11 (s, 1H), 2.31 – 2.12 (m, 1H). ^{13}C NMR (126 MHz, CD_2Cl_2, 298K) δ 173.96, 149.25, 143.45, 138.06, 133.51, 129.69, 128.75, 128.52, 127.92, 127.70, 127.56, 127.53, 127.27, 126.89, 126.78, 126.71, 126.30, 125.64, 125.12, 124.22, 124.04, 122.91, 122.71, 121.00, 120.82, 109.99, 32.13. ^{19}F NMR (376 MHz, C_6D_6, 298K) δ -51.32, -51.96, -52.30 (t, *J* = 19.5 Hz), -53.02 – -54.31 (m), -63.98, -64.37. ^{11}B NMR (128 MHz, C_6D_6, 298K) δ -1.52. HR-EIMS (m/z): [M]$^+$ calcd. for $C_{32}H_{14}BNF18S$, 797.0653; found 797.0645.

5.2.2.4 Synthesis of **5.4**
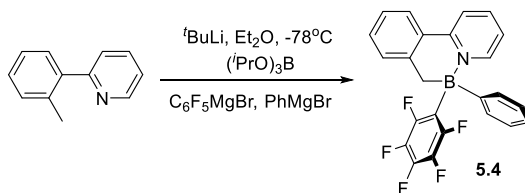
^{t}BuLi (1.68 mL, 1.7 M in hexane, 2.86 mmol) was added to a solution of 2-(*o*-tolyl)pyridine (220 mg, 1.30 mmol) in Et_2O (15 mL) at -78 ºC. After stirring at this temperature for 1 h, $B(O^iPr)_3$ (360 *u*l, 1.56 mmol) was added. The reaction solution was stirred for 1 h at the same temperature, after which pentafluorophenylmagnesium bromide (C_6F_5MgBr) (2.9 mL, 0.5 M in diethyl ether,

1.43 mmol) was added at -78°C. Next, phenylmagnesium bromide (0.43 mL, 3 M in diethyl ether, 1.30 mmol) was added at -78 °C, and the mixture was warmed slowly to room temperature and stirred overnight. The mixture was extracted with CH_2Cl_2 and water. The filtrate was purified by column chromatography on silica gel to afford product **5.4** (233 mg, 0.55 mmol, 42% yield) as a white solid, which was confirmed by X-ray diffraction analysis. ^1H NMR (400 MHz, C_6D_6, 298K) δ 8.05 (d, J = 6.1 Hz, 1H), 7.50 – 7.43 (m, 2H), 7.43 – 7.37 (m, 2H), 7.34 – 7.29 (m, 1H), 7.20 (d, J = 7.6 Hz, 1H), 7.10 (dd, J = 7.8, 1.2 Hz, 1H), 7.00 (td, J = 7.5, 1.3 Hz, 1H), 6.98 – 6.93 (m, 1H), 6.83 (tt, J = 7.6, 1.2 Hz, 1H), 6.75 (td, J = 7.9, 1.7 Hz, 1H), 6.05 (ddd, J = 7.5, 6.0, 1.4 Hz, 1H), 2.84 (dt, J = 15.3, 2.2 Hz, 1H), 2.65 (d, J = 15.4 Hz, 1H). ^{13}C NMR (101 MHz, CD_2Cl_2, 298K) δ 154.36, 146.82, 145.51, 141.59, 133.70, 131.44, 129.89, 129.57, 127.91, 126.64, 125.27, 123.31, 122.69, 26.81. (Due to the coupling of fluoride to carbon, Carbon atoms connecting to fluoride did not show up) ^{11}B NMR (128 MHz, C_6D_6, 298K) δ -0.43. ^{19}F NMR (376 MHz, C_6D_6, 298K) δ -135.16 (d, J = 24.3 Hz), -159.70 (d, J = 44.6 Hz), -164.54 – -166.59 (m). HR-EIMS (m/z): $[M]^+$ calcd. for $C_{24}H_{15}BNF_5$, 423.1218; found 423.1227.

5.2.2.5 Synthesis of **5.5**
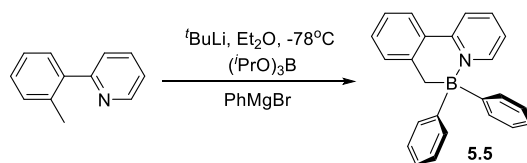
^{t}BuLi (1.3 mL, 1.7 M in hexane, 2.2 mmol) was added to a solution of 2-(o-tolyl)pyridine (169 mg, 1 mmol) in Et_2O (15 mL) at -78 °C. After stirring at this temperature for 1 h, B(O^{i}Pr)$_3$ (226 mg, 1.2 mmol) was added. The mixture was stirred for another hour at -78 °C, after which phenylmagnesium bromide (1.0 mL, 3 M in diethyl ether, 3 mmol) was added at -78 °C, then allowed to warm slowly to room temperature and stirred overnight. The mixture was extracted with

CH$_2$Cl$_2$ and water. The organic extract was purified by column chromatography on silica gel to afford product **5.5** (270 mg, 0.81 mmol, 81% yield) as a white solid, which was confirmed by X-ray diffraction analysis. ^{1}H NMR (400 MHz, CDCl$_3$, 298K) δ 8.35 (d, *J* = 5.8 Hz, 1H), 8.02 (d, *J* = 2.7 Hz, 2H), 7.59 (d, *J* = 7.8 Hz, 1H), 7.38 – 7.25 (m, 3H), 7.25 – 7.17 (m, 4H), 7.17 – 7.05 (m, 7H), 2.64 (s, 2H). ^{13}C NMR (101 MHz, CDCl$_3$, 298K) δ 154.50, 146.77, 146.31, 140.42, 133.46, 131.40, 130.63, 129.84, 127.13, 126.71, 125.15, 124.90, 122.92, 122.36, 27.90. ^{11}B NMR (128 MHz, CDCl$_3$, 298K) δ 0.06. HR-EIMS (m/z): [M]$^+$ calcd. for C$_{24}$H$_{20}$BN, 333.1689; found 333.1698.

5.2.2.6 Photoelimination of **5.1** and Generation of **5.1a**
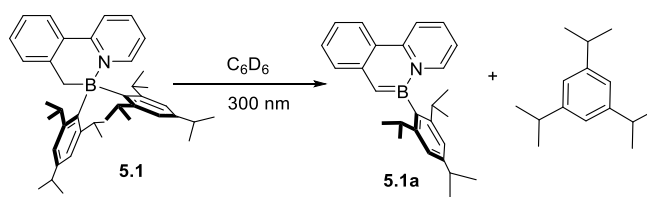
Compound **5.1** (~20 mg) was dissolved in C$_6$D$_6$ (0.5 mL) in a quartz J-Young NMR tube and sealed under nitrogen. The NMR tube was then irradiated with 300 nm UV light and the reaction progress was monitored by ^{1}H, ^{11}B and ^{19}F NMR spectra until it reached completion. The product **5.1a** can be isolated as bright yellow crystals from the slow evaporation of the benzene solution. Its structure was confirmed by X-ray diffraction analysis. ^{1}H NMR (499 MHz, C$_6$D$_6$) δ 8.43 (d, *J* = 6.9 Hz, 1H), 8.10 (d, *J* = 8.8 Hz, 1H), 8.04 (d, *J* = 9.1 Hz, 1H), 7.70 (d, *J* = 8.4 Hz, 1H), 7.37 (s, 3H), 7.28 (t, *J* = 7.5 Hz, 1H), 7.01 (d, *J* = 7.5 Hz, 1H), 6.71 (t, *J* = 7.9 Hz, 1H), 6.13 (t, *J* = 6.8 Hz, 1H), 2.99 (p, *J* = 7.0 Hz, 1H), 2.89 (q, *J* = 6.8 Hz, 2H), 1.39 (d, *J* = 6.9 Hz, 6H), 1.27 (d, *J* = 6.8 Hz, 6H), 1.15 (d, *J* = 6.9 Hz, 6H). ^{13}C NMR (101 MHz, C$_6$D$_6$, δ, ppm): 151.82, 149.01, 148.87, 144.84, 142.46, 137.58, 128.88, 128.74, 128.34, 124.71, 120.57, 119.83, 118.97, 115.46, 35.02,

34.92, 25.07, 24.42, 24.38. ^{11}B NMR (128 MHz, C_6D_6) δ 36.12. HR-ESIMS (m/z): [M+1]$^+$ calcd. for $C_{27}H_{33}NB$: 382.27006; found: 382.26844.

5.2.2.7 Photoisomerization of **5.2** and Generation of **5.2a**
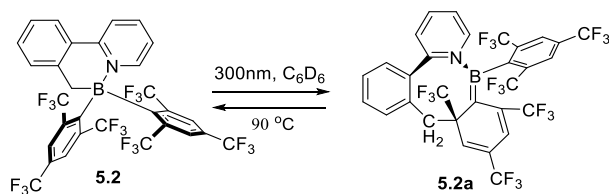
Compound **5.2** (~20 mg) was dissolved in C_6D_6 (0.5 mL) in a quartz J-Young NMR tube and sealed under nitrogen. The NMR tube was then irradiated with 300 nm UV light and the reaction progress was monitored by ^{1}H and ^{11}B NMR spectra until it reached completion. The product of **5.2a** can be isolated quantitatively as dark orange brown crystals from a benzene/hexane solution. The structure of **5.2a** was confirmed by X-ray diffraction analysis. ^{1}H NMR (400 MHz, C_6D_6) δ
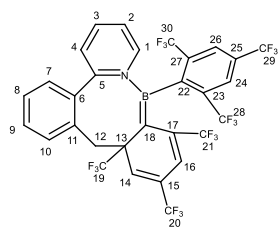
8.17 (d, J = 1.8 Hz, 1H), 8.02 (d, J = 6.4 Hz, 1H), 7.88 – 7.78 (m, 1H), 7.09 – 7.04 (m, 1H), 7.05 – 6.92 (m, 2H), 6.84 (dd, J = 7.5, 1.3 Hz, 1H), 6.50 (td, J = 7.7, 1.4 Hz, 1H), 6.42 (dd, J = 8.0, 1.6 Hz, 1H), 6.11 (s, 1H), 5.99 (s, 1H), 5.93 (ddd, J = 7.8, 6.5, 1.7 Hz, 1H), 2.60 – 2.35 (m, 2H). ^{13}C

NMR (101 MHz, C_6D_6) δ 160.14 (C5), 147.45 (d, J = 2.9 Hz, C1), 140.76 (C3), 138.11 (C11), 138.11 (q, J = 47 Hz), 136.06 (C6), 135.19 (q, J = 30 Hz), 131.52 (C9), 131.28 (q, J = 32 Hz), 130.95 (q, J = 35 Hz), 129.26 (C7), 128.95 (C4),128.71 (C10), 126.63(C8), 126.35 (br, C24 or C26), 125.94 (br, C14), 125.72 (br, C24 or C26), 123.03 (C2), 123.80 (q, J = 245 Hz, C19 (-CF$_3$), 127.80, 125.35, 122.15, 119.89), 123.39(q, J = 297 Hz, C28 or C30(-CF$_3$), 124.87,121.90), 123.25(q, J = 271 Hz, C21(-CF$_3$), 126.45, 124.60, 121.89, 118.60), 123.15(q, J = 275 Hz, C20(-CF$_3$), 127.10, 124.36, 121.64, 118.94), 123.00(q, J = 272 Hz, C29 (-CF$_3$), 124.36,121.64),128-120, 106.18 (q, J = 9 Hz, C16), 56.34 (q, J = 25 Hz, C13), 43.53 (C12). ^{19}F NMR (376 MHz, C_6D_6) δ -

56.70 (q, J = 16.4, 15.9 Hz), -58.06, -58.87 (d, J = 11.7 Hz), -64.08, -68.98, -79.70. ^{11}B NMR (128

MHz, C_6D_6, δ): 35.14. HR-ESIMS (m/z): $[M+1]^+$ calcd. for $C_{30}H_{15}NBF_{18}$, 742.10046; found

742.10156.

5.2.2.8 Fatigue Resistance of **5.2** and **5.2a**

Compound **5.2** (~10 mg) was dissolved in C_6D_6 (0.5 mL) in a quartz J-Young NMR tube and

sealed under nitrogen. The integration ratio between the peak at 6.44 ppm and the peak of C_6D_6

was recorded as cycle 0. The NMR tube was then irradiated with 300 nm UV light, after **5.2**

completely converted into **5.2a** (cycle 0.5), the integration ratio between the peak at 5.99 ppm of

5.2a and the peak of C_6D_6 was recorded. Next, **5.2a** was converted back to **5.2** at 90 [0]C (cycle 1)

and the integration ratio of the peak at 6.44 pm was recorded again. The cycling was repeated until

cycle 13.5 was reached.

5.2.2.9 Photoisomerization of **5.3** and Generation of **5.3a**
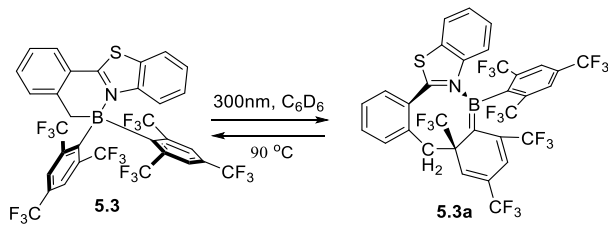
Compound **5.3a** was synthesized using the same procedure of synthesis as that for compound

5.2a. ^{1}H NMR (499 MHz, C_6D_6) δ 8.23 (s, 1H), 7.72 (d, J = 8.6 Hz, 1H), 7.69 (s, 1H), 7.28 (d, J =
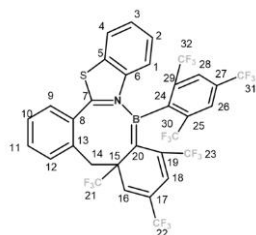
7.7 Hz, 1H), 6.97 (t, J = 7.6 Hz, 1H), 6.87 (q, J = 7.8 Hz, 2H), 6.75 (d,

J = 7.8 Hz, 1H), 6.62 (dt, J = 18.6, 7.2 Hz, 2H), 6.07 (s, 1H), 5.96 (s,

1H), 2.64 (d, J = 14.1 Hz, 1H), 2.35 (d, J = 14.0 Hz, 1H). ^{13}C NMR (126

MHz, C_6D_6) δ 178.44(C7), 146.26 (br, C20 or C24), 145.84 (C5),

139.78(q, J = 27 Hz), 139.26(C8), 138.85(C17, q, J = 25 Hz), 134.74 (q, J = 27 Hz), 133.26 (C12),

188

130.92 (C6), 130.86 (q, J = 31 Hz), 130.77 (C19, q, J = 31 Hz), 130.14 (C13), 129.46(C9), 129.09 (C11), 128.41 (C3), 127.13 (C2), 126.70 (C10), 126.65 (br, C26 or C28), 125.93 (br, C26 or C28), 124.21 (br, C16), 123.00 (C22, q, J = 272 Hz), 121.88 (C4), 120.57 (C1, q, J = 4 Hz), 131-119 (C21, C23, C25, C27, C29-C32), 105.10 (C18, q, J = 8 Hz), 100.88 (br, C20 or C24), 56.44 (C15, q, J = 24 Hz), 45.80 (C14). ^{19}F NMR (376 MHz, C$_6$D$_6$, δ, ppm) -54.44 (q, J = 13.9 Hz), -58.05 (d, J = 11.5 Hz), -59.27 (q, J = 10.3 Hz), -64.20, -69.09, -79.39 (broad). ^{11}B NMR (128 MHz, C$_6$D$_6$, δ, ppm): 33.95. HR-ESIMS (m/z): [M+H]$^+$ calcd. for C$_{32}$H$_{15}$NBF$_{18}$S: 798.07253; found: 798.07440.

5.2.2.10 Photoisomerization of **2.7** and Generation of **2.7b**
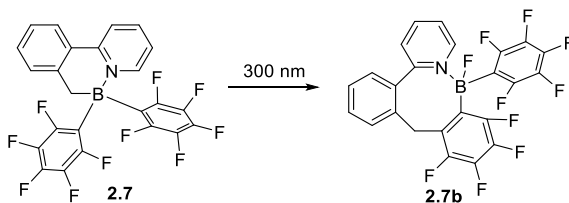
Compound **2.7b** was synthesized using the same synthetic protocol as that for compound **5.2a**. ^{1}H NMR (400 MHz, C$_6$D$_6$) δ 8.86 (dt, J = 6.3, 2.0 Hz, 1H), 6.83 (td, J = 7.6, 1.4 Hz, 1H), 6.74 (ddd, J = 15.3, 7.6, 1.5 Hz, 2H), 6.42 (ddd, J = 7.8, 6.5, 1.5 Hz, 2H), 6.27 (dd, J = 7.7, 1.5 Hz, 1H), 6.04 (dd, J = 7.7, 1.3 Hz, 1H), 3.90 (dd, J = 15.0, 1.3 Hz, 1H), 2.24 (d, J = 15.0 Hz, 1H). ^{13}C NMR (101 MHz, C$_6$D6) δ 156.56, 145.86, 145.63, 141.12, 137.34, 135.30, 130.68, 130.49, 126.52, 126.16, 125.47, 123.78, 123.75, 28.41. (Due to the coupling of fluoride to carbon, carbon atoms connected to fluorine did not show up) ^{19}F NMR (376 MHz, C$_6$D$_6$, δ): -131.18 – -131.79 (m), -132.53 – -133.47 (m), -139.87 (dd, J = 23.9, 10.6 Hz), -165.63 – -166.53 (m). ^{11}B NMR (128 MHz, C$_6$D$_6$, δ): 5.57. HR-EIMS (m/z): [M]$^+$ calcd. for C$_{24}$H$_{10}$BNF$_{10}$: 513.0747; found: 513.0765.

189

5.2.3 Photoisomerization Quantum Yield Measurement[9a,b]

Photoisomerization Quantum Yield Measurement Using Any Material as Reference (the detailed

procedure was summarized by our group former student Zachary Hudson):

Derivation:

Since:

$$\Phi = \frac{\#\ reacted\ molecules\ per\ unit\ time}{\#\ photons\ absorbed\ per\ unit\ time}$$

Let:

m = # reacted molecules per unit time

q = # photons absorbed per unit time

p = total number of photons passing through the sample

F = fraction of photons absorbed by the sample

s = sample

r = reference

Thus:

$$\Phi = \frac{m}{q}$$

$$= \frac{m}{Fp}$$

p is a constant that will not change from sample to reference if the light source is kept constant.

We can thus write:

$\Phi_s = \frac{m_s}{F_s p}$ and $\Phi_r = \frac{m_r}{F_r p}$.

Since Φ_r is known:

$$p = \frac{m_s}{\Phi_r F_s}$$

and thus:

$$\Phi_s = \Phi_r \frac{m_s F_r}{m_r F_s}$$

This equation allows us to calculate the photoisomerization quantum yield of a material using any reference compound for which the quantum yield is known.

Determining m:

The value of m is simply the slope of a graph of the number of moles of compound produced over time. We can measure the slope of a graph of A vs. time, and we know that $A = \varepsilon c l = \frac{\varepsilon n l}{V}$ where n is the number of moles of sample and V is the sample volume. We can thus determine m by converting absorbance to moles, as $n = \frac{AV}{\varepsilon l}$.

Notes:

    a.   The sample volume must be well-defined, eg. 3mL. For this reason, samples must not be degassed by bubbling N_2.

    b.   The concentration must be known.

    c.   You must also know the value of ε for the isomerized species.

Determining F:

Since $A = -log\frac{I}{I_0}$ and $F = 1 - \frac{I}{I_0}$, then $F = 1 - 10^{-A}$.

However, if $A_s \approx A_r$, then the ratio

$$\frac{1 - 10^{-A_r}}{1 - 10^{-A_s}} \cong \frac{A_r}{A_s}$$

Notes:

    a.   The absorbance of the sample at the excitation wavelength must be small (≈ 0.1).

b. The absorbance values of both samples at the excitation wavelength should be similar.

Thus the equation becomes:

$$\Phi_s = \Phi_r \frac{m_s A_r}{m_r A_s}$$

Detailed Procedure:

1. Prepare solutions of known concentrations of both sample and reference in the drybox.

2. Place 3 mL of each solution into separate airtight quartz cuvettes.

3. Turn on the fluorimeter. Set the lamp to the desired excitation wavelength. **Allow the lamp to warm up for 15-20 minutes** so the excitation intensity may stabilize.

4. Measure the absorbance of your sample.

5. Place the sample into the fluorimeter in the path of the beam for a well-defined period of time. This is usually just a few seconds; precision is important and a stopwatch may be useful here. Measure the absorbance of the sample again.

6. Repeat step 5 until significant isomerisation has been observed.

7. Obtain the data for A vs. time at the absorption maximum for the dark isomer. Convert this data to n vs. t and plot these data.

8. Determine the slope of the n vs. t curve using the first few points, over which the isomerisation rate should be approximately linear. This is the value for m_s.

9. Repeat steps 4-8 for the reference material.

10. Calculate the photoisomerization quantum yield as:

192

$$\Phi_s = \Phi_r \frac{m_s A_r}{m_r A_s}$$

where *As* and *Ar* are the absorbance values for the sample and reference at the excitation

5.2.4 Activation Energy Investigation[9c]

Compound **5.2** (~10 mg) was dissolved in C_6D_6 (0.5 mL) in a quartz J-Young NMR tube and sealed under nitrogen. The integration ratio between the peak at 6.11 ppm of **5.2a** and the peak of C_6D_6 was recorded. Irradiation with 300 nm UV light, **5.2** was completely transformed into **5.2a**. While **5.2a** was thermally converted back to **5.2** at a certain temperature, three integration ratios were measured at different progresses of this reaction and the average rate constant at this temperature (k_1) was obtained. After three cycles, three average rate constants (k_1, k_2, k_3) at different temperatures were gained.

According to Arrhenius equation,

$$ln \frac{k_2}{k_1} = -\frac{E_a}{R}\left(\frac{1}{T_2} - \frac{1}{T_1}\right)$$

The slope = $-E_a/R$, and then E_a = -(slope/R) (See figure 5.18, Section 5.5).

5.2.5 X-ray crystallographic analysis

The crystal data of **5.1**, **5.1a**, **5.2**, **5.2a**, **2.7b**, **5.4** and **5.5** were collected on a Bruker Apex II X-ray diffractometer at 180 K. Complete crystal structural data have been deposited at the Cambridge Crystallographic Data Centre [CCDC No. 1494632 (**5.1**), 1494630 (**5.1a**), 1494627 (**5.2**), 1494629 (**5.2a**), 1494631 (**2.7b**), 1494628 (**5.4**), 1495997 (**5.5**)]. These data can be obtained free of charge from The Cambridge Crystallographic Data Centre via www.ccdc.cam.ac.uk /data _request/cif.

193

5.2.6 DFT Calculations

All calculations were performed using density functional theory (DFT) with standard 6-31g* basis set implemented in Gaussian 09 package.[10] The X-ray structures of reactant and product were used as starting geometries for ground-state (S_0) optimization. Geometry optimizations in ground state were carried out with hybrid functional B3LYP.[11] In the optimizations, dispersion corrections were considered using the empirical formula by Grimme et al. (i.e., DFT-D3).[12] Analytical frequency calculations were performed to confirm the nature of stationary points (minima or transition states) at the same theory level as geometry optimizations. Critical points in the first excited singlet state (S_1) were optimized with long-range corrected hybrid exchange-correlation functional using the Coulomb-attenuating method CAM-B3LYP.[13] Vertical excitation energies at the S_0 minima were computed by means of time-dependent DFT method with CAM-B3LYP functional. The reaction path calculations were started from the transition state structure following the vector with a negative eigenvalue in forward and reverse directions, using intrinsic reaction coordinate (IRC) approach.[14] The IRC provides the minimum energy path connecting the two local minima of the reactant and product sides via a given transition state structure. This allows for easy understanding of complicated multistep mechanisms as a set of simple elementary reaction steps. To account for the solvent effects, the benzene solvent was employed by using the conducting polarizable continuum model (C-PCM)[15] in all calculations.

5.3 Results and Discussion

5.3.1 Synthesis and Structural Analysis

Compounds **5.1** - **5.5** were prepared using a modified procedure[6d] for **2.3** and the corresponding *in situ* generated Ar_2BX (X = F, Cl) reagents. Both were fully characterized by ^{1}H, ^{13}C, ^{11}B, and ^{19}F NMR, HRMS, and single crystal X-ray diffraction analyses (See Section 5.5). And Molecule

2.7 was synthesized by our reported 1,1-hydroboration.[6f] Crystal data revealed that the B−CAr bonds of **5.1** and **5.2** are about 0.02 Å longer than those of **2.3**, whereas all three B−CH$_2$ bond lengths are comparable (Figure 5.2). The DFT-calculated B−C$_{Ar}$ lengths match well with those determined experimentally, with the calculated B-Fmes lengths in **5.2** being ∼0.01 Å longer than those of B-tipp in **5.1**. This difference highlights the strong withdrawing nature of Mes^F in addition to its steric bulk. All the related bond length data are shown in Table 5.1.

Table 5.1 Experimental and DFT-calculated (in red) bond lengths of various BN-heterocycles.

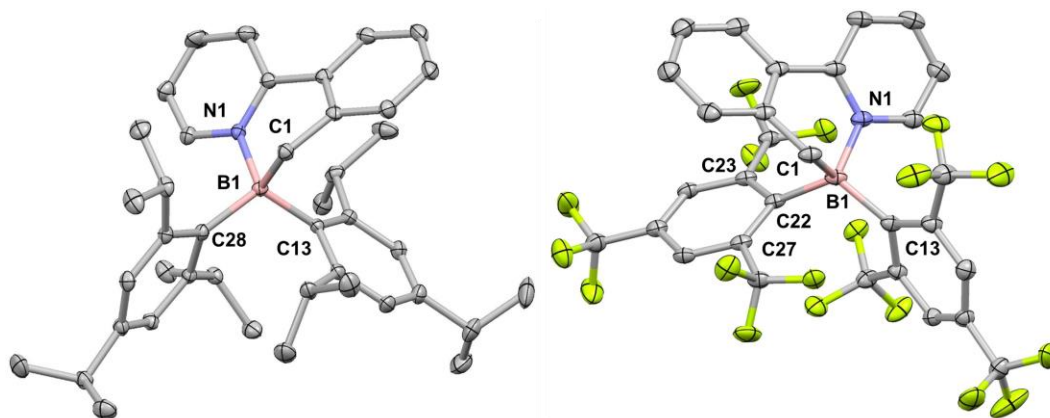| Compd	B-Ar	B-CH$_2$	B-N
2.3	1.660(3)/1.663(3) [1.664/1.657]	1.645(3) [1.647]	1.666(2) [1.693]
5.1	1.680(2)/1.682(2) [1.686/1.677]	1.639(2) [1.647]	1.684(2) [1.736]
5.2	1.681(3)/1.689(2) [1.696/1.692]	1.642(2) [1.642]	1.636(2) [1.645]
2.7	1.647(2)/1.650(2) [1.640/1.639]	1.617(2) [1.626]	1.627(2) [1.636]
5.4	C$_6$F$_5$: 1.661(2)/Ph: 1.615(3) [C$_6$F$_5$: 1.643/Ph: 1.621]	1.612(3) [1.624]	1.635(2) [1.651]
5.5	1.627(2)/1.624(2) [1.633/1.629]	1.620(2) [1.635]	1.640(2) [1.667]

Figure 5.2 Crystal structure of **5.1** (left) and **5.2** (right). Key bond lengths (Å) for **5.1**: B(1) – C(13)/C(28) 1.680(2)/1.682(2), B(1) – C(1)/N(1) 1.639(2)/1.684(2). For **5.2**: B(1) – C(13)/ C(22) 1.681(3)/1.689(2), B(1) – C(1)/N(1) 1.642(2)/1.636(2).

5.3.2 Photo- and Thermal Reactivities

5.3.2.1 Photo- and Thermal Reactivities of **5.1**

The photoreactivities of **5.1** in solution and polymer films are similar to those of **2.3**, with the brightly green fluorescent **5.1a** (λ_{em} = 500 nm, Φ_{FL} = 0.27) formed quantitatively upon irradiation at 300 nm as evidenced by UV-Vis (See Section 5.5), NMR (Figure 5.3). The planar azaborine structure and B=C bond (1.463 Å) of **5.1a** were confirmed by crystal structure data (Figure 5.4). The most striking difference between **2.3** and **5.1** is the rate of photoelimination. Because both compounds have identical absorption spectra and form similar products, the Φ_{PE} of **5.1** relative to that of **2.3** was determined to be 0.25 using competitive NMR photolysis experiments (see Section 5.5). The Φ_{PE} of **5.1** is *ca.* 6 times greater than that of **2.3** (0.044), exceptionally high for a photoelimination reaction, as they tend to have a very low Φ_{PE}. The weaker B-tipp bonds of **5.1** are clearly responsible for this significant enhancement in photoelimination efficiency. This demonstrates that the use of bulkier electron rich aryl groups on boron is an effective strategy for

achieving highly efficient aryl-elimination in such systems, thus making the use of BN-heterocycles as precursors for *in-situ* fabrication of azaborine-based optoelectronic devices[7] more viable.

With respect to retro-hydroboration, similar to that of **2.3**, When heating up to 180 °C in the sealed J-Young NMR tube, the toluene solution of **5.1** underwent retro-hydroboration with the generation of pyrido[1,2-α]isoindole **2.4** (Figure 5.15, Section 5.5).[6f] The only difference of the retro-hydroboration between **2.3** and **5.1** is the pyrido[1,2-α]isoindole **2.4** were not able to be separated from bis(triisopropylphenyl)borane in toluene, in other words, there is equilibrium between 1,1-hydroboration and retro-1,1-hydroboration.
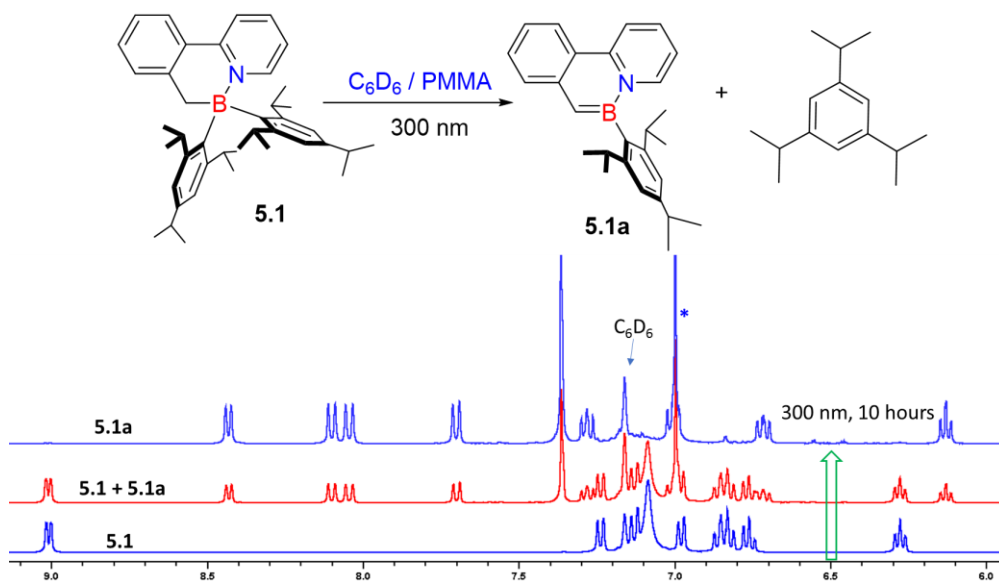

Figure 5.3 ^{1}H NMR spectra showing the clean conversion of **5.1** to **5.1a** in C$_6$D$_6$ at room temperature and 300 nm irradiation.
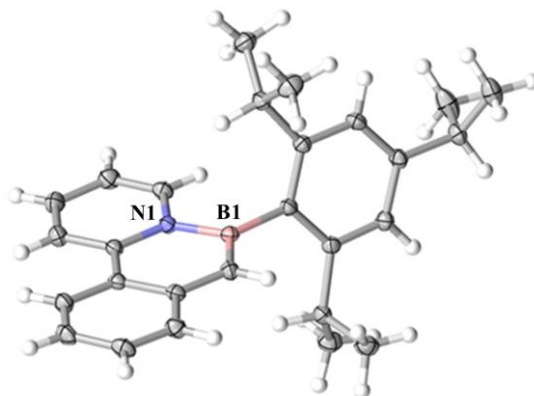
197

Figure 5.4 Crystal structure of **5.1a**

5.3.2.2 Photo- and Thermal Reactivities of **5.2** and **5.3**

Despite a similarly congested structure and long B-Mes^F bonds, **5.2** does not undergo photoelimination at all. Irradiation (300 nm) of **5.2** in C$_6$D$_6$ or THF resulted in the rapid and clean conversion of **5.2** to a new species, **5.2a**, which has sharp and well-resolved peaks in the ^{1}H NMR spectrum and a ^{11}B chemical shift at ~35 ppm, typical of a three-coordinated boron with one unsaturated bond[16] (Figure 5.5b and see Section 5.5). Accompanying the NMR spectral change was a dramatic change in solution colour from colorless to dark orange-brown as shown in Figure 5.5. In the UV-Vis spectrum, a broad low energy absorption band at $\lambda_{max} = 433$ nm (Figure 5.5d) appears with irradiation. TD-DFT data suggests that the low energy band of **5.2a** originates from a charge transfer (CT) transition from HOMO located on the π-system of the B=C and the cyclohexadiene moiety to LUMO (π^*) located on the py ring of the backbone (see Section 5.5). Remarkably, heating the orange-brown solution at 90 °C resulted in full recovery of **5.2** by NMR and restoration of the original solution colour. The activation energy of this process was determined to be ~33.3 kcal/mol (see Section 5.2.4 and Section 5.5). **5.2a** forms dark orange-brown crystals, allowing us to establish its structure unequivocally by X-ray diffraction, as shown in Figure 5.6. As is common

198

for B=C bonds,[16] **5.2a** is prone to hydrolysis which results in the formation of the 1,4-addition borinic acid product (Figure 5.17, Section 5.5).

The crystal structure of **5.2a** (Figure 5.6) revealed a previously unknown BN-embedded cyclic structure, which is formally a 4,5-dihydro-1,2-azaborocine but will be described as BN-1,3,5-cyclooctatriene (BN-1,3,5-COT) for convenience. The CH_2 group in **5.2a** is no longer bound to the boron atom, but instead forms a C-C bond with one CF_3-substituted quaternary carbon atom (C(14)) of a Mes^F ring. This converts the Mes^F to a 1,3-cyclohexadiene and the B-C bond to a B=C bond (1.465(3) Å), with similar length compared to previously reported B=C bonds.[16] Comparing the structure of **5.2a** to the photoproduct of previously reported B(ppy)Mes$_2$,[6a-6d] which forms a tricyclic 1,2-azaboratabisnorcaradiene, it is clear that the switching described for **5.2** represents a brand-new class of photochromic materials. The Φ_{PE} of **5.2** to **5.2a** transformation was determined to be 0.23 (see Section 5.2.3 and Section 5.5). BN-1,3,5-COTs are a previously unknown class of BN-embedded molecules. The clean and quantitative generation of **5.2a** *via* the photoisomerization of **5.2** provides a convenient method for accessing such unusual species. Furthermore, despite **5.2a** having a chiral carbon atom (C(14)) and chiral COT structure, only one diastereoisomer was observed by NMR in which the CF_3 (C(19)) is *syn* to the py ring while the phenyl and the cyclohexadienyl of the COT unit are *syn* to each other. Thus, the **5.2** to **5.2a** transformation proceeds with high stereoselectivity.
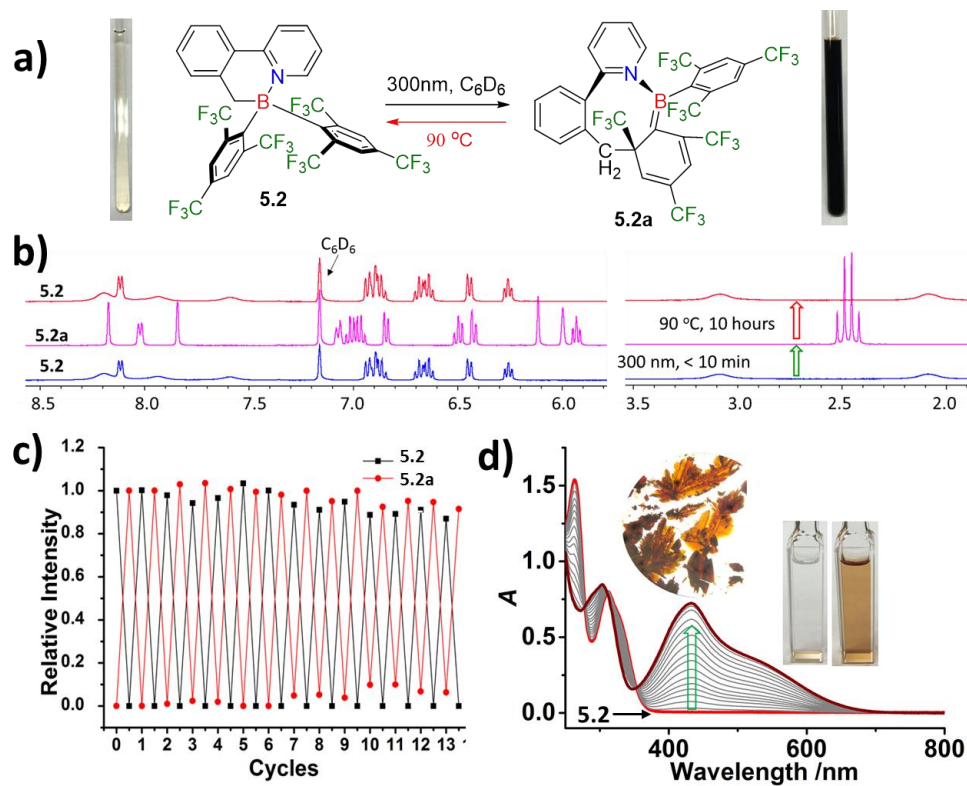
Figure 5.5 a) A scheme showing the interconversion of **5.2** and **5.2a**. b) ^{1}H NMR spectra showing the photo (300 nm) and thermal (90 °C) interconversion of **5.2** and **5.2a** in C_6D_6. c) A diagram showing the fatigue resistance of the **5.2** and **5.2a** with the irradiation and heating cycles using integrated peak intensity relative to the C_6D_6 peak in ^{1}H NMR spectra (see Section 5.5). d) UV-Vis spectra showing the conversion of **5.2** to **5.2a** in THF (1×10^{-4} M) and photographs showing the crystals of **5.2a** and solution color of **5.2** and **5.2a**.
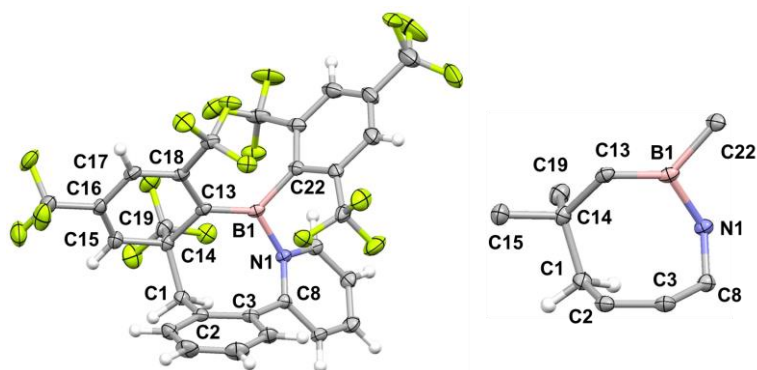
Figure 5.6 Crystal structures of **5.2a** (left) and the BN-COT cores. Important bond lengths (Å) for **5.2a**: B(1) – C(13)/C(22)/N(1) 1.465(3)/1.627(3)/1.585(3), C(8) – N(1)/C(3) 1.372(2)/1.477(3), C(2) – C(1)/C(3) 1.498(3)/1.390(3); C(14) – C(1)/C(13)/C(15)/C(19) 1.567(3)/1.564(3)/1.509(3)/ 1.528(3), C(16) – C(15)/C(17) 1.322(3)/1.427(3), C(18) – C(13)/C(17) 1.461(3) /1.352(3).
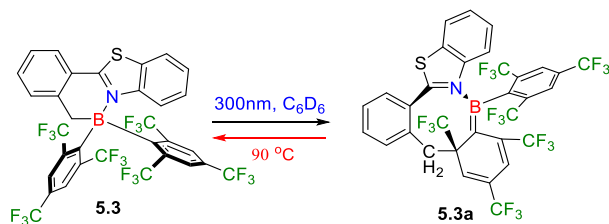

Figure 5.7 The interconversion of **5.3** and **5.3a**.

To establish if the new photo-transformation is available to other BN-heterocycles with different chelate backbones, **5.3**, an analogue of **5.2** with a 2-benzyl-benzothiazolyl backbone was prepared (Figure 5.7). Upon irradiation at 300 nm, **5.3** undergoes a similar photo-switching as observed for **5.2** (see Section 5.5), forming a deep brown colored **5.3a**, an analogue of **5.3a**, according to its diagnostic ^{1}H, ^{11}B, and ^{19}F NMR spectra (Figure 5.19, Section 5.5). Again, only one diastereoisomer was observed. **5.3a** possesses a low energy absorption band with λ_{max} = 458 nm in its UV-Vis spectrum, which is red-shifted by ~25 nm compared to **5.2a**, consistent with the greater π-conjugation of the backbone in **5.3a** (Figure 5.25, Section 5.5). The Φ_{PE} of **5.3** to **5.3a** transformation was determined to be 0.10. Thermally, **5.3a** converts back to the colorless **5.3** at 90

201

°C with ~5% decomposition observed in the process (see Section 5.5). This example shows that the new photochromic phenomenon is not limited to systems with a benzyl-pyridyl backbone.

5.3.2.3 Fatigue Resistance of **5.2** and **5.2a**

To demonstrate the robustness of this newly discovered photochromic system, the fatigue resistance of **5.2** was examined by cycling through the **5.2**→**5.2a**→**5.2** transformations repeatedly. Quite remarkably, the continuous photo-thermal cycling between these two states did not yield any appreciable decomposition until the 13th cycle as shown by ^{1}H NMR data (Figure 5.5c and Figure 5.8), indicating that **5.2**/**5.2a** possess excellent fatigue resistance. This feature makes these systems promising for future applications involving molecular switches.
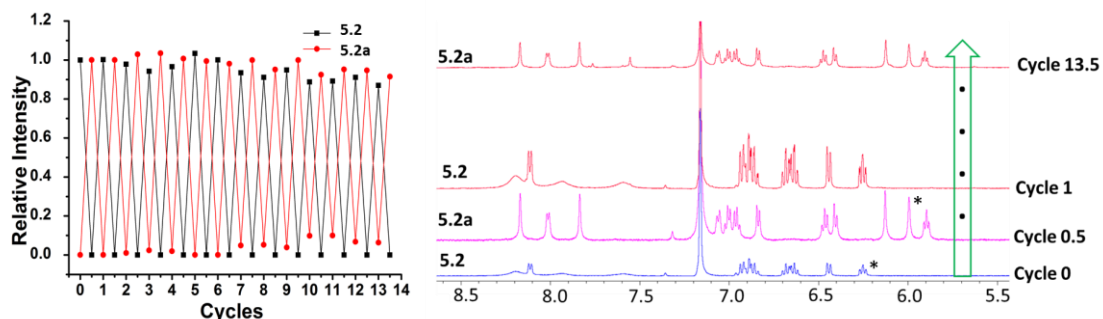

Figure 5.8 Fatigue Resistance of photoisomerization of **5.2**. X axis: the times of cycles. Y axis: relative integrated intensity of **5.2** and **5.2a** compared to cycle 0. The peaks chosen for integration relative to the solvent peak (C_6D_6) are marked by *. ^{1}H NMR data show there is no obvious decomposition until after 13 cycles.

5.3.2.4 Photo- and Thermal Reactivities of **2.7**

Given the bulky nature of the aryl groups in **5.1**, **5.2**, and **5.3**, but their distinctly different photoreactivity, the electron-deficiency of Mes[F] appears to be pivotal for the new photochromism. To probe this hypothesis, the photoreactivity of **2.7**,[6f] which has the same backbone as **5.2** and two less sterically congested but comparably electron-withdrawing C_6F_5 substituents, was examined.

Upon irradiation of **2.7** at 300 nm, no obvious color change was observed. However, ^{1}H, ^{19}F, and ^{11}B NMR revealed the quantitative formation of a new species, **2.7b**, with a typical four-coordinated [11]B chemical shift of 5.6 ppm (Figure 5.9 and see Section 5.5). Single-crystal X-ray diffraction analysis established that **2.7b** shares some structural similarities with **5.2a/5.3a** and may be described as a BN-embedded 1,3,6-COT, an isomer of BN-1,3,5-COT, as shown in Figure 5.10. The key difference between **5.2a/5.3a** and **2.7b** is that the 3rd double bond in the latter is not conjugated with the other two in the COT ring, and the boron center is four-coordinated with a B-F bond. As a consequence, **2.7b** has no low energy absorption band in the visible region, which is consistent with TD-DFT calculated data (see Section 5.5). The B atom in **2.7b** is a chiral center, which, combined with the chiral COT structure, creates the possibility of diastereomers. The fact that only one diastereomer was observed in which the B-F bond is *syn* to the py ring as shown in Figure 5.10 supports that the **2.7** to **2.7b** transformation also has high stereoselectivity. Unlike **5.2a/5.3a** which can thermally revert to **5.2/5.3**, **2.7b** is thermally stable and does not convert back to **2.7**. Given the bond energy of the C-F bond,[17] its cleavage in the **2.7** to **2.7b** transformation is highly unusual and interesting, which may be driven by the stability of **2.7b**.
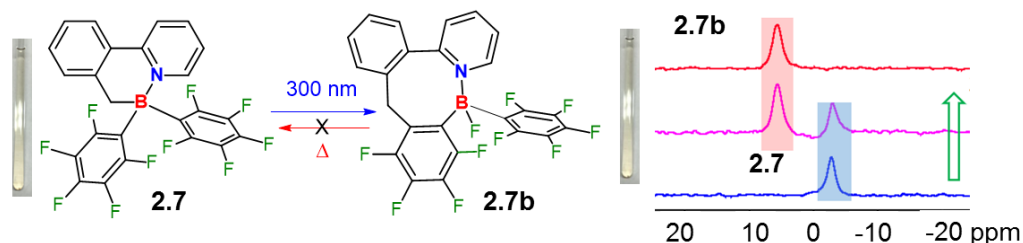

Figure 5.9 Irreversible photoisomerization of **2.7** and the ^{11}B NMR spectra in C_6D_6 showing the full conversion of **2.7** (blue) to **2.7b** (red).
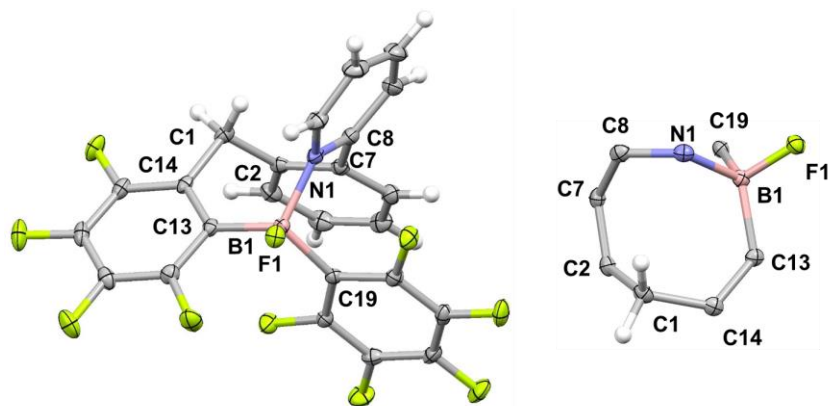
Figure 5.10 Crystal structures of **2.7b** and the BN-COT cores. Important bond lengths (Å) for **2.7b**: B(1)–F(1)/N(1)/C(13)/C(19) 1.408(2)/1.658(2)/1.628(2)/1.636(2), C(8) – N(1)/C(7) 1.356(2)/ 1.480(2); C(2) – C(1)/C(7) 1.510(2)/1.397(2), C(14) – C(1)/C(13) 1.514(2) /1.408(2).

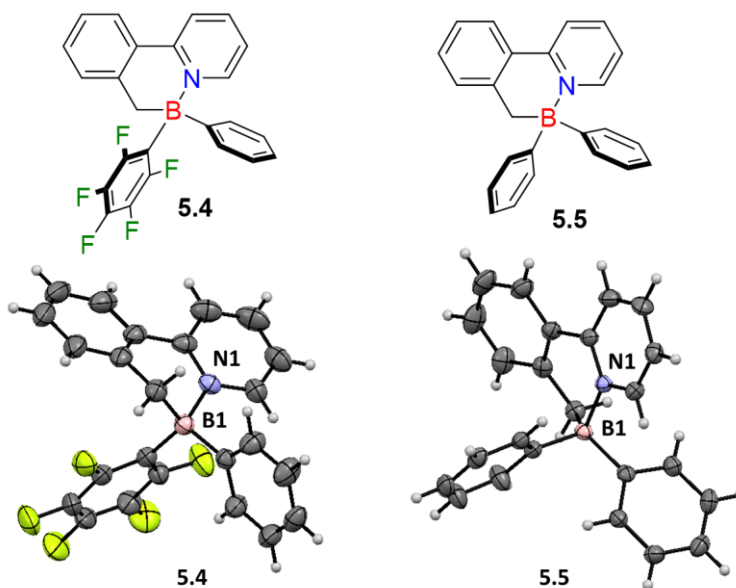### 5.3.2.5 Photo- and Thermal Reactivities of **5.4** and **5.5**

Figure 5.11 Crystal structure of **5.4** and **5.5**. Important bond lengths (Å) for **5.4**: B(1)-C_6F_5 1.661(2), B(1)-Ph 1.615(3), B(1)-CH_2 1.612(3), B(1)-N(1) 1.635(2). Important bond lengths (Å) for **5.5**: B(1)-Ph 1.627(2)/ 1.624(2), B(1)-CH_2 1.620(2), B(1)-N(1) 1.640(2).

To further probe the influence of electron deficient substituents on boron atom, compounds **5.4** and **5.5** were prepared where the pentafluorophenyl substituents have been replaced with phenyl rings. Both new structures were confirmed by X-ray diffraction analysis (Figure 5.11), which reveals that the electron withdrawing capabilities of the substituents dramatically affect the B–C$_{Ar}$ bond lengths. With increasing electron density on the aryl groups, the B–C$_{Ar}$ bonds become significantly shorter, with the difference between the B–C$_6$F$_5$ and B–C$_6$H$_6$ bonds in **5.4** being particularly noteworthy (1.661(2) and 1.615(3)**,** Å respectively). In addition to the stronger B–C$_{Ar}$ bonds, both **5.4** and **5.5** are photochemically inert under 300 nm irradiation for up to 48 hours. These results indicate that the strength of the B–C$_{Ar}$ bonds and the extent of electron-deficiency around the boron atom are essential for the newly discovered photoisomerization to occur.

5.3.3 Computational Mechanistic Studies

To understand the unusual photoisomerization of **5.2**/**2.7**, DFT and TD-DFT calculations were performed for each with the complete reaction pathway of **2.7** shown in Figure 5.12. Excitation at 300 nm populates the S$_1$ state of **2.7** at the Franck-Condon (FC) structure, which is of $\pi\pi^*$ character and mainly arises from its HOMO to LUMO transition. Relaxation leads to a minimum in the S$_1$ state, which is close in energy (~5 kcal mol^{-1}) to a conical intersection point (S$_1$/S$_0$)$_X$ between the S$_1$ and S$_0$ states, therefore allowing access to the ground state from the excited state.[18] In the S$_0$, S$_1$, and (S$_1$/S$_0$)$_X$ structures, the B-CH$_2$ distances are 1.6, 2.0, and 2.7 Å, respectively, indicating that the B-CH$_2$ is broken upon photo-excitation. At (S$_1$/S$_0$)$_X$, the excited state decays to the ground state and the reaction path leads to an intermediate (**Int1**) with a B-CH$_2$ distance of 3.3 Å, a negatively charged (-0.44 e) CH$_2$ carbon atom, and a positively charged (+0.29 e) o-carbon of one C$_6$F$_5$ ring. The latter two moieties have a separation distance of 2.3 Å at the **TS1** state, with perfect orientation for C-C bond formation or electrocyclization similar to that observed in a photochromic boron

205

system reported by Yamaguchi,[19] generating **Int2** (**2.7a**), an analogue of **5.2a**. The **TS1** state lies only 2 kcal/mol above **Int1**, suggesting that the reaction from **Int1** to **2.7a** occurs readily. Unlike **5.2a**, which does not undergo further isomerization, the F atom of **2.7a** can migrate from carbon to boron by overcoming a barrier of ~15 kcal/mol at the **TS2** state forming **2.7b**, which resembles the classic transition state structure proposed for 1,3-sigmatropic shifts, leading to the selective formation of one diastereoisomer.[17c] The attraction between the F atom and the electron deficient B atom clearly favors the rearrangement from **2.7a** to **2.7b**, which is -33.5 kcal/mol lower in energy than **2.7**. These data support that the formation of **2.7b** is thermodynamically favorable and the reverse reaction is prohibited due to the large reverse barrier of 96.3 kcal/mol.

Due to the large size of **5.2** and its analogous isomerization pathway, only the ground-state reaction pathway was determined (see Section 5.5). The key transition state of **5.2** has a similar **TS1** structure as **2.7**, with the C-C distance between CH_2 and C_{CF3} being 2.4 Å. The calculated barrier for **5.2a** reverting back to **5.2** is 34.2 kcal/mol, which agrees very well with the experimental value of 33.3 kcal/mol. The fact that the BN-1,3,6-COT isomer was not observed for **5.2** may be explained by an unfavorable transition state caused by steric crowding of the bulky CF_3 groups. The calculated reaction pathway also corroborates the stereoselective formation of **5.2a** and **2.7b**.
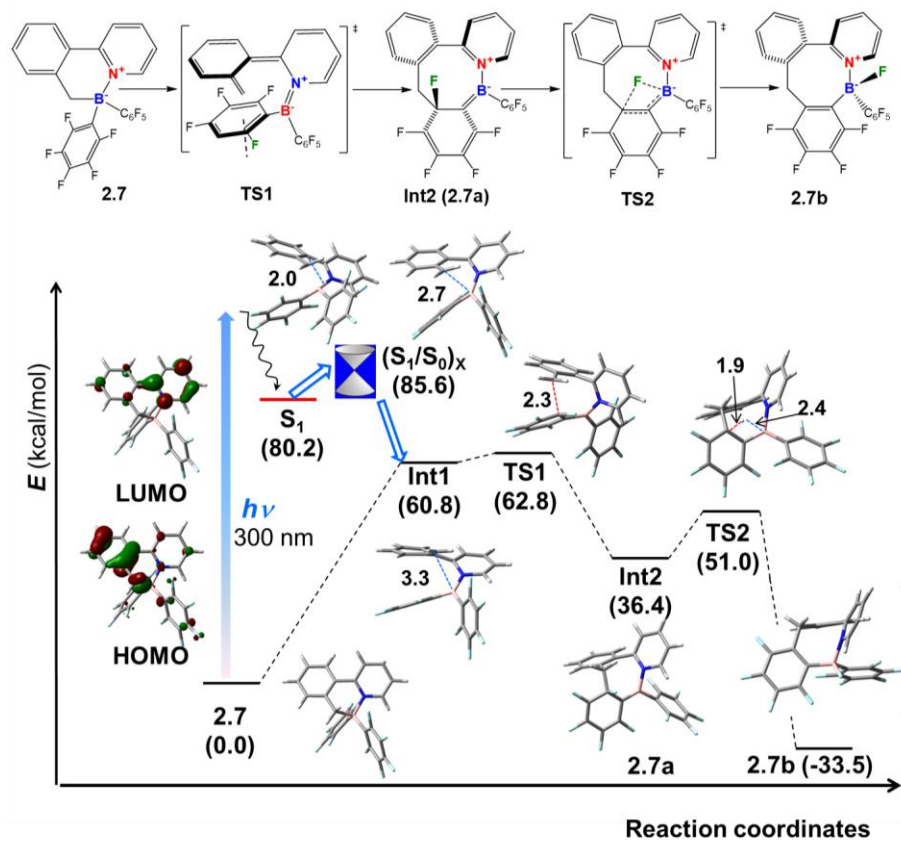
Figure 5.12 Calculated potential energy profile for the photoisomerization of **2.7**. The energies of the all key species, as well as the intersection point of the S_0 and S_1 state ((S_1/S_0)$_X$) are relative to **2.7** and given in the parentheses. Some key distances (in Å) and the HOMO/LUMO orbitals of **2.7** are also shown.
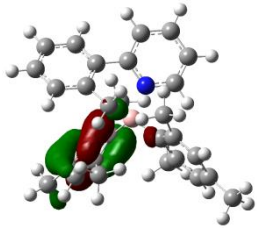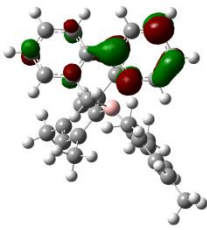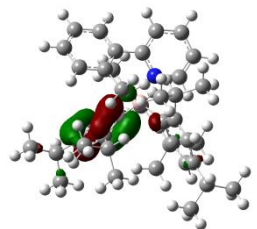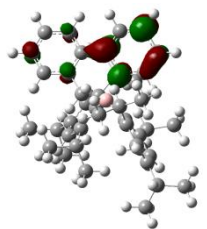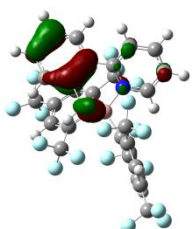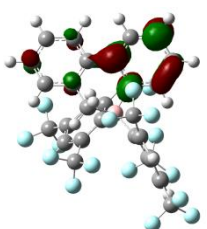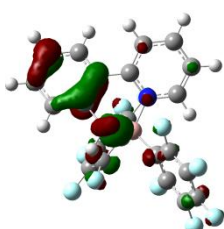
	HOMO	**LUMO**
2.3		
5.1		
5.2		
2.7		
5.4		

Figure 5.13 Comparison of HOMO and LUMO diagrams for **2.3**, **5.1**, **5.2**, **2.7** and **5.4** obtained at B3LYP/6-31g* level in benzene.

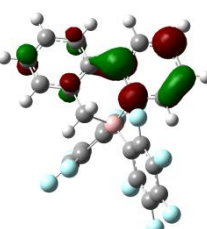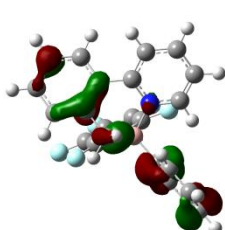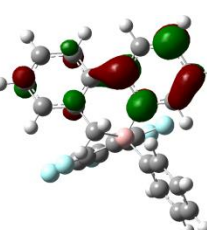One key feature revealed by DFT data is that the HOMOs of **5.2** and **2.7** is localized mainly on the benzyl ring of the chelate backbone and the B atom with very little contributions from the Mes[F] or C_6F_5 groups. This is in sharp contrast to **2.3** and **5.1**, in which the HOMOs are made of almost exclusively π orbitals on the Mes and tipp groups (Figure 5.13). The substituent groups on the aryl rings are clearly responsible for this distinct difference between the electron-rich and electron-poor BN-heterocycles, which led to their distinct photoreactivity (*i.e.* aryl-elimination *vs.* –CH$_2$ migration/isomerization). The electron-withdrawing Mes[F] and C_6F_5 likely contribute to the stabilization of the **TS1** state by strengthening the B=N bond. This stabilization effect by Mes[F] substitution is reminiscent of that reported by Marder in borole systems[20a] and Jäkle in conjugated thienylborane systems[20b].

5.4 Conclusions

In summary, both electronic and steric effects have been found to have a significant and distinct impact on the photoreaction pathways of BN-heterocycles. With bulky, electron-donating aryl rings on the B atom, the photoelimination efficiency is greatly enhanced. In contrast, with sufficiently electron-withdrawing aryl groups on the B atom, bulky or not, photoisomerization occurs exclusively with high stereoselectivity. Bulky electron-withdrawing aryl groups such as Mes[F] appear to be the key for reversible photo-thermal isomerization of this new class of photochromic molecules. Balancing steric and electronic factors is found to be critical for achieving the desired molecular transformations based on BN-heterocycles. The first examples of BN-1,3,5-COT and BN-1,3,6-COT molecules have been obtained and their relationship in structural transformation has been demonstrated.

5.5 Selected Supporting Information
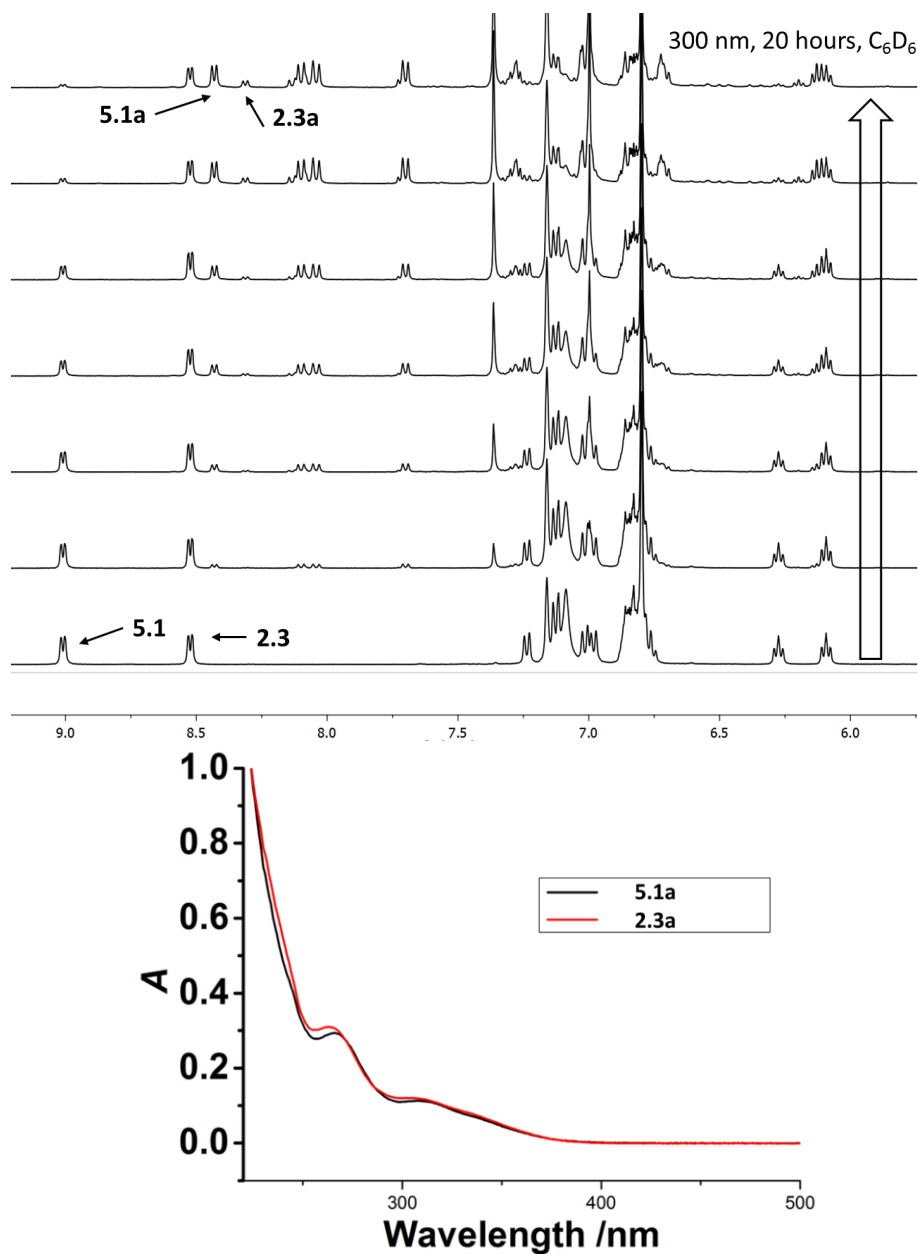
Figure 5.14 NMR competition experiment. Top: ^{1}H NMR spectra of **5.1** and **2.3** showing the relative conversion rate to **5.1** and **2.3a** after irradiation with UV (300 nm) in C_6D_6 under N_2. Bottom: UV/Vis spectra of **5.1** and **2.3** in THF (2.0×10^{-5} M) showing their similar absorption profile. The photoelimination quantum yield of **2.3** is about 4.4% and that of **5.1** was determined to be ~25%.

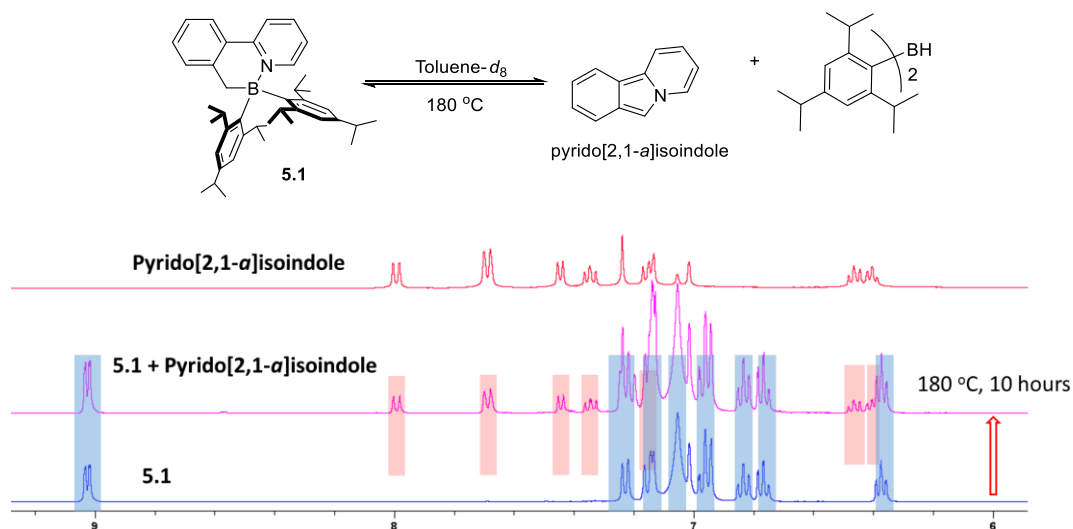**Figure 5.15** [1]H (middle and bottom spectrum) NMR spectra showing the clean conversion of **5.1** (blue highlight) to pyrido[2,1-*a*]isoindole (red highlight) in toluene-d_8 at 180 °C. ^{1}H (top) NMR spectra of pyrido[2,1-*a*]isoindole for comparison.

Figure 5.16 [1]H (middle), [11]B (top right), ^{19}F (bottom) NMR spectra showing the clean and reversible conversion of **5.2** to **5.2a** in C_6D_6.

Figure 5.17 Top: Hydrolysis of **5.2a**. Bottom: The crystal structure of **5.2a-OH**.
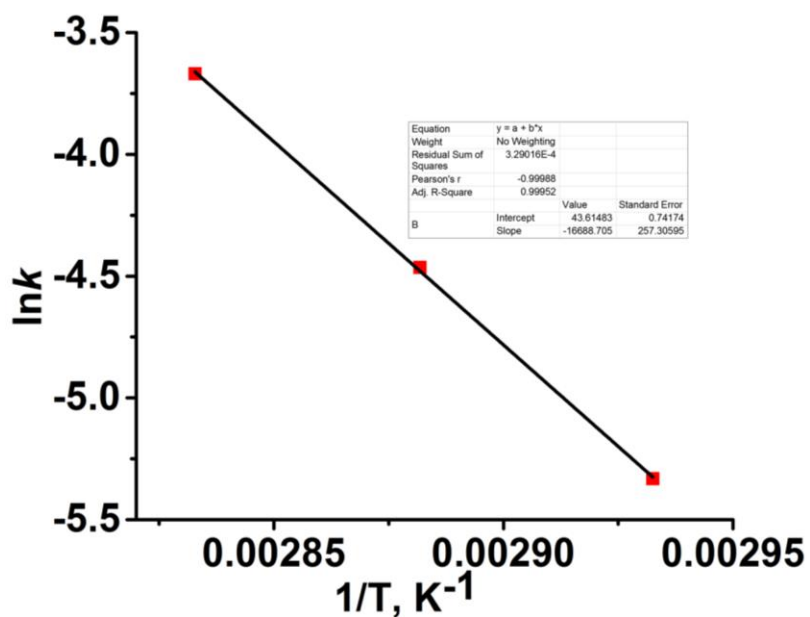
Figure 5.18 Activation energy investigation on thermal reaction 5**.2a** → **5.2**. (Intercept = 43.61483, Slope = -16688.705)
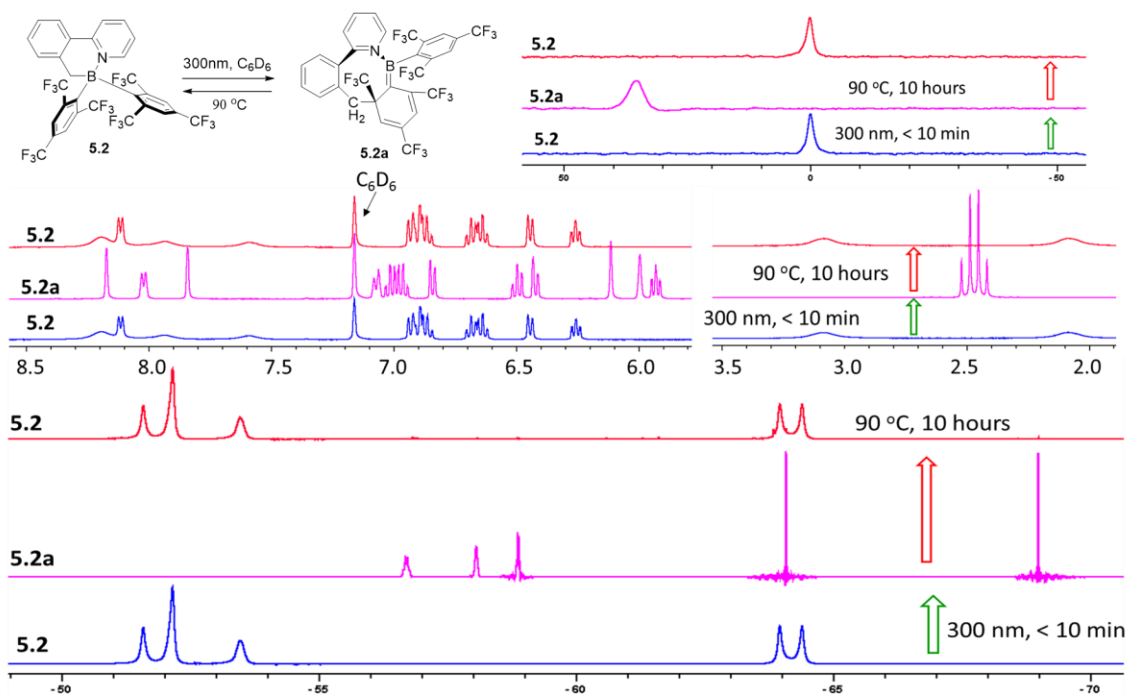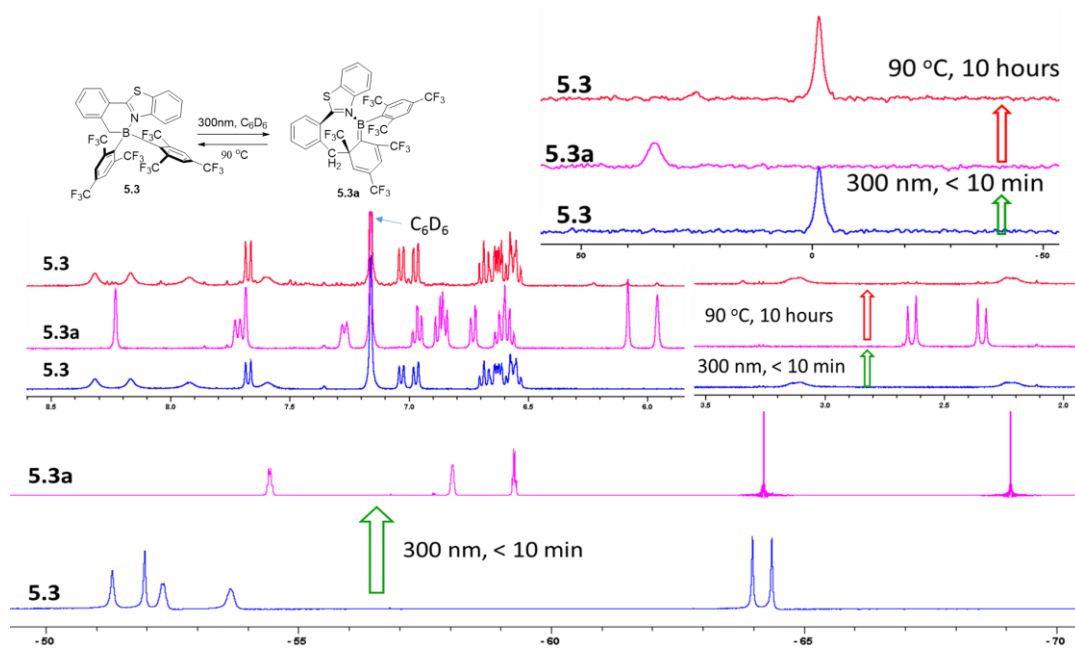
Figure 5.19 ^{1}H (middle), ^{11}B (top right), ^{19}F (bottom) NMR spectra showing the clean reversible conversion of **5.3** to **5.3a** in C$_6$D$_6$.
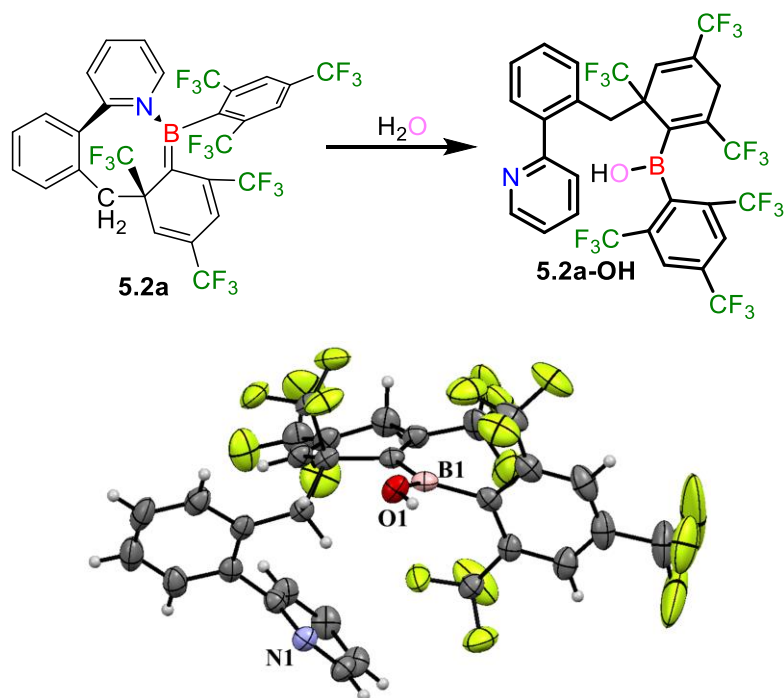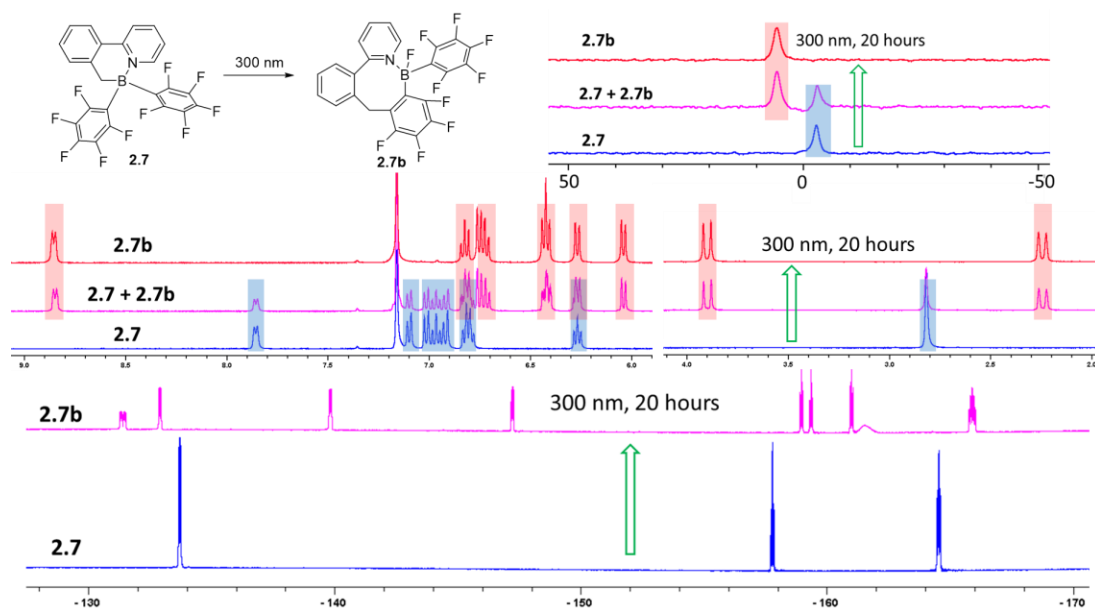

Figure 5.20 ^{1}H (middle), ^{11}B (top right), ^{19}F (bottom) NMR spectra showing the clean conversion of **2.7** to **2.7b** in C$_6$D$_6$ at room temperature and 300 nm irradiation.
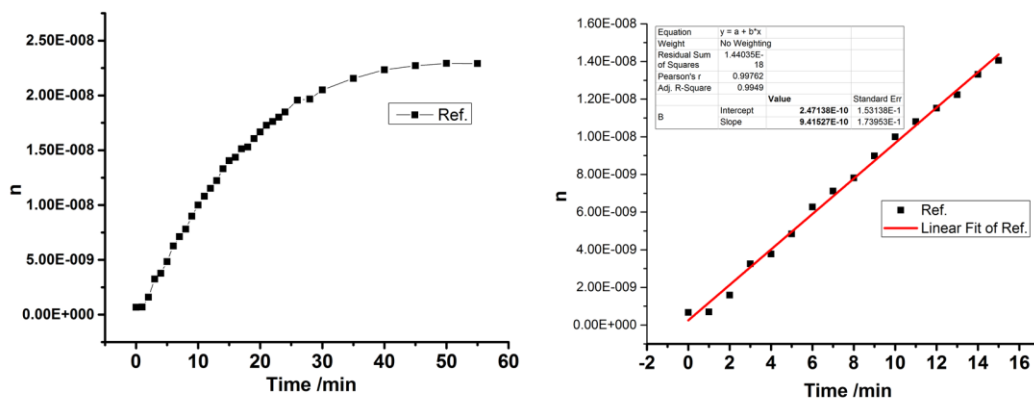
Figure 5.21 The photoisomerization kinetic data for B(ppy)Mes$_2$ in toluene ($\Phi_P = 0.86$). (Dark Isomer $\varepsilon = 5028$ M^{-1} cm^{-1})
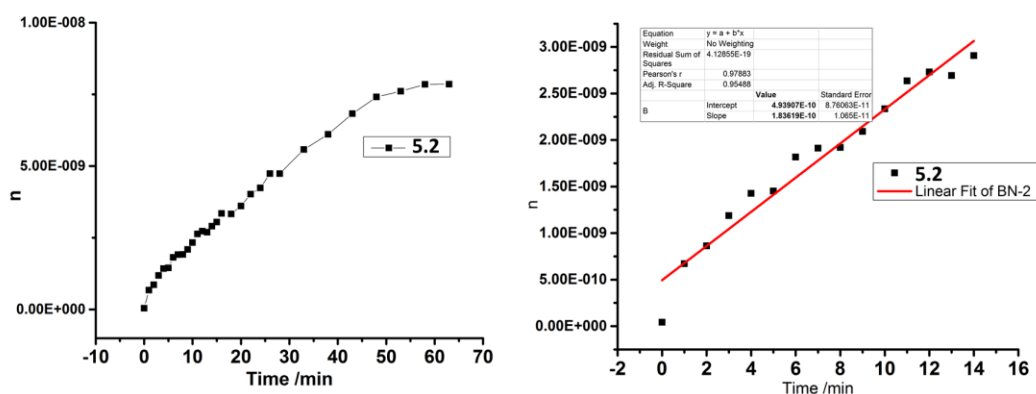
Dark Isomer $\varepsilon = 7113$ M^{-1} cm^{-1}
Measured using accurate amount dark isomer

$$\Phi_s = \Phi_r \frac{m_s A_r}{m_r A_s} = 0.86 * \frac{1.83619E{-}10 * 0.095345}{9.41527E{-}10 * 0.06814} = 23.4\%$$

Figure 5.22 The photoisomerization kinetic data for **5.2** in toluene.
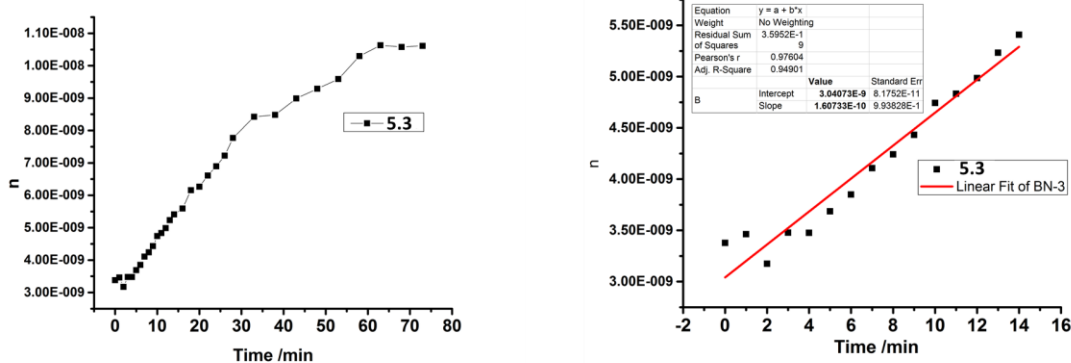
Dark Isomer ε = 8263 M^{-1} cm^{-1}
Measured using accurate amount dark isomer

$$\Phi_S = \Phi_r \frac{m_s A_r}{m_r A_s} = 0.86 * \frac{1.60733E-10*0.095345}{9.41527E-10*0.134565} = 10.4\%$$

Figure 5.23 The photoisomerization kinetic data for **5.3** in toluene.
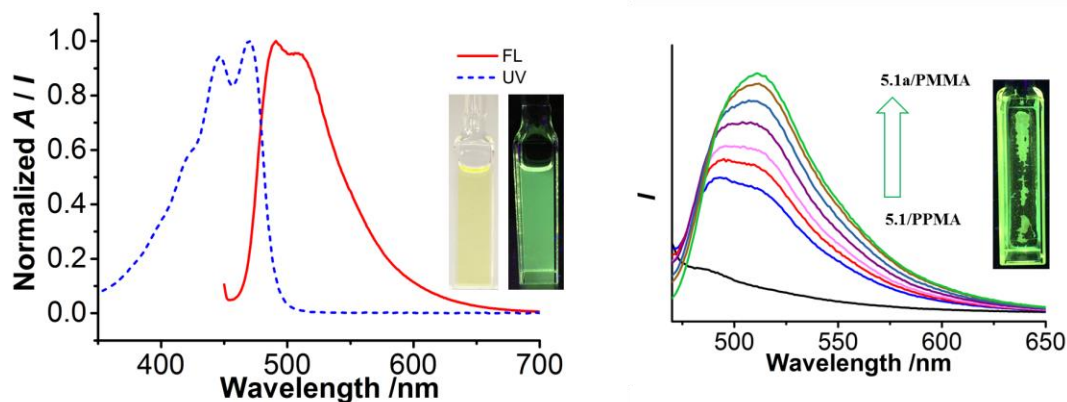
Figure 5.24 Left: UV/Vis (dot line) and fluorescence (solid line) spectra of **5.1a** in THF (1.0×10^{-4} M) and the fluorescent quantum efficiency of TIP azaborine **5.1a** is 0.27 in THF. Right: Fluorescence spectra showing the conversion of **5.1** in a PMMA film (20 wt%) to **5.1a**.

215
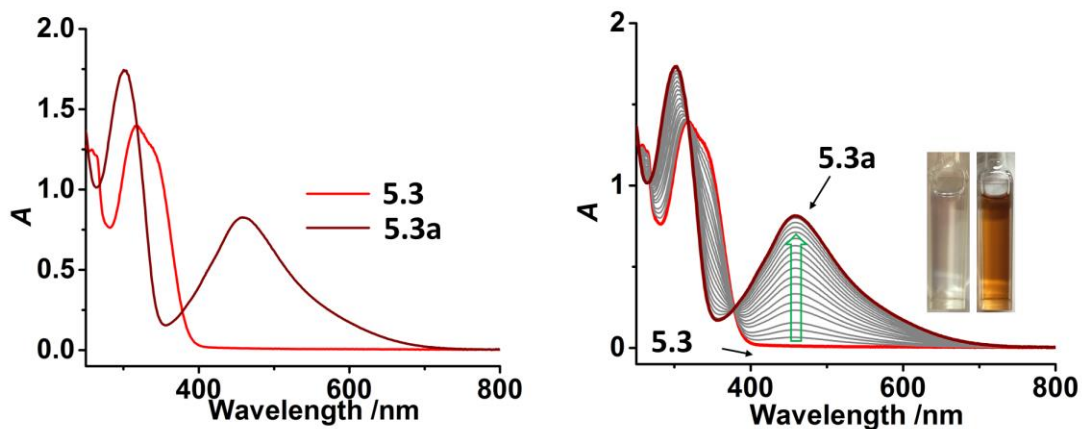
Figure 5.25 Left: UV/Vis spectra of **5.3** and **5.3a** in THF (1.0×10^{-4} M). Right: UV/Vis spectra showing the conversion of **5.3** in THF to **5.3a**.
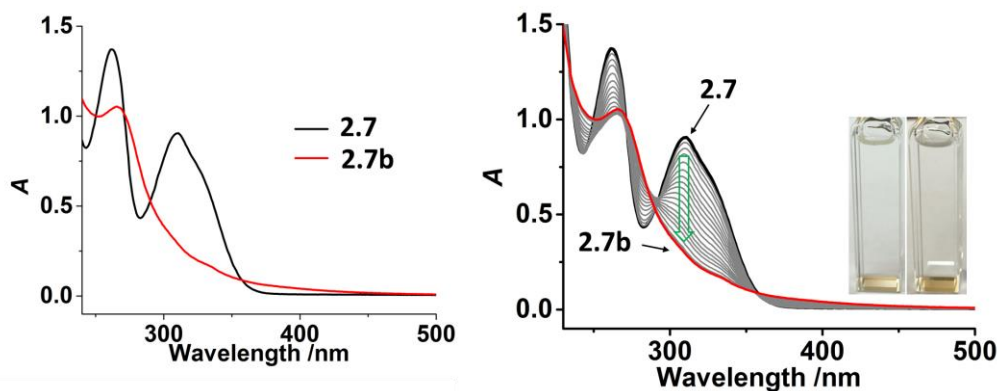
Figure 5.26 Left: UV/Vis spectra of **2.7** and **2.7b** in THF (1.0×10^{-4} M). Right: UV/Vis spectra showing the conversion of **2.7** in THF to **2.7b**.
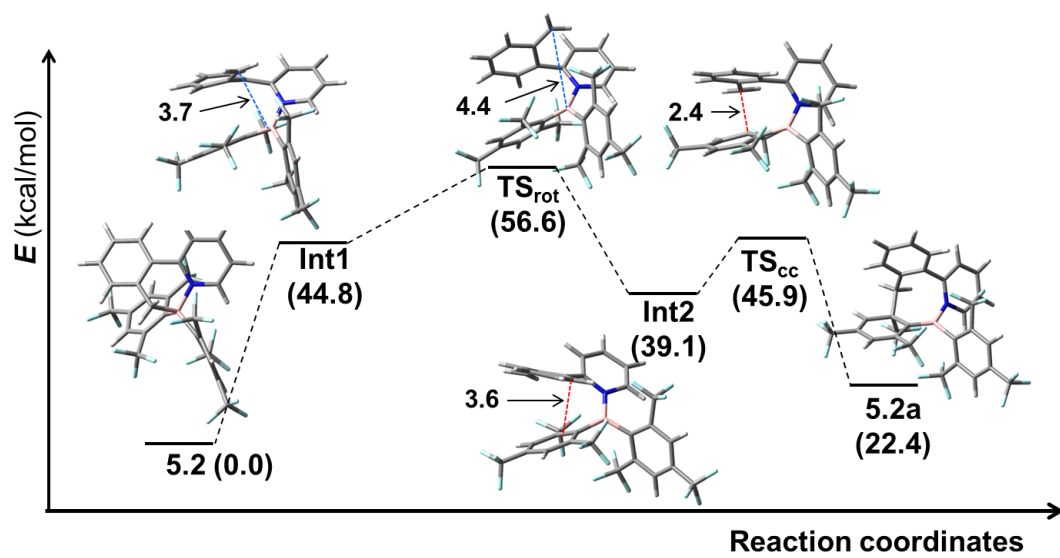
Figure 5.27 Calculated potential energy profile for the photoisomerization of **5.2**. The energies of the all key species are reported relative to **5.2** and given in the parentheses. Some key distances (in Å) are also shown.

5.6 Notes and References

The work described in this chapter includes contributions from the following publications:

- Yang, D.-T.; Mellerup, S. K.; Peng, J.-B.; Wang, X.; Li, Q.-S.; Wang, S.* *J. Am. Chem. Soc.* **2016**, *138,* 11513.

References:

(1) (a) *Microbial Enzymes and Biotechnology*; Fogarty, W. M., Kelly, C. T., Eds.; Springer Applied Science, New York, 2012, 2nd edition. (b) *Molybdenum and Molybdenum-Containing Enzymes*; Coughlan, M. P., Ed.; Pergamon Press, Willowdale, 1980. (c) *Immobilized Enzymes for Industrial Reactors*; Messing, R. A., Eds.; Academic Press, New York, 1975.

(2) (a) Grubbs, R. H.; Chang, S. *Tetrahedron* **1998**, *54*, 4413. (b) Schrock, R. R. *Tetrahedron* **1999**, *55*, 8141. (c) Anderson, J. S.; Rittle, J.; Peters, J. C. *Nature* **2013**, *501*, 804.

(3) (a) Braunschweig, H.; Dewhurst, R. D.; Schneider, A. *Chem. Rev.* **2010**, *110*, 3924. (b) Soleilhavoup, M.; Bertrand, G. *Acc. Chem. Res.* **2015**, *48*, 256. (c) Martin, C. D.; Soleilhavoup, M.; Bertrand, G. *Chem. Sci.* **2013**, *4*, 3020.

(4) (a) Berkovic, G.; Krongauz, V.; Weiss, V. *Chem. Rev.* **2000**, *100*, 1741 and references therein. (b) Irie, M. *Chem. Rev.* **2000**, *100*, 1685. (c) Ko, C.-C.; Yam, V. W.-W. *J. Mater. Chem.* **2010**, *20*, 2063.

(5) (a) *Boron Science New Technologies and Applications*; Hosmane, N. S., Eds.; CRC, Taylor & Francis, Boca Raton, 2012. (b) Entwistle, C. D.; Marder, T. B. *Chem. Mater.* **2004**, *16*, 4574. (c) Wakamiya, A.; Taniguchi, T.; Yamaguchi, S. *Angew. Chem. Int. Ed.* **2006**, *45*, 3170. (d) Chen, P.; Lalancette, R. A.; Jäkle, F. *Angew. Chem. Int. Ed.* **2012**, *51*, 7994. (e) Lorbach, A.; Hîbner, A.; Wagner, M. *Dalton Trans.* **2012**, *41*, 6048. (f) Escande, A.

Ingleson, M. J. *Chem. Commun.* **2015**, *51*, 6257. (g) Wang, X.-Y.; Wang, J.-Y.; Pei, J. *Chem. Eur. J.* **2015**, *21*, 3528. (h) Li, D.; Zhang, H.; Wang, Y. *Chem. Soc. Rev.* **2013**, *42*, 8416. (i) Stephan, D. W. Erker, G. *Angew. Chem. Int. Ed.* **2015**, *54*, 6400. (j) McGough, J. S.; Butler, S. M.; Cade, I. A.; Ingleson, M. J. *Chem. Sci.* **2016**, *7*, 3384. (k) Süsse, L.; Hermeke, J.; Oestreich, M. *J. Am. Chem. Soc.* **2016**, *138*, 6940. (l) *Boronic acids*; Hall, D. G., Ed.; Wiley-VCH, Weinheim, **2005**. (m) Brown, H. C. *Boranes in Organic Chemistry*, Cornell University Press, Ithaca, 1972. (n) Suzuki, A. *Heterocycles*, **2010**, *80*, 15. (o) Campbell, P. G.; Marwitz, A. J. V.; Liu, S.-Y. *Angew. Chem. Int. Ed.* **2012**, *51*, 6074. (p) Bosdet, M. J. D.; Piers, W. E. *Can. J. Chem.* **2009**, *87*, 8. (q) Molander, G. A. *J. Org. Chem.* **2015**, *80*, 7837.

(6) (a) Rao, Y.-L.; Amarne, H.; Zhao,S.-B.; McCormick, T.M.; Martić, S.; Sun, Y.; Wang, R.-Y.; Wang, S. *J. Am. Chem. Soc.* **2008**, *130*, 12898. (b) Rao, Y.-L.; Amarne, H.; Wang, S. *Coord. Chem. Rev.* **2012**, *256*, 759. (c) Rao, Y.-L.; Hörl, C.; Braunschweig, H.; Wang, S. *Angew. Chem. Int. Ed.* **2014**, *53*, 9086. (d) Lu, J.-S.; Ko, S.-B.; Walters, N. R.; Kang, Y.; Sauriol, F.; Wang, S. *Angew. Chem. Int. Ed.* **2013**, *52*, 4544. (e) Ko, S.-B.; Lu, J.-S.; Wang, S. *Org. Lett.* **2014**, *16*, 616. (f) Yang, D.-T.; Mellerup, S. K.; Wang, X.; Lu, J.-S.; Wang, S. *Angew. Chem. Int. Ed.* **2015**, *54*, 5498.

(7) Wang, S.; Yang, D.-T.; Lu, J.; Shimogawa, H.; Gong, S.; Wang, X.; Mellerup, S. K.; Wakamiya, A.; Chang, Y.-L.; Yang, C.; Lu, Z. H. *Angew. Chem. Int. Ed.* **2015**, 54, 15074.

(8) Pelter, A.; Smith, K.; Buss, D.; Norbury, A. *Tetrahedron Lett.* **1991**, 43, 6239.

(9) (a) Parker, C. A. *Proc. R. Soc. London A* **1953**, *220*, 104. (b) Abdallah, D.; Whelan, J.; Dust, J. M.; Hoz, S.; Buncel, E. *J. Phys. Chem. A* **2009**, *113*, 6640. (c) *General Chemistry: Principles and Modern Applications* Petrucci, R. H. *et. al.* 10th ed. Page 626-627.

(10) Frisch, M. J.; Trucks, G. W.; Schlegel, H. B.; Scuseria, G. E.; Robb, M. A.; Cheeseman, J. R.; Scalmani, G.; Barone, V.; Mennucci, B.; Petersson, G. A. H.; Nakatsuji, M.; Caricato, X.; Li, H. P. F.; Hratchian, A.; Izmaylov, J.; Bloino, G.; Zheng, J. L.; Sonnenberg, M.; Hada, M.; Ehara, K.; Toyota, R.; Fukuda, J.; Hasegawa, M.; Ishida, T.; Nakajima, Y.; Honda, O.; Kitao, H.; Nakai, T.; Vreven, J. A.; Montgomery Jr., J. E.; Peralta, F.; Ogliaro, M.; Bearpark, J. J.; Heyd, E.; Brothers, K. N.; Kudin, V. N.; Staroverov, T.; Keith, R.; Kobayashi, J.; Normand, K.; Raghavachari, A.; Rendell, J. C.; Burant, S. S.; Iyengar, J.; Tomasi, M.; Cossi, N.; Rega, J. M.; Millam, M.; Klene, J. E.; Knox, J. B.; Cross, V.; Bakken, C.; Adamo, J.; Jaramillo, R.; Gomperts, R. E.; Stratmann, O.; Yazyev, A. J.; Austin, R.; Cammi, C.; Pomelli, J. W.; Ochterski, R. L.; Martin, K.; Morokuma, V. G.; Zakrzewski, G. A.; Voth, P.; Salvador, J. J.; Dannenberg, S.; Dapprich, A. D.; Daniels, O.; Farkas, J. B.; Foresman, J. V.; Ortiz, J.; Cioslowski, J.; Fox, D. J. Gaussian 09 Revision C.01, 2010.

(11) (a) Becke, A. D. *J. Chem. Phys*. 1993, *98*, 5648. (b) Becke, A. D. *J. Chem. Phys.* **1993**, *98*, 1372. (c) Lee, C.; Yang, W.; Parr, R. G. *Phys. Rev. B* **1988**, *37*, 785.

(12) (a) Goerigk, L.; Grimme, S. *Phys. Chem. Chem. Phys*. 2011, *13*, 6670. (b) Grimme, S. *J Comput. Chem*. **2004**, *25*, 1463. (c) Grimme, S. *J Comput. Chem*. **2006**, *27*, 1787. (d) Grimme, S.; Antony, J.; Ehrlich, S.; Krieg, H. *J. Chem. Phys*. **2010**, *132*, 154104.

(13) Yanai, T.; Tew, D. P.; Handy, N. C. *Chem. Phys. Lett*. **2004**, *393*, 51.

(14) (a) Gonzalez, C.; Schlegel, H. B. *J. Chem. Phys*. **1989**, *90*, 2154. (b) Gonzalez, C.; Schlegel, H. B. *J. Phys. Chem*. **1990**, *94*, 5523.

(15) (a) Barone, V.; Cossi, M. *J. Phys. Chem. A* **1998**, *102*, 1995. (b) Cammi, R.; Mennucci, B.; Tomasi, J. *J. Phys. Chem. A*, **1999**, *103*, 9100. (c) Tomasi, J.; Mennucci, B.; Cammi, R. *Chem. Rev*. **2005**, *105*, 2999.

(16) (a) Paetzold, P.; Englert, U.; Finger, R.; Schmitz, T.; Tapper, A.; Ziembinski, R. *Z. Anorg. Allg. Chem.* **2004**, *630*, 508. (b) Hunold, R.; Pilz, M.; Allwohn, J.; Stadler, M.; Massa, W.; Schleyer, P. V. R.; Berndt, A. *Angew. Chem. Int. Ed. Engl.* **1989**, *28*, 781. (c) Pilz, M.; Stadler, M.; Hunold, R.; Allwohn, J.; Massa, W.; Berndt, A. *Angew. Chem. Int. Ed. Engl.* **1989**, *28*, 784. (d) Pilz, M.; Michel, H.; Berndt, A. *Angew. Chem. Int. Ed. Engl.***1990**, *29*, 401.

(17) (a) Klahn, M.; Rosenthal, U. *Organometallics* **2012**, *31*, 1235. (b) Caputo, C. B.; Hounjet, L. J.; Dobrovetsky, R.; Stephan, D. W. *Science*, **2013**, *341*, 1374. (c) Nair, N. G.; Mendoza-Cortes, J. L.; Abrol, R.; Goddard III, W. A.; Reddy, V. P. *J. Organomet. Chem.* **2013**, *747*, 133.

(18) (a) Polli, D.; Altoe, P.; Weingart, O.; Spillane, K. M.; Manzoni, C.; Brida, D.; Tomasello, G.; Orlandi, G.; Kukura, P.; Mathies, R. A.; Garavelli, M.; Cerullo, G. *Nature* **2010**, *467*, 440. (b) Blancafort, L. *ChemPhysChem* **2014**, *15*, 3166.

(19) Iida, A.; Saito, S.; Sasamori, T.; Yamaguchi, S. *Angew. Chem. Int. Ed*. **2013**, *52*, 3760.

(20) (a) Zhang, Z.; Edkins, R. M.; Haehnel, M.; Wehner, M.; Eichhorn, A.; Mailänder, L.; Meier, M.; Brand, J.; Brede, F.; Müller-Buschbaum, K.; Braunschweig, H.; Marder, T. B. *Chem. Sci.* **2015**, *6*, 5922. (b) Yin, X.; Chen, J.; Lalancette, R. A.; Marder, T. B.; Jäkle, F. *Angew. Chem. Int. Ed.* **2014**, *53*, 9761.

Chapter 6

Conclusions and Future Work

6.1 Conclusions

In this thesis, the reactivity and applications of BN-heterocycles have been investigated, with the aim to promote the efficiency of this novel elimination of BN-heterocycles. In the past four years, while I have been achieving the goal of increasing the efficiency of the photoelimination, I also discovered some unprecedented features, such as 1,1-hydroboration and a new photoisomerization system, which could advance the use of boron compounds in organic synthesis and molecular switching.

The elimination of BN-heterocycles with the formation of fluorescent azaborines not only can be driven by UV light, but also in some particular cases by heat. We also found that some BN-heterocycles underwent deborylation (or retro-1,1-hydroboration) generating pyrido[1,2-α]isoindole, which turns out to be a nucleophile and could undergo 1,1-hydroboration with boranes, with either electron-rich substituents (Mes$_2$BH, 9-BNN) or electron-deficient substituents ((C$_6$F$_5$)$_2$BH). Besides 1,1-hydroboration, pyrido[1,2-α]isoindole and its analogues are capable of undergoing formal [3+2] cycloaddition reactions acting as 1,3-dipoles, with the generation of Mes$_2$B-functionalized π-conjugated aromatic compounds.

A variety of new (BN)$_2$-heterocycles with extended conjugated backbones have been synthesized. The impact of the linker unit and the location and orientation of the boron chelate unit on the electronic properties and photoreactivity of this class of compounds have been examined. Furthermore, we have established that the photoelimination reaction can be extended to/and efficiently driven for several representative members of BN-heterocycles *in situ* through the

222

unprecedented EDE within an EL device. The discovery of the EDE phenomenon has a number of important synthetic and practical implications, as it provides a new approach for the design and preparation of novel organic materials as well as their implementation within optoelectronic device architectures.

Besides the investigation of external stimuli, we are finally capable of driving this photoelimination much more efficiently by introducing bulkier substituents onto the boron atom. Nevertheless, the photoreactivity could be tuned by different electronic property of substituents, that is, once electron-deficient substituents are introduced on the boron atom, bulky or not, the photoreactivity could be switched from photoelimination to photoisomerization exclusively.

All the work presented in this thesis has advanced our understanding of the unique properties and transformations of BN-heterocycles, and some of them have shown to be promising for future applications in optoelectronic devices and molecular switching.

6.2 Future Work

Although we have made some progress on the external stimuli driven transformations of BN-heterocycles, the chemoselectivity of photoelimination on boron atom is still not clear. Therefore, for the future work the selectivity of photoelimination will be investigated (Figure 6.1), with the aim to sort out the photoelimination order of different functional groups, such as H, F, acetylene, phenyl, mesityl, etc. With respect to compounds **6.1** – **6.4** and **6.11** – **6.12**, we will study if the photoelimination still occurs when the substituents on boron are switched to other functional groups, and compound **6.3** could allow to study the influence of methyl group on the carbon atom on photoreactivity. For BN-heterocycles **6.5** – **6.10**, the selectivity of photoelimination on different functional groups on boron atom will be examined, with the expectation to rank the photoelimination order of H, acetylene, phenyl, mesityl upon UV irradiation.
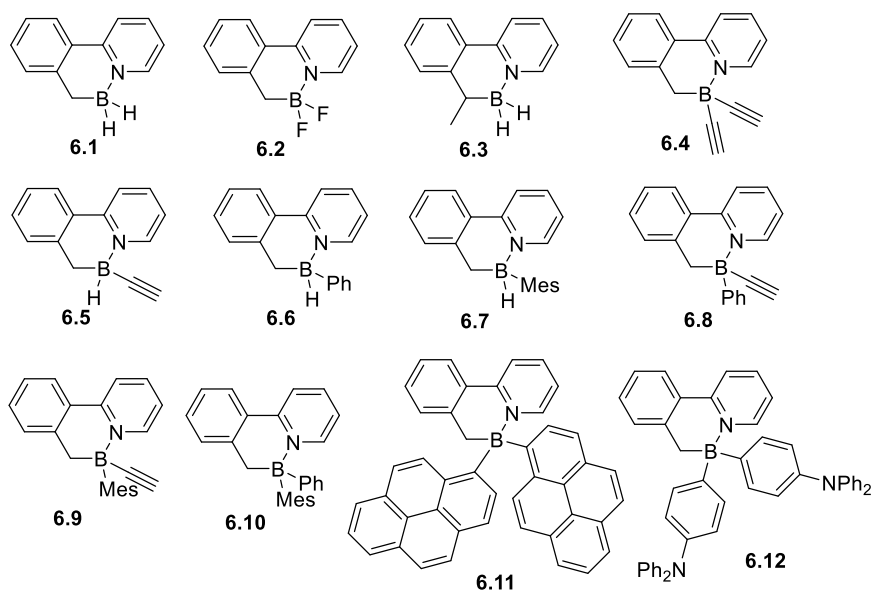
223

Figure 6.1 The structures of BN-heterocycles with different substituents on the boron atom.

According to preliminary data, compounds **6.2**, **6.4**, **6.8**, **6.11** and **6.12** were photoreactivity-inert and compounds **6.1** and **6.5** – **6.7** underwent photoelimination with the formation of H_2; however, BN-heterocycle **6.3** and **6.10** just decomposed upon UV light irradiation and **6.9** underwent photoelimination generating corresponding azaborine in low yield with the elimination of mesitylene.